



**University of  
Nottingham**

UK | CHINA | MALAYSIA

**Development of a New n-Dodecane-n-Butanol-PAH  
Reduced Mechanism and the Applications Under  
Diesel Spray Combustion**

Edwin Jia Chiet Choo, M.Eng. (Hons)

*Thesis Submitted to the University of Nottingham Malaysia for the  
Degree of Doctor of Philosophy*

August 2022

## ABSTRACT

Despite exhibiting low throttling losses and generating high thermal efficiency, it is inevitable that the heterogeneous combustion nature of a diesel engine will cause large amount of soot to be produced. Lately, n-butanol has emerged as a very competitive second-generation biofuel in diesel engine because of its similarities in physiochemical properties to diesel fuel. As an oxygenated hydrocarbon, blending n-butanol with diesel is able to reduce the harmful exhaust emissions. According to the literature, most studies related to diesel-n-butanol are conducted experimentally whereas only a handful of them are done numerically. However, numerical modelling is as important as conducting experiments as it allows researchers to gain further insights on the chemical kinetics. In order to support accurate combustion modelling results, the selection of a chemical kinetic mechanism that could describe the combustion chemistry precisely is crucial but it is found that the developments of diesel-n-butanol mechanisms in particular those using long carbon chain surrogates are still scarce. Since there is also a lack in effort on the combustion modelling of diesel-n-butanol, this study aims to address the limitations related to the chemical kinetic mechanisms for diesel-n-butanol and the applications in multi-dimensional simulations concerning the spray combustion.

First, a reduced chemical kinetic mechanism for n-dodecane-n-butanol-polycyclic aromatic hydrocarbon (PAH) is developed using the direct relation graph with error propagation (DRGEP) and isomer lumping methods. In the mechanism, n-dodecane is being used as the diesel surrogate fuel. Consequently, the n-dodecane-n-butanol-PAH mechanism consists of 105 species and 584 reactions (DB105) and it is validated under a wide range of engine operating conditions such as shock tube (ST) ignition delay (ID) times, jet-stirred reactor (JSR) and premixed laminar flame species concentrations and laminar flame speed. The DB105 mechanism shows good agreements to the experimental measurements and predictions by the detailed mechanism for majority of the tested conditions. Subsequently, a set of Computational Fluid Dynamics (CFD) sub-models is formulated to describe the spray, ignition, combustion and soot of n-dodecane-n-butanol in a diesel engine-like constant volume combustion chamber. The fidelity of the DB105 mechanism is further assessed in CFD

simulations by comparing the predicted liquid penetration length (LPL), vapour penetration length (VPL), ID, flame lift-off length (FLOL) and soot to the experimental measurements. Nine cases at various n-butanol blending ratios and ambient temperatures are tested and results show that the predicted LPL and VPL deviated with a maximum of 4% whereas the ID and FLOL deviated by 20% and 12%, respectively. For soot validation, the soot volume fraction (SVF) of pure n-dodecane (Bu0) at 850 K and 900 K are compared to the experimental measurements where the maximum errors are recorded to be 1.0 ppm (100%) and 0.3 ppm (10%), respectively. However, the location and size of the soot cloud are also well emulated. Overall, the good validation results of the DB105 mechanism indicates that improvements have been made to the present mechanism and it is more superior than the existing n-dodecane-n-butanol mechanisms in terms of its size and accuracy.

The fundamental ignition, combustion and soot characteristics of n-dodecane-n-butanol spray flames are then numerically investigated using the formulated CFD sub-models and the DB105 mechanism. Results show that n-dodecane-n-butanol blends undergo a two-stage ignition regardless of n-butanol blending ratios and ambient temperatures. The first-stage ignition site is located at the spray periphery for all test cases except for 80% n-dodecane – 20% n-butanol (Bu20) at 800 K. However, the second-stage ignition site moves to the spray head for all test cases but it remains at the spray periphery for Bu0. At quasi-steady state, key species that pertains to ignition are shifted to the fuel-lean region of the spray at higher n-butanol blending ratio and at lower ambient temperature. Moreover, combustion mode analysis shows that the low temperature combustion (M-LTC) mode is dominant at the first-stage ignition but gradually diminishes as the high temperature combustion (M-HTC) and high temperature diffusion combustion (M-HTC-diff) modes take over from the second-stage ignition onwards. Meanwhile, simulation results also show that as the n-butanol blending ratio increases and as the ambient temperature decreases, the SVF and soot particle size in the n-dodecane-n-butanol spray flames decrease. Comparing to the case of Bu0 (900 K), both peak SVF and soot particle size of Bu40 (900 K) decreases by 93.11% and 56.58%, respectively. Similarly, Bu20 (800 K) shows a decrease of 88% and 50.62% in the peak SVF and soot particle size when comparing to Bu20 (900 K). Apart from the SVF and soot particle size, the soot precursor species

also decrease at higher n-butanol blending ratio and at lower ambient temperature. Besides, the spatial distributions of soot and its relevant species shrink due to the lower local equivalence ratio. The soot formation and oxidation mechanisms are suppressed at higher n-butanol blending ratio and at lower ambient temperature. However, the soot formation mechanism is more influential to the resulting soot. Nonetheless, the high oxygen concentration in high n-butanol blends have shown to be able to compensate the deteriorated soot oxidation mechanism while suppressing the soot formation mechanism simultaneously. As a result, the SVF and soot particle size decrease more significantly with the addition of n-butanol blending ratio than the decrease in ambient temperature.

# LIST OF PUBLICATIONS

## Journal Papers:

- Choo EJC, Cheng X, Scribano G, Ng HK, Gan S. Development and validation of a n-butanol reduced chemical kinetic mechanism under engine relevant conditions. *Int J Chem Kinet* 2021;53:1285–305. doi:10.1002/kin.21533
- Choo EJC, Cheng X, Ng HK, Gan S, Scribano G. Development and validation of a new n-dodecane-n-butanol-PAH reduced mechanism under diesel engine-relevant conditions. *Fuel* 2022;319:123829. doi:10.1016/j.fuel.2022.123829
- Choo EJC, Cheng X, Scribano G, Ng HK, Gan S. Numerical investigation on the ignition and flame characteristics of n-dodecane-n-butanol spray under diesel engine conditions. *Fuel* 2022;325:124881. doi:10.1016/j.fuel.2022.124881
- Choo EJC, Cheng X, Scribano G, Ng HK, Gan S. Numerical investigation on the temporal and quasi-steady state soot characteristics of n-dodecane-n-butanol spray combustion. *Energy* 2023;268:126770. doi:10.1016/j.energy.2023.126770.
- Choo EJC, Cheng X, Scribano G, Ng HK, Gan S. Recent advancement in the chemical kinetics, combustion, emissions and spray characteristics of n-butanol in SI, CI and HCCI engines (Under Preparation).

## Conference:

- Choo EJC, Cheng X, Gan S, Ng HK and Scribano G, 2021. Spray combustion simulation study of diesel-n-butanol blend in a constant volume combustion chamber In: 4th International Conference on Mechanical Engineering and Power Engineering (MEPE 2021)

## ACKNOWLEDGEMENTS

First and foremost, I would like to express my deepest gratitude to my main supervisor, Dr. Cheng Xinwei for providing valuable advice, guidance and support since the beginning and also providing this opportunity to pursue the PhD. I am also grateful to Dr. Gianfranco Scribano for his willingness to guide me towards the end of my study and also his time and effort to review my journal papers. Besides, I would also want to thank my co-supervisors, Prof. Ng Hoon Kiat and Prof. Gan Suyin for providing me much needed moral support at times when I feel like giving up. The University of Nottingham is also deeply thanked for providing me the Engineering PhD Research Scholarship and funding the project as a whole.

I would like to thank all my family members who constantly provide the unwavering support and unconditional love and I know you all have kept me in your prayers every day. I am also extremely grateful to my partner, Ho Jinn Shyuan, who keeps cheering me up and tell me everything will be fine when everything seems so wrong. Thank you for the constant motivation and reminder that everything will be fine.

Special thanks to my seniors, Dr. Tan Jing Yang and Dr. Yap Jing Ying for giving me valuable advice and helped me settle down at the start of my PhD study. Besides them, I am particularly thankful for Chee Hock Leong, Lim Han Leong, Kow Yu Yang, Dr. Diem Nguyen, Jasmine Lee, Leong Chia Choong and Jessica Ooi for creating laughter and fun during my PhD study which helps me a lot in releasing stress. You guys have stood by me in this PhD journey and I owe you all one.

I would like to thank my Daddy God who has never leave nor forsake me even when I am walking through the valley of the shadow of death. At times, I cry to You and You answered me. I believe that everything happens during my PhD are part of Your plan and they are just meant to make me stronger.

Lastly, to all my family members, friends, colleagues, supervisors, lecturers from the Department of M3 and everyone that I have come across in university, I pray that you will remain healthy, strong and live up to a 120 years old with your eyes not dim nor your natural force abated. You all have made me who I am today. Thank you once again for making my PhD a memorable one and may the grace of God be with you all.

# TABLE OF CONTENTS

ABSTRACT.....	i
LIST OF PUBLICATIONS .....	iv
ACKNOWLEDGEMENTS .....	v
ABBREVIATIONS .....	ix
NONMENCLATURE.....	xii
LIST OF FIGURES .....	xvi
LIST OF TABLES .....	xx
CHAPTER 1 INTRODUCTION .....	1
1.1 Background .....	1
1.2 Alcohol-Based Biofuels .....	3
1.3 Potential of n-Butanol Fuel .....	5
1.4 Current Understanding on the Combustion and Emission Characteristics of Diesel/n-Dodecane-n-Butanol Blends.....	6
1.5 Research Objectives .....	9
1.6 Thesis Outline.....	11
CHAPTER 2 LITERATURE REVIEW .....	13
2.1 Introductory Remarks .....	13
2.2 Chemical Kinetic Mechanism .....	13
2.2.1 Diesel Surrogate .....	13
2.2.2 PAH.....	25
2.2.3 n-Butanol and its Isomers .....	28
2.2.4 Diesel-n-Butanol Blends .....	34
2.3 Chemical Kinetic Reduction Methods .....	36
2.3.1 DRG .....	36
2.3.2 DRGEP.....	38
2.3.3 DRGASA .....	40
2.3.4 DRGEPASA .....	41
2.3.5 Isomer Lumping.....	42
2.4 Numerical Modelling of Diesel-n-Butanol Blends under Diesel Engine Conditions .....	43
2.5 Concluding Remarks .....	45
CHAPTER 3 COMPUTATIONAL MODELS.....	48
3.1 Introductory Remarks.....	48
3.2 Chemical Kinetics .....	48

3.2.1	Homogeneous 0D Reactor Models .....	51
3.2.2	1D Premixed Laminar Flames Models .....	53
3.2.3	SA and ROP .....	55
3.3	CFD Sub-Models.....	57
3.3.1	Spray Breakup Model .....	57
3.3.2	Turbulence Model .....	59
3.3.3	Combustion Model.....	61
3.3.4	Soot Model.....	62
3.4	Concluding Remarks .....	63
CHAPTER 4 DEVELOPMENT OF A N-DODECANE-N-BUTANOL-PAH REDUCED MECHANISM .....		65
4.1	Introductory Remarks .....	65
4.2	Reduction Methodology .....	65
4.3	n-Dodecane Base Mechanism .....	66
4.4	PAH Sub-Mechanism.....	67
4.5	n-Butanol Sub-Mechanism.....	67
4.5.1	First Stage: DRGEP Method.....	68
4.5.2	Second Stage: Isomer Lumping Aided by RPA.....	68
4.5.3	Third stage: DRGEP Method.....	70
4.6	Combined Mechanism.....	70
4.7	Validation of Mechanism Under 0D and 1D Conditions .....	75
4.7.1	ID times.....	75
4.7.2	JSR Species Concentration .....	77
4.7.3	Laminar Flame Speed .....	80
4.7.4	Premixed Laminar Flame.....	82
4.8	Concluding Remarks .....	85
CHAPTER 5 2D SPRAY COMBUSTION SIMULATIONS SETUP .....		86
5.1	Introductory Remarks .....	86
5.2	Experimental Setup .....	86
5.3	Numerical Formulations.....	88
5.3.1	Mesh Independence Test.....	91
5.3.2	Time-step Parametric Study.....	95
5.3.3	Turbulence Model Parametric Study .....	97
5.3.4	Spray Breakup Model Parametric Study.....	100
5.3.5	Optimised Numerical Setup.....	101
5.4	Non-reacting Spray Simulations .....	102



5.5	Reacting Spray Simulations .....	103
5.5.1	ID and FLOL Predictions .....	103
5.5.2	Soot Predictions .....	106
5.6	Concluding Remarks .....	109
CHAPTER 6 IGNITION AND COMBUSTION CHARACTERISTICS OF N-DODECANE-N-BUTANOL SPRAY .....		110
6.1	Introductory Remarks .....	110
6.2	Global Combustion Characteristics .....	110
6.3	Flame Ignition Characteristics .....	112
6.4	Transitioning to Quasi-Steady State .....	120
6.5	Quasi-Steady Flame .....	126
6.6	Combustion Mode Analysis .....	130
6.7	Concluding Remarks .....	134
CHAPTER 7 SOOT MODELLING OF N-DODECANE-N-BUTANOL SPRAY		135
7.1	Introductory Remarks .....	135
7.2	Transient SVF and Soot Particle Size .....	135
7.3	Temporal Evolution of Soot Intermediate Species .....	138
7.4	Normalised SVF, Particle Size and Intermediate Species .....	145
7.5	Quasi-Steady Spatial Distributions of Soot and its Intermediate Species .....	147
7.6	Quasi-Steady Distributions of Soot Particle Size and Number Density ...	152
7.7	Soot Relevant Rates at Quasi-Steady State .....	154
7.8	Concluding Remarks .....	158
CHAPTER 8 CONCLUSIONS AND FUTURE WORK .....		159
8.1	Conclusions .....	159
8.1.1	Development and Validation of n-Dodecane-n-Butanol-PAH Mechanism .....	159
8.1.2	Formulation and Validation of a CFD-Chemical Kinetic Modelling Approach in a Constant Volume Combustion Chamber .....	160
8.1.3	Investigation on the Ignition and Combustion Characteristics of n-Dodecane-n-Butanol Spray .....	161
8.1.4	Soot Modelling of n-Dodecane-n-Butanol Spray .....	162
8.2	Future work .....	163
REFERENCES .....		165
APPENDIX .....		186
Appendix A: Chemical Reactions for the DB105 Mechanism .....		186

## ABBREVIATIONS

0D	Zero-dimensional
1D	One-dimensional
2D	Two-dimensional
3D	Three-dimensional
A <sub>1</sub>	Benzene
A <sub>2</sub>	Naphthalene
A <sub>2</sub> R <sub>5</sub>	Acenaphthylene
A <sub>3</sub>	Phenanthrene
A <sub>4</sub>	Pyrene
A <sub>7</sub>	Coronene
a-C <sub>3</sub> H <sub>4</sub>	Allenes
ASOI	After start of injection
BFS	Breadth-first search
BSFC	Brake specific fuel consumption
BTE	Brake thermal efficiency
Bu0	100% n-dodecane
Bu20	80% n-dodecane-20% n-butanol
Bu40	60% n-dodecane-40% n-butanol
C	Carbon
C <sub>10</sub> H <sub>22</sub>	n-Decane
C <sub>12</sub> H <sub>26</sub>	n-Dodecane
C <sub>14</sub> H <sub>30</sub>	n-Tetradecane
C <sub>16</sub> H <sub>34</sub>	n-Hexadecane
C <sub>2</sub> H <sub>2</sub>	Acetylene
C <sub>2</sub> H <sub>4</sub>	Ethylene
C <sub>2</sub> H <sub>6</sub>	Ethane
C <sub>3</sub> H <sub>3</sub>	Propargyl
C <sub>4</sub> H <sub>2</sub>	Diacetylene
C <sub>4</sub> H <sub>4</sub>	Vinylacetylene, Cyclobutadiene
C <sub>4</sub> H <sub>8</sub> OH	Hydroxybutyl radical
C <sub>4</sub> H <sub>9</sub> OH	Butanol
CAD	Crank angle degree
CFD	Computational fluid dynamics
CH <sub>2</sub> CHO	Vinoxy radical
CH <sub>2</sub> O	Formaldehyde
CH <sub>3</sub> CHO	Acetaldehyde
CH <sub>4</sub>	Methane
CI	Compression ignition
CO	Carbon monoxide

CO <sub>2</sub>	Carbon dioxide
COV	Coefficient of variance
DFS	Depth-first search
DIC	Direct interaction coefficient
DME	Dimethyl ether
DRG	Direct relation graph
DRGASA	Direct relation graph and sensitivity analysis
DRGEP	Direct relation graph with error propagation
DRGEP SA	Direction relation graph with error propagation and sensitivity analysis
ECN	Engine combustion network
FLOL	Flame lift-off length
H	Hydrogen atom
H <sub>2</sub>	Hydrogen
H <sub>2</sub> O	Water
H <sub>2</sub> O <sub>2</sub>	Hydrogen peroxide
HAB	Height above burner
HACA	H-Abstraction-Carbon-Addition
HCCI	Homogeneous charge compression ignition
HO <sub>2</sub>	Hydroperoxyl
HRR	Heat release rate
ID	Ignition delay
IMEP	Indicated mean effective pressure
JSR	Jet-stirred reactor
KH-RT	Kelvin-Helmholtz – Rayleigh-Taylor
LPL	Liquid penetration length
LTC	Low temperature combustion
M-HTC	High temperature combustion mode
M-HTC-diff	High temperature diffusion combustion mode
M-LTC	Low temperature combustion mode
N <sub>2</sub>	Nitrogen
nC <sub>4</sub> H <sub>9</sub> OH	n-Butanol
NOSE	New One Shot Engine
NO <sub>x</sub>	Nitrogen oxides
NTC	Negative temperature coefficient
O <sub>2</sub>	Oxygen
OC <sub>12</sub> H <sub>23</sub> OOH	Ketohydroperoxide
OH	Hydroxyl radical
OIC	Overall interaction coefficient
OPPDIF F	Opposed-flow diffusion flame
PAH	Polycyclic aromatic hydrocarbon
PIC	Path-dependent interaction coefficient



---

PISO	Pressure-Implicit with Splitting of Operators
PPC	Partially premixed combustion
PPCI	Partially premixed compression ignition
PPM	Parts per million
PSR	Perfectly stirred reactor
RANS	Reynolds-averaged Navier-Stokes
RCCI	Reactivity controlled compression ignition
RCM	Rapid compression machine
RNG	Re-normalisation group
ROC	Rate of consumption
ROP	Rate of production
RPA	Reaction pathway analysis
SA	Sensitivity analysis
SI	Spark ignition
ST	Shock tube
SVF	Soot volume fraction
TRF	Toluene reference fuel
UHC	Unburned hydrocarbon
VPL	Vapour penetration length

# NONMENCLATURE

$A$	Pre-exponential factor [Varies]; Cross-section area [ $\text{m}^2$ ]
$a$	Radius of liquid jet [m]
$a_{ki}$	Model parameter [-]
$A_m$	Surface area of the $m$ th material [ $\text{m}^2$ ]
$a_n$	Coefficient of polynomial fit [-]
$b^*_{\text{nuc}}$	Normalised radical nuclei concentration [No. of particles $\times 10^{-15}/\text{kg}$ ]
$B_0$	Model constant [-]
$B_1$	Breakup time model constant due to KH [-]
$C_{1\varepsilon}$	Model constant [-]
$C_{2\varepsilon}$	Model constant [-]
$C_{3\varepsilon}$	Model constant [-]
$C_A$	Rate of consumption of species A [-]
$\bar{C}^d_{ki}$	Normalised species destruction [-]
$C_L$	Levich constant [-]
$C_{\text{oxid}}$	Model constant [-]
$C_p$	Constant pressure specific heat capacity [ $\text{J}/\text{kgK}$ ]
$C_{Pk}$	Constant pressure specific heat capacity of the $k$ th species [ $\text{J}/\text{kgK}$ ]
$\bar{C}^p_{ki}$	Normalised species production [-]
$C_{RT}$	Model constant [-]
$C_a$	Model constant [-]
$C_\alpha$	Rate of soot inception [ $1/\text{s}$ ]
$C_\beta$	Model constant [-]
$C_\gamma$	Model constant [-]
$C_\gamma$	Rate of soot surface growth [ $\text{kg}/\text{m}^{0.5}\text{kmols}$ ]
$C_\mu$	Model constant [-]
$C_\tau$	Model constant [-]
$C_\omega$	Model constant [-]
$d_0$	Reference nozzle diameter [m]
$D_{i,m}$	Mass diffusion coefficient for species $i$ [-]
$D_{km}$	Mixture-averaged diffusion coefficient [-]
$d_p$	Mean diameter of soot particle [m]
$D_{T,i}$	Thermal diffusion coefficient for species $i$ [-]
$E$	Activation energy [ $\text{J}/\text{mol}$ ]
$F$	Residual vector [Varies]
$G_b$	Turbulence kinetic energy due to buoyancy [ $\text{m}^2/\text{s}^2$ ]
$G_k$	Turbulence kinetic energy due to mean velocity gradients [ $\text{m}^2/\text{s}^2$ ]

$g_t$	Droplet acceleration [m/s <sup>2</sup> ]
$H$	Enthalpy [J/mol]
$h_k$	Specific enthalpy of $k$ th species [J/mol]
$I$	Total number of reactions [-]
$\bar{J}_i$	Diffusion flux for species $i$ [kg/m <sup>2</sup> s]
$j$	Reactor number [-]
$k$	Turbulence kinetic energy [m <sup>2</sup> /s <sup>2</sup> ]
$K_{ci}$	Equilibrium constant of the $i$ th species [Varies]
$k_{fi}$	Forward rate constant for the $i$ th reaction [Varies]
$K_{pi}$	Equilibrium constant of the $i$ th species [Varies]
$k_{ri}$	Reverse rate constant for the $i$ th reaction [Varies]
$K_{RT}$	Wave number [1/m]
$L$	Breakup length of liquid core [m]
$l$	Model constant [-]
$M$	Soot mass concentration [kg/m <sup>3</sup> ]
$m$	Model constant [-]
$\dot{m}$	Outlet mass flow rate [kg/s]
$\dot{M}$	Mass flow rate [kg/s]
$\dot{m}^*$	Inlet mass flow rate [kg/s]
$M_p$	Constant for mass of soot particle inception [kg/kgmol]
$MW_c$	Molar mass of carbon [kg/mol]
$MW_H$	Molar mass of hydrogen [kg/mol]
$MW_\alpha$	Molar mass of species $\alpha$ [kg/mol]
$n$	Number of species along the pathway [-]
$N$	Soot particle number density [Number of particle/m <sup>3</sup> ]
$n$	Model constant [-]
$N_A$	Avogadro number [1/mol]
$n_{c,\alpha}$	Number of carbon atom of species $\alpha$ [-]
$n_{h,\alpha}$	Number of hydrogen atom of species $\alpha$ [-]
$N_{inlet}^{(j)}$	Number of inlets in each reactor $j$ [-]
$N_{norm}$	Value used to normalise soot number density [particles]
$N_{PSR}$	Total number of reactor modules in the reactor network [-]
$n_R$	Total number of reactions [-]
$Oh$	Ohnesorge number [-]
$P$	Pressure [bar]
$P_A$	Rate of production of species A [-]
$P_{atm}$	Atmospheric pressure [Pa]
$P_k$	Molar production [mol/m <sup>3</sup> s]
$q_i$	Rate of progress for the $i$ th reaction [Varies]

$\dot{Q}_{rad}$	Heat loss due to radiation [J/s]
$R$	Universal gas constant [J/molK]
$r_{AB}$	Species coupling dependency ratio [-]
$R_{AB}$	Overall interaction coefficient [-]
$r_c$	Radius of child droplet [m]
$Re_l$	Reynolds number [-]
$R_i$	Net production rate of species $i$ [mol/s]
$R_{rj}$	Fraction of the outflow [-]
$S$	Entropy [J/molK]
$Sc_t$	Turbulent Schmidt number [-]
$S_i$	Rate of creation from the dispersed phase plus any user-defined source for species $i$ [mol/s]
$\dot{s}_{k,m}$	Molar surface production rate [mol/m <sup>2</sup> s]
$T$	Temperature [K]
$Ta$	Taylor number [-]
$T_a$	Activation temperature for nucleation [K]
$u$	Fluid velocity [m/s]
$U$	Relative velocity [m/s]
$V$	Reactor volume [m <sup>3</sup> ]
$\Lambda$	Wavelength [m]
$v''_{k,i}$	Reverse stoichiometric coefficient for the $i$ th reaction [-]
$\nu_l$	Viscosity of liquid fuel [Pa s]
$\nu_{A,i}$	Stoichiometric coefficient of species A in reaction $i$ [-]
$V_c$	Correction velocity [-]
$V_d$	Diffusion velocity [m/s]
$V_k$	Diffusion velocity of $k$ th species [m/s]
$\nu_{k,i}$	Difference between forward and backward stoichiometric coefficients [-]
$\nu'_{k,i}$	Forward stoichiometric coefficient for the $i$ th reaction [-]
$\nu_{ki}$	Stoichiometric coefficient for gas reactions [-]
$V_o$	Ordinary diffusion velocity [m/s]
$W_d$	Thermal diffusion velocity [m/s]
$We_l$	Weber number of liquid [-]
$We_g$	Weber number of gas [-]
$w_{j,i}$	First-order sensitivity coefficient matrix [-]
$W_k$	Molecular weight [kg/mol]
$x$	Placeholder of intermediate species [-]; Spatial coordinates [m]
$X_k$	Mole fraction [-]
$[X_k]$	Molar concentration [mol/m <sup>3</sup> ]
$X_{Prec}$	Mole fraction of soot precursor [-]

$X_{sgs}$	Mole fraction of surface growth species [-]
$Y_k$	Mass fraction [-]
$Y_M$	Contribution of the fluctuating dilatation in compressible turbulence to the overall dissipation rate [-]
$Y_{soot}$	Soot mass fraction [-]
$Y_\alpha$	Mass fraction [-]
$Z$	Mixture fraction [-]
$Z_{mr}$	Most reactive mixture fraction [-]
$\alpha$	Model parameter [-]
$\beta$	Temperature exponent [-]
$\Delta$	Changes of reactants to products [-]
$\delta_{Bi}$	Involvement of species B in the $i$ th reaction [-]
$\varepsilon$	Dissipation rate [ $m^2/s^3$ ]
$\varepsilon_{EP}$	User-defined threshold [-]
$\Theta_k$	Thermal diffusion ratio [-]
$\lambda$	Thermal conductivity [W/mK]
$\mu_t$	Turbulent viscosity [kg/ms]
$\phi$	Equivalence ratio [-]; Solution vector [-]
$\rho$	Density [ $kg/m^3$ ]
$\rho_l$	Liquid density [ $kg/m^3$ ]
$\rho_2$	Gas density [ $kg/m^3$ ]
$\rho_g$	Gas density [ $kg/m^3$ ]
$\rho_l$	Liquid density [ $kg/m^3$ ]
$\rho_{soot}$	Mass density of soot [ $kg/m^3$ ]
$\sigma$	Surface tension [N/m]
$\sigma_k$	Turbulent Prandtl number for turbulence kinetic energy [-]
$\sigma_{soot}$	Soot turbulent Schmidt number [-]
$\sigma_\varepsilon$	Turbulent Prandtl number for dissipation rate [-]
$\tau$	Nominal residence time [s]; Breakup time [s]
$\tau_{RT}$	Breakup time due to RT [-]
$\Omega$	Growth rate of the fastest growing wave due to KH [1/s]
$\omega_i$	Net production rate of $i$ th reaction [mol/s]
$\omega_k$	Production rate of the $k$ th species [mol/ $m^3s$ ]
$\Omega_{RT}$	Frequency of fastest growing wave due to RT [1/s]



## LIST OF FIGURES

Figure 1-1: $\phi$ – temperature map for soot and NO <sub>x</sub> emissions in diesel engine [1]. ....2	2
Figure 1-2: Temporal sequence of a diesel spray from start of injection up till early-part of mixing-controlled combustion [2]. ....2	2
Figure 2-1: Pathway diagram describing the high and low temperature ignition for hydrocarbon [103]. ....24	24
Figure 2-2: Schematic diagram of soot formation processes from gas phase to solid agglomerate particles [137]. ....25	25
Figure 2-3: Bond dissociation energies of the n-butanol fuel structure [162]. The values shown are the dissociation energies in kJ/mol. ....29	29
Figure 2-4: Example of species coupling relations for the DRG method. ....36	36
Figure 2-5: Example of species coupling relation for the DRGEP method. ....39	39
Figure 4-1: Formation of C <sub>4</sub> H <sub>8</sub> OH radicals at low-temperature combustion with 20% n-butanol fuel consumption, at the initial temperature of 750 K, initial pressure of 40 bar and equivalence ratios of 0.5 (black), 1.0 (red) and 2.0 (green). Percentage values denote the ROP of C <sub>4</sub> H <sub>8</sub> OH radicals. ....69	69
Figure 4-2: Formation of C <sub>4</sub> H <sub>8</sub> OH radicals at high-temperature combustion with 20% n-butanol fuel consumption, at the initial temperature of 1250 K, initial pressure of 40 bar and equivalence ratios of 0.5 (black), 1.0 (red) and 2.0 (green). Percentage values denote the ROPS of C <sub>4</sub> H <sub>8</sub> OH radicals. ....70	70
Figure 4-3: Normalised temperature A-factor sensitivity at the point of ignition at initial temperatures of (a) 750 K and (b) 850 K, the initial pressure of 40 bar and equivalence ratios of 0.5 – 2.0. ....73	73
Figure 4-4: Flowchart of the development of DB105 mechanism. ....74	74
Figure 4-5: Comparison of the n-dodecane ST ID times predicted by the DB105 mechanism against the experimental measurements [212–214] and SK54 mechanism [94] at (a) initial temperatures of 700 – 1800 K, initial pressures of 14.2 and 40.5 bar and equivalence ratio of 0.5, (b) initial temperatures of 700 – 1800 K, initial pressures of 14.2 and 40.5 bar and equivalence ratio of 1.0, (c) initial temperatures of 700 – 1800 K, initial pressure of 20.2 bar and equivalence ratios of 0.5 and 1.0, and (d) initial temperatures of 700 – 1800 K, initial pressures of 17.2 and 60.8 bar and equivalence ratio of 1.0. ....76	76
Figure 4-6: Comparison of the stoichiometric n-butanol ST ID times predicted by the DB105 mechanism against the detailed mechanism [160] and experimental measurements [215,216] at initial temperatures of 750 – 1350 K and initial pressures of 20 – 80 bar. ....77	77
Figure 4-7: Comparison of the n-dodecane JSR species concentration profiles predicted by the DB105 mechanism (lines) against the experimental measurements (symbols) [113] for nC <sub>12</sub> H <sub>26</sub> , C <sub>2</sub> H <sub>6</sub> , C <sub>2</sub> H <sub>4</sub> , C <sub>2</sub> H <sub>2</sub> , CH <sub>4</sub> , CO <sub>2</sub> , H <sub>2</sub> O, CO and O <sub>2</sub> , at initial temperatures of 600 – 1100 K, initial pressure of 10.1 bar and equivalence ratio of 0.5 (top row), 1.0 (middle row), and 2.0 (bottom row). ....78	78
Figure 4-8: Comparison of the n-butanol JSR species concentration profiles predicted by the DB105 mechanism (lines) against the experimental measurements	

(symbols) [163] for $nC_4H_9OH$ , $C_2H_6$ , $C_2H_4$ , $C_2H_2$ , $CH_4$ , $CO_2$ , $H_2O$ and $CO$ , at initial temperatures of 600 – 1100 K, initial pressure of 10.1 bar and equivalence ratio of 0.5 (top row), 1.0 (middle row), and 2.0 (bottom row).....	79
Figure 4-9: Comparison of the n-dodecane laminar flame speed predicted by the SK54 mechanism [94] (solid lines) and DB105 mechanism (dash lines) against the experimental measurements (symbols) [217–219] at (a) initial pressure of 1.01 bar, unburned temperatures of 403 K and 470 K and (b) initial pressures of 1.01 – 3.03 bar, unburned temperature of 400 K. ....	81
Figure 4-10: Comparison of the n-butanol laminar flame speed predicted by the detailed mechanism [160] (solid lines) and DB105 mechanism (dash lines) against the experimental measurements (symbols) [173,220] at initial pressure of 1.0 bar and unburned temperatures of 343 K and 353 K. ....	82
Figure 4-11: Comparison of the predicted mole fractions of $C_2H_2$ , $C_2H_4$ , $C_4H_2$ , $C_4H_4$ , $A_1$ , $A_2$ , $A_3$ and $A_4$ by the DB105 mechanism (lines) against the experimental measurements (symbols) [222] under $C_2H_4$ premixed flame.....	83
Figure 4-12: Comparison of the predicted mole fractions of $C_4H_9OH$ , $O_2$ , $CO$ , $CO_2$ , $H_2$ , $H_2O$ and $Ar$ by the DB105 mechanism (lines) against the experimental measurements (symbols) [223] under Flame 1, Flame 2 and Flame 3 conditions.....	84
Figure 5-1: The NOSE combustion chamber experimental setup [79,81].....	87
Figure 5-2: Mesh model of the 2D axis-symmetrical plane.....	88
Figure 5-3: Average mass flow rate from 20 repetitive injections at pressure of 60 bar, injection pressure of 150 MPa and injection command duration of 1.5 ms [79,81]. ....	91
Figure 5-4: Comparison of the predicted (a) LPL and (b) VPL using different mesh size under non-reacting spray conditions, at ambient temperature of 900 K.....	92
Figure 5-5: Comparison of the predicted (a) LPL and (b) VPL using different mesh gradings under non-reacting spray conditions, at ambient temperature of 900 K. ....	94
Figure 5-6: Comparison of the predicted (a) LPL and (b) VPL using different time-step size under non-reacting spray conditions, at ambient temperature of 900 K. ....	96
Figure 5-7: Comparison of the predicted (a) LPL and (b) VPL against the experimental measurements using different turbulence model under non-reacting spray conditions, at ambient temperature of 900 K. ....	98
Figure 5-8: Comparison of the predicted (a) LPL and (b) VPL against the experimental measurements using different $C_{1\varepsilon}$ values under non-reacting spray conditions, at ambient temperature of 900 K. ....	99
Figure 5-9: Comparison of the predicted (a) LPL and (b) VPL against the experimental measurements using different $B_1$ values under non-reacting spray conditions, at ambient temperature of 900 K. ....	101
Figure 5-10: Comparison of the predicted non-reacting LPL and VPL (solid lines) against experimental measurements (dash lines) [79] for Bu0, Bu20 and Bu40 fuels at ambient temperatures of 800 K, 850 K and 900 K.....	103
Figure 5-11: Comparison of the predicted ID and FLOL for (a) Bu0, (b) Bu20 and (c) Bu40 fuels against the experimental measurements [79] at ambient temperatures of 800 K, 850 K and 900 K. ....	105
Figure 5-12: Test matrix for the calibration of $C_\alpha$ and $C_\gamma$ values. ....	106

Figure 5-13: Effects of $C_\alpha$ and $C_\gamma$ values on the predicted SVF of Bu0 fuel at ambient temperature of 900 K. The figure legend is labelled using the convention of ‘ $C_\alpha$ ; $C_\gamma \times$ magnification factor’ .....	107
Figure 5-14: Comparison of the predicted SVF against experimental measurements [70] for Bu0 fuel at ambient temperatures of 850 K and 900 K. ....	108
Figure 5-15: Comparison of the predicted SVF contours for Bu0 fuel against the experimental measurements [70] at ambient temperature of (a) 850 K and (b) 900 K. Red line denotes the FLOL. ....	109
Figure 6-1: Predicted (a) flame temperature and (b) HRR for different test cases. .	111
Figure 6-2: Temporal evolution of the flame temperature and HRR for (a) Bu0 (900 K), (b) Bu20 (900 K), (c) Bu40 (900 K) and (d) Bu20 (800 K). ....	113
Figure 6-3: Predicted contours of temperature, OH and CH <sub>2</sub> O mass fractions for different test cases at $t_1$ . Black line in the contour denotes the stoichiometric line. ....	116
Figure 6-4: Predicted contours of temperature, OH and CH <sub>2</sub> O mass fractions for different test cases at $t_2$ . Black line in the contour denotes the stoichiometric line. ....	116
Figure 6-5: Predicted contours of temperature, OH and CH <sub>2</sub> O mass fractions for different test cases at $t_3$ . Black line in the contour denotes the stoichiometric line. ....	117
Figure 6-6: Predicted mass fraction profiles of OH and CH <sub>2</sub> O for different test cases along the centre spray axis at $t_1$ (first row), $t_2$ (second row) and $t_3$ (third row). ....	119
Figure 6-7: Predicted mass fraction profiles of HO <sub>2</sub> and H <sub>2</sub> O <sub>2</sub> for different test cases along the centre spray axis at $t_1$ (first row), $t_2$ (second row) and $t_3$ (third row). ....	120
Figure 6-8: Temporal evolution of the temperature versus mixture fraction for different test cases. The vertical black and red dash line are the stoichiometric and $Z_{mr}$ lines. The orange solid line is the adiabatic mixing line. The scatter plots legend are as follows: time prior to first-stage ignition (black), $t_1$ (red), $t_2$ (green), semi-developed flame (blue), quasi-steady flame (purple).....	123
Figure 6-9: Temporal evolution of the flame overlapped with velocity vectors for different test cases. The black and red dash lines denote the stoichiometric line and FLOL, respectively. ....	124
Figure 6-10: Temporal FLOL for the case of Bu0 (900 K), Bu20 (900 K) and Bu40 (900 K). ....	125
Figure 6-11: Predicted axial flame development rate for different test cases.....	126
Figure 6-12: Predicted contours of mixture fraction, flame temperature, OH, CH <sub>2</sub> O, HO <sub>2</sub> , H <sub>2</sub> O <sub>2</sub> and CO at quasi-steady state for different test cases. The maximum value of the colour contour is listed in the corresponding colour bar while the minimum value is 500 K for temperature and zero for the mixture fraction and mass fractions. ....	128
Figure 6-13: Maps of OH, CH <sub>2</sub> O, HO <sub>2</sub> and H <sub>2</sub> O <sub>2</sub> mass fractions onto the temperature versus mixture fraction space at quasi-steady state for different test cases. Vertical dash line is the stoichiometric mixture fraction line. ....	129
Figure 6-14: Evolution of combustion modes for (a) Bu0 (900 K), (b) Bu40 (900 K) and (c) Bu20 (800 K) with the corresponding HRR profile on the left. ....	133
Figure 7-1: Predicted transient SVF for the test cases across the spray axis at (a) ID + 0.5 ms, (b) ID + 1.0 ms and (c) 3.0 ms. The experimental data is for Bu0 fuel at ambient temperature of 900 K.....	137

Figure 7-2: Predicted transient soot particle size for the test cases across the spray axis at (a) ID + 0.5 ms, (b) ID + 1.0 ms and (c) 3.0 ms. The experimental data is for Bu0 fuel at ambient temperature of 900 K.....	138
Figure 7-3: Predicted temporal evolution for the mass fractions of A <sub>1</sub> at time (a) ID + 0.5 ms, (b) ID + 1.0 ms and (c) 3.0 ms for the test cases.....	141
Figure 7-4: Predicted temporal evolution for the mass fractions of A <sub>4</sub> at time (a) ID + 0.5 ms, (b) ID + 1.0 ms and (c) 3.0 ms for the test cases.....	142
Figure 7-5: Predicted temporal evolution for the mass fractions of C <sub>2</sub> H <sub>2</sub> at time (a) ID + 0.5 ms, (b) ID + 1.0 ms and (c) 3.0 ms for the test cases. ....	143
Figure 7-6: Predicted temporal evolution for the mass fractions of OH at time (a) ID + 0.5 ms, (b) ID + 1.0 ms and (c) 3.0 ms for the test cases.....	144
Figure 7-7: Normalised peak (a) SVF and (b) soot particle size for the test cases. .	146
Figure 7-8: Normalised peak mass fractions of (a) A <sub>1</sub> , (b) A <sub>4</sub> , (c) C <sub>2</sub> H <sub>2</sub> and (d) OH for the test cases. ....	147
Figure 7-9: Spatial distributions of temperature, equivalence ratio, SVF, C <sub>2</sub> H <sub>2</sub> , A <sub>1</sub> , A <sub>4</sub> and OH for the test cases at quasi-steady state. The black line is the stoichiometric line. The maximum value of the colour contour is listed in the corresponding colour bar while the minimum value is 500 K for temperature and zero for the remaining contours. ....	149
Figure 7-10: Maps of SVF, A <sub>1</sub> , A <sub>4</sub> , C <sub>2</sub> H <sub>2</sub> and OH onto the temperature-equivalence ratio space for the test cases at quasi-steady state. The black dash line denotes the stoichiometric line.....	151
Figure 7-11: Spatial distributions of soot particle size for the test cases at quasi-steady state. Black line represents the stoichiometric line.....	153
Figure 7-12: Spatial distributions of soot number density for the test cases at quasi-steady state. Black line denotes the stoichiometric line.....	153
Figure 7-13: Predicted soot relevant rates for the test cases at quasi-steady state. Black line denotes stoichiometric line. The value in the corresponding colour bar for the rates of soot mass nucleation, surface growth, coagulation and oxidation are the maximum value.....	157

## LIST OF TABLES

Table 1-1: Comparison of physiochemical properties of n-butanol with gasoline, diesel and other lower carbon alcohol fuels [31–35].	4
Table 1-2: Comparison of physiochemical properties between diesel and n-dodecane fuels [70].	7
Table 2-1: Compilation of large diesel surrogate mechanisms (C =>10).	16
Table 2-2: Low and high temperature reaction classes [103].	23
Table 2-3: Compilation of detailed and reduced mechanisms for n-butanol and its isomers.	30
Table 2-4: Comparison of the skeletal mechanism size of n-heptane using DRG, DRGEP, DRGASA and DRGEP SA methods [104].	41
Table 2-5: Comparison of the skeletal mechanism size of iso-octane using DRG, DRGEP, DRGASA and DRGEP SA methods [104].	42
Table 3-1: Details of the chemical data required to run the simulations in CHEMKIN-PRO.	49
Table 3-2: Descriptions of reactor models used in the simulations.	51
Table 3-3: Model constants in the standard $k$ - $\epsilon$ turbulence model.	60
Table 3-4: Numerical models used for the simulations in CHEMKIN-PRO and ANSYS FLUENT.	64
Table 4-1: Initial conditions for the premixed flame simulations.	82
Table 5-1: Testing conditions for ECN spray A conditions [79,81].	87
Table 5-2: Definition of parameters used for the non-reacting and reacting spray simulations.	90
Table 5-3: Baseline physical models used for the simulations.	90
Table 5-4: Computational time using different mesh size.	93
Table 5-5: Description of the mesh with different grading applied.	93
Table 5-6: Default model constants in the Standard, RNG and Realisable $k$ - $\epsilon$ models.	97
Table 5-7: Optimised numerical settings.	102
Table 6-1: Test cases investigated.	110

# CHAPTER 1

## INTRODUCTION

### 1.1 Background

Compression ignition (CI) engine or also known as diesel engine is considered as the most fuel-efficient engine ever developed due to its high compression ratio and the lack of throttling losses [1]. However, harmful pollutants such as soot and nitrogen oxides ( $\text{NO}_x$ ) that arises from diesel combustion pose a serious threat to human health and the environment [1]. The ever-increasing stringent environmental and fuel economy requirements have led automotive engineers into developing low-emission and high efficiency diesel engine. Nonetheless, the heterogeneous nature of diesel combustion proves challenging to meet the emission targets where high soot and  $\text{NO}_x$  are still found despite numerous research efforts such as employing various combustion strategies are being attempted.

Figure 1-1 shows the mapping of soot and  $\text{NO}_x$  emissions as a function of equivalence ratio ( $\phi$ ) and temperature in a diesel engine [1]. From Figure 1-1, it is observed that  $\text{NO}_x$  is mainly formed at high temperatures ( $> 2500$  K) and close to stoichiometric. On the other hand, soot is mainly formed at fuel-rich regions ( $\phi > 3$ ) and at temperatures between 1800 – 2200 K. Meanwhile, Figure 1-2 shows the temporal sequence of a diesel spray from the start of injection till the early part of mixing-controlled combustion [2]. Auto-ignition is observed to take place at  $\phi = 2 - 4$  and subsequently the outer diffusion flame is at stoichiometric [2]. Since the adiabatic flame temperature line for conventional diesel combustion traverses both soot and  $\text{NO}_x$  regions as shown in Figure 1-1, it is inevitable that soot and  $\text{NO}_x$  emissions would be high in diesel combustion.

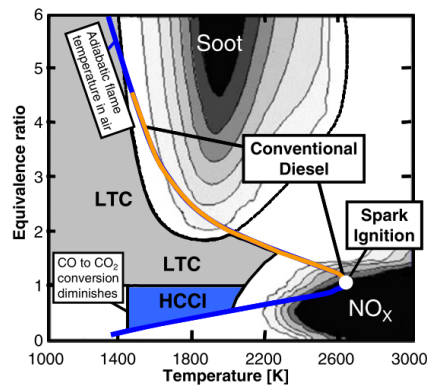


Figure 1-1:  $\phi$  – temperature map for soot and NO<sub>x</sub> emissions in diesel engine [1].

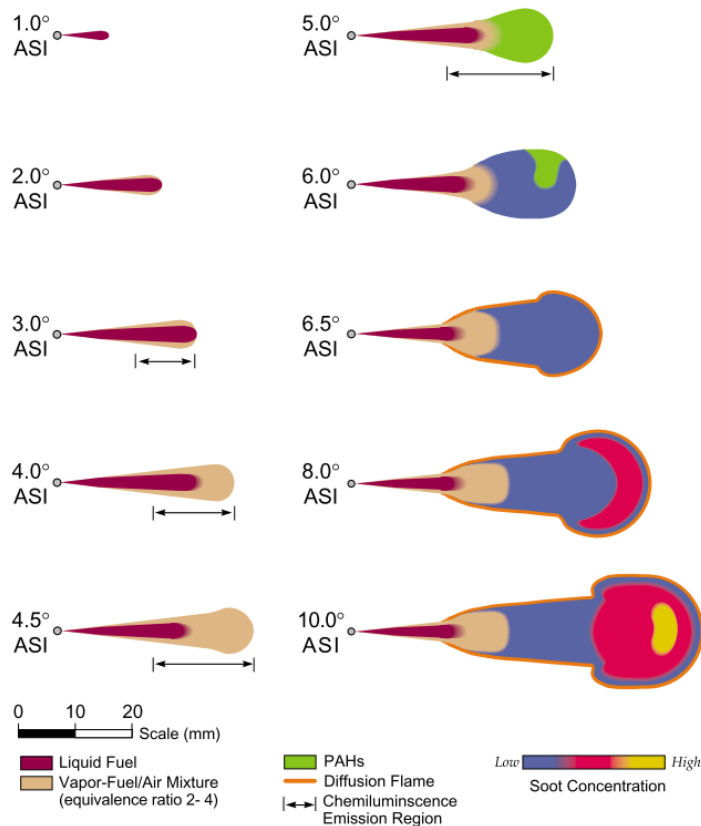


Figure 1-2: Temporal sequence of a diesel spray from start of injection up till early-part of mixing-controlled combustion [2].

In order to reduce or even avoid the formation of soot and NO<sub>x</sub>, a novel combustion concept called the low temperature combustion (LTC) is proposed and the homogeneous charge compression ignition (HCCI) combustion mode is the most common form of LTC [3]. The HCCI mode is a combination of the premixed charge from spark ignition (SI) engine and the CI from diesel engine. The HCCI mode is reported to have similar efficiency as conventional diesel combustion but soot and NO<sub>x</sub> emissions are reduced significantly [4]. However, as the ignition under HCCI

mode solely depends on the fuel's chemical kinetics, problems such as difficulty in controlling the combustion phasing, high levels of unburned hydrocarbon (UHC) and carbon monoxide (CO) and cold start misfiring occur [4–6]. Nevertheless, due to its novelty, other LTC combustion modes such as partially premixed compression ignition (PPCI), partially premixed combustion (PPC) and reactivity controlled compression ignition (RCCI) have been proposed to achieve the LTC target which is to obtain high engine efficiency and producing ultra-low soot and NO<sub>x</sub> emissions simultaneously [3].

Ideally, harmful toxic pollutants could be eliminated altogether if diesel engine is replaced with electric or hybrid power. However, despite the recent rise of electric vehicles in various countries, its usage is still limited to urban driving and not favourable for long distance driving [7]. Moreover, medium and heavy-duty vehicles such as tractors, ocean liners and ships require high torque, power, reliability and durability and all these requirements could only be met by a diesel engine [8]. As such, diesel engine is still very much relevant in present times although the world is moving into an era of electrification. Therefore, on the grounds of this, researchers have been focusing on the usage of biofuels in internal combustion engines. The usage of biofuels such as biodiesel [9–12], dimethyl ether (DME) [13–15] and alcohol fuels [16–19] have been investigated in previous research. Overall, the blending of biofuels with gasoline and diesel fuels is found to have comparable engine performance such as brake thermal efficiency (BTE) and fuel consumption when compared to pure gasoline and diesel fuels. On top of that, emissions such as CO, NO<sub>x</sub>, UHC and soot are reduced significantly. This suggest that the blending of biofuels with conventional fossil fuels is also one of the solutions to meet the stringent emission regulations set by governments worldwide.

## 1.2 Alcohol-Based Biofuels

According to [20,21], countries such as United States, China, Brazil and Indonesia have started implementing mandates on the biofuel blend. The most popular biofuel used for blending is ethanol followed by biodiesel, with the blending ratio ranging from 2 – 20% [20]. Besides, the global biofuel demand is estimated to increase by 51.6 billion litres, or 43%, reaching 170.9 billion litres in year 2025. This is a huge



growth where only 17 billion litres of ethanol is used for transportation fuel in year 2000 [22]. The increasing trend of biofuel usage gives a clear sign that the transportation sector is decreasing its dependency on the depleting fossil fuels for energy generation.

While ethanol is favourable for biofuel blending, production of ethanol creates a threat in food security and the destruction of local habitat's home for feedstock planting [23,24]. This is because ethanol is mainly derived from edible feedstocks such as sugar plants, corn, barley and wheat [25–27]. As a result, the drawbacks from the production of ethanol or also known as the first-generation biofuel have led researchers to shift their focus to the second-generation biofuel which is mainly made from lignocellulosic materials, wooden crops and agricultural waste that are non-edible, cheap and found abundantly in plants [28,29].

Among others, butanol ( $C_4H_9OH$ ) has recently emerged as a competitive second-generation biofuel in internal combustion engines. Butanol consists of four isomers namely n-butanol, sec-butanol, iso-butanol and tert-butanol. However, n-butanol ( $nC_4H_9OH$ ) has been typically used in internal combustion engines due to its relatively higher lower heating value and lower solubility in water as compared to the other isomers [30]. The comparison of physiochemical properties of n-butanol with gasoline, diesel and other lower carbon alcohol fuels are tabulated in Table 1-1 [31–35]. The closer resemblance in physiochemical properties between n-butanol and gasoline/diesel fuels implies that it could give better engine performance than the lower carbon alcohols such as ethanol and methanol.

Table 1-1: Comparison of physiochemical properties of n-butanol with gasoline, diesel and other lower carbon alcohol fuels [31–35].

Properties	Gasoline	Diesel	Methanol	Ethanol	n-butanol
Molecular Formula	$C_4 - C_{12}$	$C_{12} - C_{25}$	$CH_3OH$	$C_2H_5OH$	$nC_4H_9OH$
Research octane number	91-99	0	109	109	98
Motor octane number	81-89	0	89	90	85
Cetane number	0-10	40-55	3	8	25
Oxygen Content (% weight)	-	-	50	34.8	21.6
Density (g/mL) at 20°C	0.72-0.78	0.82-0.86	0.796	0.79	0.808
Autoignition Temp (°C)	~300	~210	470	434	385
Lower heating value (MJ/kg)	42.7	42.5	19.9	26.8	33.1
Boiling point (°C)	25-215	180-370	64.5	78.4	117.7
Stoichiometric air/fuel ratio	14.6	14.3	6.49	9.02	11.13

Latent heating (kJ/kg) at 25°C	380-500	270	1109	904	582
Energy Density (MJ/L)	32	39	16	19.6	29
Vapor Pressure (kPa) at 20°C	0.7-207	>0.7	12.8	7.58	0.53
Saturation Pressure (kPa) at 38°C	31.01	1.86	31.69	13.8	2.27
Viscosity (mm <sup>2</sup> /s) at 40°C	0.4-0.8	1.9-4.1	0.59	1.08	2.63
	(20°C)				
Compatibility with existing infrastructure	Yes	Yes	No	No	Yes

### 1.3 Potential of n-Butanol Fuel

The experimental investigations on gasoline-n-butanol and diesel-n-butanol blends have been conducted in various engine setups such as in SI engine [36–44], CI engine [45–53] and HCCI engine [54–58]. While n-butanol is suitable for blending with gasoline and diesel fuel, the oxygen content of n-butanol is anticipated to minimise soot emission more significantly in diesel engine as soot is one of the major pollutants from diesel combustion [45,47,48,51,59]. Moreover, some studies reported that the NO<sub>x</sub> emission is reduced due to lower in-cylinder temperature [46,52,60]. This indicates that n-butanol could cancel off the soot-NO<sub>x</sub> trade-off relationship that has been a problem in diesel combustion. On the contrary, soot emission in SI and HCCI engines are significantly lower than in diesel engine even without the usage of n-butanol due to the increased in mixture homogeneity which lowers the local equivalence ratio [5]. However, gasoline-n-butanol blends are reported to produce higher UHC [61] and non-regulated emissions such as formaldehyde (CH<sub>2</sub>O), acetaldehyde (CH<sub>3</sub>CHO) and acetylene (C<sub>2</sub>H<sub>2</sub>) [38] which is harmful to human health and the environment. Meanwhile, as compared to pure gasoline and diesel fuels, the addition of n-butanol gives similar BTE with slightly higher fuel consumption which is due to a lower heating value of n-butanol [38–40,45,50].

Although n-butanol provides many benefits when blending with gasoline and diesel fuels, studies related to pure n-butanol in internal combustion engines are rather limited. This is mainly due to rapid heat release and high pressure rise rate which could lead to unstable combustion [62]. In order to minimise the maximum pressure rise rate, air dilution method is attempted but this further deteriorates the combustion stability of pure n-butanol combustion [63]. Yanai et al. [64] also observed that pure n-butanol could not ignite under natural aspirated conditions at engine load of 6.5 bar indicated

mean effective pressure (IMEP) and compression ratio of 18.2 due to low reactivity. In SI engine, the spark timing window for a stable operation for n-butanol combustion is relatively narrow at only 3 crank angle degree (CAD) [65]. Besides, adjustment to the spark timing has to be done to obtain maximum brake torque as n-butanol has faster laminar flame speed than gasoline [66].

The problems faced using pure n-butanol directly in internal combustion engines collectively indicates that several engine modifications have to be done to improve the engine performance. Therefore, it can be concluded that for the time being it is more feasible to blend n-butanol with gasoline or diesel fuel in modern internal combustion engines. Nonetheless, as highlighted previously, the effects of blending n-butanol with diesel is more pronounced than with gasoline in terms of the reduction of emission such as soot. This shows the advantages of blending n-butanol with diesel outweighs those with gasoline and thus more research effort should be directed towards the fuel development of diesel-n-butanol blend in diesel engine.

#### **1.4 Current Understanding on the Combustion and Emission Characteristics of Diesel/n-Dodecane-n-Butanol Blends**

Diesel fuel is complex and instead a diesel surrogate fuel such as n-heptane or n-dodecane will be usually used as a substitute in experiments. However, it is found that longer carbon chain surrogates ( $C > 10$ ) are much more suitable to represent real diesel because it has a closer resemblance in physiochemical properties to diesel fuel [67]. Hence, based on the aforementioned fact, n-dodecane is more favourable to be used as a diesel surrogate than n-heptane. As shown in Table 1-2, both diesel and n-dodecane have very similar physiochemical properties but experimental results showed that there is slight noticeable differences in the spray characteristics under non-reacting and reacting conditions [68,69]. For instance, the liquid penetration length (LPL) of n-dodecane is slightly shorter than diesel fuel by around 5 mm but the vapour penetration length (VPL) between both fuels is similar. Moreover, due to the higher cetane number of n-dodecane fuel, the ignition delay (ID) and flame lift-off length (FLOL) are shorter than diesel fuel by 0.5 ms and 5 mm, respectively. Nonetheless, in the context of fuel combustion, these differences are considered marginal and researchers will still opt to use a diesel surrogate fuel due to its simplicity.

This practice is even more widely adopted in combustion modelling where there is a need to simplify the fuel chemistry and reduce the number of species and reactions to avoid high computational time.

Table 1-2: Comparison of physiochemical properties between diesel and n-dodecane fuels [70].

Fuel properties	Diesel	n-Dodecane
Fuel density (kg/m <sup>3</sup> )	846	752.1
Cetane number	46	87
Lower heating value (MJ/kg)	42.97	44.17
Kinematic viscosity (mm <sup>2</sup> /s)	2.32	1.5
Aromatics vol. %	27	0
Flash point (°C)	73	83

To date, the combustion and emission characteristics of diesel/n-dodecane-n-butanol blends are investigated in both diesel engine and constant volume combustion chamber where the typical n-butanol blending ratio is in the range of 5 – 30% [47–50,52,71–77], with some as high as 40% [51,53,78–81]. Various engine-out measurements such as BTE, brake specific fuel consumption (BSFC), coefficient of variance (COV) and downstream tailpipe emission data for soot, NO<sub>x</sub>, CO and UHC are obtained from the diesel engine experiments. Results from diesel engine indicate that when n-butanol is added as an additive to diesel fuel, the BTE is still comparable to that of pure diesel but the BSFC increases slightly [45]. Soot and CO emissions of diesel-n-butanol blends are reduced while UHC emission is higher due to improper fuel atomisation [46]. However, there are contradicting results in the NO<sub>x</sub> emission where it depends on the engine setup/configuration and blending ratio. For the experiments in a constant volume combustion chamber, the results obtained are such as the LPL, VPL, spray cone angle, ID and FLOL. According to the experimental results, there is a general consensus that the LPL of diesel-n-butanol and n-dodecane-n-butanol are longer than their respective pure fuel components whereas the differences in VPL and spray cone angle between are only marginal. The ID and FLOL of n-butanol blends with diesel or n-dodecane are also extended as compared to pure component fuels which is attributed to the lower cetane number of n-butanol that reduces the auto-ignition tendency.

While the results in both diesel engine and constant volume combustion chamber are valuable to the fuel development of diesel/n-dodecane-n-butanol, it remains a daunting task to study the chemical kinetics behind the spray combustion events. To this end, numerical modelling through Computational Fluid Dynamics (CFD), could be used as a cost-effective approach to overcome this challenge. Within the context, only very limited numerical research has been done on diesel/n-dodecane-n-butanol as n-butanol is considered one of the newer alcoholic biofuels as compared to ethanol and methanol. Moreover, the currently available chemical kinetic mechanisms that are used to simulate the combustion and emission of diesel-n-butanol have also mainly used n-heptane as the diesel surrogate fuel whereas mechanisms that utilise long carbon chain surrogates are extremely scarce. All these collectively suggest that the application of diesel/n-dodecane-n-butanol blends in numerical research is still in the nascent stage. Nonetheless, due to the potential of n-butanol, there is a pressing need to enhance the fundamental knowledge of diesel/n-dodecane-n-butanol from a joint viewpoint of CFD and chemical kinetics, which could support and complement the findings from experimental measurements.

To follow up on the above summary, a few research questions are presented and they are as follows:

1. What is the availability of a diesel-n-butanol kinetic mechanism that utilises long carbon chain diesel surrogate fuel?
2. Are the existing diesel/n-dodecane-n-butanol kinetic mechanisms well validated under a wide range of engine operating conditions?
3. How do the fundamental ignition, combustion and flame characteristics of diesel/n-dodecane-n-butanol differ from the pure diesel/n-dodecane?
4. How do the fundamental soot characteristics of diesel/n-dodecane-n-butanol differ from pure diesel/n-dodecane?

## 1.5 Research Objectives

In view of the current state of knowledge, the aim of the present study is to address the limitations related to the chemical kinetic mechanisms for diesel-n-butanol blends and the applications in multi-dimensional simulations concerning the spray combustion. To achieve the aim, four main objectives are carried out and they are as follows:

1. *Develop a n-dodecane-n-butanol-polycyclic aromatic hydrocarbon (PAH) reduced mechanism and validate it under a wide range of diesel engine relevant conditions.*

In combustion modelling, a set of chemical kinetics that is able to describe the combustion chemistry precisely is crucial to obtain accurate results. Currently, chemical kinetic mechanisms for diesel-n-butanol that are available in literature mainly utilise n-heptane as the diesel surrogate fuel [82–85]. In spite of that, higher carbon alkanes are more suitable to be used to mimic diesel fuel but the diesel-n-butanol mechanisms that utilise these large alkanes are scarce.

For this reason, a reduced chemical kinetic mechanism for n-dodecane-n-butanol is developed where n-dodecane is the diesel surrogate fuel. The detailed mechanism of n-butanol is reduced using various reduction methods to accommodate the current computational power for practical CFD simulations. Moreover, the chemistry of PAH is also added in as it is crucial for soot formation. Validations under a wide range of diesel engine conditions such as shock tube (ST) ID times, jet-stirred reactor (JSR) species concentration, laminar flame speed and premixed flame species concentration are then performed to ensure the reduced mechanism is robust and comprehensive.

2. *Formulation of CFD sub-models with the integration of chemical kinetics and validate the approach against constant volume experimental measurements.*

The developed n-dodecane-n-butanol-PAH reduced mechanism is integrated into the CFD solver to resolve the combustion chemistry of the spray combustion. Besides, various parametric studies are conducted to select a set

of CFD sub-models to simulate the fuel spray breakup, turbulence, ignition, combustion and soot emission in a constant volume combustion chamber. To validate the CFD sub-models and the chemical kinetic mechanism, the predicted LPL, VPL, ID, FLOL and soot emission are compared to the experimental measurements under both non-reacting and reacting conditions.

3. *Investigate the effects of n-butanol blending ratio and ambient temperature on the fundamental ignition, combustion and flame characteristics of n-dodecane-n-butanol spray.*

Understanding the fundamental ignition and flame characteristics of n-dodecane-n-butanol is essential in developing clean combustion engines. However, most of the existing studies related to n-dodecane-n-butanol focus only on the engine-out measurements whereas there is a lack of understanding on the detailed spray processes of n-dodecane-n-butanol. Hence, to cover the knowledge gap, detailed investigation on the spray processes starting from fuel injection till quasi-steady state for n-dodecane-n-butanol blends are conducted. The effects of n-butanol blending ratio and ambient temperature towards the ignition and flame characteristics are simulated and analysed. Combustion mode analysis is also performed on the n-dodecane-n-butanol flame development as it is beneficial in understanding the pollutant formation and other intermediate species within the reacting flame [86].

4. *Investigate the effects of n-butanol blending ratio and ambient temperature on the soot processes and mechanisms of n-dodecane-n-butanol spray.*

Soot emission for n-dodecane-n-butanol blend is generally reduced due to the oxygen content in n-butanol. Nevertheless, the detailed soot evolving processes of n-dodecane-n-butanol from the perspective of chemical kinetics is still less understood. Even so, the numerical soot studies related to diesel-n-butanol (n-heptane and n-dodecane diesel surrogate) in a constant volume combustion chamber are only limited to low n-butanol blending ratio (<20%) [87,88] and the quasi-steady soot is also not well explained. Set against these backgrounds, soot modelling study of n-dodecane-n-butanol blends are

conducted here where the effects of n-butanol blending ratio (as high as 40%) and ambient temperature towards the soot volume fraction (SVF), soot particle size, soot density and its relevant intermediate species are examined. Soot relevant rates are also analysed to elucidate the underlying soot formation and oxidation mechanisms in the n-dodecane-n-butanol spray flames.

## 1.6 Thesis Outline

The current chapter, Chapter 1 gives a brief overview of alcohol-based fuel in particular n-butanol and the potential of it in diesel engines. The overall scope and objectives of this thesis are also defined. Following that, a comprehensive literature review on the developments of existing chemical kinetic mechanisms for diesel surrogate fuel, n-butanol, PAH and diesel-n-butanol mechanisms are presented in Chapter 2. Reduction methods that are commonly used for reducing large scale mechanism are also appraised. Moreover, a thorough discussion regarding recent CFD modelling study of diesel-n-butanol blends under diesel engine or constant volume combustion chamber conditions are also presented.

In Chapter 3, the theoretical background and mathematical governing equations of the CFD sub-models that are involved for the chemical kinetics and CFD simulations are presented. Chapter 4 describes the developmental work of a n-dodecane-n-butanol-PAH chemical kinetic mechanism where n-dodecane is the diesel surrogate fuel. The methodology used to construct the reduced n-dodecane-n-butanol-PAH mechanism is discussed in detailed. Zero-dimensional (0D) and one-dimensional (1D) model validations under a wide range of engine relevant conditions are conducted by comparing the predictions by the reduced mechanism against those of the predictions by the detailed mechanism and experimental measurements. Subsequently, mesh independence test and parametric studies such as time-step, spray breakup and turbulence are conducted in Chapter 5 to select the optimum settings for the two-dimensional (2D) spray combustion simulations in a constant volume combustion chamber. The reduced mechanism developed in Chapter 4 is then integrated into the CFD solver where its fidelity is also being evaluated under 2D simulations.

Chapter 6 investigates the effect of n-butanol blending ratio and ambient temperature on the ignition and flame characteristics of n-dodecane-n-butanol spray



flames. The flame development of n-dodecane-n-butanol are highlighted alongside the formation of intermediate species within the reacting flame. Furthermore, Chapter 7 focuses on the soot modelling for the n-dodecane-n-butanol spray flames with the emphasis on the evolution of soot and its intermediate species. Soot relevant rates are also presented to further establish the soot formation and oxidation mechanisms in n-dodecane-n-butanol spray flames. Lastly, Chapter 8 summarises the key findings of this entire research study and highlights the potential future work.

# CHAPTER 2

## LITERATURE REVIEW

### 2.1 Introductory Remarks

This chapter provides a comprehensive literature review to the current study. Section 2.2 reports the recent developments on the chemical kinetic mechanisms for diesel surrogate, PAH, n-butanol and diesel-n-butanol. In Section 2.3, the available chemical kinetic reduction methods for reducing large scale mechanisms are reviewed. The CFD modelling studies of diesel-n-butanol blends in both diesel engine and constant volume combustion chamber are reviewed in Section 2.4. Lastly, key points from the literature review are highlighted in Section 2.5.

### 2.2 Chemical Kinetic Mechanism

In combustion modelling, chemical kinetic mechanisms are often integrated with CFD to describe the detailed reactions of the combustion. Therefore, the selection of mechanisms is crucial to obtain reliable modelling results. This section aims to review the recent developments of chemical mechanisms for diesel surrogate, PAH, n-butanol and diesel-n-butanol.

#### 2.2.1 Diesel Surrogate

Diesel fuel that is derived from petroleum sources typically consists of hundreds to thousands of compounds and the development of models to represent all those compounds would be too computational demanding for current computing power [89]. For example, Herbinet et al. [90] showed that a large biodiesel mechanism with 3012 species requires around 3 hours to complete one cycle of engine simulation whereas a n-heptane mechanism requires only 10 minutes. On the account of this, diesel fuel has been often represented by simpler straight-alkanes called “surrogate fuels” [89]. A surrogate fuel is used to mimic the combustion and emission characteristics of real diesel fuel in various combustion applications but it might lack components that are representative of molecules contained in real diesel fuel [91]. This is why surrogate fuel is formulated based on the application of interest and “targets” such as property targets, development targets and application targets are used to

determine the accuracy of surrogate fuel with respect to real diesel fuel [91]. The definition of each target is explained in detailed in the publication by Farrell et al. [91].

Among the surrogate fuel, n-heptane is frequently used to represent diesel fuel in diesel combustion simulations [82,86,92,93]. This is because n-heptane has a cetane number of 55 which is comparable to the European and Japanese diesel fuel [91]. Nevertheless, the number of carbon in n-heptane is fewer than those of practical diesel fuel, which is in the range of 10 to 25 carbon atoms [91,94]. The carbon chain length of a surrogate fuel is found to have an impact on the auto-ignition behaviour as longer chain alkanes exhibit higher reactivity than shorter chain alkanes at low temperatures [91]. This is because hydrogen atoms attached to the tertiary carbon atom tend to have a higher rate of H-atom abstraction followed by those attached to the secondary and primary carbon atom [95]. Besides, the longer the carbon chain, the greater the ratio of secondary to primary hydrogen atoms which explains why longer chain alkanes exhibit higher reactivity [96]. As such, a surrogate fuel with carbon atoms between 10 to 25 is more favourable to be used to represent diesel fuel.

The compilation of the available straight alkane surrogate kinetic mechanisms with carbon chain length between 10 to 25 carbon atoms are tabulated in Table 2-1 alongside their validating conditions. Among the large surrogate mechanisms listed in Table 2-1, there are more kinetic mechanisms for n-decane ( $C_{10}H_{22}$ ) and n-dodecane ( $C_{12}H_{26}$ ) than those higher carbon surrogate mechanisms such as n-tetradecane ( $C_{14}H_{30}$ ) and n-hexadecane ( $C_{16}H_{34}$ ). This is due to the lack of experimental data for the validation of large carbon surrogate mechanisms. Furthermore, the kinetic mechanism generally increases in number of species and reactions as the carbon number increases which makes it unfavourable for CFD simulations.

Recently, much developmental effort on diesel surrogate mechanism has been focused on n-dodecane fuel. This is because the boiling characteristics of n-dodecane falls in the mid-range of diesel fuel and is expected to simulate the air-fuel mixing process better than n-heptane fuel [67,94,97]. Furthermore, as mixing-controlled combustion is dominant in diesel engine, the high volatility of n-heptane might not capture the mixing processes accurately [67]. Nevertheless, one might argue that employing a higher carbon surrogate mechanism could better simulate the spray and

combustion characteristics of diesel fuel. However, Narayanaswamy et al. [98] pointed out that n-dodecane has been identified to give a good compromise between having a long carbon chain and also a reasonable molecule size, which shows that n-dodecane is a promising surrogate candidate to represent diesel fuel.

Table 2-1: Compilation of large diesel surrogate mechanisms (C =&gt;10).

Fuel type	Author	Type of mechanism	Number of species	Number of reaction	Validating conditions			Ref	
					Types of validation	Equivalence ratio	Temperature		Pressure
C <sub>10</sub> H <sub>22</sub>	Zeppieri et al.	Reduced	52	407	Pyrolysis in flow reactor	-	1060 K	1.01 bar	[99]
					Oxidation in flow reactor	1.0	1019 K	1.01 bar	
					ST ID times	1.0, 2.0	1000 – 1333 K	13 ± 1.5 bar	
					JSR species concentration	1.0	1033 K	1.01 bar	
	Bikas and Peters	Reduced	67	600	ST ID times	1.0, 2.0	667 – 1250 K	12, 50 bar	[100]
					JSR species concentration	0.1 – 1.5	550 – 1110 K	10.13 bar	
					Premixed laminar flames	1.7	-	1.01 bar	
					Laminar flame speed	0.7 – 1.4	298 K	1 bar	
	Buda et al.	Detailed	715	3872	ST ID times	1.0	660 – 1200 K	12, 50 bar	[101]
	Moreac et al.	Detailed	506	3684	ST ID times	0.5 – 2.0	700 – 1350 K	13, 50 ± 3 bar	[102]
Westbrook et al.	Detailed	940	3878	ST ID times	0.5 – 3.0	667 – 1616 K	13.0 – 81.6 bar	[103]	
				RCM ID times	1.0	680 – 740 K	14.3 bar		
				Pyrolysis in flow reactor	-	1060 K	1.01 bar		
				Oxidation in flow reactor	1.0	1019 K	1.01 bar		
				JSR species concentration	1.0	500 – 1100 K	1.01, 10.1 bar		
Niemeyer et al.	Reduced	202 51	846 256	ST ID times	0.5 – 1.5	600 – 1600 K	1.01 – 40.53 bar	[104]	
				Laminar flame speed	0.8 – 1.4	400 K	1.01 – 40.53 bar		
				Perfectly stirred reactor (PSR)	0.5 – 1.5	300 K	1.01 – 40.53 bar		
Titova et al.	Reduced	144	1021	Pyrolysis in flow reactor	-	900 – 1200 K	1.01 bar	[105]	
				ST ID times	0.5 – 2.0	700 – 1250 K	13.17 – 81.6 bar		
Chang et al.	Reduced	40	141	ST ID times	0.5 – 2.0	650 – 1500 K	5.06 – 81.6 bar	[106]	

				RCM ID times	0.5, 0.8	650 – 692 K	7 – 30 bar	
				JSR species concentration	0.5 – 2.0	550 – 1150 K	1.01, 10.13 bar	
				Premixed laminar flame	1.7	-	1.01 bar	
				Oxidation in flow reactor	1.0	520 – 1019 K	1.01 – 12.66 bar	
				Opposed-flow diffusion flame (OPPDIFF)	-	400 K	1.013 bar	
				Laminar flame speed	0.7 – 1.4	300 – 500 K	1.01, 2.02 bar	
Chang et al.	Reduced	36	128	ST ID times	1.0	650 – 1250 K	5.06 – 80.6 bar	[107]
				ST oxidation	0.57, 1.96	1000 – 1700 K	52.48 – 68.8 bar	
				Laminar flame speed	0.7 – 1.4	400 K	1.01 – 3.03 bar	
Zeng et al.	Detailed	234	1452	ST ID times	0.25 – 3.0	700 – 1810 K	1.84 – 81.6 bar	
				Oxidation in ST	0.57 – 1.96	940 – 1745 K	46.6 – 75 bar	
				JSR species concentration	0.5 – 2.0	900 – 1300 K	1.01 bar	
				Pyrolysis in flow reactor	-	780 – 1500 K	0.006 – 1.01 bar	[108]
				Premixed laminar flame	0.7 – 1.8	500 – 2200 K	0.04, 1.01 bar	
				OPPDIFF	-	298 – 1700 K	1.01 bar	
				Laminar flame speed	0.6 – 3.0	360 – 500 K	1.01 – 3.03 bar	
Jia et al.	Detailed	164	842	Pyrolysis in flow reactor	-	780 – 940 K	30 bar	[109]
Xi et al.	Reduced	126	523	ST ID times	0.5 – 2.0	700 – 1300 K	13.17, 50.66 bar	
				JSR species concentration	1.0	750 – 1100 K	1.01, 10.1 bar	[110]
				Laminar flame speed	0.7 – 1.4	360 – 470 K	1.01 bar	
<b>C<sub>12</sub>H<sub>26</sub></b>				Pyrolysis in flow reactor	-	893 K	1.01 bar	
Westbrook et al	Detailed	1282	5030	Pyrolysis in JSR	-	773 – 1073 K	1.01 bar	[103]
				JSR species concentration	1.0	900 – 1100 K	1.01 bar	
				Pressurized flow reactor	0.2, 0.3	625 – 875 K	8.1 bar	
You et al.	Detailed	171	1306	Pyrolysis in plug flow reactor	-	950 – 1150 K	1.01 bar	[111]

				Pyrolysis in JSR	-	873 – 1073 K	1.01 bar	
				Laminar flame speed	0.6 – 1.6	403, 470 K	1.01 bar	
				ST ID times	0.5, 1.0	714 – 1176 K	20.2 bar	
				ST ID times	0.5, 2.0	700 – 1700 K	1.01 – 101.3 bar	
				PSR	0.5, 2.0	300 K	1.01 – 101.3 bar	
Som et al.	Reduced	103	370	JSR species concentration	-	850 – 1100 K	1.01 bar	[112]
				OPPDIFF	-	-	1.01 bar	
				Three-dimensional (3D) spray simulation	-	900 K	60 bar	
Mze- Ahmed et al.	Detailed	1377	5864	JSR species concentration	0.5 – 2.0	550 – 1200 K	10 bar	[113]
				ST ID times	0.5, 1.0	720 – 1150 K	15 – 34 bar	
				ST oxidation	-	1392 – 1418 K	~2.2 bar	
				ST ID times	0.5, 1.0	750 – 1200 K	8.1 – 40.4 bar	
				ST oxidation	0.46, 2.05	1000 – 1700 K	20.2 – 62 bar	
Chang et al.	Reduced	36	128	JSR species concentration	0.5 – 2.0	550 – 1200 K	10.1 bar	[107]
				Pressurized flow reactor	0.2 – 0.3	600 – 800 K	8.08 bar	
				Laminar flame speed	0.7 – 1.4	400 – 470 K	1.01 – 3.03 bar	
				ST ID times	0.5, 2.0	700 – 1700 K	1.01 – 101.3 bar	
				PSR	0.5, 2.0	300 K	1.01 – 101.3 bar	
Luo et al.	Reduced	557	2546	JSR species concentration	1.0	600 – 1150 K	10 bar	[67]
		105	420	Laminar flame speed	0.7 – 1.4	403 K	1.01 bar	
				OPPDIFF	-	-	1.01 bar	
				3D spray simulation	-	900 K	60 bar	
				ST ID times	0.67 – 2.0	714 – 1250 K	20 – 80 bar	
Wang et al.	Reduced	100	432	JSR species concentration	0.5 – 2.0	500 – 1000 K	10.1 bar	[114]
				ST oxidation	0.46 – 2.05	1000 – 1700 K	50.1 – 51.4 bar	
				Spray combustion simulation	-	850 – 1200 K	~ 60 bar	

Narayananaswamy et al.	Reduced	255	2289	ST ID times	0.5 – 1.0	625 – 1450 K	14.2 – 40.4 bar	[98]
				ST oxidation	0.46	900 – 1700 K	50.5 bar	
				ST pyrolysis	-	1000 – 1800 K	22.3 bar	
				Pressurized flow reactor	0.23, 1.0	550 – 1000 K	8.08 bar	
				Laminar flame speed	0.7 – 1.7	353 – 470 K	1.01 – 10.1 bar	
Frassoldati et al.	Reduced	96 133	993 2275	ST ID times	0.5 – 2.0	727 – 1739 K	2.02 – 40.4 bar	[115]
				JSR species concentration	0.5 – 2.0	550 – 1150 K	1.01, 10.1 bar	
				Plug flow reactor	0.23, 1.0	500 – 1000 K	8.08 bar	
				Batch reactor	1.0	523 – 623 K	0.13 – 0.54 bar	
				Laminar flame speed	0.7 – 1.5	400 – 470 K	1.01 – 3.03 bar	
Yao et al.	Reduced	54	269	Spray combustion simulation	-	800 – 1100 K	~ 60 bar	[94,97]
				ST ID times	0.5 – 2.0	714 – 1111 K	20, 50 bar	
				Pyrolysis in JSR	-	873 – 1050 K	1.1 bar	
				Pyrolysis in flow reactor	-	1050 K	1.01 bar	
				JSR species concentration	1.0, 2.0	550 – 1150 K	10 bar	
Zeng et al.	Detailed	264 1734	2331 6520	Laminar flame speed	0.6 – 1.5	400 – 470 K	1.01 – 3.03 bar	[116]
				3D spray simulation	-	800 – 1200 K	~ 60 bar	
				Pyrolysis in flow reactor	-	1100 K	1.01 bar	
				JSR species concentration	0.5 – 2.0	550 – 1030 K	1.01, 10 bar	
				ST pyrolysis	-	860 – 1740 K	25.3, 50.7 bar	
Mao et al.	Detailed	737	3629	ST oxidation	0.46 – 2.05	860 – 1740 K	25.3, 50.7 bar	[117]
				ST ID times	0.5, 1.0	833 – 1250 K	6.78 – 40.4 bar	
				Laminar flame speed	0.6 – 1.6	400 K	1.01 – 3.03 bar	
				ST ID times	0.5 – 1.5	600 – 1300 K	8 – 40.4 bar	
				ST oxidation	0.46, 2.05	867 – 1739 K	24.87 – 50.2 bar	
Oxidation in flow reactor	0.5 – 1.5	600 – 1150 K	1.01 bar					
Laminar flame speed	0.7 – 1.5	400 – 470 K	1.01 – 3.03 bar					



					ST ID times	0.67 – 2.0	700 – 1300 K	50 bar	
	Xi et al.	Reduced	162	631	JSR species concentration	0.5, 1.0	700 – 1025 K	10 bar	[110]
					Laminar flame speed	0.7 – 1.4	400, 470 K	1.01 bar	
<b>C<sub>14</sub>H<sub>30</sub></b>	Westbrook et al.	Detailed	1668	6449	JSR species concentration	1.0	900 – 1200 K	1.01 bar	[103]
	Chang et al.	Reduced	36	128	ST ID times	0.5,1.0	900 – 1350 K	13.17 – 40.5 bar	[107]
	Mze-Ahmed et al.	Detailed	1813	7885	ST ID times	0.5, 1.0	750 – 1300 K	13.17 bar	[118]
					JSR	0.5 – 2.0	560 – 1030 K	10.1 bar	
	Sun et al.	Semi-reduced	74	341	ST ID times	0.5, 1.0	900 – 1300 K	13.17 – 40.5 bar	[119]
		Reduced	62	279	Internal combustion engine	1.0,1.2	325, 350 K	1.01, 1.2 bar	
				JSR	2.2	1630 K	-		
				Pyrolysis in flow reactor	-	825 – 1275 K	0.04 – 1.0 bar		
Zeng et al.	Detailed		254	2217	JSR species concentration	0.5 – 2.0	560 – 1030 K	10 bar	[120]
					ST ID times	0.5, 1.0	833 – 1250 K	13.17 – 40.5 bar	
					Laminar flame speed	0.7 – 1.4	423, 443 K	1.01 bar	
					ST ID times	0.5, 1.0	850 – 1300 K	9.11 – 50.6 bar	
Sun et al.	Reduced	85	317	Internal combustion engine	1.0	350 K	1.01 bar	[121]	
				Oxidation in flow reactor	-	1173 K	1.01 bar		
				JSR species concentration	0.5	1040 – 1240 K	1.01 bar		
<b>C<sub>16</sub>H<sub>34</sub></b>	Westbrook et al.	Detailed	2116	8130	ST ID times	1.0	625 – 1250 K	13.5 bar	[103]
					JSR species concentration	0.5 – 1.5	900 – 1400 K	1.01 bar	
	Ristori et al.	Detailed	242	1801	JSR species concentration	0.5 – 1.5	1000 – 1250 K	1.01 bar	[122]
					JSR species concentration	0.5 – 1.5	1000 – 1250 K	1.01 bar	
	Chaos et al.	Reduced	98	944	Pyrolysis in quartz reactor	-	973 K	1.01 bar	[123]
					Laminar flame speed	0.7 – 1.4	-	-	
Poon et al.	Reduced	49	97	ST ID times	0.5 – 2.0	650 – 1350 K	60 bar	[124]	

				Spray combustion simulation	-	1300 K	~60 bar	
				ST ID times	0.5 – 2.0	650 – 1350 K	40, 60, 80 bar	
Poon et al.	Reduced	79	289	ST species concentration	1.0	650 – 1350 K	60 bar	[125]
				JSR species concentration	1.0	650 – 1350 K	60 bar	
				Spray combustion simulation	-	900 K	~60 bar	
Kourdis and Bellan	Reduced	20	-	Internal combustion engine	0.36, 1.03, 1.5	650, 1000 K	40, 60 bar	[126]

Westbrook et al. [103] developed a detailed chemical kinetic mechanism for n-alkane hydrocarbons from n-octane to n-hexadecane and this mechanism consists of 2116 species and 8130 reactions. With the removal of several species and reactions for larger component fuels, the resulting detailed mechanism for n-dodecane consists of 1282 species and 5030 reactions. Westbrook et al. [103] further explained that a n-alkane reaction mechanism can be classified into 25 classes by which 9 classes in the high-temperature mechanism and 16 in the low-temperature mechanism. These reaction classes are tabulated in Table 2-2 [103]. Additionally, the overall reaction path diagram that describes the ignition of n-alkane hydrocarbon is shown in Figure 2-1 [103]. In Figure 2-1, the top section describes the oxidation pathway under high-temperature combustion where the decomposition of alkyl radicals occurs while the lower section shows that low-temperature combustion is initiated by the addition of oxygen ( $O_2$ ) to the alkyl radicals.

Moreover, in contrast to Westbrook et al.'s [103] detailed mechanism, the n-dodecane detailed mechanism developed by You et al. [111] is relatively compact in size than the aforementioned detailed mechanism [103] with only 171 species and 1306 reactions. This detailed mechanism [111] is developed through the merging of a 111 species and 784 reactions mechanism, that describes the oxidation of hydrogen ( $H_2$ ) and CO and the high-temperature chemistry of  $C_1$  to  $C_4$  hydrocarbons, with a 60 species and 522 reactions mechanism that describes the high-temperature oxidation of alkanes. From then on, successive studies have utilised those detailed mechanisms [103,111] as a starting mechanism for the development of skeletal or reduced n-dodecane mechanisms [67,94,97,112]. Several detailed and reduced mechanisms for n-dodecane [110,116,117] have also been developed in recent years to improve the predictions of the earlier developed n-dodecane mechanisms. Although improvements to the predictions such as the ID times could be observed, the size of those mechanisms [110,116,117] are large and this would likely increase the computational time.

Apart from standalone n-dodecane mechanisms, Wang et al. [114], Narayanaswamy et al. [98] and Frassoldati et al. [115] developed their respective n-dodecane mechanisms that includes a PAH mechanism. Since the PAH mechanism is included as a sub-mechanism, the size of the mechanism increases and thus increasing

the computational time in CFD simulations. In Wang et al.'s [114] study, they have also reported that the ID and FLOL of n-heptane are over-predicted as compared to n-dodecane whereas its soot mass is around two to three times lower. This shows that there is noticeable difference in the combustion characteristics between n-heptane and n-dodecane fuels.

Table 2-2: Low and high temperature reaction classes [103].

Reaction classes	Types of reaction
<u>High-temperature reaction classes</u>	
1	Unimolecular fuel decomposition
2	H-atom abstraction from fuel
3	Alkyl radical decomposition
4	Alkyl radical + O <sub>2</sub> = olefin + HO <sub>2</sub>
5	Alkyl radical isomerisation
6	H atom abstraction from olefins
7	Addition of radical species to olefins
8	Alkenyl radical decomposition
9	Olefin decomposition
<u>Low-temperature reaction classes</u>	
10	Alkyl radical addition to O <sub>2</sub>
11	R + R'O <sub>2</sub> = RO + R'O
12	Alkylperoxy radical isomerisation
13	RO <sub>2</sub> + HO <sub>2</sub> = ROOH + O <sub>2</sub>
14	RO <sub>2</sub> + H <sub>2</sub> O <sub>2</sub> = ROOH + HO <sub>2</sub>
15	RO <sub>2</sub> + CH <sub>3</sub> O <sub>2</sub> = RO + CH <sub>3</sub> O + O <sub>2</sub>
16	RO <sub>2</sub> + R'O <sub>2</sub> = RO + R'O + O <sub>2</sub>
17	RO <sub>2</sub> H = RO + OH
18	Alkoxy radical decomposition
19	QOOH decomposition and production of cyclic ethers
20	QOOH beta decomposition to produce olefin + HO <sub>2</sub>
21	QOOH decomposition to small olefin, aldehyde and OH
22	Addition of QOOH to molecular oxygen O <sub>2</sub>
23	O <sub>2</sub> QOOH isomerisation to carbonylhydroperoxide + OH
24	Carbonylhydroperoxide decomposition
25	Reactions of cyclic ethers with OH and HO <sub>2</sub>

Note: R and R' both have same number of carbon atoms.

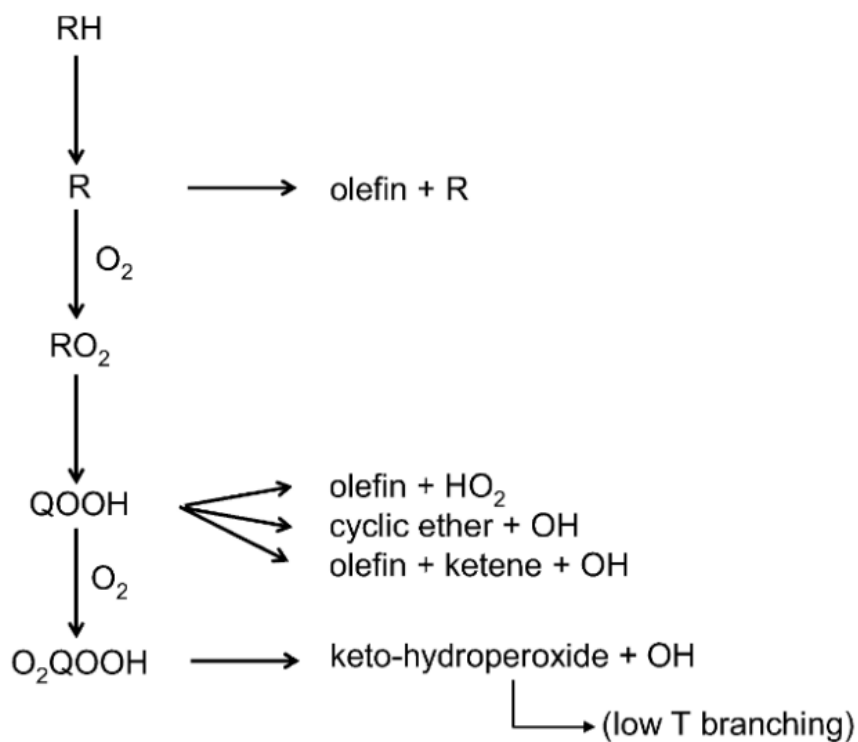


Figure 2-1: Pathway diagram describing the high and low temperature ignition for hydrocarbon [103].

### 2.2.2 PAH

High soot formation remains as one of the major drawbacks in diesel engines and the understanding of the soot mechanism is of paramount importance to facilitate various combustion strategies to minimise soot [127].  $C_2H_2$  has been widely regarded as a soot precursor and it has been used in many previous soot modelling studies [93,128–133]. However, Schuetz and Frenklach [134] observed through molecular dynamics simulation that soot nucleation is initiated through the collision of PAH molecules. Moreover, Wen et al. [135] compared the usage a  $C_2H_2$  and a PAH based inception model for the prediction of soot formation in kerosene flames and it is observed that there are significant improvements in the prediction of SVF when the PAH inception model is utilised as compared to the  $C_2H_2$  inception model [135]. This shows the importance of PAH as an intermediate species in the soot formation process and should be thus employed as the soot inception model [135].

The formation of PAH and their sequential growth into soot was discussed in detailed by Richter and Howard [136] and a brief schematic diagram depicting the soot formation processes is shown in Figure 2-2 [137]. PAHs are generally considered as species that acts as building blocks for the transition of gaseous phase to solid phase [138,139]. The pyrolysis of fuel produces various soot precursors and species such as benzene ( $A_1$ ) and  $C_2H_2$  have been often recognised as a soot precursor [136]. While the usage of  $C_2H_2$  as soot precursor has resulted in several successful soot modelling studies [93,128–133],  $A_1$  plays a vital role in the formation of larger PAH species. On the other hand,  $C_2H_2$  aids the formation of larger PAH species through the “H-Abstraction-Carbon-Addition” (HACA) mechanism that was proposed by Frenklach and Wang [140,141]. However, Frenklach [142] mentioned that  $C_2H_2$  is not the only surface growth species as species such as methyl, propargyl and cyclopentadienyl have also been discovered to contribute to soot surface growth.

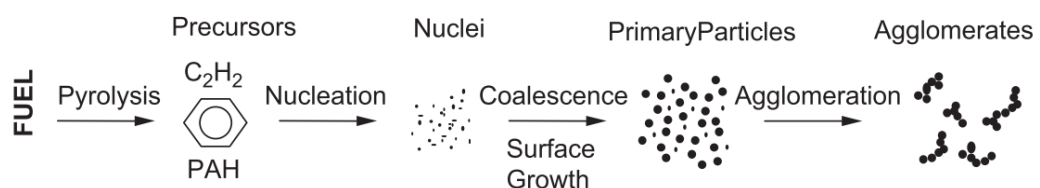


Figure 2-2: Schematic diagram of soot formation processes from gas phase to solid agglomerate particles [137].

For the past two decades, researchers have been developing PAH chemical kinetic mechanisms in order to obtain reliable soot modelling results. For instance, Wang and Frenklach [143] developed a 99 species and 527 reactions PAH mechanism to describe the fuel pyrolysis, oxidation,  $A_1$  formation and PAH mass growth/oxidation. Predictions by the mechanism [143] have shown that mass growth of PAH up to pyrene ( $A_4$ ) is well described by the HACA mechanism. Nevertheless, the predicted peak mole fractions for the PAH deviated by a factor of three to the experimental data under  $C_2H_2$  flame conditions. Furthermore, Appel et al. [138] updated Wang and Frenklach's [143] mechanism by including reactions of acenaphthylene ( $A_2R_5$ ) and vinylacetylene ( $C_4H_4$ ). However, despite the changes made to the reaction rate constant of allenes ( $\alpha-C_3H_4$ ),  $A_4$  is still under-predicted with a factor of 10 to the experimental data under ethane ( $C_2H_6$ ) flame. Similarly, Marinov et al. [144,145] also observed that the concentration of  $A_4$  is under-predicted around two orders magnitude despite having reasonable prediction for the two-ring and three-ring PAHs. Besides, D'Anna and co-workers [146,147] noticed that their developed PAH mechanisms over-predicts the  $A_1$  concentration by a factor of three to four but the peak SVF is under-predicted by a factor of two under coflowing diffusion ethylene ( $C_2H_4$ ) flames. This suggests that their chemical kinetic mechanisms [146,147] probably lacks the reactions that are able to link the transition of gaseous species to the solid phase soot. Moreover, the under-prediction of  $A_4$  concentration in the work of Appel et al. [138] and Marinov et al. [144,145] indicates that reactions that contributes to the formation of  $A_4$  could be incomplete.

Set against this drawback, Slavinskaya et al. [148,149] constructed a 93 species and 729 reactions chemical kinetic mechanism that contains up to five aromatic rings species. In the formation of larger PAH species, it is noted that apart from the HACA mechanism, reactions of aromatic molecules/radicals – small molecules and aromatic molecules – aromatic radicals are also responsible for it [148]. Slavinskaya et al. [149] also compared their newly developed PAH mechanism to the previous PAH mechanisms [138,145] and found that the previous mechanisms [138,145] only consider the HACA mechanism for the growth of  $A_4$  from phenanthrene ( $A_3$ ). This explains why there is a huge deviation in the prediction of  $A_4$  in the previous modelling studies [138,145]. Hence, in order to improve the prediction of  $A_4$ , Slavinskaya et al.

[149] added two additional routes:  $A_2R_5 + \text{diacetylene (C}_4\text{H}_2) = A_4$  and  $A_1C_2H + A_1C_2H = A_4 + H$  into their mechanism and the prediction of  $A_4$  improves significantly. This improvement consolidates their earlier theory [148] that the formation of large PAH species does not depend only on the HACA mechanism.

In terms of PAH reduced mechanisms, Wang et al. [82] developed a PAH reduced mechanism based on the detailed mechanism by Slavinskaya et al. [148,149] with 41 species and 228 reactions that describes the PAH formation up to  $A_4$ . Meanwhile, Zeng and Chen [150] constructed a PAH reduced mechanism for  $C_2H_6$  combustion that comprises of 52 species and 83 reactions. Both reduced mechanisms [82,150] showed good validation results for the predictions of building blocks species such as  $C_2H_2$ ,  $C_2H_4$ ,  $C_4H_2$  and  $C_4H_4$  and PAH species such as  $A_1$ , naphthalene ( $A_2$ ),  $A_3$  and  $A_4$ . However, the PAH reduced mechanism by Wang et al. [82] has shown to be more accurate and has been used in many subsequent soot modelling studies [114,151–153].

Recently, Dong et al. [154] developed a reaction mechanism for PAH up to coronene ( $A_7$ ) for a multi-component diesel surrogate mechanism because it is observed that there are discrepancies between the measured and calculated soot emissions with  $A_4$  as the soot precursor. Nevertheless, Yoshihara et al. [155] found that the inclusion of PAH species larger than  $A_4$  only resulted in a final soot amount not more than a factor of two. Hence, a PAH mechanism up to  $A_4$  should give reasonable soot prediction without incurring high computational cost.



### 2.2.3 n-Butanol and its Isomers

From the kinetic modelling standpoint, the development of chemical kinetic mechanisms for n-butanol and its isomers is one of the main focus over the past decade. The available detailed chemical kinetic mechanisms for n-butanol and its isomers with its corresponding validating conditions are summarised in Table 2-3. Although the size of the n-butanol mechanisms is relatively smaller than those of diesel fuel, it is still large with up to a few hundred of species and a few thousands of reactions. Nonetheless, it should be noted that several detailed mechanisms [156–161] consists of all the butanol isomers and hence the large mechanism size. According to Table 2-3, the developed butanol detailed mechanisms [156–167] have been generally validated over a wide range of operating conditions such as ST ID times, JSR species concentration, laminar flame speed, pyrolysis species concentration and premixed laminar flame species concentration. The predictions by the butanol detailed mechanisms [156–167] have shown reasonable agreement to each validating conditions which then can be used as a starting point for the development of butanol reduced mechanism. The kinetic modelling of detailed butanol mechanism shows that the reactivity of the butanol isomers under ST auto-ignition conditions is in the descending order of n-butanol, iso-butanol, sec-butanol and tert-butanol [156]. Besides, it is found that butanol is mainly consumed through the H-atom abstraction followed by the  $\beta$ -scission which results in the production of fuel radicals [164] and these reactions have an influence on the ID times and species concentration profiles [159]. Meanwhile, Black et al. [162] discovered that the  $\alpha$  position in the n-butanol fuel structure has the highest tendency for H-atom abstraction followed by  $\gamma$ ,  $\beta$ ,  $\delta$  position. This is due to the lowest bond dissociation energy at the  $\alpha$  position as compared to other positions as shown in Figure 2-3. Contrarily, the abstraction from the OH group is least important [162]. Furthermore, in Zhang et al.'s [167] experiment, the H-atom abstraction is deduced to be an important reaction for the oxidation of n-butanol while unimolecular decomposition reaction only becomes dominant at higher temperatures.

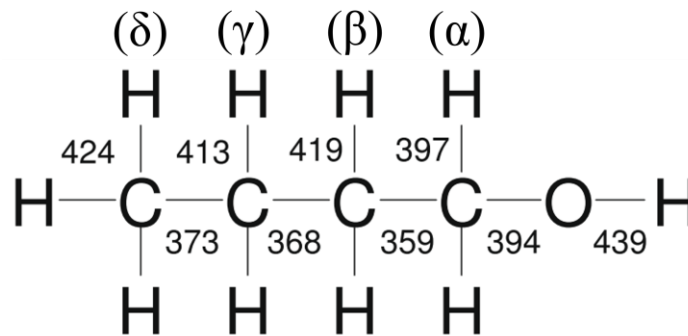


Figure 2-3: Bond dissociation energies of the n-butanol fuel structure [162]. The values shown are the dissociation energies in kJ/mol.

Despite the abundance of butanol detailed mechanisms, butanol reduced mechanism is more preferable for CFD simulations. Table 2-3 shows that the development of butanol reduced mechanisms mainly focuses on the n-butanol isomer. However, Chang et al. [168] managed to develop a compact reduced mechanism that consists of all butanol isomers with only 66 species and 196 reactions. On the other hand, Hui et al. [169] separately developed reduced mechanisms for each butanol isomer using the detailed mechanisms of Sarathy et al. [160] and Merchant et al. [170]. Although the number of species in the reduced mechanisms developed by Hui et al. [169] is generally lower than 100, the number of reactions are still high at around 1000 reactions averagely. Nonetheless, the n-butanol reduced mechanisms by Feng et al. [171] and Díaz-González et al. [172] are relatively compact in size and have been validated in various engine relevant operating conditions such as ST ID times, JSR species concentration and laminar flame speed. However, it is noticed that the reduced mechanism by Feng et al. [171] was not validated under lean operating conditions for ST ID times which is the main feature in HCCI engine [6]. Furthermore, Wang et al. [82] developed a n-butanol reduced mechanism that consists of 44 species and 177 reactions and has shown good validation results under ST ID times and premixed laminar flame species concentration. Despite that, it is only validated under a small range of operating conditions in which the fidelity of the mechanism remains unknown at other operating conditions apart from those being validated.

Table 2-3: Compilation of detailed and reduced mechanisms for n-butanol and its isomers.

Author	Type of mechanism	Number of species	Number of reaction	Validating conditions				Ref.
				Types of reactor	Equivalence ratio	Temperature	Pressure	
Moss et al.	Detailed <sup>a</sup>	158	1250	ST ID times	0.25 – 1.0	1200 – 1800 K	1.0 – 4.0 bar	[156]
Sarathy et al.	Detailed	118	878	JSR species concentration	0.25 – 2.0	800 – 1250 K	1.0 bar	[164]
				Laminar flame speed	0.7 – 1.4	350 K	0.9 bar	
				OPPDIFF	-	-	1.0 bar	
Dagaut et al.	Detailed	116	880	JSR species concentration	0.5 – 2.0	800 – 1150 K	10.1 bar	[163]
Grana et al.	Detailed <sup>a</sup>	249	7933	Pyrolysis in ST	-	1200 – 1600 K	1.0 bar	[157]
				Pyrolysis in flow reactors	0.67	1027 K	1.0 bar	
				ST ID times	0.25 – 2.0	1250 – 2000 K	1.0 bar	
				JSR species concentration	1.0	800 – 1250 K	1.0, 10.1 bar	
				Laminar flame speed	0.7 – 1.5	343 K	1.0 bar	
OPPDIFF	0.23, 0.5283	-	-					
Black et al.	Detailed	234	1399	ST ID times	0.5 – 2.0	1100 – 1800 K	1.0 – 8.1 bar	[162]
				JSR species concentration	0.5 – 2.0	800 – 1150 K	10.1 bar	
Geem et al.	Detailed <sup>a</sup>	281	3608	Pyrolysis	-	673 – 1010 K	1.72 bar	[158]
				ST ID times	0.25 – 1.0	1250 – 1818 K	1.30 – 3.95 bar	
				Doped methane flames	-	445 – 1898 K	-	
Liu et al.	Reduced	91	-	Ignition temperature	-	-	1.0, 3.0 bar	[173]
				Laminar flame speed	0.6-1.6	353 K	1.0, 2.0 bar	
Harper et al.	Detailed	263	3381	Pyrolysis	-	640 – 820 K	1.72 bar	[165]
				ST ID times	0.25 – 2.0	1100 – 1800 K	1.01 – 1.38 bar	
				JSR species concentration	0.25 – 2.0	800 – 1250 K	1.0, 10.1 bar	
				OPPDIFF	-	-	1.0 bar	
Doped methane flames	-	~450 K	-					
Cai et al.	Detailed	121	656	Pyrolysis	-	900 – 1200 K	0.006 – 1.0 bar	[166]

				ST ID times	0.5 – 2.0	1100 – 1800 K	1.0 – 45.6 bar	
				JSR species concentration	0.5 – 2.0	800 – 1250 K	1.0 bar	
				Premixed laminar flames	0.7, 1.0, 1.3, 1.8	-	0.02 – 0.03 bar	
Yasunaga et al.	Detailed <sup>a</sup>	284	1892	ST ID times	0.25 – 2.0	1000 – 1800 K	1.0 – 4.1 bar	[159]
				ST ID times	1.0	770 – 1667 K	1.4 – 81.0 bar	
				JSR species concentration	1.0	700 – 1200 K	10.1 bar	
Sarathy et al.	Detailed <sup>a</sup>	426	2335	Laminar flame speed	0.6 – 1.6	343 K	1.0 bar	[160]
				Premixed laminar flame	1.0	-	0.02 bar	
				Rapid compression machine	0.5 – 2.0	725 – 855 K	15.2 bar	
Zhang et al.	Detailed	243	1475	ST ID times	0.5 – 2.0	1200 – 1650 K	2.0, 10.1 bar	[167]
				JSR species concentration	1.0	800 – 1200 K	1.0 – 10.1 bar	
				Pyrolysis	-	1274 K, 1431 K	1.5, 1.6 bar	
Frassoldati et al.	Detailed <sup>a</sup>	317	12353	JSR species concentration	-	800 – 1150 K	10.1 bar	[161]
				Laminar flame speed	0.6 – 1.6	343 K	1.0 bar	
				Premixed laminar flame	-	-	-	
Wang et al.	Reduced	44	177	ST ID times	0.5 – 2.0	700 – 1250 K	40, 80 bar	[82]
				Premixed laminar flame	1.7	-	0.03 bar	
	Reduced <sup>b</sup>	126	832					
	Reduced <sup>c</sup>	149	953					
	Reduced <sup>d</sup>	126	929					
Brady et al.	Reduced <sup>e</sup>	84	543	Ignition temperature	-	380 K	1.0 – 4.1 bar	[174]
	Reduced <sup>f</sup>	102	1904					
	Reduced <sup>h</sup>	108	2197					
	Reduced <sup>i</sup>	117	1755					
				ST ID times	1.0	750 – 1550 K	10 – 80 bar	
Chang et al.	Reduced <sup>a</sup>	66	196	JSR species concentration	1.0	800 – 1150 K	10.1 bar	[168]
				Laminar flame speed	0.6-1.4	353 – 373 K	1.0 – 5.1 bar	
				Premixed laminar flame	1.7	-	0.04 bar	

				OPPDIFF	-	-	1.0 bar	
				Rapid compression machine	0.5 – 2.0	650 – 1000 K	15.2, 30.4 bar	
				HCCI simulator	0.22	-	-	
				ST ID times	1.0	770-1600 K	1.5 – 80 bar	
				JSR species concentration	0.5 – 2.0	800-1150 K	10.1 bar	
Feng et al.	Reduced	75	285	Laminar flame speed	0.6 – 1.6	353 – 433 K	1.0 – 10 bar	[171]
				Premixed laminar flame	1.0	-	0.02 bar	
				HCCI simulator	0.325	425 K	1.0 bar	
	Reduced <sup>b</sup>	86	637					
	Reduced <sup>c</sup>	85	574					
	Reduced <sup>d</sup>	95	687					
	Reduced <sup>e</sup>	81	536					
	Reduced <sup>b</sup>	61	409					
	Reduced <sup>c</sup>	58	385					
	Reduced <sup>d</sup>	62	425	ST ID times	0.2 – 2.0	700 – 1600 K	1.0 – 40.5 bar	
Hui et al.	Reduced <sup>e</sup>	64	445	Laminar flame speed	0.6 – 1.6	400 K	1.0 – 40.5 bar	[169]
	Reduced <sup>f</sup>	102	1904	PSR	0.5 – 1.5	400 K	1.0, 40.5 bar	
	Reduced <sup>g</sup>	153	3405	HCCI simulator	0.5	489 K	1.5 bar	
	Reduced <sup>h</sup>	108	2197					
	Reduced <sup>i</sup>	117	1755					
	Reduced <sup>f</sup>	68	1046					
	Reduced <sup>g</sup>	81	1709					
	Reduced <sup>h</sup>	69	1357					
	Reduced <sup>i</sup>	78	1114					
Liu et al.	Reduced	65	188	ST ID times	0.5 – 2.0	900 – 1800 K	1 – 30 bar	[175]
				ST ID times	0.5 – 2.0	770 – 1250 K	1.13 – 81.0 bar	
Gonzalez et al.	Reduced	62	279	JSR species concentration	0.25 – 2.0	800 – 1250 K	1.0 – 10.1 bar	[172]
				Laminar flame speed	0.6 – 1.6	343 – 373 K	1.0 – 10 bar	

- <sup>a</sup> Detailed mechanism contains butanol isomers (2-butanol, iso-butanol, tert-butanol)
- <sup>b</sup> n-butanol reduced mechanism based on Sarathy et al. [160] detailed mechanism
- <sup>c</sup> iso-butanol reduced mechanism based on Sarathy et al. [160] detailed mechanism
- <sup>d</sup> 2-butanol reduced mechanism based on Sarathy et al. [160] detailed mechanism
- <sup>e</sup> tert-butanol reduced mechanism based on Sarathy et al. [160] detailed mechanism
- <sup>f</sup> n-butanol reduced mechanism based on Merchant et al. [170] detailed mechanism
- <sup>g</sup> iso-butanol reduced mechanism based on Merchant et al. [170] detailed mechanism
- <sup>h</sup> 2-butanol reduced mechanism based on Merchant et al. [170] detailed mechanism
- <sup>i</sup> tert-butanol reduced mechanism based on Merchant et al. [170] detailed mechanism

#### 2.2.4 Diesel-n-Butanol Blends

As compared to the pure fuels, the mechanism development for fuel blends is limited partly due to the absence of experimental data for validation. In the context of diesel-n-butanol mechanism where it covers the diesel surrogate fuels such as n-heptane and n-dodecane, Wang et al. [82] merged a n-butanol reduced mechanism with 44 species and 177 reactions to a 41 species and 130 reactions base n-heptane mechanism. A reduced PAH mechanism is also merged into the n-butanol-n-heptane mechanism to form a final reduced n-heptane-n-butanol-PAH mechanism with 76 species and 349 reactions. Although this mechanism has shown good agreements to the experimental measurements under ST ID times, premixed laminar flame species concentration and 3D engine simulations, the mechanism is not validated for the laminar flame speed which is a key parameter for analysis of fuel reactivity, diffusivity and exothermicity [171]. Following that, Zhou et al. [83] added toluene into the Wang et al.'s [82] mechanism to form a n-heptane-n-butanol-toluene-PAH reduced mechanism because a research carried out by Golovitchev et al. [176] indicates that mixtures of n-heptane and toluene would better simulate the diesel combustion characteristics. Nevertheless, there is a lack of experimental validations under fundamental reactors such as ST and JSR [83] and for this reason Huang et al. [84] developed and optimised a new 101 species and 531 reactions mechanism for the combustion of n-heptane-n-butanol-toluene-PAH. The mechanism [84] has shown good agreements under a wide range of operating conditions such as ST ID times, laminar flame speed, premixed laminar flame species concentration, 0D HCCI engine and most importantly under 3D engine simulations. Upon recognising the potential limitations of the previous mechanisms [82–84] such as the neglect of low-temperature reaction pathways of toluene, Li et al. [85] constructed a 116 species and 433 reactions skeletal mechanism for the combustion of diesel-n-butanol blend with n-heptane acting as the diesel surrogate fuel. It should be highlighted that PAH reactions are absent in this mechanism [85] but toluene and a NO<sub>x</sub> sub-mechanism are included. Nevertheless, the diesel-n-butanol mechanism [85] well predicts the experimental conditions of ST ID times, laminar flame speed, premixed laminar flame species concentration and 3D engine simulations.

In spite of the development efforts for diesel-n-butanol mechanisms, the aforementioned mechanisms have utilised n-heptane as the surrogate fuel which is not suitable for representing diesel fuel as highlighted previously. On the contrary, as n-dodecane is a promising diesel surrogate fuel due to its close resemblance in physiochemical properties to diesel fuel and also its reasonable molecular size, Wakale et al. [75] developed a n-dodecane-n-butanol mechanism that consists of 203 species and 709 reactions by combining two existing n-dodecane [67] and n-butanol [177] reduced mechanisms. Subsequently, the reduced mechanism [75] is only validated under ST ID times and CFD simulations in an ignition quality tester where the trends of the experimental ID are well replicated. However, as a mechanism that is developed for diesel engine applications, additional validations under conditions such as JSR, laminar flame speed and premixed laminar flame are needed because those validation targets are crucial for diesel combustion processes. In a following study, Wakale et al. [88] added the PAH and NO<sub>x</sub> sub-mechanisms into the previous n-dodecane-n-butanol mechanism [75] to form a 246 species and 1062 reactions n-dodecane-n-butanol-PAH-NO<sub>x</sub> mechanism. Despite showing good predictions under ST ID times, JSR and premixed laminar flame species, the spray combustion ID is observed to over-predict by nearly a factor of three at ambient temperature of 800 K. Moreover, the size of the mechanism is considered huge (> 1000 reactions), which could increase the computational time. Nonetheless, the mechanisms by Wakale et al. [75,88] are among the first developments of diesel-n-butanol mechanism that utilise n-dodecane as the diesel surrogate fuel. Lately, Li et al. [178,179] developed a diesel-n-butanol-PAH mechanism using the decoupling method and this mechanism consists of 149 species and 497 reactions. In their mechanism, they have used multi-fuel surrogates such as n-dodecane, iso-cetane, iso-octane, toluene and decalin to represent diesel fuel. Although multi-fuel surrogates better represent the physiochemical properties of diesel fuel, the larger mechanism size will increase the computational time as there will be a higher number of conservation equations to solve for each species. Nonetheless, the mechanism showed satisfactory validation results when it is validated against the ID times, laminar flame speed, premixed flame species profile and 3D engine simulations.



## 2.3 Chemical Kinetic Reduction Methods

Modern chemical kinetics reduction methods are derived from mathematical algorithms and they are used to reduce detailed chemical kinetic mechanism by calculating the dependency among species. Each reduction methods gives different level of reduction and accuracy of the resulting skeletal mechanism. Therefore, proper selection of the reduction methods is needed to obtain the desired size and accuracy of the skeletal mechanism.

### 2.3.1 DRG

Lu and Law [180] first introduced a simple reduction algorithm that is called the direct relation graph (DRG) method which eliminates species and reaction that are deemed to be unimportant through the assessment on the rate of production (ROP). A species in the mechanism is represented as a node and it is connected to other species through a vertex. A simple illustration of the dependency between different species, with the width of the connecting lines showing its strength is presented in Figure 2-4.

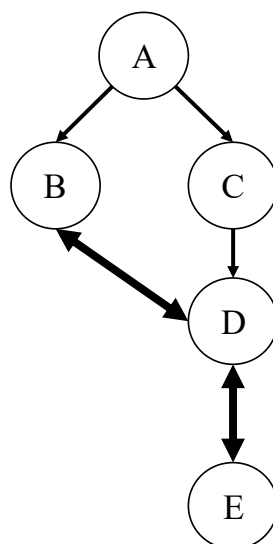


Figure 2-4: Example of species coupling relations for the DRG method.

From Figure 2-4, if the removal of species B causes a significant error in the production of species A, then species B should be retained in the mechanism. In other words, species A strongly depends on species B. The coupling dependency between two types of species can be calculated through the species coupling dependency ratio,  $r_{AB}$ , as follows:

$$r_{AB} = \frac{\sum_{i=1,I} |v_{A,i} \omega_i \delta_{Bi}|}{\sum_{i=1,I} |v_{A,i} \omega_i|} \quad (2-1)$$

where  $I$  is the total number of elementary reactions in the mechanism,  $v_{A,i}$  is the stoichiometric coefficient of species A,  $\omega_i$  is the net production rate of the  $i^{th}$  reaction and lastly  $\delta_{Bi}$  is the involvement of species B in the  $i^{th}$  reaction and it is expressed as follows:

$$\delta_{Bi} = \begin{cases} 1, & \text{if species B participates in the } i^{th} \text{ reaction} \\ 0, & \text{otherwise} \end{cases} \quad (2-2)$$

Based on Equations (2-1) and (2-2), a user-defined threshold  $\varepsilon$ , is needed to quantify the dependency strength of species A and species B, such that if  $r_{AB}$  is less than the user-defined threshold, species B is considered insignificant and can be safely eliminated without causing any significant errors to the mechanism. Moreover, it should also be noted that the DRG method considers a set of strong coupling species group that is reachable from species A. For instance, in Figure 2-4, if one were to remain species A in the mechanism, species B has to be kept which in turn relies on species D and these two species form a strong coupling species group to species A. Hence, both species B and D have to be retained for accurate prediction of species A. Nagy and Turányi [181] noticed this characteristics and mentioned it retains many unnecessary and redundant species in the mechanism as it considers all species to be equally important. To overcome the aforementioned drawback, Lu and Law [182] proposed an improvement to the DRG method which is called the “two-stage DRG”. This method restarts the procedure again after the first-stage reduction to further eliminate any unimportant species and reactions in the mechanism. Nonetheless, it can be argued that more than two stages of DRG reduction are needed for large-scale mechanism to achieve a compact size reduced mechanism but Lu and Law [182] confirmed that a two stage DRG is adequate, given that a typical skeletal mechanism generated from the first stage reduction is sufficiently small compared to the original mechanism. The mechanism size will only reduce slightly when the second stage reduction is performed. Any subsequent reduction after the second stage reduction is considered trivial and would not reduce the size of the mechanism significantly [182].

### 2.3.2 DRGEP

Due to the downside of the DRG method where it considers all species and reactions to be equally important and tends to retain the unnecessary ones, Pepiot-Desjardins and Pitsch [183] proposed a new method called the direct relation graph with error propagation (DRGEP) method. Unlike the DRG method, this new method considers species that is further away from the target species (e.g. fuel, oxidiser, key radicals, pollutants) to be less important. The species coupling dependency ratio of the DRG method [180] is modified slightly in the DRGEP method where it considers the contributions of the overall production and consumption rate of one species to the other. The newly modified dependency ratio or also known as the direct interaction coefficient (DIC) is expressed as follows:

$$r_{AB} = \frac{\sum_{i=1, n_R} |v_{A,i} \omega_i \delta_{Bi}|}{\max(P_A, C_A)} \quad (2-3)$$

$$P_A = \sum_{i=1}^{n_R} \max(0, v_{A,i} \omega_i) \quad (2-4)$$

$$C_A = \sum_{i=1}^{n_R} \max(0, -v_{A,i} \omega_i) \quad (2-5)$$

$$\delta_{Bi} = \begin{cases} 1, & \text{otherwise} \\ 0, & \text{if species B participates in the } i^{\text{th}} \text{ reaction} \end{cases} \quad (2-6)$$

where  $n_R$  is the total number of elementary reactions in the mechanism,  $v_{A,i}$  is the stoichiometric coefficient of species A,  $\omega_i$  is the net production rate of the  $i^{\text{th}}$  reaction,  $\delta_{Bi}$  is the involvement of species B in the  $i^{\text{th}}$  reaction,  $P_A$  is the ROP of species A and  $C_A$  is the rate of consumption (ROC) of species A.

Next, the path-dependent interaction coefficient (PIC) is calculated by taking the product of all DICs from the target species to the species of interest. Once the PICs for all possible pathways from the target species to the species of interest are determined, the maximum among all PICs is then defined as the overall interaction coefficient (OIC). The expressions for the PIC and OIC are listed as follows:

$$r_{AB,p} = \prod_{i=1}^{n-1} r_{x_i x_{i+1}} \quad (2-7)$$

$$R_{AB} = \max(r_{AB,p}) \quad (2-8)$$

where  $n$  is the number of species along the pathway from species A to species B and  $x$  is a placeholder of the intermediate species from species A to B.

For example, considering the species mapping in Figure 2-5, the PIC values from species A to species D are calculated as follows:

$$r_{AD1} = (r_{AB} \cdot r_{BC} \cdot r_{CD})$$

$$r_{AD2} = (r_{AB} \cdot r_{BD})$$

After that, the OIC is determined through the maximum of the two PICs listed above. From there, a user-defined threshold  $\varepsilon_{EP}$  is defined and species with OIC value lower than the threshold value is considered unimportant and eliminated from the mechanism. The main difference of the DRGEP method compared to the DRG method is that it offers finer selection of the species by tracing the error that is propagated from the species of interest up to the target species [183,184]. Therefore, the selection of the target species related to chemical processes of interest is vital to maximise the reduction by better aligning the OIC value with error in the global phenomena such as ID times and laminar flame speed [104].

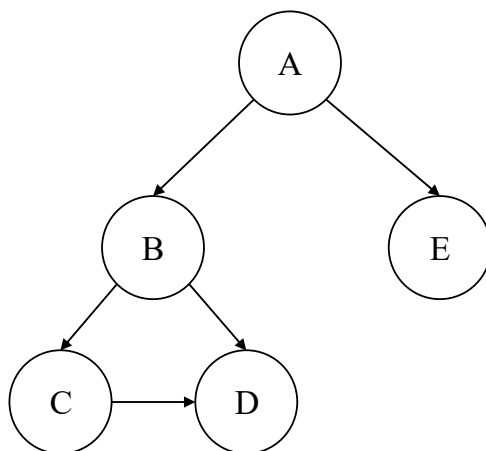


Figure 2-5: Example of species coupling relation for the DRGEP method.

Meanwhile, Niemeyer and Sung [185,186] investigated several graph search algorithms that is based on the DRGEP method. The algorithms include the depth-first search (DFS), breadth-first search (BFS) and the Dijkstra's algorithm. Detailed explanation and discussion of the DFS, BFS and Dijkstra algorithm can be found in the book published by Cormen et al. [187]. From the findings of Niemeyer and Sung [185], the DFS and BFS are among the most favourable algorithms adopted in mechanism reduction work. The DFS and BFS based algorithms initiate the search of a species through exploring their connection to other species along the pathway of the graph. On the other hand, the Dijkstra's algorithm is programmed to determine the shortest pathway from the target species to all other species. Therefore, although all the algorithms have comparable accuracy performance, the Dijkstra's algorithm is able to produce the smallest skeletal mechanism with the lowest computational time.

### 2.3.3 DRGASA

The concept of extending the DRG method with the sensitivity analysis (SA) is first introduced by Zheng et al. [188]. This development is done upon noticing the flaw of the DRG method where it retains species that is unimportant to the target species or the global phenomena. The DRGASA method performs brute-force SA right after the DRG to further minimise the size of the mechanism. As a result, it is more computational demanding and is not recommended to be used as the first stage reduction for large scale mechanisms. Despite improvements made to the DRG-based method, Niemeyer et al. [104] discovered that the DRGASA method could not identify all the unimportant species in the mechanism due to species "shielding". This occurs because the DRG method uses the species coupling dependency ratio or known as the DIC to rank the importance of a species relative to the target species. Hence, many species are automatically retained in the mechanism rather than being brought forward for assessment in the SA phase. As such, this method is not recommended for reduction work due to its inefficiency and high computational cost caused by the DRG method and SA phase, respectively.

### 2.3.4 DRGEPSA

By taking the advantage of the DRGEP and DRGASA methods, Niemeyer et al. [104] developed a new reduction method called the DRGEPSA method. This method combines the strength of the DRGEP method [183] and the SA phase in the DRGASA method [188], making it superior compared to the other methods discussed previously. This is proven in the study of Niemeyer et al. [104] where all previous methods including the DRGEPSA are applied to the n-heptane and iso-octane mechanism.

From Table 2-4 and Table 2-5, it can be observed that the DRGEPSA method produces the smallest skeletal mechanism size while maintaining the accuracy in the same range as the other methods which is below the error limit of 30%. In fact, for the iso-octane reduction, the DRGEPSA method generates a smaller skeletal mechanism yet with better accuracy when compared to the skeletal mechanism generated through DRGASA method. This is expected as the DRGEP phase can overcome the species “shielding” limitation induced by the DRGASA method and provides a more optimised mechanism in terms of mechanism size and accuracy. Nevertheless, since the DRGEPSA method involves SA, it is inevitable that this method will be more time consuming than the DRG and DRGEP methods. As a result, method is also not recommended to be used as the first step reduction for large scale mechanism.

Table 2-4: Comparison of the skeletal mechanism size of n-heptane using DRG, DRGEP, DRGASA and DRGEPSA methods [104].

Method	No. of species	No. of reactions	Maximum error (%)
DRG	211	1044	21
DRGASA	153	691	24
DRGEP	173	868	28
DRGEPSA	108	406	27

Table 2-5: Comparison of the skeletal mechanism size of iso-octane using DRG, DRGEP, DRGASA and DRGEP SA methods [104].

Method	No. of species	No. of reactions	Maximum error (%)
DRG	275	722	13
DRGASA	211	885	26
DRGEP	232	1140	15
DRGEP SA	165	779	19

### 2.3.5 Isomer Lumping

It is often that large-scale detailed mechanism contains species that have the same molecular weight but with distinct molecular structure and thermo-physical properties which are known as isomers. Isomer lumping is a reduction method that lumps all isomer species together into a single pseudo-species and hence reducing the size of the mechanism. For instance, Huang et al. [189] developed a novel chemical species lumping approach and successfully reduces a skeletal mechanism from 75 species to 53 species. On top of that, the lumped scheme allows the user to have direct control on the reduction scale through a user-defined threshold. In another study, Ahmed et al. [190] applied the isomer lumping method to the n-heptane detailed mechanism and it is able to reduce the parallel pathways isomeric species from 18 to 8 by lumping the heptyl peroxy radicals together. Meanwhile, Lu and Law [191] proposed a new isomer lumping approach by grouping isomers with similar thermal and diffusion properties together to reduce the number of species transport equations. In their approach [191], isomers with a concentration level lesser than  $1 \times 10^{-10}$  mole/cm<sup>3</sup> are directly removed from their mechanism while the remaining isomers are assessed to select the representative isomer for each group. The isomer lumping method managed to further reduce a 78 species skeletal mechanism to a 68 species skeletal mechanism by lumping 15 species into 5 different isomer groups. Furthermore, Stagni et al. [192] applied the isomer lumping method together with an automatic reduction scheme to formulate reduced mechanisms for n-heptane and n-dodecane and both reduced mechanisms show very similar prediction accuracy to the detailed mechanism under laminar co-flow flame simulations. Moreover, a reduction in computational time of about 35 times is achieved [192]. Generally, from these studies [189–192], it can be deduced that the isomer lumping method could be utilised

in combination with the other reduction methods such as the graph-based methods to obtain a compact yet robust reduced mechanism. While the graph-based methods require certain knowledge on the selection of target species, the isomer lumping method is a rather straightforward process as it only requires the selection of a representative species to represent the whole group of isomers.

#### **2.4 Numerical Modelling of Diesel-n-Butanol Blends under Diesel Engine Conditions**

Having realised the potential of blending n-butanol with diesel fuel, substantial effort has been made to investigate the combustion and emission characteristics of diesel-n-butanol blends experimentally and numerically. Experimental investigations have been conducted extensively and the engine-out measurement results for diesel-n-butanol have been briefly mentioned in Section 1.4. On the other hand, numerical investigations on diesel-n-butanol blends are rather scarce but they are equally important to acquire detailed insights on the in-cylinder events. As such, Chen et al. [78] numerically investigated the combustion and emission characteristics of diesel-n-butanol blend with 40% n-butanol blending ratio and results indicate that diesel-n-butanol blend has a longer ID which lowers the equivalence ratio and resulted in lower soot emission. However,  $\text{NO}_x$  emission is higher for diesel-n-butanol blend as compared to pure diesel due to wider region of high-temperature combustion [78]. Meanwhile, Zhou et al. [83] observed that the addition of n-butanol (10 – 30 % blending ratio) in diesel plays a significant role in soot suppression by slowing the formation of PAH soot precursor species. Additionally, Zhu et al. [59] found that the soot emission of diesel-n-butanol blend with 30% n-butanol blending ratio follows a non-monotonic trend when the oxygen concentration decreases from 21% to 15%. This is unlike the sooting behaviour of pure diesel where soot increases gradually as oxygen concentration decreases [59]. As oxygen concentration decreases, the increased in soot for the diesel-n-butanol blend was mainly caused by the decrease in soot oxidation while decreased in soot was caused by the decrease in soot formation [59]. The  $\text{NO}_x$  emission for diesel-n-butanol blend is lower than pure diesel and it decreases with lower oxygen concentration due to lower in-cylinder temperature and oxygen deficiency [59]. Furthermore, Huang et al. [193] numerically investigated diesel-n-butanol blend with 30% n-butanol blending ratio under a multi-injection



strategy in a diesel engine and results indicate that soot emission decreases with the increase in pre-injection interval but increases with the increase in pre-injection ratio. The  $\text{NO}_x$  emission increases with pre-injection interval but show no obvious difference with respect to the changes in pre-injection ratio. Besides, CO and UHC emissions increased with the increase in both pre-injection interval and pre-injection ratio. The UHC emission, which mainly composed of alkanes, olefins and methylbenzene are found to be mainly distributed in the central region and walls of the combustion chamber where the in-cylinder temperature and oxidation rate is low. Nevertheless, Kattela et al. [194] suggests that the increasing the in-cylinder swirl ratio and subsequently the turbulent kinetic energy could help mitigate high UHC emission by improving the air-fuel mixing within the combustion chamber. Lately, Zhang et al. [195] compared the combustion and emission characteristics of diesel-methanol, diesel-ethanol, diesel-n-butanol, diesel-methanol-n-butanol and diesel-ethanol-n-butanol in a diesel engine using CFD. The dual fuel blends are tested with an alcohol blending ratio of 10% and 20% whereas the ternary blends are set to 10% blending ratio for each alcohol fuel. Results show that with the increase in alcohol blending ratio, the cylinder pressure, cylinder temperature, heat release rate (HRR), ID increase whereas the combustion duration shortens. Soot, UHC and CO emissions of the blended fuels also decrease with diesel-methanol blends giving the most significant decrement. Contrarily, the  $\text{NO}_x$  emission increases due to increased cylinder temperature and high oxygen concentration in alcohol fuels. More importantly, all test fuels are found to effectively improve the combustion, performance and emission characteristics of a diesel engine with the diesel-methanol-n-butanol blend having the best balance between the three aforementioned aspects.

Besides engine test bed experiments, the combustion and emission characteristics of diesel-n-butanol blends are numerically investigated in a constant volume combustion chamber. Hou et al. [87] developed a nine steps phenomenological soot model to study the soot formation of diesel-n-butanol blend with 20% n-butanol blending ratio and it is revealed that the addition of n-butanol and the decrease in ambient temperature lowers the soot formation mechanism through the shrinking of high-temperature and fuel-rich zone in the fuel spray. On the other hand, Wakale et al. [88] reported that the  $\text{NO}_x$  and soot profiles in addition to the ID, FLOL

and LPL of n-dodecane-n-butanol blends up to 20% of n-butanol blending ratio are very similar to pure n-dodecane. This suggest that n-butanol is an ideal “drop-in” fuel for diesel combustion [88]. The flame structure of the n-dodecane-n-butanol blend with 20% n-butanol blending ratio is more compact as the ambient pressure and temperature increases, which could possibly minimised the  $\text{NO}_x$  formation regions at the outer core of the diffusion flame [88].

From the literature, the numerical studies related to diesel-n-butanol blends in both multi-dimensional engine and constant volume combustion chamber focus on the global combustion and emission characteristics only. However, the detailed processes of ignition, combustion and soot of diesel-n-butanol are not well understood and elucidated in previous modelling studies which is particularly important in the quest to design and optimise clean combustion engines. Having said that, these fundamental studies are not suitable to be conducted in a diesel engine due to the cycle-to-cycle variations of the ambient conditions in the engine [196]. Therefore, it is inevitable that the constant volume combustion chamber with ambient conditions similar to real diesel engines would be used to conduct the spray combustion fundamental study because it does not contain any surfaces such as piston and valves which makes it easier to segregate the effect of one parameter to the others. This also allows key processes such as fuel droplet breakup, evaporation, air-fuel mixing, ignition, combustion and soot formation to be well replicated and studied.

## 2.5 Concluding Remarks

Based on the literature review conducted above, it is found that n-heptane has been widely used as a diesel surrogate fuel in earlier diesel modelling studies. However, in recent years, n-dodecane is becoming more favourable because the carbon number and boiling characteristics of n-dodecane is within the range of real diesel fuel which allows the air-fuel mixing processes of diesel fuel to be well replicated. On the other hand, the species and reactions of PAH are crucial for reliable soot modelling results but it is unnecessary to include PAH species larger than  $\text{A}_4$  in the mechanism because simulation results show that there are no significant changes in final soot amount when larger PAH species are used. For the mechanisms of n-butanol, most work focuses on constructing detailed mechanisms whereas there are

only a few for the reduced mechanisms. Even so, the available n-butanol reduced mechanisms in literature are either large in mechanism size or validated only under limited engine conditions in which is also not favourable for practical high-fidelity simulations. Meanwhile, for the developments of diesel-n-butanol mechanism, a large majority of the mechanisms utilise n-heptane as their diesel surrogate fuel whereas the availability for n-dodecane-n-butanol mechanism is extremely scarce. To the author's best knowledge, there are only two mechanisms for n-dodecane-n-butanol in the literature but those mechanisms are having high number of species and reactions. The spray combustion simulations are also poorly predicted by the mechanisms. As such, it can be concluded that it is necessary to construct a compact yet comprehensive n-butanol reduced mechanism and combined it with a n-dodecane diesel surrogate mechanism where there is a need to further improve the existing n-dodecane-n-butanol mechanisms in terms of its size and accuracy.

To aid the development of the n-dodecane-n-butanol reduced mechanism, modern reduction methods such as DRG, DRGEP, DRGASA, DRGEP SA and isomer lumping are reviewed. In particular, the reduction methods that consists of the SA phase are not recommended to be used as the first-stage reduction as the computational cost is high [188]. Besides, the isomer lumping method is way more straightforward than the DRG-based methods as it does not require the identification of target species. Most importantly, studies [189–192] have proven that isomer lumping could be used in combination with the DRG-based methods to produce compact yet robust reduced mechanisms.

In terms of the combustion and emission characteristics of diesel-n-butanol, it has been studied extensively over the past decade in a diesel engine and constant volume combustion chamber. However, most studies are conducted experimentally and only a few of them are done numerically despite the importance of it to gain detailed understanding on the in-cylinder events. Nevertheless, the numerical studies that pertains to diesel-n-butanol in both 3D engine and constant volume combustion chamber have thus far only reported the engine-out measurements and the global spray combustion characteristics such as the ID, HRR, LPL, VPL and FLOL. There are very limited information regarding the chemical kinetics and the fundamental key processes

such as the ignition, combustion, flame and soot characteristics of diesel-n-butanol are not well understood. This shows that the overall understanding on diesel-n-butanol is still somehow limited and additional research should be done particularly in a constant volume combustion chamber to further develop and extract the potential of this fuel blend.

# CHAPTER 3

## COMPUTATIONAL MODELS

### 3.1 Introductory Remarks

This chapter presents the theoretical background of the chemical kinetics and CFD models used in this entire study with a detailed description on the governing equations. The software packages that are used in this study are ANSYS CHEMKIN-PRO 17.2 and ANSYS FLUENT 19.1. CHEMKIN-PRO is used to develop and solve the chemical kinetics of the detailed and reduced mechanisms and the governing equations are presented in Section 3.2. On the other hand, ANSYS FLUENT is used as a CFD tool to simulate the multidimensional simulations. The sub-models and its associated governing equations are presented in Section 3.3. Lastly, the numerical models that are used in this study are summarised in Section 3.4.

### 3.2 Chemical Kinetics

ANSYS CHEMKIN-PRO is a chemical kinetic modelling software used to solve complex gas phase and surface chemistry reactions for the development of reaction models in practical combustion systems. In order to run the simulations, the gas-phase chemistry (chem.inp) and thermodynamic data (therm.dat) are required and both of these files are categorised as the reaction mechanism. Details regarding each of the data files are tabulated in Table 3-1. In CHEMKIN-PRO, a set of state variables is used to define the thermodynamic and chemical state of the fluid mixture. The state variables that are available in CHEMKIN-PRO include the pressure ( $P$ ), density ( $\rho$ ), temperature ( $T$ ), mass fraction ( $Y_k$ ), mole fraction ( $X_k$ ) and molar concentration ( $[X_k]$ ). The calculations throughout CHEMKIN-PRO are performed using the equation of state of an ideal multi-fluid as shown in Equation (3-1),

Table 3-1: Details of the chemical data required to run the simulations in CHEMKIN-PRO.

File name	Contents
chem.inp	Chemical reactions and the Arrhenius rate in the gas phase
therm.dat	Thermochemical data of each species

$$P = \sum_{k=1}^{N_s} [X_k]RT_k \quad (3-1)$$

where  $R$  is the universal gas constant and  $N_s$  is the number of species.

In the therm.dat file, the standard-state thermodynamic properties for the species are expressed as functions of temperatures in the form of polynomial fits. These fits take the following form where the specific heat capacity ( $C_p$ ), enthalpy ( $H$ ) and entropy ( $S$ ) are calculated using Equations (3-2) to (3-4),

$$\frac{C_p}{R} = a_1 + a_2T + a_3T^2 + a_4T^3 + a_5T^4 \quad (3-2)$$

$$\frac{H}{RT} = a_1 + \frac{a_2}{2}T + \frac{a_3}{3}T^2 + \frac{a_4}{4}T^3 + \frac{a_5}{5}T^4 + \frac{a_6}{T} \quad (3-3)$$

$$\frac{S}{R} = a_1 \ln(T) + a_2T + \frac{a_3}{2}T^2 + \frac{a_4}{3}T^3 + \frac{a_5}{4}T^4 + a_7 \quad (3-4)$$

where  $a_n$  is the  $n$ -th polynomial fit coefficient. Meanwhile, the interactions of the gas-phase species are described by the gas-phase reactions and each species that participates in the reaction must contain a respective thermodynamic data. The equilibrium constants and reverse-rate coefficients for a reaction are then calculated using the thermodynamic data. The production rate of  $k$ th species ( $\dot{\omega}_k$ ) is written as the sum of the rate of progress for all reactions involving the  $k$ th species and it is defined in Equation (3-5),

$$\dot{\omega}_k = \sum_{i=1}^I v_{k,i} q_i \quad (3-5)$$

where  $I$  is the number of reactions involving  $k$ th species.  $v_{k,i}$  is the difference between the forward and backward stoichiometric coefficients as shown in Equation (3-6) and the rate of progress for the  $i$ th reaction ( $q_i$ ) is the difference of the forward and reverse rates as shown in Equation (3-7),

$$v_{k,i} = v''_{k,i} - v'_{k,i} \quad (3-6)$$

$$q_i = k_{fi} \prod_{k=1}^K [X_k]^{v'_{k,i}} - k_{ri} \prod_{k=1}^K [X_k]^{v''_{k,i}} \quad (3-7)$$

where  $v'_{k,i}$  and  $v''_{k,i}$  are the forward and reverse stoichiometric coefficients whereas  $k_{fi}$  and  $k_{ri}$  are the forward and reverse rate constants for the  $i$ th reaction.

The forward rate constant is described using the following Arrhenius temperature dependence equation:

$$k_{fi} = A_i T^{\beta_i} \exp\left(-\frac{E_i}{RT}\right) \quad (3-8)$$

where  $A$  is the pre-exponential factor,  $\beta_i$  as the temperature exponent and  $E_i$  as the activation energy. Following that, the reverse rate constant is calculated using the following equations:

$$k_{ri} = \frac{k_{fi}}{K_{ci}} \quad (3-9)$$

$$K_{ci} = K_{pi} \left(\frac{P_{atm}}{RT}\right)^{\sum_{k=1}^K v_{ki}} \quad (3-10)$$

$$K_{pi} = \exp\left(\frac{\Delta S_i}{R} - \frac{\Delta H_i}{RT}\right) \quad (3-11)$$

where  $K_{ci}$  and  $K_{pi}$  are the equilibrium constants determined from thermodynamic properties of the species.  $P_{atm}$  is the atmospheric pressure and  $\Delta$  refers to the changes that occurs when the reactants is completely passed to products for the  $i$ th reaction.





In some cases, a “third body” is present in the reaction in order for the reaction to proceed. Therefore, the concentration of the third body must appear in the equation for the rate of progress. Accordingly, Equation (3-7) is modified as follows:

$$q_i = \left( \sum_{k=1}^K (a_{ki}) [X_k] \right) \left( (k_{fi} \prod_{k=1}^K [X_k]^{v'_{k,i}} - k_{ri} \prod_{k=1}^K [X_k]^{v''_{k,i}}) \right) \quad (3-12)$$

where  $a_{ki}$  is set to 1 for every species if all species in the mixture contribute equally as third bodies.

In CHEMKIN-PRO, there is a wide range of 0D and 1D reactor models that are available to model industry reacting flow conditions such as open and closed homogeneous reactor, flow reactor, flame simulator and engine simulator. The reactor models employed in this study are tabulated in Table 3-2 to model the auto-ignition, species concentration and the flame characteristics of the reduced and detailed mechanisms. On the other hand, the understanding of the effects of chemical kinetics towards the target solutions (e.g., ID) is achieved through the sensitivity and ROP analyses.

Table 3-2: Descriptions of reactor models used in the simulations.

Model	Reactor name	Type	Description
	Closed Homogeneous Batch Reactor	0D	Transient, constant volume, homogeneous
	PSR	0D	Transient, PSR
	Premixed Laminar Flame-Speed Calculation	1D	Freely propagating flame for flame speed calculation
	Premixed Laminar Burner-Stabilized Flame	1D	Premixed, stabilised flame on a burner port.

### 3.2.1 Homogeneous 0D Reactor Models

The Closed Homogeneous Batch Reactor and PSR are 0D homogeneous reactors where it allows the investigation of systems with close coupling between the



gas-phase kinetics and surface kinetics. In these well mixed or stirred reactors, the reactant's rate of conversion to products is controlled by chemical reaction rates but not by mixing processes. Hence, it can be said that the reactor is "limited" by reaction kinetics. As a results, these reactors are very suitable to be used to model the ST ignition and JSR species concentration as the operating principles of a ST and JSR do not involved any physical processes such as fuel atomisation, breakup and mixing and the occurrence of combustion is purely dependent on the chemical kinetics.

In modelling these homogeneous reactors, the mass transport to the reactor walls is assumed to be infinitely fast. Besides, the flow through the reactor is quantified by a nominal residence time, where it can be deduced from the flow rate and the reactor volume. The conservation of mass, energy and species of a homogeneous system include net generation of chemical species within the reactor volume, net loss of species and mass to surfaces in the reactor. In the closed batch reactor, no inlets or outlets flow are available during the entire period of interest, although heat flow to the environment may or may not happen. Such batch systems are transient in nature and the chemical state changes as production and destruction of a species occur through chemical reaction. On the other hand, the PSR consists of a chamber and having inlet and outlet ducts where there may be more than one inlet defined for each reactor.

The global mass conservation in a reactor, where the time-rate of change for the mass is equal to the difference between mass flow in and out plus any material that is added or subtracted from the surfaces within the chamber, is describe as the following equation:

$$\begin{aligned} \frac{d}{dt}(\rho V)^{(j)} = & \sum_{i=1}^{N_{inlet(j)}} \dot{m}_i^{*(j)} \\ & + \sum_{r=1}^{N_{PSR}} \dot{m}^{(r)} R_{rj} - \dot{m}^{(j)} + \sum_{m=1}^M A_m^{(j)} \sum_{k=1}^{K_g} \dot{s}^{(j)}_{k,m} W_k \end{aligned} \quad (3-13)$$

where  $j$  is the reactor number,  $V$  is the reactor volume,  $\dot{m}^*$  is the inlet mass flow rate,  $\dot{m}$  is the outlet mass flow rate,  $N_{inlet(j)}$  is the number of inlets for each reactor  $j$ ,  $N_{PSR}$

is the total number of reactor modules in the reactor network and  $R_{rj}$  is the fraction of the outflow of reactor  $r$  that is recycled into reactor  $j$ . In Equation (3-13), the last term towards the right represents the difference between the outlet mass flow and the sum of the inlet and recycled mass flow due to deposition or etching of materials within the reactor. In that term,  $A_m$  is the surface area of the  $m$ th material within the reactor,  $\dot{s}_{k,m}$  is the molar surface production rate of the  $k$ th species on the  $m$ th material per unit surface area and  $W_k$  is the molecular weight of the  $k$ th species. There are  $K_g$  gas-phase species and  $M$  materials. Following the mass conservation equation, the time-dependent equation for mass conservation of each gas-phase species is given as follows:

$$\begin{aligned}
 (\rho V)^{(j)} \frac{dY_k^{(j)}}{dt} &= \sum_{i=1}^{N_{inlet(j)}} \dot{m}_i^{*(j)} (Y_{k,i}^* - Y_k) + \\
 \sum_{r=1}^{N_{PSR}} \dot{m}^{(r)} R_{rj} (Y_k^{(r)} - Y_k^{(j)}) - & \\
 Y_k^{(j)} \sum_{m=1}^M A_m^{(j)} \sum_{k=1}^{K_g} \dot{s}_{k,m}^{(j)} W_k + (\dot{\omega}_k V)^{(j)} W_k + & \\
 \sum_{m=1}^M A_m^{(j)} \dot{s}_{k,m}^{(j)} W_k &
 \end{aligned} \tag{3-14}$$

The superscript \* denotes the inlet stream quantities.

For steady-state conditions, the nominal residence time ( $\tau$ ) in the reactor is calculated as follows:

$$\tau = \frac{\rho V}{[\sum_{i=1}^{N_{inlet(j)}} \dot{m}_i^{*(j)} + \sum_{r=1}^{N_{PSR}} \dot{m}^{(r)} R_{rj}]} \tag{3-15}$$

The residence time is often a characteristic parameter of a reactor instead of the mass flow rate of the steady-state flow. Thus, Equation (3-15) can be used to calculate  $\dot{m}^*$  from the specified residence time. However, in the case where the mass flow rate is zero, the reactor may not be characterised by the residence time.

### 3.2.2 1D Premixed Laminar Flames Models

The equations governing the Premixed Laminar Flame-Speed Calculation and Premixed Laminar Burner-Stabilized Flame models are treated as steady, isobaric and 1D. The Premixed Laminar Flame-Speed Calculation model is used to characterise the flame speed of the fuel-oxidiser mixture and also determine its flammability limits.

Contrarily, the Premixed Laminar Burner-Stabilized Flame model is often used to analyse the species profiles in flame experiments. Both models uses the implicit finite difference methods and a combination of time-dependent and steady state methods to solve the set of governing equations. Moreover, in order to enhance the convergence properties of the steady-state approach and to provide optimal mesh placement, the solver algorithm automates the coarse-to-fine grid refinement method. With the assumption the flow is 1D and the inlet conditions are uniform, the conservation equations for continuity, energy and species are presented in Equations (3-16), (3-17) and (3-18), respectively,

$$\dot{M} = \rho u A \quad (3-16)$$

$$\begin{aligned} \dot{M} \frac{dT}{dx} - \frac{1}{C_p} \frac{d}{dx} \left( \lambda A \frac{dT}{dx} \right) \\ + \frac{A}{C_p} \sum_{k=1}^K \rho Y_k V_k C_{pk} \frac{dT}{dx} + \frac{A}{C_p} \sum_{k=1}^K \dot{\omega}_k h_k W_k + \frac{A}{C_p} \dot{Q}_{rad} = 0 \end{aligned} \quad (3-17)$$

$$\dot{M} \frac{dY_k}{dx} + \frac{d}{dx} (\rho A Y_k V_k) - A \dot{\omega}_k W_k = 0 \quad (3-18)$$

where  $x$  denotes the spatial coordinates,  $\dot{M}$  is the mass flow rate,  $u$  is the velocity of fluid mixture,  $\lambda$  is the thermal conductivity of mixture,  $C_{pk}$  is the constant pressure heat capacity of the  $k$ th species,  $h_k$  is the specific enthalpy of the  $k$ th species,  $V_k$  is the diffusion velocity of the  $k$ th species,  $\dot{Q}_{rad}$  is the heat loss due to gas and particle radiation and  $A$  is the cross-sectional area of the steam tube encompassing the flame normalised by the burner area.

By using the mixture-averaged transport approach, the diffusion velocity  $V_d$  is assumed to consists of three parts as follows:

$$V_d = V_o + W_d + V_c \quad (3-19)$$

$$V_o = -D_{km} \frac{1}{X_k} \frac{dX_k}{dx} \quad (3-20)$$

$$D_{km} = \frac{1 - Y_k}{\sum_{j \neq k}^K \frac{X_j}{D_{kj}}} \quad (3-21)$$

$$W_d = \frac{D_{km}\theta_k}{X_k} \frac{1}{T} \frac{dT}{dx} \quad (3-22)$$

where  $V_o$  is the ordinary diffusion velocity,  $D_{km}$  is the mixture-averaged diffusion coefficient,  $W_d$  is the thermal diffusion velocity,  $\theta_k$  is the thermal diffusion ratio and  $V_c$  is the correction velocity.

### 3.2.3 SA and ROP

The SA of a solution is performed to understand quantitatively on how the solution is affected by various parameters contained in a model. For steady-state computations, the sensitivity coefficients is represented as follows:

$$F(\phi(\alpha); \alpha) = 0 \quad (3-23)$$

where the residual vector ( $F$ ) is dependent both explicitly and implicitly on the solution vector ( $\phi$ ) and also a set of model parameters ( $\alpha$ ). By differentiating Equation (3-23) with respect to  $\alpha$ , a matrix equation for the sensitivity coefficient is obtained as follows:

$$\frac{\partial F}{\partial \phi} \frac{\partial \phi}{\partial \alpha} + \frac{\partial F}{\partial \alpha} = 0 \quad (3-24)$$

The matrix  $\frac{\partial F}{\partial \phi}$  is the Jacobian of the original system and  $\frac{\partial F}{\partial \alpha}$  is the matrix of partial derivatives of  $F$  with respect to the parameters. Meanwhile,  $\frac{\partial \phi}{\partial \alpha}$  is the sensitivity coefficients matrix and it contains quantitative information on the effects of each reaction-rate coefficient towards the temperatures and species fraction.

In addition, the system of ordinary differential equations for transient problems is of the general form of:

$$\frac{d\phi}{dt} = F(\phi, t; \alpha) \quad (3-25)$$

where  $\phi$  is the vector of temperature, mass fractions, surface site fractions and bulk activities. The first-order sensitivity coefficient matrix is defined as:

$$w_{j,i} = \frac{\partial \phi}{\partial \alpha_i} \quad (3-26)$$

where indices  $j$  and  $i$  refer to the dependent variables and reactions, respectively. CHEMKIN further processed the raw sensitivity coefficients to make them more useful by computing the normalised sensitivity coefficients in the form of logarithmic derivatives as follows:

$$\left. \frac{\partial \ln Y_k}{\partial \ln \alpha_i} \right|_F = \frac{\alpha_i}{Y_k} \left. \frac{\partial Y_k}{\partial \alpha_i} \right|_F \quad (3-27)$$

$$\left. \frac{\partial \ln T}{\partial \ln \alpha_i} \right|_F = \frac{\alpha_i}{T} \left. \frac{\partial T}{\partial \alpha_i} \right|_F \quad (3-28)$$

Apart from SA, the ROP analysis is also another useful tool to determine the contribution of each reaction to the net production or destruction rates of a species. For 0D homogeneous system, the molar production of a species per unit volume  $P_k$  is expressed as:

$$P_k = \sum_{i=1}^I v_{ki} q_i \quad (3-29)$$

where  $v_{ki}$  is the stoichiometric coefficients for gas reactions and  $q_i$  is the rate of progress of the  $I$ th gas-phase reactions. From here, the contribution to the ROP of species  $k$  from gas-phase reaction  $I$  is calculated as:

$$C_{ki} = v_{ki} q_i \quad (3-30)$$

Additionally, the computed normalised values of the reaction contributions to the species production ( $\bar{C}_{ki}^p$ ) and destruction ( $\bar{C}_{ki}^d$ ) rates are given as:

$$\bar{C}_{ki}^p = \frac{\max(v_{ki}, 0) q_i}{\sum_{i=1}^I \max(v_{ki}, 0) q_i} \quad (3-31)$$

$$\bar{C}_{ki}^d = \frac{\min(v_{ki}, 0) q_i}{\sum_{i=1}^I \min(v_{ki}, 0) q_i} \quad (3-32)$$

### 3.3 CFD Sub-Models

ANSYS FLUENT is a CFD package that acts as a solver for various flow-related cases such as laminar, turbulent, multiphase and reacting. Therefore, the selection of appropriate CFD sub-models is crucial to ensure that accurate results are obtained. In this section, the CFD sub-models that are employed to model the complex processes of the spray, ignition, combustion and emission are discussed. Among those that are described below includes the spray breakup model, turbulence model, combustion model and soot model.

#### 3.3.1 Spray Breakup Model

Accurate prediction of the fuel spray droplet breakup is important as it affects the subsequent air-fuel mixing process and ultimately the auto-ignition. There are three main spray breakup models available in ANSYS FLUENT and they are the Taylor analogy breakup model, Wave model and Kelvin-Helmholtz – Rayleigh-Taylor (KHRT) model. The Taylor analogy breakup model is not suitable for diesel sprays because it is developed for low-Weber-number, low-speed sprays. Meanwhile, the Wave model is more suitable for high-speed fuel injections where it considers the Kelvin – Helmholtz instability. Nevertheless, as compared to the Wave model, the KHRT model is much more superior because it takes into account both the KH waves driven by aerodynamic forces and the RT instabilities due to acceleration of shed drops injected into freestream conditions [197] (Further discussion regarding the spray breakup model is found in Chapter 5). For this reason, the KHRT model is selected to be used in this study to model the diesel spray breakup.

The KHRT model is suitable for High-Weber-number sprays and is not for low pressure sprays. In the KH breakup model, the newly formed droplets are assumed to have a radius that is proportional to the wavelength of the fast-growing unstable surface wave on the parent droplet as describe in Equation (3-33),

$$r = B_0 \Lambda \quad (3-33)$$

where  $B_0$  is a model constant normally taken as 0.61 based on the suggestion of Reitz [198].  $\Lambda$  is the corresponding wavelength and is given as:

$$\frac{\Lambda}{a} = 9.02 \frac{(1 + 0.45Oh^{0.5})(1 + 0.4Ta^{0.7})}{(1 + 0.87We_2^{1.67})^{0.6}} \quad (3-34)$$

where  $Oh = \sqrt{We_1}/Re_1$  is the Ohnesorge number and  $Ta = Oh\sqrt{We_2}$  is the Taylor number. In addition,  $We_1 = \rho_1 U^2 a / \sigma$  and  $We_2 = \rho_2 U^2 a / \sigma$  are the Weber numbers of liquid and gas, respectively, and  $Re_1 = Ua/v_1$  is the Reynolds number.  $\rho_1$  and  $\rho_2$  are the densities of liquid and gas, respectively,  $\sigma$  is the surface tension,  $U$  is the relative velocity between liquid droplets and gas phase,  $a$  is the radius of the liquid jet and  $v_1$  is the viscosity of liquid fuel. Furthermore, the rate of change of the droplet radius in a parent parcel due to drop breakup is given as:

$$\frac{da}{dt} = -\frac{(a-r)}{\tau}, r \leq a \quad (3-35)$$

where the breakup time,  $\tau$  is expressed as:

$$\tau = \frac{3.726B_1 a}{\Lambda \Omega} \quad (3-36)$$

and  $\Lambda$  is obtained from Equation (3-34) while the growth rate of the fastest growing wave,  $\Omega$  is expressed as:

$$\Omega \left( \frac{\rho_1 a^3}{\sigma} \right) = \frac{(0.34 + 0.38We_2^{1.5})}{(1 + Oh)(1 + 1.4Ta^{0.6})} \quad (3-37)$$

$B_1$  is a breakup time model constant and it can be varied between 1 to 60, depending on the injector characterisation.

For the RT model, the frequency of the fastest growing wave,  $\Omega_{RT}$  is computed by

$$\Omega_{RT} = \sqrt{\frac{2[-g_t(\rho_l - \rho_g)]^{3/2}}{3\sqrt{3}\sigma(\rho_l + \rho_g)}} \quad (3-38)$$

and the corresponding wave number is given by

$$K_{RT} = \sqrt{\frac{-g_t((\rho_l - \rho_g))}{3\sigma}} \quad (3-39)$$

where  $g_t$  is the droplet acceleration in the direction of the droplet travel,  $\rho_l$  and  $\rho_g$  are the densities of liquid and gas, respectively.

The wavelength that corresponds to the fastest wave growth rate is given as  $2\pi C_{RT}/K_{RT}$  and this is compared to the droplet radius. The RT waves are assumed to be growing if the wavelength is smaller than the droplet diameter and the wave growth time is tracked. The wave growth time is then compared with the breakup time as defined by Equation (3-40),

$$\tau_{RT} = \frac{C_\tau}{\Omega_{RT}} \quad (3-40)$$

where  $C_\tau$  is a model constant with a default value of 0.5. Droplets are assumed to breakup if the RT waves have been growing for a time larger than the breakup time and the radius of the child droplet is calculated using Equation (3-41),

$$r_c = \frac{\pi C_{RT}}{K_{RT}} \quad (3-41)$$

where  $C_{RT}$  is an adjustable model constant with a default value of 0.1.

The KHRT model also assumes the existence of a liquid core near the nozzle region and child droplets are shed from this liquid core which is then subjected to sudden acceleration in the freestream conditions where the RT model becomes a dominant effect. The breakup length of this liquid core is calculated from the Levich theory [199] as presented in Equation (3-42),

$$L = C_L d_0 \sqrt{\frac{\rho_l}{\rho_g}} \quad (3-42)$$

where  $C_L$  is the Levich constant and  $d_0$  is the reference nozzle diameter.

### 3.3.2 Turbulence Model

In this study, the standard Reynolds-averaged  $k-\varepsilon$  turbulence model is applied to the simulations to predict the turbulence flow conditions during the spray combustion (Further discussions related to the selection of turbulence model is found in Chapter 5). The selection of Reynolds-averaged over large-eddy simulation is mainly due to the consideration of the computational cost and also the popularity of



Reynolds-averaged simulations in the industry [200]. The standard  $k$ - $\varepsilon$  turbulence model is a two-equation semi-empirical model where the transport equations are solved separately to determine the turbulent length and time scale. In the derivation of the model, the flow is assumed to be fully turbulent and the effects of molecular viscosity are negligible.

The turbulence kinetic energy ( $k$ ) and the rate of dissipation ( $\varepsilon$ ) are obtained from transport equations are follows:

$$\frac{\partial}{\partial t}(\rho k) + \frac{\partial}{\partial x_i}(\rho k u_i) = \frac{\partial}{\partial x_j} \left[ \left( \mu + \frac{\mu_t}{\sigma_k} \right) \frac{\partial k}{\partial x_j} \right] + G_k + G_b - \rho \varepsilon - Y_M + S_k \quad (3-43)$$

$$\begin{aligned} \frac{\partial}{\partial t}(\rho \varepsilon) + \frac{\partial}{\partial x_i}(\rho \varepsilon u_i) \\ = \frac{\partial}{\partial x_j} \left[ \left( \mu + \frac{\mu_t}{\sigma_\varepsilon} \right) \frac{\partial \varepsilon}{\partial x_j} \right] + C_{1\varepsilon} \frac{\varepsilon}{k} (G_k + C_{3\varepsilon} G_b) - C_{2\varepsilon} \rho \frac{\varepsilon^2}{k} + S_\varepsilon \end{aligned} \quad (3-44)$$

where  $G_k$  is the generation of turbulence kinetic energy due to mean velocity gradients,  $G_b$  is the generation of turbulence kinetic energy due to buoyancy and  $Y_M$  represents the contribution of the fluctuating dilatation in compressible turbulence to the overall dissipation rate.  $C_{1\varepsilon}$ ,  $C_{2\varepsilon}$  and  $C_{3\varepsilon}$  are model constants while  $\sigma_k$  and  $\sigma_\varepsilon$  are the turbulent Prandtl numbers for  $k$  and  $\varepsilon$ , respectively. The turbulent viscosity ( $\mu_t$ ) in both transport equations above is computed using the equation as follows:

$$\mu_t = \rho C_\mu \frac{k^2}{\varepsilon} \quad (3-45)$$

where  $C_\mu$  is a model constant.

In ANSYS FLUENT, the aforementioned model constants in the standard  $k$ - $\varepsilon$  model have default values and they are being tabulated in Table 3-3.

Table 3-3: Model constants in the standard  $k$ - $\varepsilon$  turbulence model.

Model constant	$C_{1\varepsilon}$	$C_{2\varepsilon}$	$C_\mu$	$\sigma_k$	$\sigma_\varepsilon$
Default value	1.44	1.92	0.09	1.0	1.3

### 3.3.3 Combustion Model

In this study, the species transport with finite rate chemistry combustion model is used to model the combustion processes in the reacting flow and the CFD-CHEMKIN chemistry solver is employed as the chemistry acceleration tool. This model is chosen because it solves a sequence of reactions and the transport equations for each species to characterise the combustion and emission events. In order to achieve high-fidelity combustion simulations, a detailed chemistry model is much needed as compared to a pre-tabulated chemistry model where it consists only a one-step global mechanism which is unrealistic for the combustion process.

In this species transport model, the conservation equations for chemical species are resolved and the local mass fraction of each species is predicted through the solution of a convection-diffusion equation for the  $i$ th species as follows:

$$\frac{\partial}{\partial t}(\rho Y_i) + \nabla \cdot (\rho \vec{v} Y_i) = -\nabla \cdot \vec{J}_i + R_i + S_i \quad (3-46)$$

where  $R_i$  is the net production rate of species  $i$  by chemical reaction and  $S_i$  is the rate of creation by addition from the dispersed phase plus any user-defined source.

In Equation (3-46),  $\vec{J}_i$  is the diffusion flux of species  $I$  which is due to the gradients of concentration and temperature. By default, ANSYS FLUENT utilises the dilute approximation or known as Fick's law to compute the mass diffusion due to concentration gradients as given below:

$$\vec{J}_i = -\rho D_{i,m} \nabla Y_i - D_{T,i} \frac{\nabla T}{T} \quad (3-47)$$

where  $D_{i,m}$  is the mass diffusion coefficient for species  $I$  and  $D_{T,i}$  is the thermal diffusion coefficient. Contrarily, in turbulent flows, the mass diffusion is written as follows:

$$\vec{J}_i = -\left(\rho D_{i,m} + \frac{\mu_t}{Sc_t}\right) \nabla Y_i - D_{T,i} \frac{\nabla T}{T} \quad (3-48)$$

where  $Sc_t$  is the turbulent Schmidt number.

### 3.3.4 Soot Model

ANSYS FLUENT provides three soot models which is the one-step Khan and Greeves model [201], two-step Tesner model [201] and the Moss-Brookes model [202]. Both the one-step and two-step soot models are empirical and the detailed chemistry and physics of soot formation are only approximated in these models. Contrarily, the Moss-Brookes soot model is a semi-empirical, multi-step model that incorporates the soot nucleation, surface growth, coagulation and oxidation processes. As such, the Moss-Brookes model should theoretically provide much higher accuracy than the one-step and two-step models and is thus selected to be used in this study to simulate soot. To further support the selection of model, the Moss-Brookes soot model has also been widely used to predict soot in diesel combustion simulations [130,203,204].

The soot model solves the transport equations for the normalised radical nuclei concentration ( $b^*_{nuc}$ ) and soot mass fraction ( $Y_{soot}$ ) and they are expressed as follows:

$$\frac{\partial}{\partial t}(\rho b^*_{nuc}) + \nabla \cdot (\rho \vec{v} b^*_{nuc}) = \nabla \cdot \left( \frac{\mu_t}{\sigma_{nuc}} \nabla b^*_{nuc} \right) + \frac{1}{N_{norm}} \frac{dN}{dt} \quad (3-49)$$

$$\frac{\partial}{\partial t}(\rho Y_{soot}) + \nabla \cdot (\rho \vec{v} Y_{soot}) = \nabla \cdot \left( \frac{\mu_t}{\sigma_{soot}} \nabla Y_{soot} \right) + \frac{dM}{dt} \quad (3-50)$$

where  $\sigma_{soot}$  is the turbulent Schmidt number,  $M$  is the soot mass concentration and  $N$  is the soot particle number density.  $N_{norm}$  is the value used to normalised the soot number density and it is set at  $10^{15}$  particles [201]. The source term in Equation (3-49),  $\frac{dN}{dt}$ , represents the instantaneous production rate of soot particles that is subjected to nucleation from the gas phase and coagulation in the free molecular regime. It is expressed as follows:

$$\frac{dN}{dt} = C_\alpha N_A \left( \frac{X_{prec} P}{RT} \right)^l \exp \left\{ -\frac{T_\alpha}{T} \right\} - C_\beta \left( \frac{24RT}{\rho_{soot} N_A} \right)^{\frac{1}{2}} d_p^{\frac{1}{2}} N^2 \quad (3-51)$$

where  $C_\alpha$ ,  $C_\beta$  and  $l$  are model constants.  $N_A$  is the Avogadro number and it has a value of  $6.022045 \times 10^{26} \text{ kmol}^{-1}$  while  $X_{prec}$  is the mole fraction of the soot precursor

where it is selected as A4. Moreover,  $d_p$ ,  $T_\alpha$  are the mean diameter of soot particle and activation temperature for the nucleation reaction, respectively.  $\rho_{soot}$  is denoted as the mass density of soot and it is assumed to be 2000 kg/m<sup>3</sup> [201]. For the soot mass concentration source term in Equation (3-50), it is modelled as follows:

$$\begin{aligned} \frac{dM}{dt} = & M_p C_\alpha \left( \frac{X_{prec} P}{RT} \right)^l \exp \left\{ -\frac{T_\alpha}{T} \right\} \\ & + C_\gamma \left( \frac{X_{sgs} P}{RT} \right)^m \exp \left\{ -\frac{T_\gamma}{T} \right\} \left[ (\pi N)^{\frac{1}{3}} \left( \frac{6M}{\rho_{soot}} \right)^{\frac{2}{3}} \right]^n \\ & - C_{oxid} C_\omega \eta_{coll} \left( \frac{X_{OH} P}{RT} \right) \sqrt{T} (\pi N)^{\frac{1}{3}} \left( \frac{6M}{\rho_{soot}} \right)^{\frac{2}{3}} \end{aligned} \quad (3-52)$$

Here, the  $C_\gamma$ ,  $C_{oxid}$ ,  $C_\omega$ ,  $m$  and  $n$  are additional model constants.  $M_p$  is the constant for mass of soot particle inception and it is set to 1200 kg/kgmol, which consists of 100 carbon atoms [201]. Meanwhile,  $X_{sgs}$  is the mole fraction of the participating soot surface growth species. Furthermore, the last term in Equation (3-52) are the soot oxidation reactions through hydroxyl radical (OH). The OH soot oxidation reaction mainly assumes the OH radical as the dominant oxidising agent and this process is formulated according to the model as proposed by Fenimore and Jones [205].

### 3.4 Concluding Remarks

The theory and the governing equations of the chemical kinetics and CFD sub-models are discussed in this chapter. The 0D and 1D models in CHEMKIN-PRO are used simulate the experimental chemical kinetic measurements. Furthermore, conclusions on the relationship between the chemical kinetics and the solutions are drawn through sensitivity and ROP analyses. Subsequently, the CFD sub-models in ANSYS FLUENT are employed for the spray combustion simulations. Table 3-4 shows a summary on the chemical kinetics models and CFD sub-models used in this entire study.

Table 3-4: Numerical models used for the simulations in CHEMKIN-PRO and ANSYS FLUENT.

Measurement	Type	Model
ID time	0D	Closed Homogeneous Batch Reactor
JSR species	0D	PSR
Flame speed	1D	Premixed Laminar Flame-Speed Calculation
Premixed flame species	1D	Premixed Laminar Burner-Stabilised Flame
Process		
Spray breakup	2D	KH-RT
Turbulence	2D	Standard $k-\varepsilon$
Combustion	2D	Species transport with finite-rate chemistry
Soot	2D	Moss-Brookes

# CHAPTER 4

## DEVELOPMENT OF A N-DODECANE- N-BUTANOL-PAH REDUCED MECHANISM

### 4.1 Introductory Remarks

In this chapter, the development and validation of a practical chemical kinetic mechanism for n-dodecane-n-butanol is presented with n-dodecane being used as the single component diesel surrogate fuel. As n-butanol is most often used in internal combustion engine applications, the development work here focuses on the n-butanol isomer only. Furthermore, a PAH mechanism is also integrated into the n-dodecane-n-butanol mechanism to give an accurate prediction of the soot formation processes. The entire development process of the n-dodecane-n-butanol-PAH mechanism is presented in Section 4.2 to 4.6. In Section 4.7, the n-dodecane-n-butanol-PAH mechanism is then validated under engine relevant conditions such as ST ID times, JSR species concentrations, laminar flame speed and premixed laminar flame species concentration. The last section highlights the main findings of this chapter.

### 4.2 Reduction Methodology

Generally, applying only a single reduction method limits the extend of reduction and it is usually insufficient to reduce the size of large mechanism to a size that is suitable for practical CFD simulations. For this reason, it is necessary to reduce large mechanism using a combination of different reduction methods. Here, the reduction work will be applied only to the n-butanol sub-mechanism because as reviewed in Chapter 2, the n-butanol reduced mechanisms in literature are either too large in size or have only been validated in a limited range of engine conditions. As such, first of all, the DRGEP method [183] is employed to remove unimportant species and reactions in the detailed mechanism [160] since it allows a larger reduction in mechanism size as compared to that of the DRG method [180]. Then, isomer lumping [191], which calculates the significance of radical isomer species based on the net

production rates, is utilised with the aid of reaction pathway analysis (RPA) to select the representative species for each isomer group and lump the remaining isomer species and reactions together. The sequence of performing DRGEP first before isomer lumping is selected based on the suggestion of Pepiot-Desjardins and Pitsch [206] as it provides better accuracy than the reversed sequence. Following that, the DRGEP method [183] is employed again to remove unimportant species and reactions that have lost connections to the target species due to their lumped parent isomers [124,125]. Finally, if necessary, the pre-exponential factor of key reactions in the n-butanol reduced mechanism are adjusted after it is merged with the base n-dodecane and PAH sub mechanisms to match the experimental ID times [82].

### 4.3 n-Dodecane Base Mechanism

The n-dodecane reduced mechanism developed by Yao et al. [94] is selected as the diesel surrogate mechanism and is used as the base mechanism here. This n-dodecane reduced mechanism [94] is derived from the n-dodecane detailed mechanism by You et al. [111]. In the development process, the C<sub>5</sub> – C<sub>12</sub> sub-mechanism is simplified through the elimination of unimportant species and reactions and isomer lumping. The simplified C<sub>5</sub> – C<sub>12</sub> sub-mechanism is then combined with a simplified H<sub>2</sub>/CO/C<sub>1</sub> – C<sub>4</sub> base mechanism adopted from Vié et al. [207]. Additionally, the low-temperature n-decane chemistry that was developed by Bikas and Peters [100] is modified to be suitable for n-dodecane and is added to the skeletal mechanism to form an optimised n-dodecane reduced mechanism with 54 species and 269 reactions, known as SK54a [94]. However, spray combustion simulations at ambient temperature of 800 K show that the ID predicted by SK54a mechanism is more than 6 ms whereas experimental measurement is 0.8 ms. As a result, the decomposition reaction of ketohydroperoxide (OC<sub>12</sub>H<sub>23</sub>OOH) is changed from  $OC_{12}H_{23}OOH = CH_2O + 3C_2H_4 + C_2H_5 + C_2H_3CHO + OH$  to  $OC_{12}H_{23}OOH = 3C_2H_4 + C_2H_5 + 2CH_2CHO + OH$  to produce vinoxy radical (CH<sub>2</sub>CHO) that could facilitate the chain branching reactions at low temperatures [94]. The pre-exponential factor of the aforementioned reaction is also adjusted by a factor of two lower than the original value and this newly modified mechanism is known as SK54b [94]. Nevertheless, the SK54b mechanism still over-predicts the spray combustion ID by around 25% at ambient temperature of 800 K.

Consequently, the pre-exponential factor of the  $\text{OC}_{12}\text{H}_{23}\text{OOH} = 3\text{C}_2\text{H}_4 + \text{C}_2\text{H}_5 + 2\text{CH}_2\text{CHO} + \text{OH}$  reaction is further decreased by approximately 25% and this resulted in the final n-dodecane mechanism known as SK54 [94]. The SK54 reduced mechanism [94] shows good agreement to the experimental ST ID times, JSR species concentrations, laminar flame speed and pyrolysis species concentrations. Most importantly, the SK54 reduced mechanism [94] is able to well predict the spray combustion ID at ambient temperature of 800 K with a deviation of less than 15%. This result is also even more accurate than the other previously developed n-dodecane reduced mechanisms [67,114]. On top of that, the SK54 reduced mechanism [94] is able to well predict the spray combustion ID and FLOL under different oxygen concentrations, injection pressures and ambient densities.

#### 4.4 PAH Sub-Mechanism

The PAH reduced mechanism developed by Wang et al. [82] is utilised in the current work. This PAH reduced mechanism [82] is constructed based on the detailed PAH mechanism developed by Slavinskaya et al. [149]. This PAH reduced mechanism is generally split into two major sections. The first part of the mechanism consists of the PAH species “building blocks” such as propargyl ( $\text{C}_3\text{H}_3$ ),  $\text{C}_4\text{H}_2$  and cyclobutadiene ( $\text{C}_4\text{H}_4$ ), which are necessary and responsible for the formation of larger PAH species. On the other hand, the second part of the mechanism consists of the reactions that describe the formation of PAH from  $\text{A}_1$  up to  $\text{A}_4$ . In this mechanism [82], the formation of the first-ring PAH species,  $\text{A}_1$ , is mainly through the combination of two  $\text{C}_3$  radicals and  $\text{C}_4$  with  $\text{C}_2$  radicals. Subsequently, the growth of larger PAH species is primarily through three main pathways: the HACA mechanism; reactions between aromatic molecules/radicals and small molecules; and reactions between aromatic molecules and aromatic radicals [148].

#### 4.5 n-Butanol Sub-Mechanism

Among the detailed mechanisms found in literature, the detailed mechanism built by Sarathy et al. [160], which contained the oxidation pathways at both low-temperature and high-temperature, is selected here to describe the chemical kinetics for n-butanol fuel. This is because good validation results were obtained for the detailed mechanism by Sarathy et al. [160] against the experimental measurements



under the operating conditions of ST, JSR, premixed laminar flame, laminar flame speed and RCM. Apart from that, the mechanism [160] is the only detailed mechanism which had been validated under a high initial ST pressure of 80 bar. Further details on the validation of the detailed mechanism [160] are found in Ref. [160].

#### 4.5.1 First Stage: DRGEP Method

The detailed mechanism [160] with 426 species and 2335 reactions is reduced using the DRGEP method [183]. In order to retain the comprehensiveness of the detailed mechanism [160], key species including  $n\text{C}_4\text{H}_9\text{OH}$ ,  $\text{O}_2$ , carbon dioxide ( $\text{CO}_2$ ), hydrogen peroxide ( $\text{H}_2\text{O}_2$ ) and nitrogen ( $\text{N}_2$ ) which are pertinent to the fuel oxidation, auto-ignition and also chain branching are selected as target species. Besides, the maximum error for the ID prediction between the detailed and reduced mechanisms is set to 30%, which is in line with that used by Niemeyer et al. [104,208] to develop skeletal mechanisms for n-heptane, iso-octane and toluene reference fuel (TRF). As a result, a n-butanol skeletal mechanism with 213 species and 1289 reactions is obtained. A deviation of 19.26% is recorded when the predicted ID times by the skeletal mechanism are compared to those of the detailed mechanism [160] at initial temperatures of 750 – 1350 K, initial pressures of 10 – 80 bar and equivalence ratios of 0.5 – 2.0.

#### 4.5.2 Second Stage: Isomer Lumping Aided by RPA

In order to further reduce the size of the skeletal mechanism by the isomer lumping method, the RPA in CHEMKIN-PRO [209] is employed to identify the suitable representative isomer species for each isomer group. The low-temperature (750 K) and high-temperature (1250 K) combustion of n-butanol after 20% of fuel consumption at the initial pressure of 40 bar and equivalence ratios of 0.5 – 2.0 are depicted in Figure 4-1 and Figure 4-2, respectively.

Based on Figure 4-1, during low-temperature combustion, n-butanol initially breaks down into four hydroxybutyl ( $\text{C}_4\text{H}_8\text{OH}$ ) radical isomers namely  $\text{C}_4\text{H}_8\text{OH-1}$ ,  $\text{C}_4\text{H}_8\text{OH-2}$ ,  $\text{C}_4\text{H}_8\text{OH-3}$ ,  $\text{C}_4\text{H}_8\text{OH-4}$ , through the H-atom abstraction from the parent fuel molecule. It is found that the  $\text{C}_4\text{H}_8\text{OH-1}$  radical is the most dominant species with a production rate of more than 50% when n-butanol is consumed by OH and

hydroperoxyl ( $\text{HO}_2$ ). The production rate of  $\text{C}_4\text{H}_8\text{OH-1}$  radical is also the highest when n-butanol undergoes high-temperature combustion as presented in Figure 4-2. These results are similar to those by Wang et al. [210] where they have also found that the  $\text{C}_4\text{H}_8\text{OH-1}$  radical has the highest production rate among the remaining  $\text{C}_4\text{H}_8\text{OH}$  isomers at initial temperatures of 800 – 1200 K, initial pressure of 20.2 bar and equivalence ratio of 0.5. As such,  $\text{C}_4\text{H}_8\text{OH-1}$  is selected as the representative isomer species for the  $\text{C}_4\text{H}_8\text{OH}$  isomer group and the remaining  $\text{C}_4\text{H}_8\text{OH}$  isomers and reactions associated to it are therefore eliminated. This approach, which is similar to the previous works [82,124,125,171,211], is applied to other isomer groups in the 213 species skeletal mechanism. At this reduction stage, a total of 83 species and 517 reactions are removed and the resulting skeletal mechanism contains 130 species and 772 reactions.

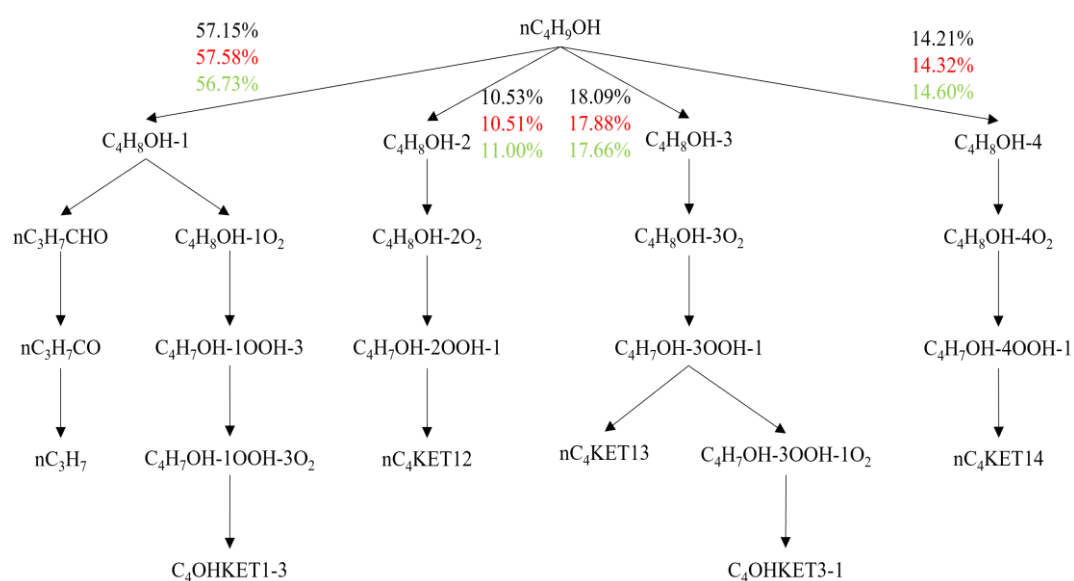


Figure 4-1: Formation of  $\text{C}_4\text{H}_8\text{OH}$  radicals at low-temperature combustion with 20% n-butanol fuel consumption, at the initial temperature of 750 K, initial pressure of 40 bar and equivalence ratios of 0.5 (black), 1.0 (red) and 2.0 (green). Percentage values denote the ROP of  $\text{C}_4\text{H}_8\text{OH}$  radicals.

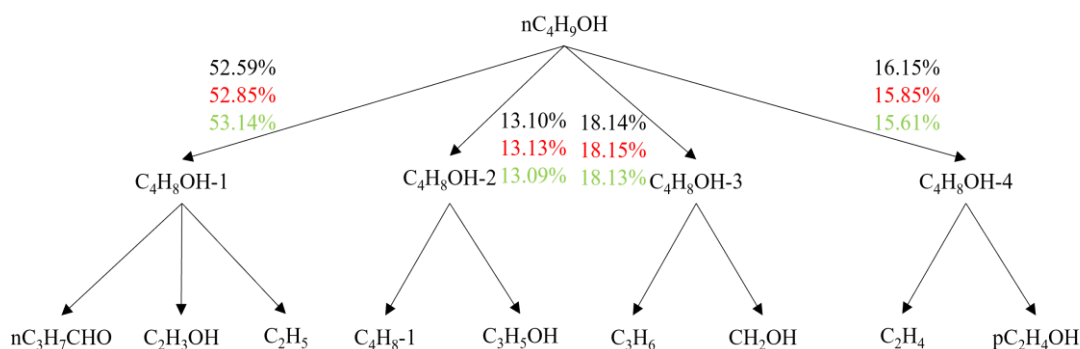


Figure 4-2: Formation of  $C_4H_8OH$  radicals at high-temperature combustion with 20% n-butanol fuel consumption, at the initial temperature of 1250 K, initial pressure of 40 bar and equivalence ratios of 0.5 (black), 1.0 (red) and 2.0 (green). Percentage values denote the ROPS of  $C_4H_8OH$  radicals.

### 4.5.3 Third stage: DRGEP Method

Since several reaction pathways are removed during isomer lumping, species that are connected to those lumped isomer species tend to also lose their connections to the target species [124,125]. As such, the DRGEP method [183] is employed again to identify those species that have lost connections to the target species and to eliminate them from the skeletal mechanism. The settings here are similar to those in the first stage DRGEP reduction, with additional target species such as carbon monoxide (CO),  $HO_2$  and  $H_2$  specified to further retain the comprehensiveness of the detailed mechanism [160] due to the changes in species pathways. Here, 70 species and 466 reactions are removed and this resulted in a n-butanol reduced mechanism of 60 species and 306 reactions. The maximum deviation in ID times for the initial n-butanol reduced mechanism is approximately 23% when compared to those of the 130 species and 772 reactions skeletal mechanism at initial temperatures of 750 – 1350 K, initial pressures of 10 – 80 bar and equivalence ratios of 0.5 – 2.0.

## 4.6 Combined Mechanism

The developed 60 species and 306 reactions n-butanol reduced mechanism is merged with the n-dodecane reduced mechanism [94] that contains 54 species and 269 reactions. Subsequently, the PAH reduced mechanism [82] of 41 species and 228 reactions is integrated into the n-dodecane-n-butanol mechanism to form a n-dodecane-n-butanol-PAH mechanism. The duplicated reactions in the n-butanol and PAH sub-mechanisms are removed from the combined mechanism to retain the

predicting capabilities of the base n-dodecane mechanism. This leads to the final n-dodecane-n-butanol-PAH mechanism that consists of 105 species and 584 reactions and is henceforth referred as the DB105 mechanism hereafter.

Preliminary validation of the DB105 mechanism reveals that the predicted n-butanol ID times deviated highly from that of the detailed mechanism [160] particularly at temperatures of 700 – 900 K. As such, adjustment to the pre-exponential factor is necessary to improve the n-butanol ID predictions at the aforementioned temperature range. The temperature A-factor SA is performed to determine the important reactions that are sensitive to the ID times when the pre-exponential factors are perturbed [160]. The SA is performed using the constant volume batch reactor at initial temperatures of 750 K and 850 K, initial pressure of 40 bar and equivalence ratios of 0.5 – 2.0. The initial pressure of 40 bar used here is to mimic the in-cylinder pressure during the onset of fuel injection of a diesel engine [125]. The normalised sensitivity coefficient charts obtained at different conditions are presented in Figure 4-3. Here, a negative sensitivity value indicates low reactivity while a positive sensitivity value indicates high reactivity.

According to Figure 4-3, it is observed that the  $C_4H_8OH-1 + O_2 = C_4H_8OH-1O_2$  reaction shows the highest reactivity at initial temperature of 750 K regardless of the equivalence ratios. On the other hand, the  $C_4H_8OH-1 + O_2 = nC_3H_7CHO + HO_2$  reaction shows the lowest reactivity at both initial temperatures of 750 K and 850 K. The reactions related to the consumption of n-butanol by  $HO_2$  and  $OH$  are found to also exhibit a positive sensitivity value, which shows that increasing the pre-exponential factor of these reactions could increase the reactivity of the mechanism. However, this could lead to under-prediction of the n-butanol concentration under JSR conditions. Meanwhile, the  $H_2-O_2$  elementary reactions are all adopted from the n-dodecane reduced mechanism [94] and thus the pre-exponential factor of these reactions should not be modified so that the accuracy of the n-dodecane reduced mechanism [94] is retained. Specifically, the  $C_4H_8OH-1 + O_2 = C_4H_8OH-1O_2$  reaction is part of the low-temperature reaction class for n-butanol and increasing the pre-exponential factor could increase the overall reactivity of the mechanism at low temperatures. Therefore, the pre-exponential factor of the  $C_4H_8OH-1 + O_2 = C_4H_8OH-$

$1\text{O}_2$  reaction is adjusted from  $1.0\text{E}+12$  to  $6.0\text{E}+12$  to improve the accuracy of the combined mechanism and reproduce the auto-ignition behaviour of n-butanol. The newly adjusted pre-exponential factor is determined using the iteration steps as follows:

- (1) The pre-exponential factor of the n-butanol reactions in the DB105 mechanism are initially adopted from the detailed mechanism [160]. The ID times predicted by the DB105 mechanism are then validated against the experimental measurements under ST conditions to determine the accuracy of the predictions.
- (2) The pre-exponential factor of  $\text{C}_4\text{H}_8\text{OH-1} + \text{O}_2 = \text{C}_4\text{H}_8\text{OH-1O}_2$  is then modified to match the experimental ID times under ST conditions.
- (3) After each modification process, the ID times predicted by the DB105 mechanism are validated against the experimental measurements to ensure that the predictions are within the acceptable error limit over the entire temperature range.
- (4) Steps 2 and 3 are repeated until the DB105 mechanism is able to reproduce the experimental ID times satisfactorily under ST conditions.

The entire development process of the DB105 mechanism is summarised in a flowchart as shown in Figure 4-4.

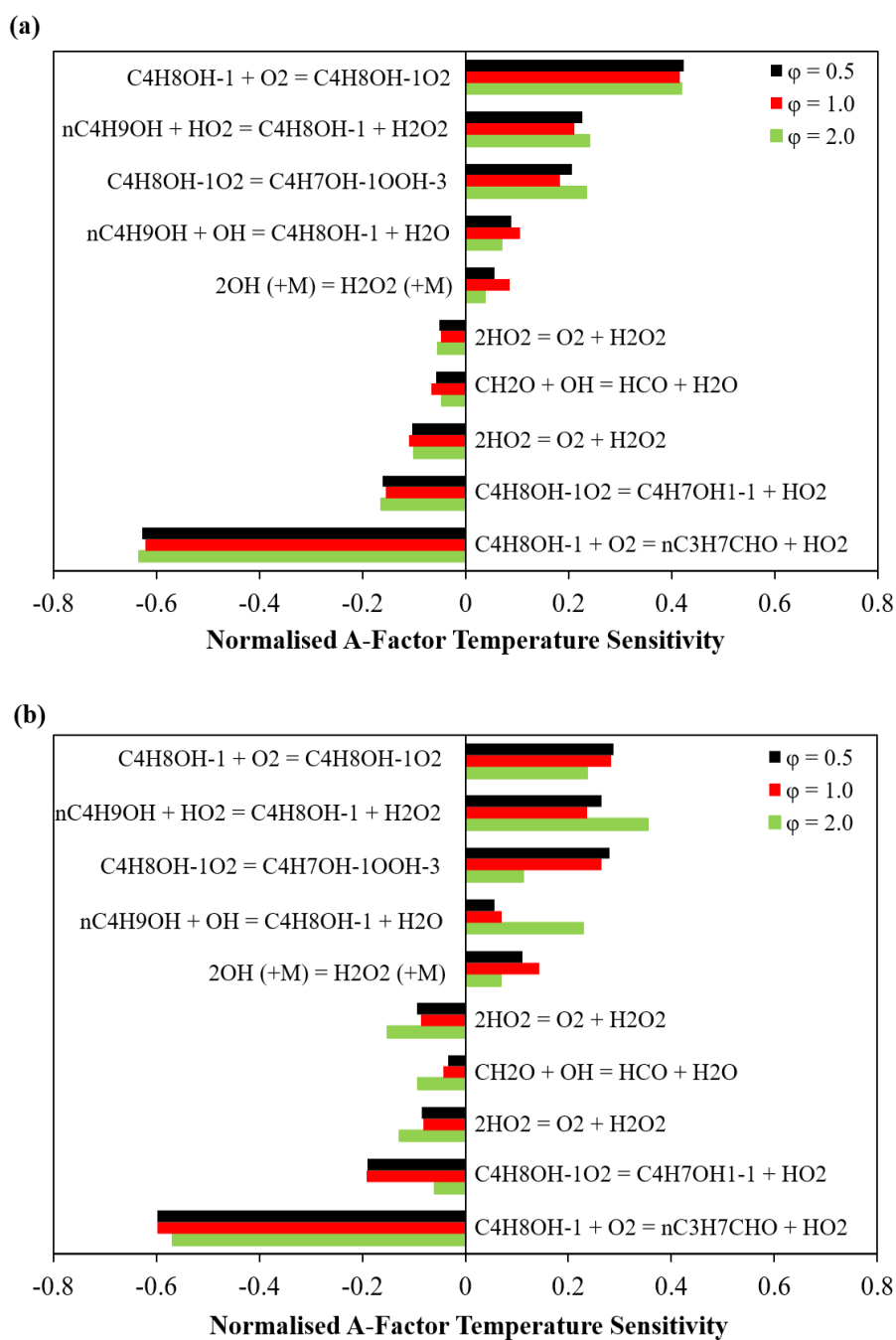


Figure 4-3: Normalised temperature A-factor sensitivity at the point of ignition at initial temperatures of (a) 750 K and (b) 850 K, the initial pressure of 40 bar and equivalence ratios of 0.5 – 2.0.

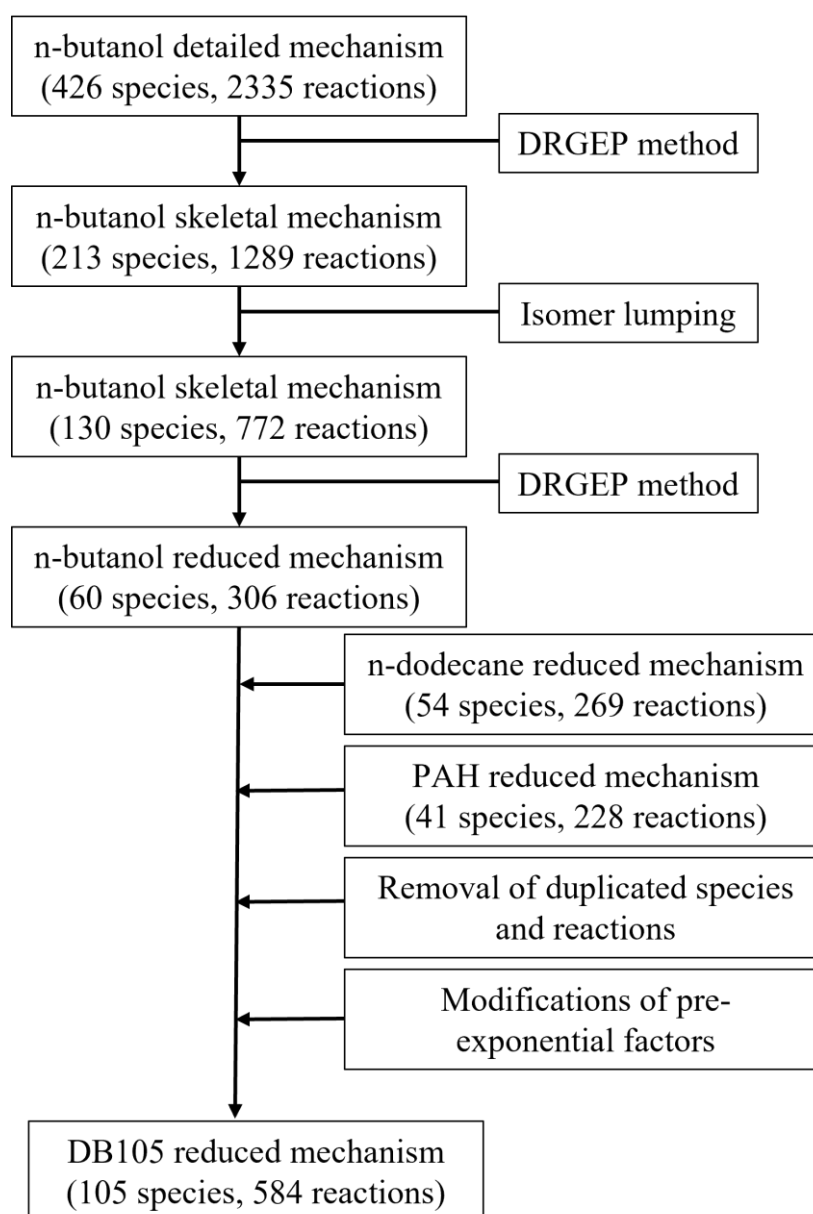


Figure 4-4: Flowchart of the development of DB105 mechanism.

## 4.7 Validation of Mechanism Under 0D and 1D Conditions

### 4.7.1 ID times

The DB105 mechanism is validated under ST ID times by comparing the predicted ID times to the experimental measurements. The experimental measurements for the n-dodecane/air mixtures under ST conditions were obtained from the work conducted by Shen et al. [212], Vasu et al. [213] and Shao et al. [214]. The 0D closed homogenous constant volume batch reactor in CHEMKIN-PRO is used to compute the predicted ID times by the DB105 mechanism under ST conditions. Here, the ID is defined as the maximum temperature gradient with respect to time (maximum  $dT/dt$ ). From Figure 4-5, it can be observed that the DB105 mechanism shows good agreement to the predictions by the SK54 mechanism [94] and experimental measurements over a wide range of initial pressures, initial temperatures and equivalence ratios. The predictions by the DB105 mechanism also closely match those predictions by the SK54 mechanism [94] in the negative temperature coefficient (NTC) region despite having deviations against the experimental measurements. Nevertheless, these validation results have already shown that the current DB105 mechanism is more accurate than Wakale et al.'s [75,88] mechanisms as their mechanisms show deviations in the low temperature regions. The good validation results are also sufficient to confirm that the oxidation of n-dodecane is well represented in the DB105 mechanism and the merging of the n-butanol and PAH sub-mechanisms did not deteriorate the overall predictions for n-dodecane.



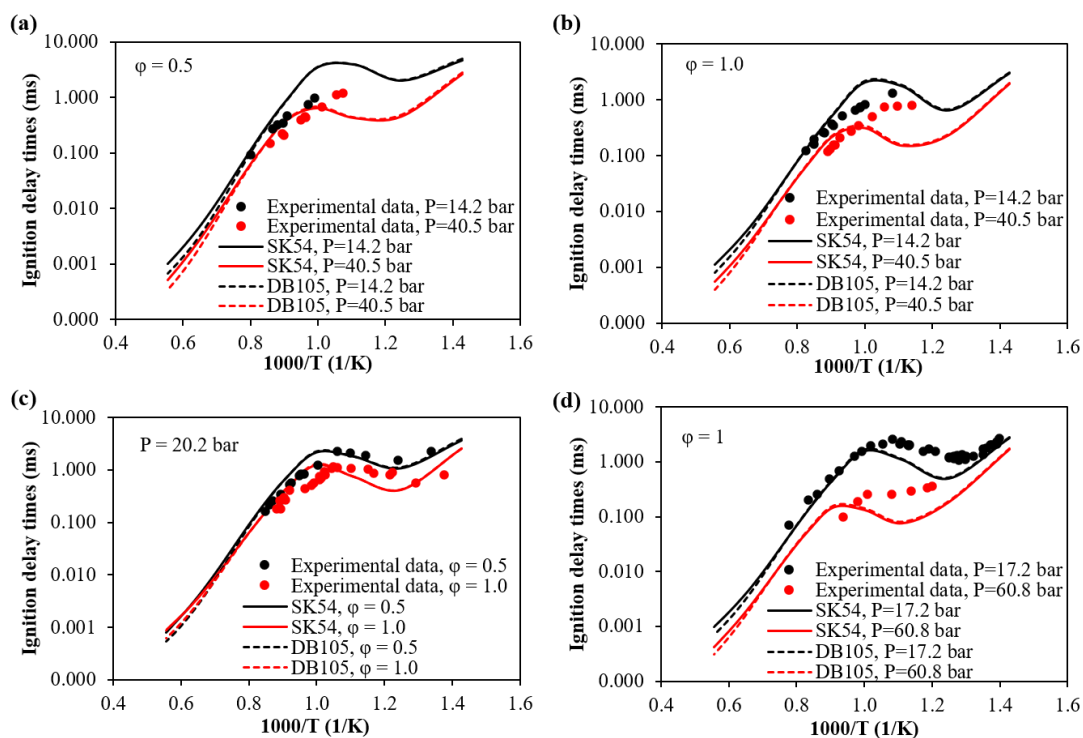


Figure 4-5: Comparison of the n-dodecane ST ID times predicted by the DB105 mechanism against the experimental measurements [212–214] and SK54 mechanism [94] at (a) initial temperatures of 700 – 1800 K, initial pressures of 14.2 and 40.5 bar and equivalence ratio of 0.5, (b) initial temperatures of 700 – 1800 K, initial pressures of 14.2 and 40.5 bar and equivalence ratio of 1.0, (c) initial temperatures of 700 – 1800 K, initial pressure of 20.2 bar and equivalence ratios of 0.5 and 1.0, and (d) initial temperatures of 700 – 1800 K, initial pressures of 17.2 and 60.8 bar and equivalence ratio of 1.0.

The experimental measurements for the stoichiometric n-butanol/air mixtures under ST conditions were obtained from Heufer et al. [215] at initial pressures of 20 and 40 bar, and Vranckx et al. [216] at initial pressure of 80 bar. According to Figure 4-6, the ID times predicted by the DB105 mechanism are in good agreement with the predictions by the detailed mechanism [160] and experimental measurements over the entire range of temperature. The trends of the n-butanol ID times are also well reproduced by the DB105 mechanism, where n-butanol does not exhibit the NTC behaviour as n-dodecane does. Although the deviation in ID predicted by the DB105 mechanism and the detailed mechanism [160] is as high as 43% at initial temperature of 1350 K and initial pressure of 20 bar, the prediction by the DB105 mechanism is in better agreement with the experimental measurements at that particular operating condition. Since the typical in-cylinder pressures of a CI engine are at 40 and 60 bar

[211], it can be concluded that the DB105 mechanism has reasonable accuracy for the predictions of n-butanol ID times under CI engine relevant conditions.

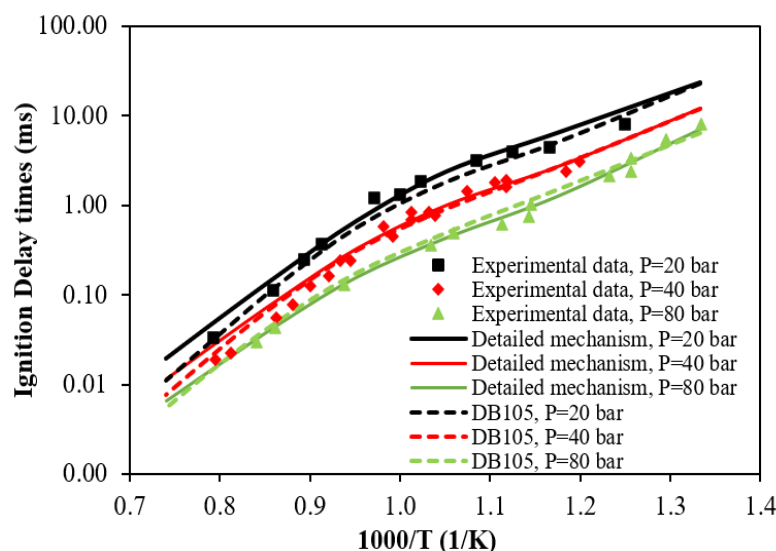


Figure 4-6: Comparison of the stoichiometric n-butanol ST ID times predicted by the DB105 mechanism against the detailed mechanism [160] and experimental measurements [215,216] at initial temperatures of 750 – 1350 K and initial pressures of 20 – 80 bar.

#### 4.7.2 JSR Species Concentration

The PSR in CHEMKIN-PRO is employed for the simulations of species concentration under JSR conditions. The experimental measurements for n-dodecane under JSR conditions at initial temperatures of 550 – 1100 K, initial pressure of 10.1 bar and equivalence ratios of 0.5 – 2.0 were obtained from Mz -Ahmed et al. [113].

Based on Figure 4-7, the trends of  $C_{12}H_{26}$ ,  $C_2H_6$ ,  $C_2H_4$ ,  $C_2H_2$ , methane ( $CH_4$ ),  $CO_2$ , water ( $H_2O$ ),  $CO$  and  $O_2$  are well replicated by the DB105 mechanism over the entire range of temperatures and equivalence ratios. The experimental NTC region of  $C_{12}H_{26}$  at temperatures of 650 – 750 K exhibit a non-monotonic trend whereas the predictions do not and this could be due to model uncertainty in which was also observed in the original work by Yao et al. [94]. Specifically, the predicted mole fractions for  $C_2H_4$  and  $CO_2$  show slight deviations at temperatures of 600 – 700 K, where the former species is over-predicted and the latter species is under-predicted. This could be due to the discrepancy in predicting the n-dodecane consumption at the NTC region which subsequently affects the prediction of the end products. Such

results are also found in the work by Wakale et al. [88] where the predictions for species such as  $\text{H}_2\text{O}$ ,  $\text{CO}$  and  $\text{CO}_2$  also deviate as compared to the experimental measurements.

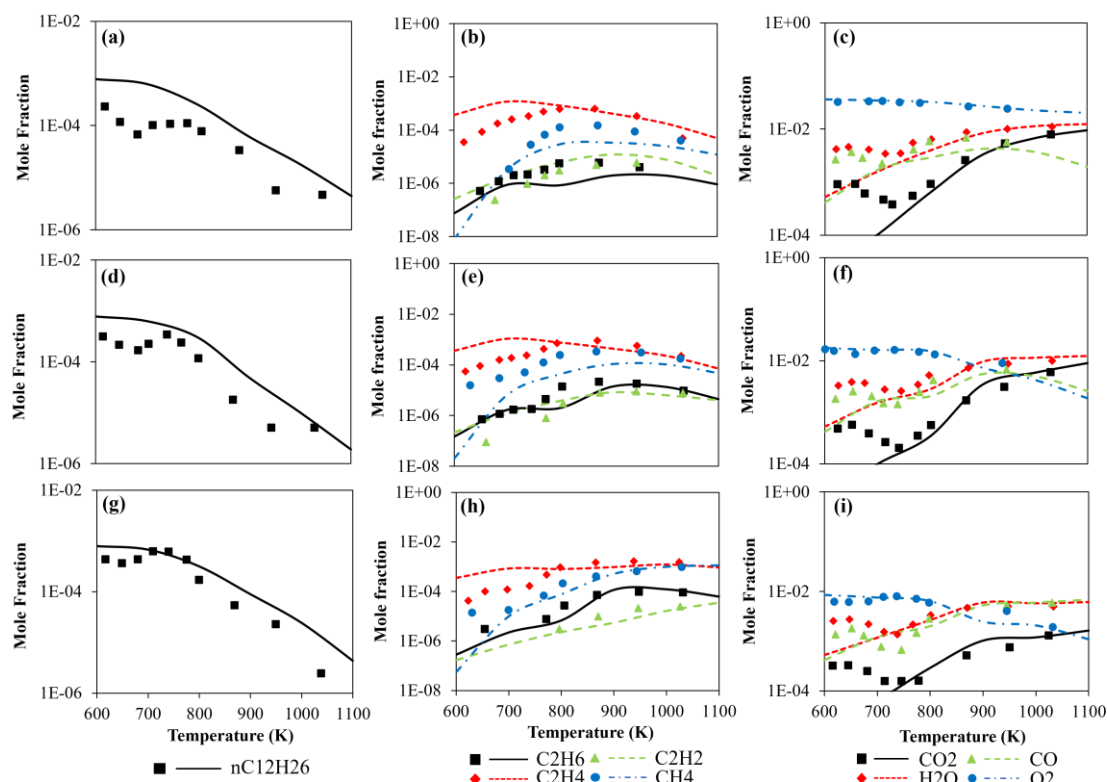


Figure 4-7: Comparison of the n-dodecane JSR species concentration profiles predicted by the DB105 mechanism (lines) against the experimental measurements (symbols) [113] for  $\text{nC}_{12}\text{H}_{26}$ ,  $\text{C}_2\text{H}_6$ ,  $\text{C}_2\text{H}_4$ ,  $\text{C}_2\text{H}_2$ ,  $\text{CH}_4$ ,  $\text{CO}_2$ ,  $\text{H}_2\text{O}$ ,  $\text{CO}$  and  $\text{O}_2$ , at initial temperatures of 600 – 1100 K, initial pressure of 10.1 bar and equivalence ratio of 0.5 (top row), 1.0 (middle row), and 2.0 (bottom row).

In addition, the experimental measurements for n-butanol under JSR conditions at initial temperatures of 800 – 1150 K, initial pressure of 10.1 bar and equivalence ratios of 0.5 – 2.0 were obtained from Dagaut et al. [163]. From Figure 4-8, the mole fractions of  $\text{C}_4\text{H}_9\text{OH}$ ,  $\text{CO}$ ,  $\text{CO}_2$  and  $\text{H}_2\text{O}$  are well predicted by the DB105 mechanism over the entire range of temperatures. For all equivalence ratios, the intermediate species such as  $\text{C}_2\text{H}_2$ ,  $\text{C}_2\text{H}_4$  and  $\text{C}_2\text{H}_6$  are also well predicted by the DB105 mechanism over the entire range of temperatures. However, the mole fraction for  $\text{CH}_4$  is under-predicted at equivalence ratio of 0.5 and at temperatures above 850 K, which could be attributed to the removal of isomer species that leads to the formation of  $\text{CH}_4$ . Interestingly, the prediction of  $\text{CH}_4$  mole fraction improves

significantly at equivalence ratios of 1.0 and 2.0, which shows that there could be a possibility that the eliminated isomer species are pertinent to fuel-lean condition only.

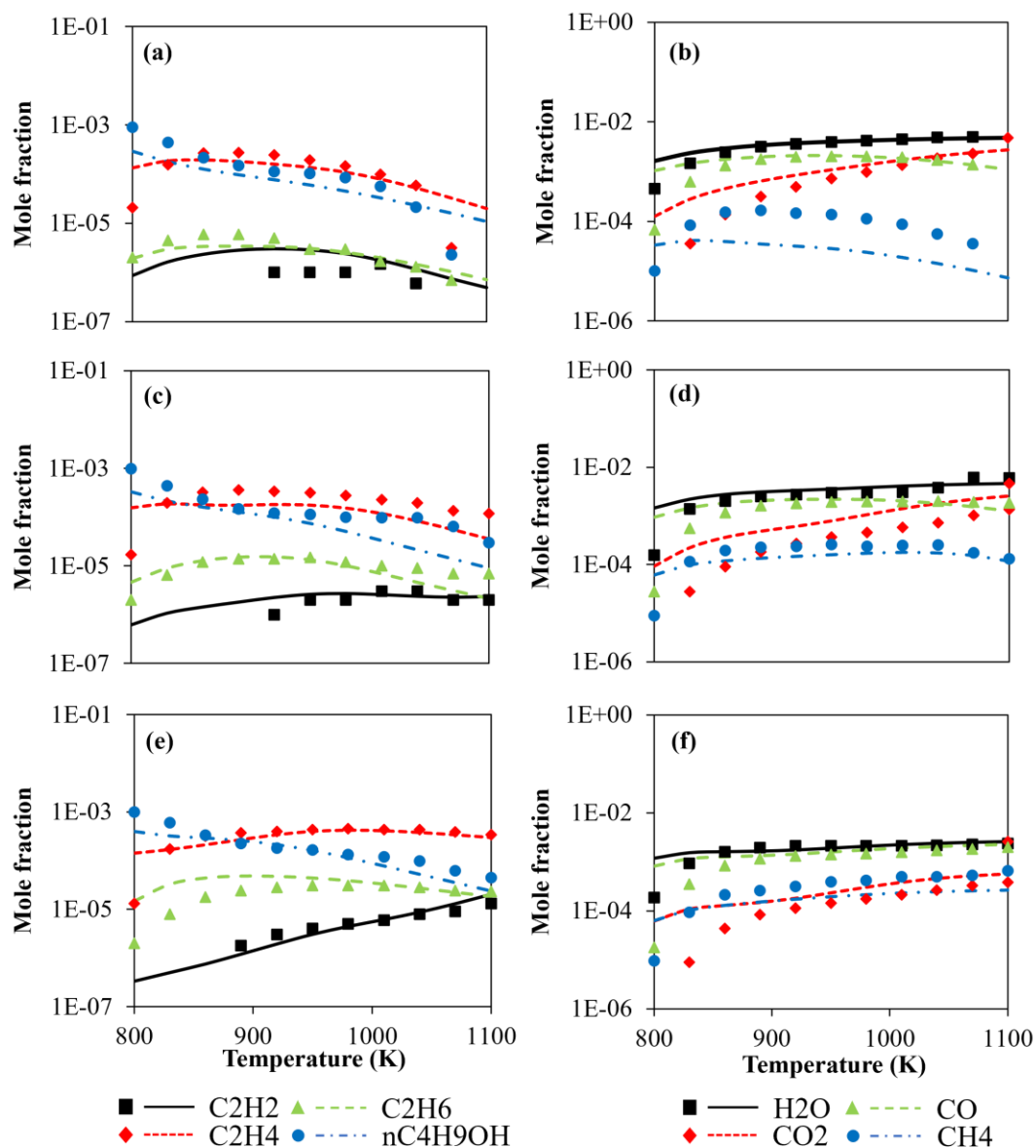


Figure 4-8: Comparison of the n-butanol JSR species concentration profiles predicted by the DB105 mechanism (lines) against the experimental measurements (symbols) [163] for nC<sub>4</sub>H<sub>9</sub>OH, C<sub>2</sub>H<sub>6</sub>, C<sub>2</sub>H<sub>4</sub>, C<sub>2</sub>H<sub>2</sub>, CH<sub>4</sub>, CO<sub>2</sub>, H<sub>2</sub>O and CO, at initial temperatures of 600 – 1100 K, initial pressure of 10.1 bar and equivalence ratio of 0.5 (top row), 1.0 (middle row), and 2.0 (bottom row).

### 4.7.3 Laminar Flame Speed

The CHEMKIN-PRO 1D premixed laminar flame speed code is used to simulate the laminar flame speed of n-dodecane and n-butanol. The simulation assumes a mixture-average transport and considers the Soret effect. As shown in Figure 4-9, the n-dodecane laminar flame speed predicted by the SK54 mechanism [94] and the DB105 mechanism are compared to the experimental measurements obtained from Ji et al. [217], Kumar and Sung [218] and Hui and Sung [219] at ambient pressures of 1.01 – 3.03 bar, unburned temperatures of 400, 403 and 470 K and equivalence ratios of 0.7 – 1.4. From Figure 4-9(a), the DB105 mechanism well predicts the experimental n-dodecane laminar flame speed and the predictions by the SK54 mechanism [94] with respect to the changes in unburned temperatures. However, in Figure 4-9(b), the DB105 mechanism over-predicts the experimental n-dodecane laminar flame speed as the ambient pressure increases to 3.03 bar, with a maximum deviation of 8 cm/s at equivalence ratio of 0.7. Nonetheless, the trends of the laminar flame speed are well replicated at all conditions, where the maximum flame speed occurs approximately at equivalence ratio of 1.1.

The n-butanol laminar flame speed predicted by the DB105 mechanism are compared against the predictions by the detailed mechanism [160] and the experimental measurements of Veloo et al. [220] and Liu et al. [173] at ambient pressure of 1.01 bar, unburned temperatures of 343 and 353 K and equivalence ratios of 0.7 – 1.4. From Figure 4-10, the DB105 mechanism generally over-predicts the experimental n-butanol laminar flame speed and the results by the detailed mechanism [160] despite replicating the trends well. The maximum deviation between the predictions by the DB105 mechanism and the experimental measurements is 9 cm/s at equivalence ratio of 1.1. Since the laminar flame speed is found to be governed by the H<sub>2</sub>-O<sub>2</sub> reactions that are responsible in chain developing and chain branching [221], the predictions of the n-butanol laminar flame speed here are considered reasonable owing to the fact that the H<sub>2</sub>-O<sub>2</sub> reactions in the DB105 mechanism are mostly adopted from the n-dodecane mechanism [94].

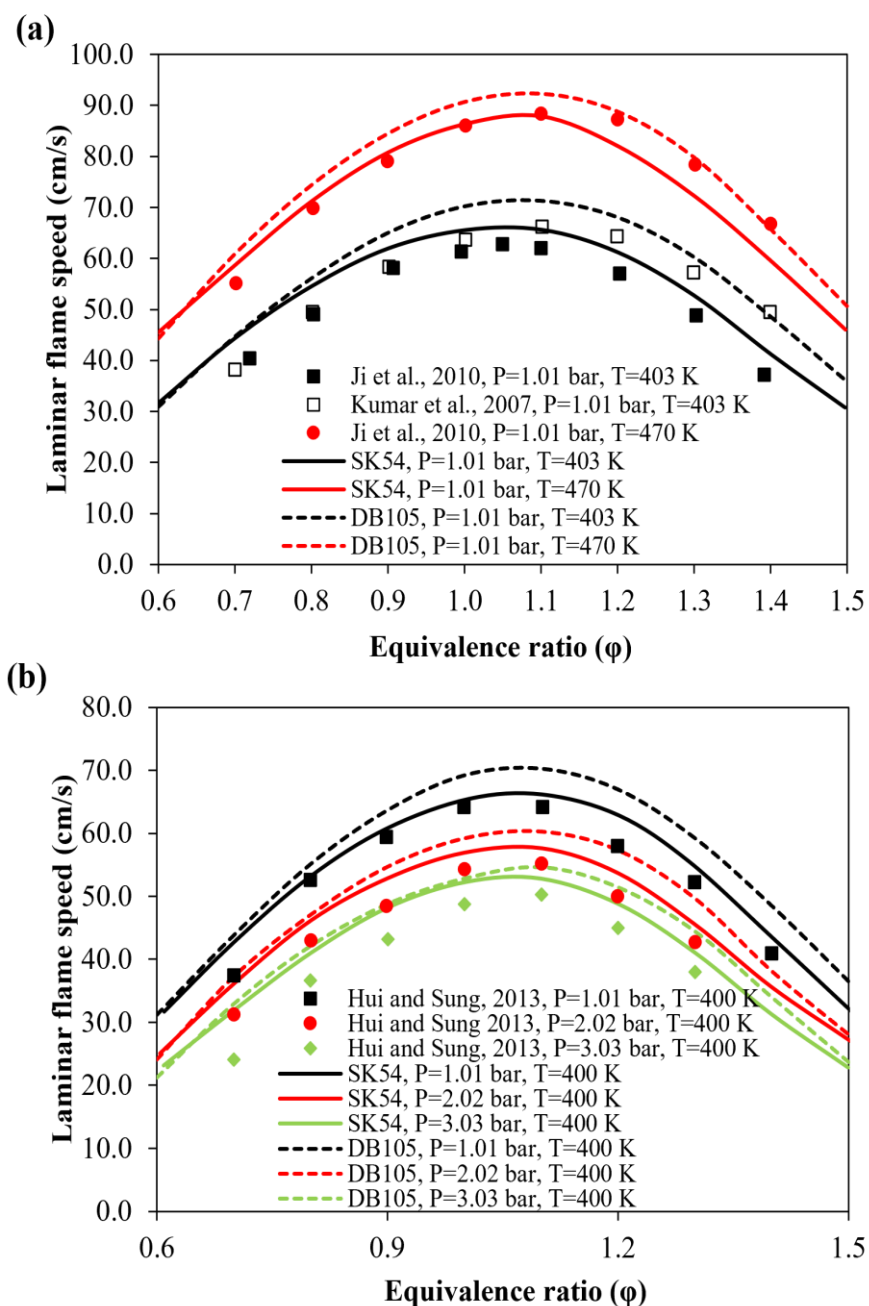


Figure 4-9: Comparison of the n-dodecane laminar flame speed predicted by the SK54 mechanism [94] (solid lines) and DB105 mechanism (dash lines) against the experimental measurements (symbols) [217–219] at (a) initial pressure of 1.01 bar, unburned temperatures of 403 K and 470 K and (b) initial pressures of 1.01 – 3.03 bar, unburned temperature of 400 K.

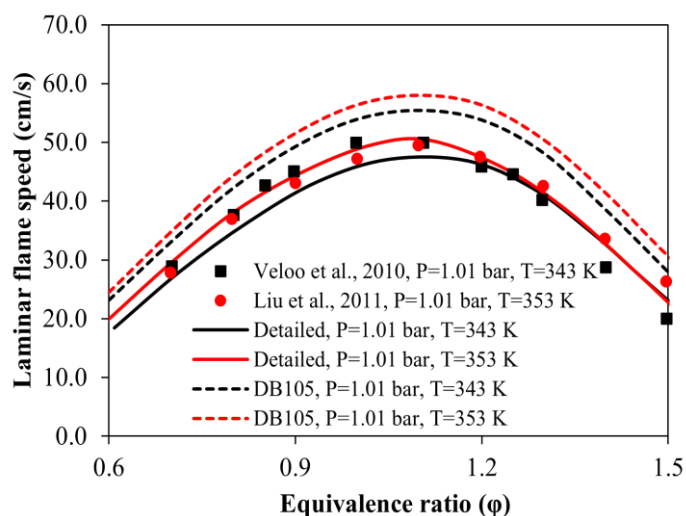


Figure 4-10: Comparison of the n-butanol laminar flame speed predicted by the detailed mechanism [160] (solid lines) and DB105 mechanism (dash lines) against the experimental measurements (symbols) [173,220] at initial pressure of 1.0 bar and unburned temperatures of 343 K and 353 K.

#### 4.7.4 Premixed Laminar Flame

The CHEMKIN-PRO 1D premixed laminar burner-stabilised flame code is used to simulate the species concentration profiles under premixed laminar flame. The initial conditions used for the validations under premixed laminar flame are tabulated in Table 4-1.

Table 4-1: Initial conditions for the premixed flame simulations.

Flame	Fuel (%)	O <sub>2</sub> (%)	H <sub>2</sub> (%)	Ar (%)	P (bar)	$\phi$ (-)	Ref
C <sub>2</sub> H <sub>4</sub>	21.3	20.9	-	57.8	1.01	3.06	[222]
C <sub>4</sub> H <sub>9</sub> OH (Flame 1)	3.6	24.1	24.1	48.2	0.02	1.4	[223]
C <sub>4</sub> H <sub>9</sub> OH (Flame 2)	3.3	16.7	-	80	0.03	1.2	[223]
C <sub>4</sub> H <sub>9</sub> OH (Flame 3)	7.2	42.8	-	50.0	0.02	1.0	[223]

The DB105 mechanism is validated against the experimental measurements of C<sub>2</sub>H<sub>4</sub> premixed flame. As seen in Figure 4-11, the predicted mole fractions of C<sub>2</sub>H<sub>2</sub>, C<sub>2</sub>H<sub>4</sub>, C<sub>4</sub>H<sub>2</sub> and C<sub>4</sub>H<sub>4</sub>, which act as “building blocks” for the formation of PAH species are in good agreement with the experimental measurements with a maximum deviation of an order magnitude. On the contrary, the mole fractions of large PAH species such as A<sub>3</sub> and A<sub>4</sub> are slightly under-predicted but the predictions improved as

the height above burner (HAB) increases. Meanwhile, the mole fractions of  $A_1$  and naphthalene ( $A_2$ ) are generally well predicted by the DB105 mechanism. This demonstrates that the formation reaction pathways from  $C_2$  species to PAH are accurate and well-represented in the DB105 mechanism. As the experimental uncertainties could be as high as an order magnitude [82], the level of agreement between the DB105 mechanism and the experimental measurements are considered reasonable since the deviations are mostly within the uncertainty limit.

Figure 4-12 shows the n-butanol premixed laminar flame species concentrations predicted by the DB105 mechanism against the experimental measurements. Referring to Figure 4-12, the mole fractions of  $C_4H_9OH$  and other major species such as  $O_2$ ,  $CO$ ,  $CO_2$ ,  $H_2O$  and  $H_2$  are in good agreement with the experimental measurements, with a maximum error of 20%. The highest error occurs close to the burner port and this could be due to the uncertainties in local temperature and flame/sampling-probe interactions [223]. Nevertheless, the DB105 mechanism is able to reproduce the trends of the species mole fractions, where the species tend to reach equilibrium as the HAB increases to 30 mm. Additionally, the validation results here are much more promising than those by Wakale et al.'s [88] mechanism because their modelling results have shown noticeable discrepancies to the experimental data. To this end, Wakale et al. [88] suggested that optimisation is needed to be done to the detailed mechanism that they have used in developing their n-dodecane-n-butanol mechanism which then leads to a doubt on the accuracy of subsequent modelling results.

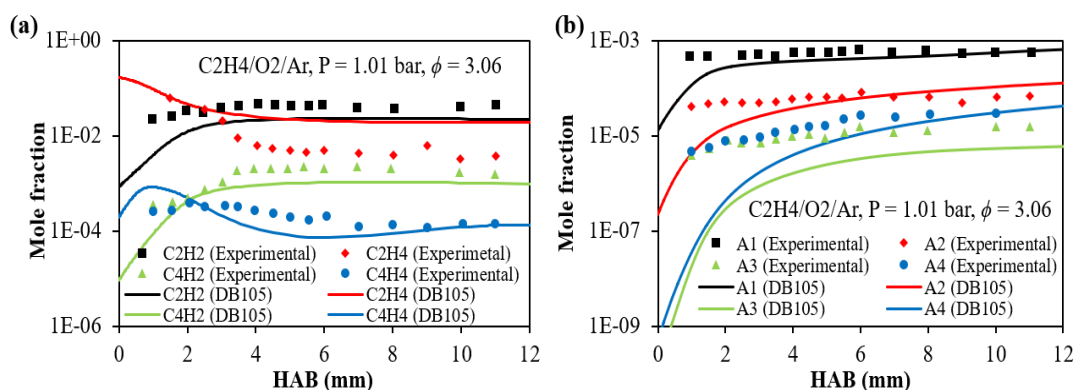


Figure 4-11: Comparison of the predicted mole fractions of  $C_2H_2$ ,  $C_2H_4$ ,  $C_4H_2$ ,  $C_4H_4$ ,  $A_1$ ,  $A_2$ ,  $A_3$  and  $A_4$  by the DB105 mechanism (lines) against the experimental measurements (symbols) [222] under  $C_2H_4$  premixed flame.



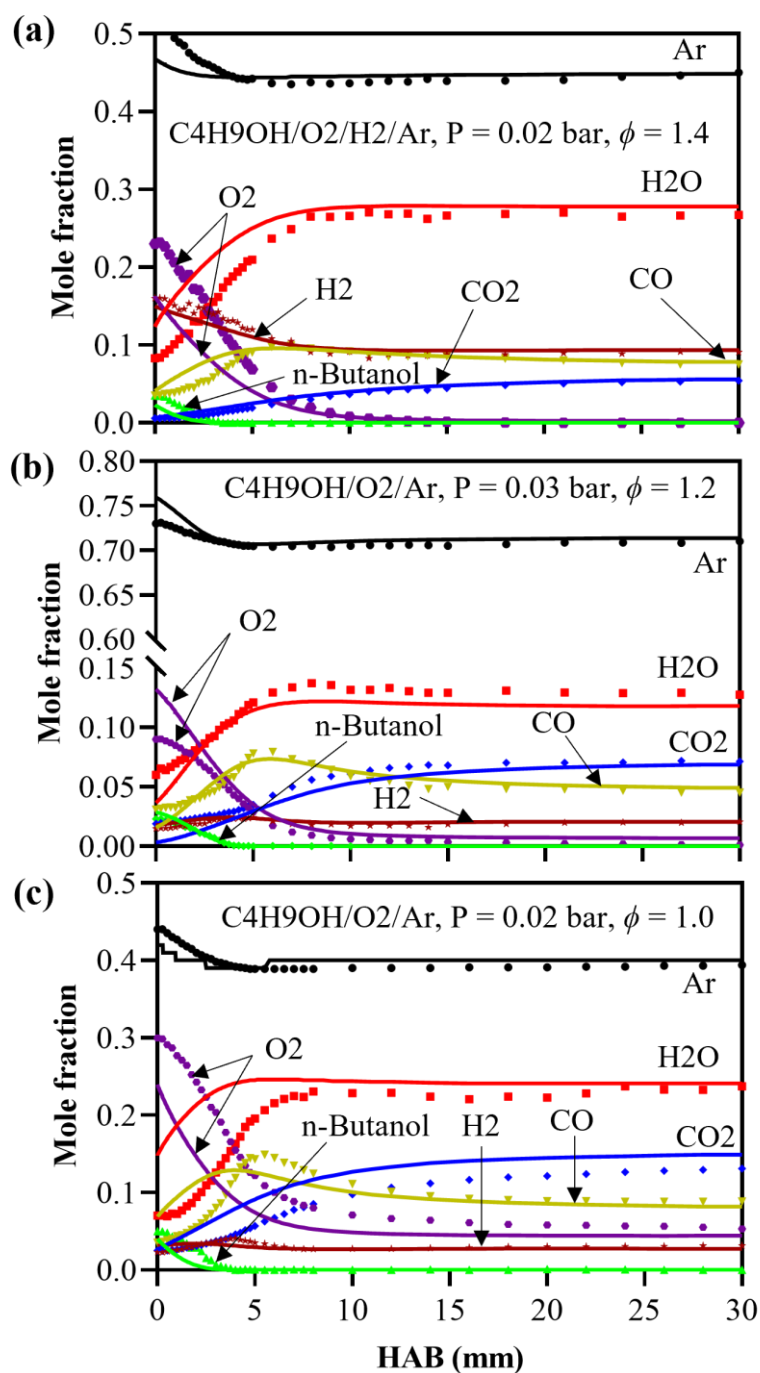


Figure 4-12: Comparison of the predicted mole fractions of C<sub>4</sub>H<sub>9</sub>OH, O<sub>2</sub>, CO, CO<sub>2</sub>, H<sub>2</sub>, H<sub>2</sub>O and Ar by the DB105 mechanism (lines) against the experimental measurements (symbols) [223] under Flame 1, Flame 2 and Flame 3 conditions.

#### 4.8 Concluding Remarks

A n-dodecane-n-butanol-PAH mechanism that consists of 105 species and 584 reactions (DB105) is constructed by merging a n-butanol reduced mechanism that is reduced using DRGEP, isomer lumping and RPA methods to the reduced mechanisms of n-dodecane and PAH. Subsequently, the DB105 mechanism is validated under a wide range of 0D and 1D diesel engine relevant conditions such as ST ID times, JSR species concentrations, laminar flame speed and premixed laminar flames for both n-dodecane and n-butanol. Good agreements are obtained between the predicted results and the experimental measurements at all conditions. However, in some conditions such as the ST ID times and laminar flame speed, it could be seen that the DB105 mechanism could better replicate the experimental measurements for n-dodecane than n-butanol. This is because the n-dodecane mechanism is selected as the base mechanism and many reactions of lighter weight species (e.g.,  $C_1/C_2/H_2/O_2$ ) from the n-dodecane mechanism are used to predict n-butanol combustion. As such, there would obviously be a higher deviation for the results of n-butanol. Nevertheless, from the validation results in Section 4.7.1 to 4.7.4, it can be deduced that the DB105 mechanism is accurate, compact and comprehensive. To further support this fact, the DB105 mechanism is more superior than the previous n-dodecane-n-butanol mechanisms by Wakale et al. [75,88] in terms of size and accuracy. The DB105 mechanism is smaller in size, validated under a wider range of engine operating conditions and shown more accurate validation results than Wakale et al.'s [75,88] mechanisms. This makes the DB105 mechanism to be well accepted by the combustion modelling community for high-fidelity practical CFD simulations.

# CHAPTER 5

## 2D SPRAY COMBUSTION SIMULATIONS SETUP

### 5.1 Introductory Remarks

The modelling of diesel combustion in a diesel engine is complex and time consuming. Therefore, experimental and computational research are often conducted in a constant volume combustion chamber to study the detailed combustion processes. In this chapter, the experimental setup that is used for validations and the numerical formulations for the 2D spray combustion simulations in a constant volume combustion chamber are described in Section 5.2 and 5.3, respectively. Subsequently, simulations under non-reacting condition are presented in Section 5.4 whereas Section 5.5 shows the simulations under reacting condition where the CFD models and the DB105 mechanism developed in Chapter 4 are further assessed. Finally, the results from this chapter are summarised in the Section 5.6.

### 5.2 Experimental Setup

The modelling of non-reacting and reacting spray in a constant volume combustion chamber is based on the experiments conducted by Nilaphai et al. [79,81]. The spray experiments are conducted in a High-Pressure High-Temperature chamber called the “New One Shot Engine” (NOSE), as shown in Figure 5-1. It is modified from a single cylinder low speed diesel engine by adding an optical accessible chamber to it. The testing conditions used for the experiment are based on the Spray A conditions from the Engine Combustion Network (ECN) [70] as shown in Table 5-1. The combustion chamber shown in Figure 5-1 has a square length and width of 44 mm x 44 mm and a height of 90 mm. The experiments are conducted at ambient temperatures of 800 K, 850 K and 900 K while the ambient density is maintained at  $22.8 \text{ kg/m}^3$ . The term ‘ambient’ here refers to the working conditions in the constant volume combustion chamber. The test fuels used for the experiments include 100% n-dodecane (Bu0), 80% n-dodecane-20% – n-butanol (Bu20) and 60% n-dodecane – 40% n-butanol (Bu40).

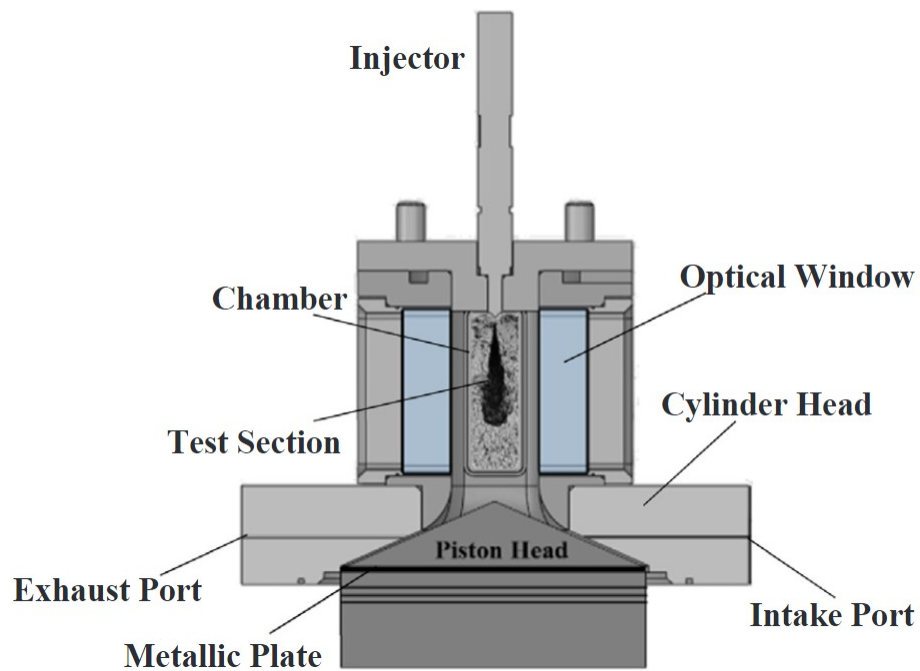


Figure 5-1: The NOSE combustion chamber experimental setup [79,81].

Table 5-1: Testing conditions for ECN spray A conditions [79,81].

Parameters	Value
Ambient gas temperature	800, 850, 900 K
Ambient gas pressure	Near 60 bar
Ambient gas density	22.8 kg/m <sup>3</sup>
Ambient gas composition	
Non-reactive:	0% O <sub>2</sub> , 100% N <sub>2</sub>
Reactive:	15% O <sub>2</sub> , 85% N <sub>2</sub>
Fuel injection pressure	150 MPa
Fuel temperature at nozzle	363 K
Injection duration	1.5 ms
Nozzle diameter	89.7 μm
Number of repetitive test	12

### 5.3 Numerical Formulations

The simulations are performed using ANSYS FLUENT 19.1 [201]. The experimental data from the work of Nilaphai et al. [79,81] is used for the model validation. The constant volume combustion chamber used for the simulation study is a cylinder with a volume identical to those from the experimental measurements [79,81]. In order to achieve that, the diameter of the cylindrical chamber is adjusted while the height remains the same as the actual combustion chamber. The cylinder chamber used in the simulation work is also modelled as an axis-symmetrical 2D plane in order to take advantage of the symmetrical boundary conditions [200]. The resulting 2D plane consists of a radius of 25 mm and a height of 90 mm as shown in Figure 5-2. The zero-flux heat condition is employed in the current simulations and the wall-jet model [224] is used to model the spray impingement on the walls of the combustion chamber. Other boundary conditions applied to the current mesh includes a no-slip for velocity components and zero diffusive flux for the species variables.

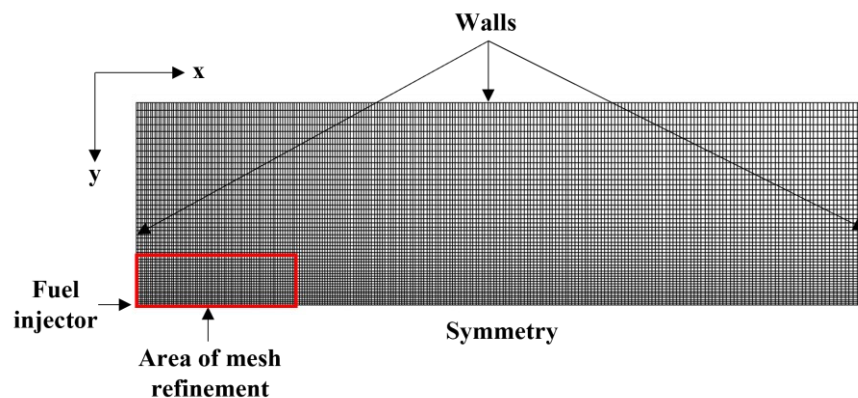


Figure 5-2: Mesh model of the 2D axis-symmetrical plane.

The non-reacting and reacting spray simulations are carried out using the unsteady Reynolds-averaged Navier-Stokes (URANS) turbulence modelling approach to solve the conservation equations for mass, momentum, energy and other scalar quantities such as turbulence and chemical species. The Pressure-Implicit with Splitting of Operators (PISO) pressure-velocity coupling algorithm is employed. For the combustion model, the species transport with finite-rate chemistry is used where it solves the conservation equations that describes the convection, diffusion and reaction source for each species. The DB105 mechanism is integrated into the CFD

solver to describe the combustion and emission characteristics of n-dodecane-n-butanol.

The liquid fuel spray is assumed as a constant size blob that has the same size as the nozzle diameter [225]. This assumption allows the uncertainties related to the effects of internal nozzle passage flow and nozzle geometry on the initial disturbance and atomisation process to be incorporated into just one model constant [226]. The Lagrangian approach is used to track the liquid fuel particles where the trajectories and heat/mass transfer of each liquid droplets are computed. The dynamic drag model is employed to model the drag force that exerts on the fuel droplets during the acceleration in freestream conditions [225]. The two-way turbulence coupling model is also used to capture the effect of changes in turbulent quantities caused by particle damping and turbulent eddies.

The validation under non-reacting spray conditions are conducted by comparing the predicted LPL and VPL against the experimental measurements. Validations under reacting spray conditions are done by comparing the predicted ID, FLOL and SVF against the experimental measurements. The LPL is defined as the furthest location from the injector along the spray axis where 99% of the total liquid mass is found [130,211] and the VPL is defined as the axial distance from the injector along the spray axis where the fuel vapour mass fraction is 0.1% [131,227,228]. The ID is defined as the time at which the maximum temperature gradient occurs in the temperature profile ( $dT/dt$ ) [130]. Although there are several definitions for the ID, Pang et al. [93] reported that there was no significant difference in the ID among the definitions. Moreover, the FLOL can be determined using a well-defined mean temperature iso-contour [229] and the OH chemiluminescence [230] which represents the high-temperature combustion chemistry. Both of these definitions [229,230] were evaluated by Zhang et al. [231] and results show negligible differences between the two definitions. Therefore, in this work, the FLOL is defined as the first location from the injector where the Favre-average OH mass fraction reaching 2% of its maximum. The definitions of the validating parameters used for the non-reacting and reacting simulations are tabulated in Table 5-2 and the baseline physical models used for the simulations are listed in Table 5-3.

Table 5-2: Definition of parameters used for the non-reacting and reacting spray simulations.

Parameters	Definitions
LPL	Maximum location from the injector where 99% of the total liquid mass is found.
VPL	Maximum location from the injector where the fuel vapour mass fraction is 0.1%.
ID	The time of the maximum temperature gradient after start of injection (ASOI).
FLOL	The location where the Favre-average OH mass fraction is 2% of its maximum.

Table 5-3: Baseline physical models used for the simulations.

Models/Parameters	Value
Grid Size	1.0 mm x 1.0 mm (radial x axial)
Time-step	1.00E-06 s
Turbulence model	Standard $k - \varepsilon$ ( $C_{1\varepsilon} = 1.44$ )
Spray breakup model	KHRT ( $B_1 = 20$ , $C_\tau = 0.5$ , $C_{rt} = 1.0$ , $C_L = 17$ )
Drag model	Dynamic
Injector type	Single injection (constant-size blob)
Injection pressure	150 MPa
Injector nozzle diameter	89.7 $\mu\text{m}$

In the experimental measurements [79,81], the liquid fuel is injected according to a square-shaped injection profile as depicted in Figure 5-3. However, it should be noted that there are two hydraulic delays; one at the beginning of the injection command and the other at the end of injection command. The initial hydraulic delay is around 310  $\mu\text{s}$  while the end hydraulic delay is around 2080  $\mu\text{s}$  [79,81]. Although the injection command is only for 1.5 ms, the actual injection period lasted until approximately 3.58 ms before the mass flow rate returns to zero. As such, by taking into consideration of both the initial and end hydraulic delays, the end of injection timing are set to 3.27 ms in the simulations as the hydraulic delays are not detectable in the simulations.

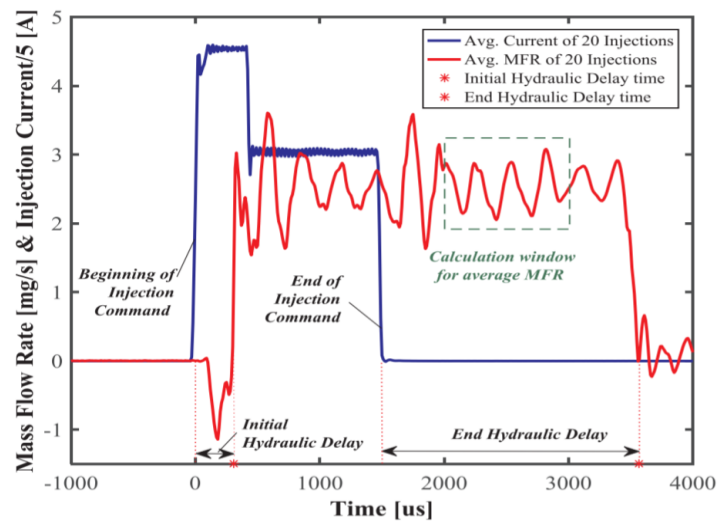


Figure 5-3: Average mass flow rate from 20 repetitive injections at pressure of 60 bar, injection pressure of 150 MPa and injection command duration of 1.5 ms [79,81].

### 5.3.1 Mesh Independence Test

In order to ensure high fidelity simulations, the mesh independence test is first carried out to obtain a suitable mesh for successive numerical studies. The mesh independence test is carried by comparing the computed non-reacting LPL and VPL using five different mesh sizes of 1.00 mm, 0.75 mm, 0.50 mm, 0.25 mm and 0.125 mm. It should be noted that the mesh sizes used here are uniform in the radial and axial directions. The non-reacting simulations are performed using the baseline settings in Table 5-3 at ambient temperature of 900 K and Bu0 as the test fuel.

Figure 5-4 shows the predicted LPL and VPL of the non-reacting Bu0 spray. From Figure 5-4(a), LPL decreases as the mesh size decreases. On the other hand, the VPL increases with the decreased in mesh size, as shown in Figure 5-4(b). The LPL was also seen to be fluctuating more when larger mesh sizes (i.e., 1.0 mm and 0.75 mm) are used. As such, it is obvious that a smaller mesh size should be used for reliable numerical results. The mesh size of 0.25 mm is found to provide mesh independence results as further refinement of the mesh size to 0.125 mm does not show any significant changes in the predictions of LPL and VPL. In fact, as shown in Table 5-4, the computational time of using the 0.125 mm mesh size is higher than those at 0.25 mm by two times, which is expected due to a four times increment in number of cells



as compared to those at 0.25 mm. Therefore, the mesh size of 0.25 mm is considered adequate for accurate simulation results as it has proven to produce mesh independence results.

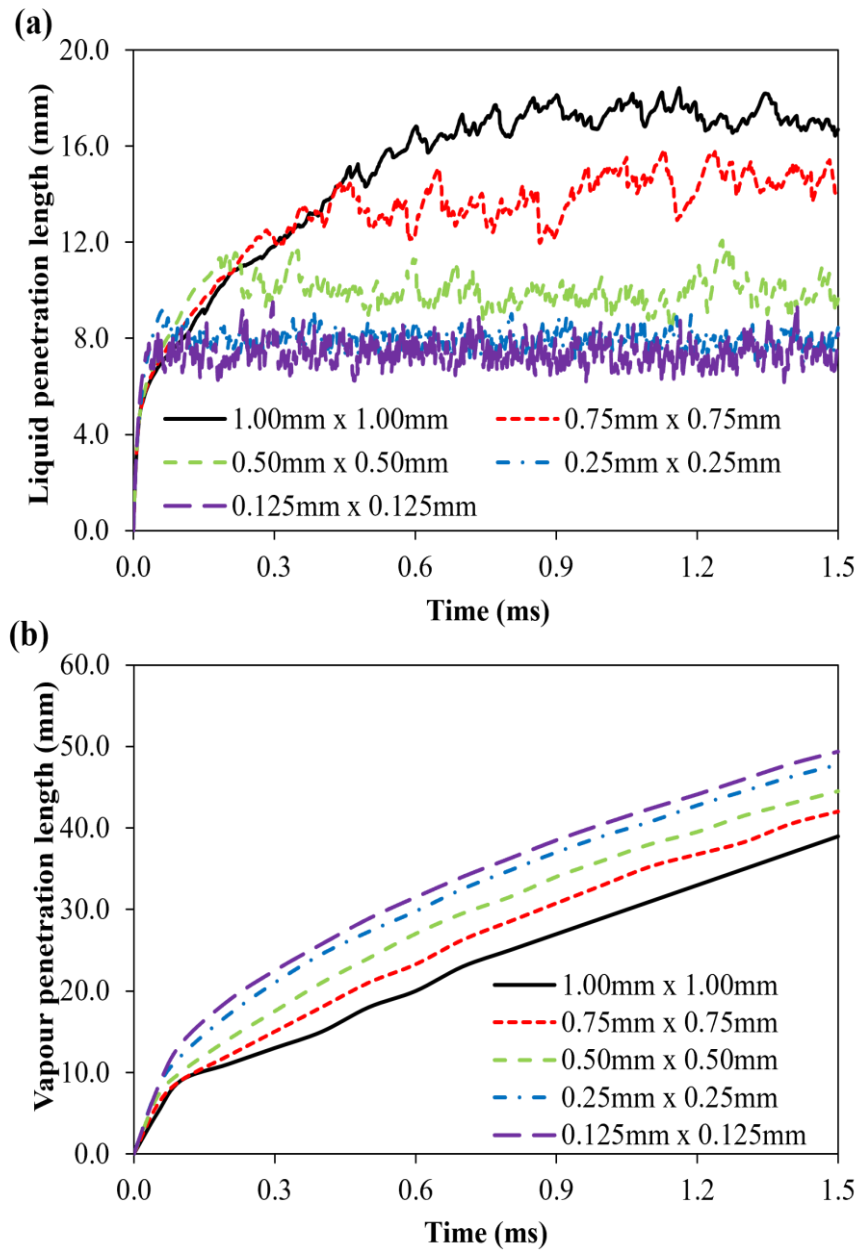


Figure 5-4: Comparison of the predicted (a) LPL and (b) VPL using different mesh size under non-reacting spray conditions, at ambient temperature of 900 K.

Table 5-4: Computational time using different mesh size.

Mesh size (mm)	Number of cells	Computational time (minutes)
1.00 x 1.00	2250	155
0.75 x 0.75	3960	234
0.50 x 0.50	9600	526
0.25 x 0.25	36000	916
0.125 x 0.125	144000	1860

Nevertheless, the computational time can be further reduced as it is unnecessary to apply the fine mesh size across the entire mesh model. The common practice in CFD modelling is to apply fine mesh size only at the area of interest, which in this case is the area close to the injector tip to capture the LPL and VPL profiles of the spray jet. Hence, mesh grading is applied close to the injector tip to reduce the number of cells in the mesh and fasten the computational time (Refer to Figure 5-2). Since 0.25 mm was proven to give mesh independence results, it is selected as the baseline mesh and also the minimum mesh size for the mesh gradings. Table 5-5 shows a tabulation of the details of the mesh with different gradings being applied.

Table 5-5: Description of the mesh with different grading applied.

Mesh size	Baseline	Mesh 1	Mesh 2	Mesh 3	Mesh 4
Minimum mesh size (mm):					
Radial	0.25	0.25	0.25	0.25	0.25
Axial	0.25	0.25	0.25	0.25	0.25
Maximum mesh size (mm):					
Radial	0.25	1.00	0.50	0.50	1.00
Axial	0.25	0.50	0.50	1.00	1.00
Number of cells	36000	12500	17500	11550	7590
Computational time (minutes)	916	261	307	253	208

The predicted LPL and VPL for the non-reacting spray using different mesh gradings are shown in Figure 5-5. From Figure 5-5, as compared to the baseline mesh, there are only slight changes in the LPL and VPL when different mesh gradings are used. Despite the computational time for all the mesh gradings decreases around three to four times as compared to the baseline mesh, Mesh 3 and Mesh 4 are not selected as it is preferable to keep the axial mesh size as small as possible for accurate soot and FLOL predictions [232]. Mesh 2 is not selected as well because the predicted LPL and

VPL did not show any differences to those predicted using Mesh 1 and yet the computational time is 17.62% higher than Mesh 1. Moreover, the radial mesh size that is further away from the injector can be maximised as it does not affect the LPL and VPL [232]. Therefore, Mesh 1 is selected for further parametric studies as it is able to achieve mesh independence results and the computational time is approximately 3.5 times lower than the baseline mesh.

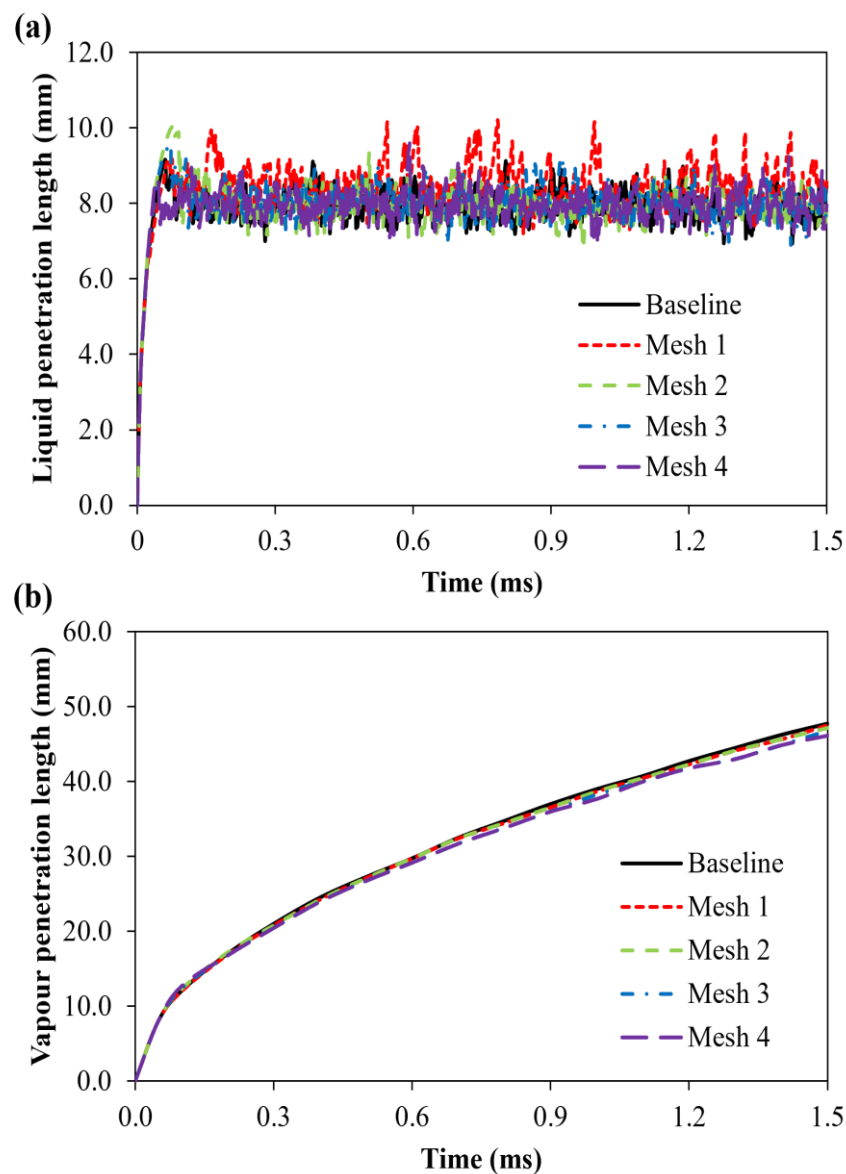


Figure 5-5: Comparison of the predicted (a) LPL and (b) VPL using different mesh gradings under non-reacting spray conditions, at ambient temperature of 900 K.

### 5.3.2 Time-step Parametric Study

After finalising on the optimum mesh size, the time-step parametric test is carried out to obtain a suitable time-step for the simulations. Three time-step sizes of  $5.0 \mu\text{s}$ ,  $1.0 \mu\text{s}$  and  $0.5 \mu\text{s}$  are tested in this parametric test where they are commonly used in other studies [125,130,131]. The time-step parametric study is conducted using Mesh 1 and the predicted non-reacting LPL and VPL at different time-steps are presented in Figure 5-6. From Figure 5-6(a), the LPL is seen to be fluctuating more at larger time-step size and the magnitude of the fluctuation decreases as the time-step size decreases to  $0.5 \mu\text{s}$ . The VPL is however less sensitive to the changes in time-step size as shown in Figure 5-6(b). As smaller time-step size leads to higher computational time, the time-step size of  $1.0 \mu\text{s}$  is considered sufficient to provide a steady predictions for LPL and VPL and a reasonable computational time.

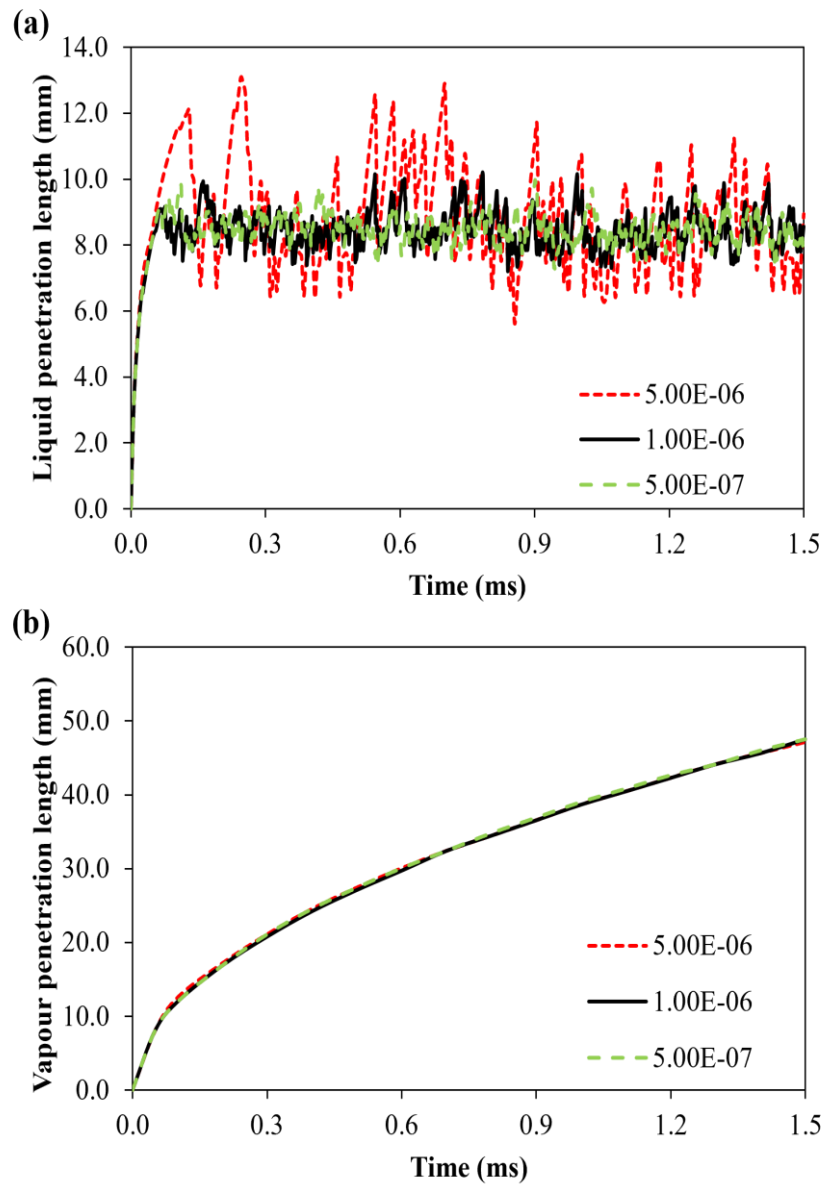


Figure 5-6: Comparison of the predicted (a) LPL and (b) VPL using different time-step size under non-reacting spray conditions, at ambient temperature of 900 K.

### 5.3.3 Turbulence Model Parametric Study

The turbulence model parametric study is carried out to determine the optimum turbulence model and model constants for the simulations. Three RANS based turbulence models are evaluated namely Standard  $k-\varepsilon$  model, Re-Normalisation Group (RNG)  $k-\varepsilon$  model and the Realisable  $k-\varepsilon$  model. The default model constants for each turbulence model are listed in Table 5-6. The turbulence model parametric study is carried out using Mesh 1 and the time-step size of  $1.0 \mu\text{s}$ .

Table 5-6: Default model constants in the Standard, RNG and Realisable  $k-\varepsilon$  models.

Turbulence models	Model constants
Standard $k-\varepsilon$	$C_{\mu} = 0.09$ , $C_{1\varepsilon} = 1.44$ , $C_{2\varepsilon} = 1.92$ , $\sigma_k = 1.0$ , $\sigma_{\varepsilon} = 1.3$
RNG $k-\varepsilon$	$C_{\mu} = 0.0845$ , $C_{1\varepsilon} = 1.42$ , $C_{2\varepsilon} = 1.68$
Realisable $k-\varepsilon$	$C_{1\varepsilon} = 1.44$ , $C_{2\varepsilon} = 1.90$ , $\sigma_k = 1.0$ , $\sigma_{\varepsilon} = 1.2$

Figure 5-7 shows the effect of turbulence model on the predicted LPL and VPL against the experimental measurements under non-reacting spray conditions. Referring to Figure 5-7, the standard  $k-\varepsilon$  model was found to under-predict the experimental LPL and VPL with the default model constants. However, it can be observed that the predicted VPL using the standard  $k-\varepsilon$  model matches the trend of the experimental measurements well. The RNG  $k-\varepsilon$  model predicts a comparable LPL with the standard  $k-\varepsilon$  model but the VPL is over-predicted at the early phase of the injection. Nonetheless, the RNG model predicts a lower rate of increment for the VPL and the VPL is eventually under-predicted at 1.5 ms. For the realisable  $k-\varepsilon$  model, the LPL is over-predicted at the early phase of the injection but decreases to a stabilised level for the rest of the injection period. The predicted VPL using the realisable  $k-\varepsilon$  model is similar to those of the RNG  $k-\varepsilon$  model at the early part of the injection where over-predictions occur but slowly converges to a level similar to those predicted using the standard  $k-\varepsilon$  model. In spite of that, as mentioned previously, the standard  $k-\varepsilon$  model predicts a better fit to the trend of the experimental measurements and is thus selected for this simulation work.

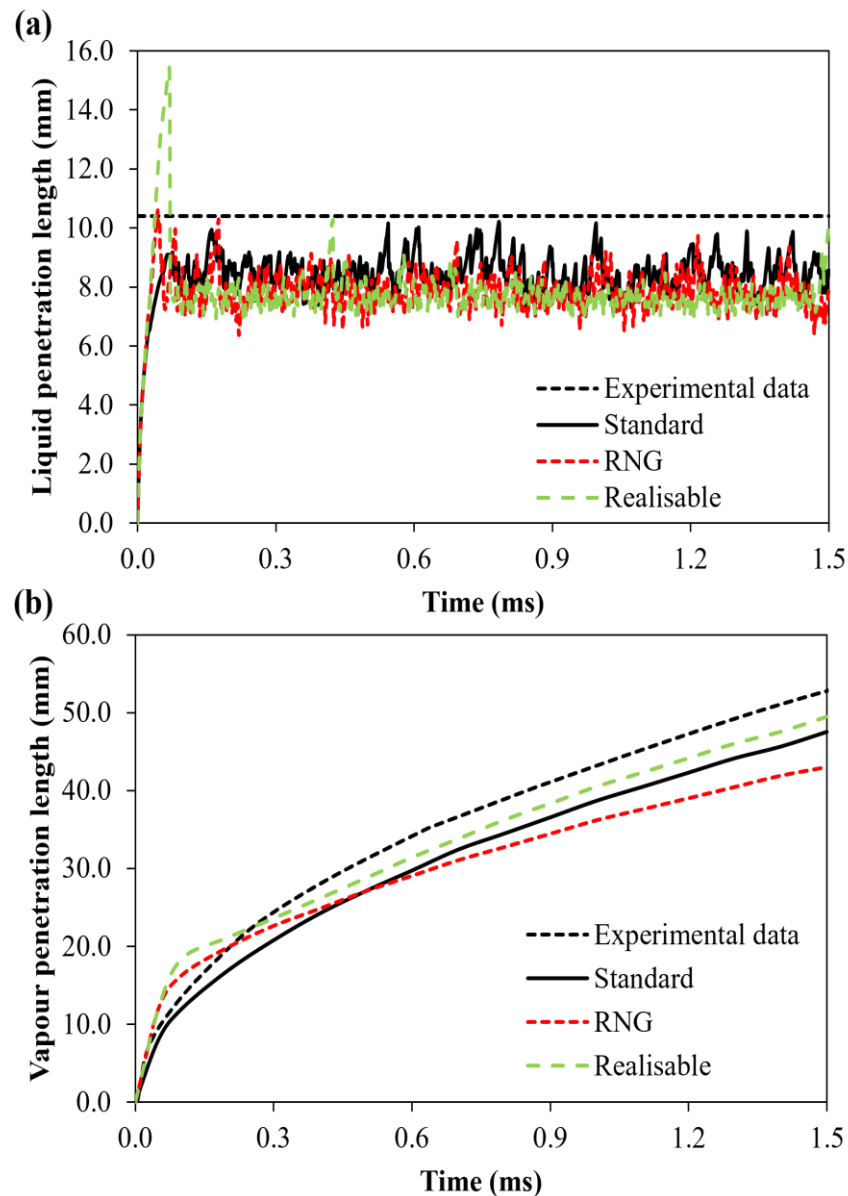


Figure 5-7: Comparison of the predicted (a) LPL and (b) VPL against the experimental measurements using different turbulence model under non-reacting spray conditions, at ambient temperature of 900 K.

Following the selection of the standard  $k-\varepsilon$  model turbulence model, the effect of adjusting the  $C_{1\varepsilon}$  model constant on the predicted LPL and VPL is evaluated and the results are shown in Figure 5-8. Based on Figure 5-8, it is observed that the increment of the  $C_{1\varepsilon}$  model constant value from 1.44 to 1.60 increases the VPL. On the contrary, the LPL is found to be insensitive to the changes of  $C_{1\varepsilon}$  value. Therefore, the  $C_{1\varepsilon}$  model constant value should be increased to match the experimental measurements, especially for the VPL measurements.

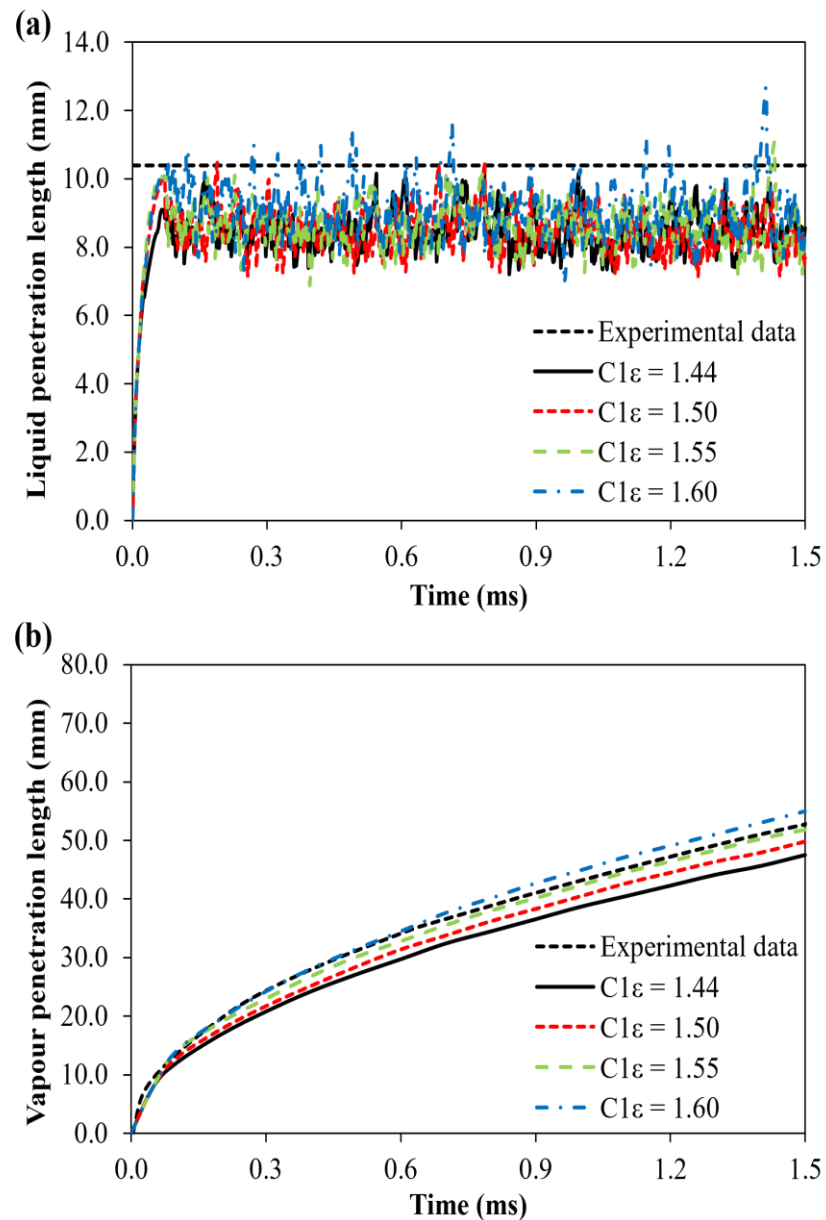


Figure 5-8: Comparison of the predicted (a) LPL and (b) VPL against the experimental measurements using different  $C_{1\varepsilon}$  values under non-reacting spray conditions, at ambient temperature of 900 K.



### 5.3.4 Spray Breakup Model Parametric Study

The effect of adjusting the  $B_1$  constant in the KHRT model on the predicted LPL and VPL under non-reacting spray conditions is studied here. The  $B_1$  constant is the breakup time constant that determines the time at which the fuel droplets are broken up into child droplets. The  $B_1$  constant is also the most important model constant in the KHRT model as it has a huge influence on the spray penetration length [233]. The value of the  $B_1$  constant can be in the range of 1 to 60, depending on the injector characterisation [201]. According to Figure 5-9, the effect of the adjustment of the  $B_1$  constant value is more pronounced in the prediction of LPL. On the contrary, the predicted VPL shows only a slight difference with the changes in  $B_1$  constant value. A higher  $B_1$  value prolongs the spray breakup timing and increases the diameter of the fuel droplets. As a result, a longer LPL is observed due to larger momentum of the fuel droplets.

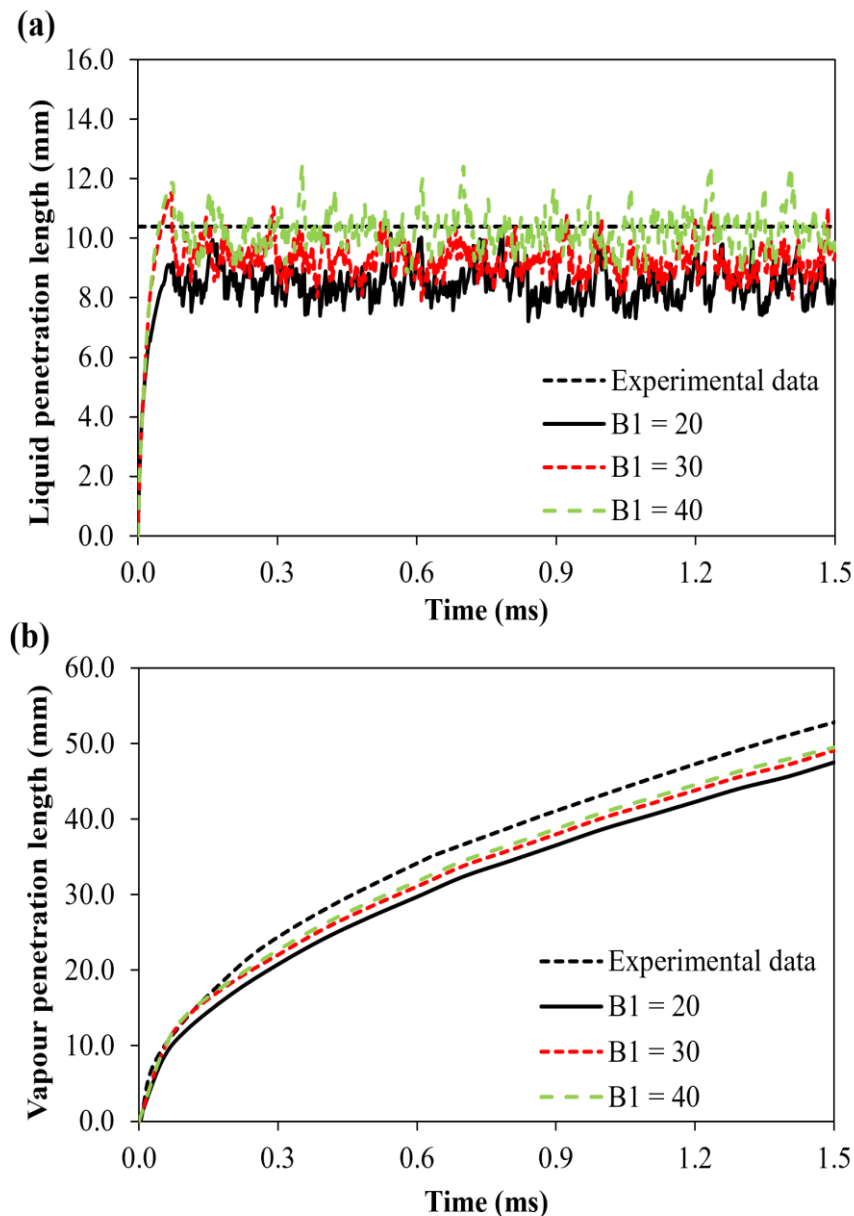


Figure 5-9: Comparison of the predicted (a) LPL and (b) VPL against the experimental measurements using different  $B_1$  values under non-reacting spray conditions, at ambient temperature of 900 K.

### 5.3.5 Optimised Numerical Setup

From the mesh independence test and all the parametric studies from Section 5.3.1 to 5.3.4, it can be deduced that the LPL is more sensitive to the  $B_1$  value in the KHRT model while the VPL is more sensitive to the  $C_{1\varepsilon}$  in the standard  $k-\varepsilon$  model. Hence, the  $B_1$  and  $C_{1\varepsilon}$  model constants must be calibrated to match the non-reacting experimental LPL and VPL. Table 5-7 shows a set of optimised numerical settings for

the non-reacting spray simulations for Bu0 fuel. It is noteworthy to mention that the numerical settings listed in Table 5-7 are used to simulate the non-reacting sprays for the remaining cases of Bu0, Bu20 and Bu40 fuel at ambient temperatures of 800 K, 850 K and 900 K.

Table 5-7: Optimised numerical settings.

Models/Parameters	Selection/Value
Mesh size	Mesh 1; 0.25 mm x 0.25 mm (minimum), 1.00 mm x 0.50 mm (maximum) in both radial and axial directions
Time-step	1.00E-06 s
Turbulence model	Standard $k-\varepsilon$
Model constant $C_{1\varepsilon}$	1.50
Breakup model	KHRT
Model constant $B_1$	40

#### 5.4 Non-reacting Spray Simulations

The predicted non-reacting penetration lengths for Bu0, Bu20 and Bu40 fuels at ambient temperatures of 800 K, 850 K and 900 K are compared against the experimental measurements as shown in Figure 5-10. For brevity, the test cases are denoted by the ‘fuel blend (ambient temperature)’ convention hereafter. From the results in Figure 5-10, the optimised numerical settings are able to replicate the trends of the LPL and VPL well with respect to the changes in n-butanol blending ratios and ambient temperatures. However, the VPLs of Bu20 and Bu40 are slightly under-predicted as the numerical settings are formulated based on the Bu0 fuel. The higher density of Bu20 and Bu40 fuel exhibit higher fuel momentum and causes the fuel vapour to penetration further into the combustion chamber and thus higher VPL. Nonetheless, for all cases, the maximum deviation between the predicted penetration lengths and the experimental measurements is 4% which implies a good prediction of the air-fuel mixing is achieved.

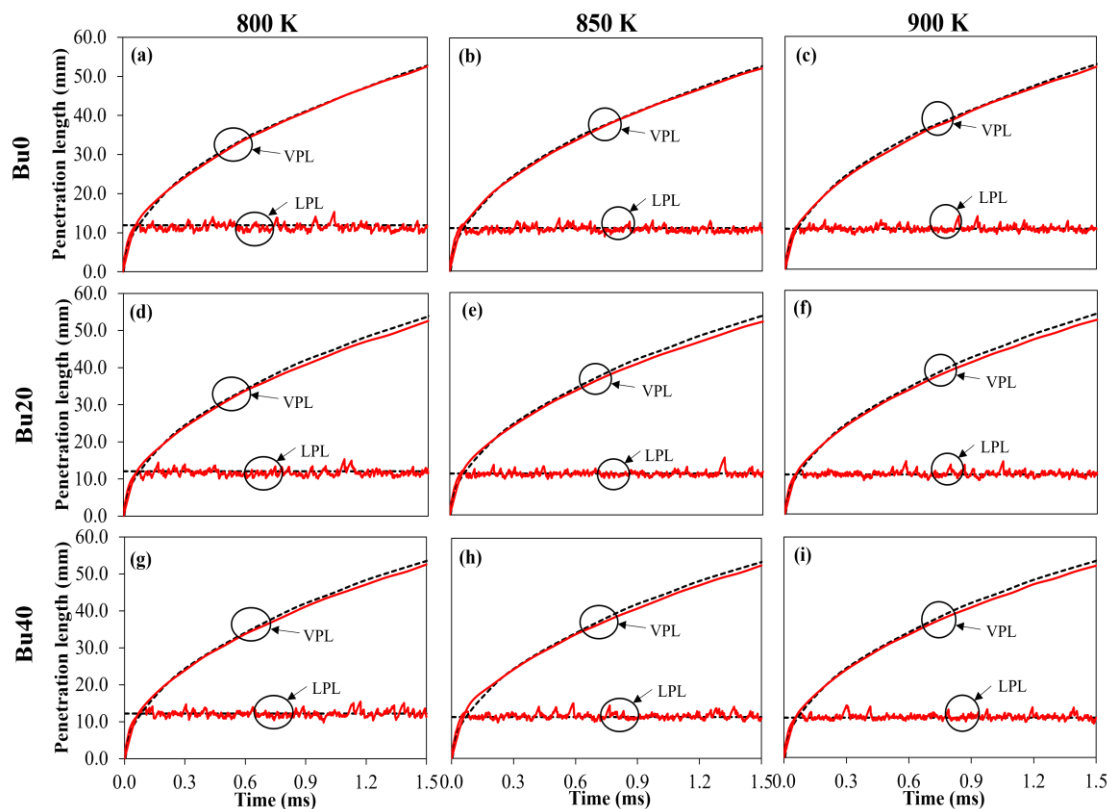


Figure 5-10: Comparison of the predicted non-reacting LPL and VPL (solid lines) against experimental measurements (dash lines) [79] for Bu0, Bu20 and Bu40 fuels at ambient temperatures of 800 K, 850 K and 900 K.

## 5.5 Reacting Spray Simulations

### 5.5.1 ID and FLOL Predictions

Following the validations under non-reacting conditions, the simulations are extended to under reacting conditions. As fuel ignition depends on the chemical kinetics, the ID is a suitable parameter to determine the accuracy of the chemical kinetics. Meanwhile, accurate prediction of the FLOL is particularly important for the soot formation process as it determines the amount of air being entrained by the fuel vapour prior to combustion [234,235]. The numerical settings used for the reacting spray simulations are identical to those listed in Table 5-7. The ambient oxygen concentration used for the reacting simulations is 15% while the ambient density is maintained at  $22.8\text{kg/m}^3$ .

According to the results in Figure 5-11, the DB105 mechanism gives good predictions in ID and FLOL as compared to the experimental measurements for Bu0, Bu20 and Bu40 fuels at ambient temperatures of 800 K, 850 K and 900 K. The maximum percentage error for ID and FLOL are recorded to be 20% and 12%, respectively, for all test cases. Besides, the trends of the ID and FLOL for all test cases are correctly replicated by the DB105 mechanism where a lower ambient temperature and a higher n-butanol blending ratio leads to higher ID and FLOL. Overall, the ID and FLOL prediction results here are considered as an improvement as compared to the previous n-dodecane-n-butanol mechanisms by Wakale et al. [75,88] where the predicted ID deviated by a factor of three at ambient temperature of 800 K.

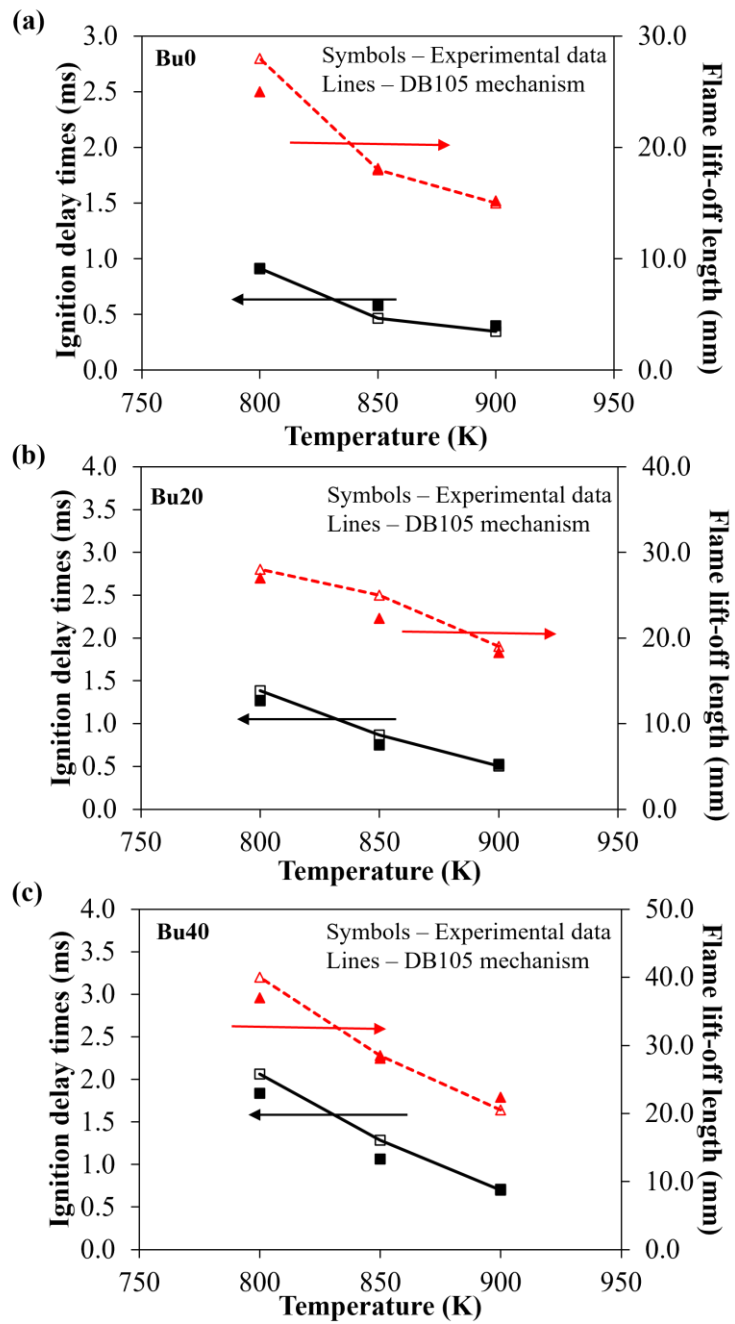


Figure 5-11: Comparison of the predicted ID and FLOL for (a) Bu0, (b) Bu20 and (c) Bu40 fuels against the experimental measurements [79] at ambient temperatures of 800 K, 850 K and 900 K.

### 5.5.2 Soot Predictions

As the default model constants in the Moss-Brookes soot model are mainly developed to predict methane combustion [202], it is necessary to calibrate the model constant values to match the present experimental measurements [70]. Among others, the rates of soot inception ( $C_\alpha$ ) and soot surface growth ( $C_\gamma$ ) are selected to be adjusted to match the experimental measurements due to their significant contributions in the resulting soot formation [93,236,237].

From the literature, the typical value of  $C_\alpha$  used in simulations is 10000 [131,237]. On the contrary, the  $C_\gamma$  value varies from 6000 [93,236,237] to 72000 [238]. Meanwhile, Chishty et al. [131] and Vishwanathan and Reitz [239] adopted a value of 9000 for  $C_\gamma$  in their respective soot modelling studies. Based on the values recommended in the literature, a test matrix is constructed as shown in Figure 5-12 for the parametric study of  $C_\alpha$  and  $C_\gamma$  values. For  $C_\alpha$ , the lower limit is set to 54 as suggested by ANSYS FLUENT while the upper limit is set to 10000 as suggested in the literature. An intermediate value of 5000 is also included in the test matrix. Meanwhile, for  $C_\gamma$ , both the values for the lower and upper limit are adopted from the literature. The values highlighted in bold are those default values recommended by ANSYS FLUENT.

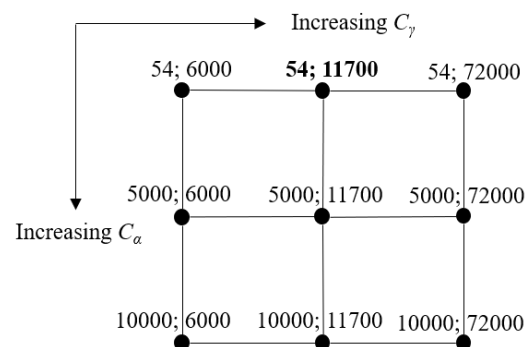


Figure 5-12: Test matrix for the calibration of  $C_\alpha$  and  $C_\gamma$  values.

Figure 5-13 shows the simulated SVF against the experimental measurements [70] for Bu0 fuel at ambient temperatures of 900 K using different  $C_\alpha$  and  $C_\gamma$  values. From the trends of the predicted SVF in Figure 5-13, it can be deduced that the  $C_\alpha$  value has an influence on the peak SVF only while the  $C_\gamma$  value affects both the peak SVF and the size of the soot cloud. Besides, it is obvious that the default values for  $C_\alpha$

and  $C_\gamma$  tend to under-predict the peak SVF and the location at which the peak SVF occurs is predicted to be around 5 mm upstream as compared to the experimental measurements. As a result, the  $C_\alpha$  and  $C_\gamma$  values must higher than the default values in order to replicate the experimental measurements and thus the values for  $C_\alpha$  and  $C_\gamma$  are selected as 5000 and 72000, respectively.

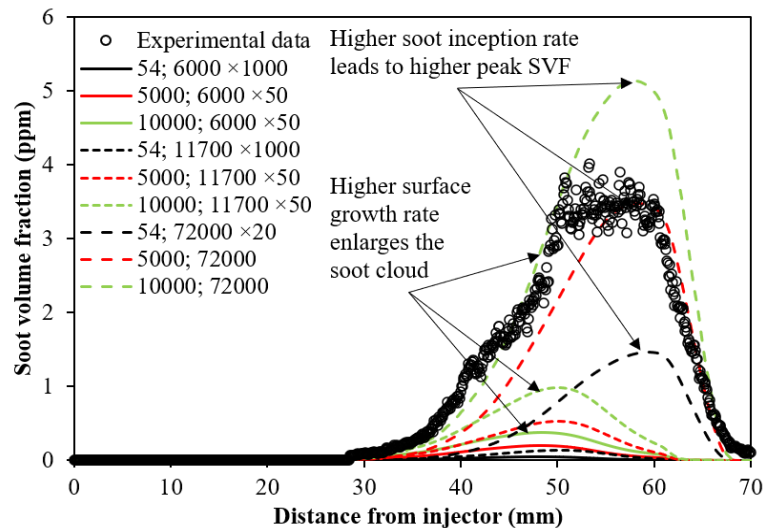


Figure 5-13: Effects of  $C_\alpha$  and  $C_\gamma$  values on the predicted SVF of Bu0 fuel at ambient temperature of 900 K. The figure legend is labelled using the convention of ‘ $C_\alpha$ ;  $C_\gamma \times$  magnification factor’.

Figure 5-14 shows the predicted SVF against the experimental measurements [70] for Bu0 fuel at ambient temperatures of 850 K and 900 K. Soot validation at ambient temperature of 800 K was not performed because the laser induced incandescence experiments could not detect any signal, indicating ultra-low or no soot formed within the measured conditions [240]. From Figure 5-14, the peak SVF at 850 K is over-predicted by around 1.0 parts per million (ppm) (100%) while the peak SVF at 900 K is well predicted with a maximum error of 0.3 ppm (10%). The discrepancy of the predicted peak SVF at 850 K was also observed by Chishty et al. [131] and this could be attributed to the temperature insensitivity of the soot formation rates. Nevertheless, the simulations are able to well replicate the soot onset location at both ambient temperatures, where it is slightly further downstream as the ambient temperature decreases. Furthermore, Figure 5-15 shows the predicted soot contours for Bu0 fuel against the experimental measurements at ambient temperatures of 850 K and 900 K. The red dash line in the images represents the FLOL. Referring to the



results in Figure 5-15, the shape and location of the experimental soot clouds are well emulated by the simulations. However, the predicted peak SVF at ambient temperature of 900 K is located slightly downstream as compared to the experimental measurements. Despite that, more importantly, the predicted SVF contours agree well with the conceptual model proposed by Dec [2], where soot is mainly formed in the fuel-rich zone of the spray jet. It should be noted that due to the lack of soot experimental data for n-dodecane-n-butanol blends, the soot model settings are retained to be identical to those used for Bu0 fuel to ensure that only the effects of n-butanol blending ratio and ambient temperature and its associated chemical kinetics are present in the results produced for n-dodecane-n-butanol blends (soot modelling results in Chapter 7). Such approach is also similarly adopted by Cheng et al. [241] in their soot modelling study of soybean methyl ester – ethanol blends.

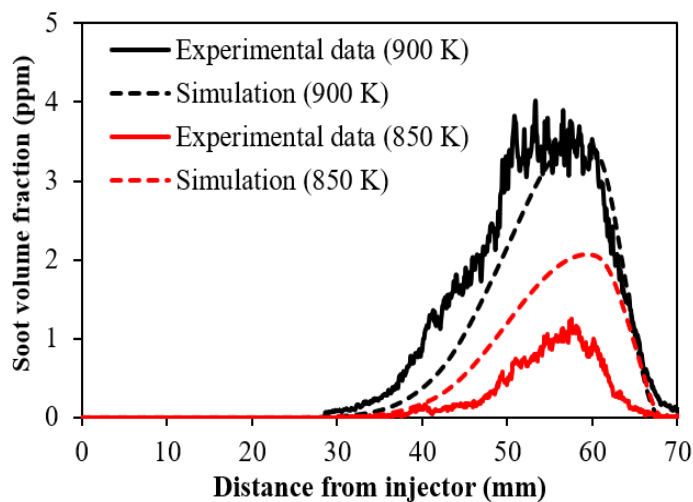


Figure 5-14: Comparison of the predicted SVF against experimental measurements [70] for Bu0 fuel at ambient temperatures of 850 K and 900 K.

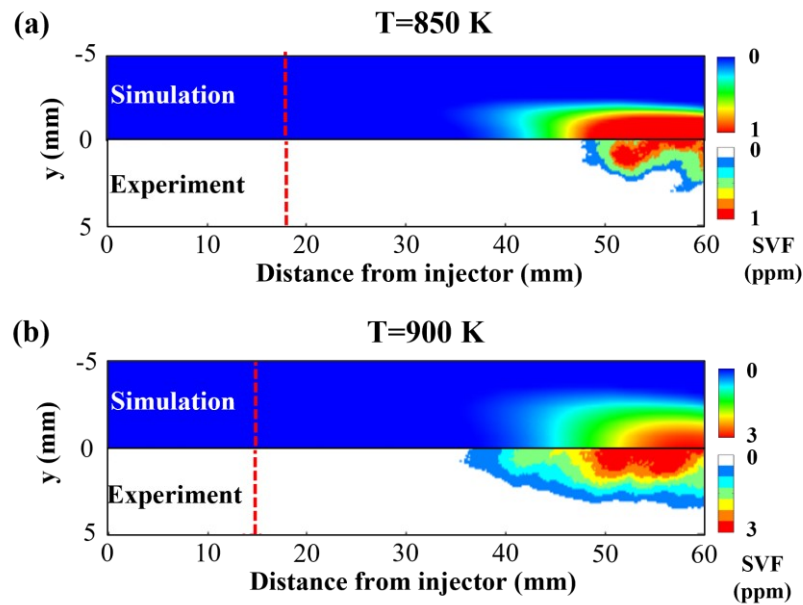


Figure 5-15: Comparison of the predicted SVF contours for Bu0 fuel against the experimental measurements [70] at ambient temperature of (a) 850 K and (b) 900 K. Red line denotes the FLOL.

## 5.6 Concluding Remarks

The numerical formulations for the 2D spray combustion simulations in a constant volume combustion chamber are performed in this chapter. The mesh independence test and parametric studies for the time-step, turbulence model and spray breakup model are conducted to obtain an optimised set of CFD sub-models for the simulations. Subsequently, by using the optimised CFD sub-models, the simulations are conducted under non-reacting condition by comparing the LPL and VPL of Bu0, Bu20 and Bu40 fuels at ambient temperatures of 800 K, 850 K and 900 K to the experimental measurements. The simulations for the test cases are also extended to reacting condition where the predicted ID, FLOL and soot results are compared to the simulation results. A maximum deviation of 4% is recorded for the LPL and VPL whereas it is at 20% and 12% for the ID and FLOL, respectively. For the soot validation, the predicted peak SVF for Bu0 fuel at 850 K and 900 K deviated by around 1.0 ppm (100%) and 0.3 ppm (10%), respectively, to the experimental measurements. However, the experimental soot clouds are well emulated. Soot validations for n-dodecane-n-butanol blends are not presented as there is a lack of soot experimental data but the CFD sub-models and model constants formulated here are retained to be identical for the numerical studies in Chapter 6 and 7.

# CHAPTER 6

## IGNITION AND COMBUSTION CHARACTERISTICS OF N- DODECANE-N-BUTANOL SPRAY

### 6.1 Introductory Remarks

Following the numerical setup and validations of the CFD sub-models and the DB105 mechanism under 2D spray combustion simulations in Chapter 5, Table 6-1 tabulates five test cases that are selected to study the ignition, combustion and flame characteristics of n-dodecane-n-butanol at various n-butanol blending ratios and ambient temperatures. The effects of n-butanol blending ratio and ambient temperature towards the global combustion characteristics of n-dodecane-n-butanol spray combustion are first presented in Section 6.2. The ignition characteristics of n-dodecane-n-butanol blends are then studied in Section 6.3 alongside the species that pertains to ignition. Moreover, Section 6.4 describes the transitioning behaviour of the n-dodecane-n-butanol blends towards quasi-steady state and Section 6.5 presents their flame characteristics at quasi-steady state. The combustion mode analysis on the evolution of n-dodecane-n-butanol spray is performed in Section 6.6. Finally, the conclusions from this chapter are highlighted in Section 6.7.

Table 6-1: Test cases investigated.

No	Test case	Ambient pressure (bar)	Oxygen level (%)
1	Bu0 (900 K)	59.65	15
2	Bu20 (900 K)	59.65	15
3	Bu40 (900 K)	59.65	15
4	Bu20 (850 K)	56.34	15
5	Bu20 (800 K)	53.02	15

### 6.2 Global Combustion Characteristics

The temporal evolution of the flame temperature and HRR at different n-butanol blending ratios and ambient temperatures are shown in Figure 6-1. The HRR is calculated from the sum of heat that is produced from all the reactions. From Figure

6-1, the flame temperature decreases and the HRR is delayed as the n-butanol blending ratio increases and as the ambient temperature decreases. This is due to the slower reaction rate at higher n-butanol blending ratio and at lower ambient temperature. Besides, according to Figure 6-1(b), it could be observed that the predicted HRR for all cases consists of two peaks where the first peak is associated to the first-stage ignition and the second peak associated to the second-stage ignition. This is in contrast to the spray combustion of pure n-butanol where it only consists of a single stage ignition [242]. Besides, the trends of the predicted HRR show that after the first-stage ignition, there is a decrease in HRR before the second-stage ignition. During this time, the liquid fuel absorbs heat from the surroundings for further vaporisation and air entrainment in order to achieve a combustible mixture prior to the second-stage ignition. This is an endothermic process and thus the predicted HRR decreases. Moreover, the combustion duration is observed to be the longest for Bu20 (800 K) as evident from the slowest rate of decrease in HRR after the peak of the second-stage ignition as shown in Figure 6-1(b).

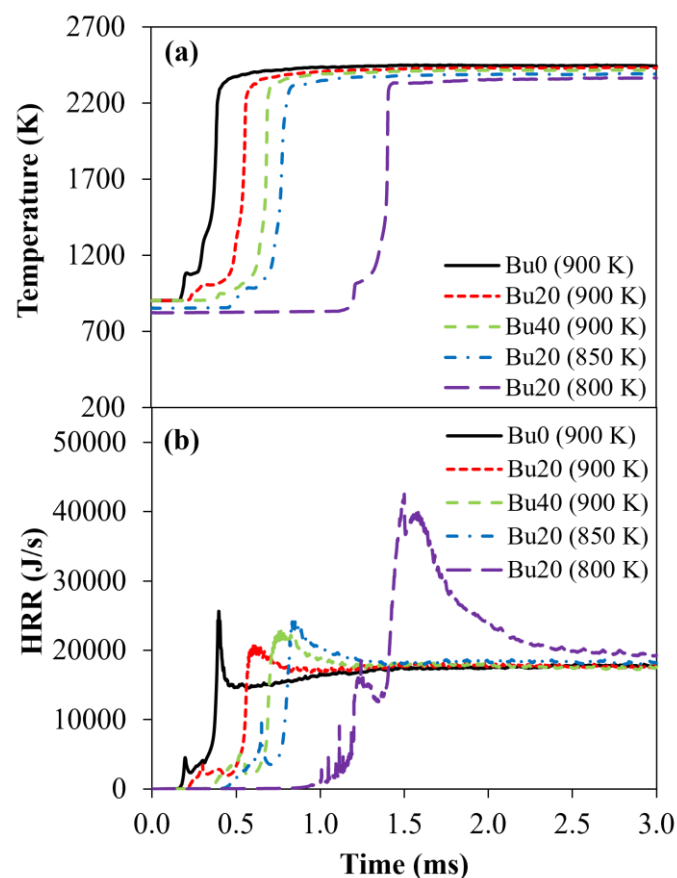


Figure 6-1: Predicted (a) flame temperature and (b) HRR for different test cases.

### 6.3 Flame Ignition Characteristics

In order to understand the ignition process of n-dodecane-n-butanol blend, three characteristic timings are adopted to distinguish the important stages of the flame during the spray combustion event. The characteristic timings were first introduced by Salehi et al. [243] and were subsequently adopted by Wei et al. [86] for their n-heptane spray combustion study. All the characteristic timings are defined with respect to the start of injection timing and they are as follows:

- $t_1$  – the time at which the first-stage ignition occurs.
- $t_2$  – time at which maximum temperature gradient occurs, which also corresponds to the second-stage ignition.
- $t_3$  – time at which the flame reaches the high-temperature combustion.

Based on Figure 6-2, the first-stage ignition of Bu0 (900 K) at  $t_1$  occurs very rapidly as can be seen from the sudden spike and decrease in the HRR. On the contrary, the first-stage ignition of Bu20 (900 K) and Bu40 (900 K) are slower than Bu0 (900 K), as can be seen in Figure 6-2(b) and (c), where the HRR curves of Bu20 (900 K) and Bu40 (900 K) at the first-stage ignition are increasing gradually as compared to the rapid increase of HRR for Bu0 (900 K). However, it should be noted that the peak HRR at the first-stage ignition for Bu40 (900 K) is marginally higher than Bu0 (900 K) and Bu20 (900 K). This could be attributed to the higher degree of homogeneity of air-fuel mixture that was formulated prior to the first-stage ignition, which resulted in a more intense combustion. Similarly, Bu20 (800 K) consists of a longer duration of air-fuel mixing and this subsequently resulted in a much higher peak HRR at the first-stage ignition. After the first-stage ignition, the flame moves towards the second-stage ignition at  $t_2$ . From Figure 6-2, it could be seen that the flame temperature and HRR for all test cases increase drastically at  $t_2$ , which indicates that the combustion reaction at the second-stage ignition is very intensive. It can also be seen that the time difference between  $t_1$  and  $t_2$  is the shortest for Bu0 (900 K) as compared to the other cases. This is due to the higher cetane number of n-dodecane as compared n-dodecane-n-butanol blends, which increases the tendency of n-dodecane to auto-ignite. From the viewpoint of chemical kinetics, the inclusion of n-butanol creates a competition with n-dodecane for the consumption of OH [59]. This thus slows down the oxidation of n-

dodecane and the difference between  $t_1$  and  $t_2$  increases as n-butanol blending ratio increases. Moreover, the lower overall combustion reaction at lower ambient temperature also leads to a larger difference between  $t_1$  and  $t_2$ . Nevertheless, at the end of  $t_2$ , the flame temperature for all cases have reached its maximum and is at the onset of high-temperature combustion as the combustion progresses to  $t_3$ . Thereafter, the flame temperature remains constant throughout the entire period of time while the HRR decreases gradually from its peak until it reaches a steady-state value.

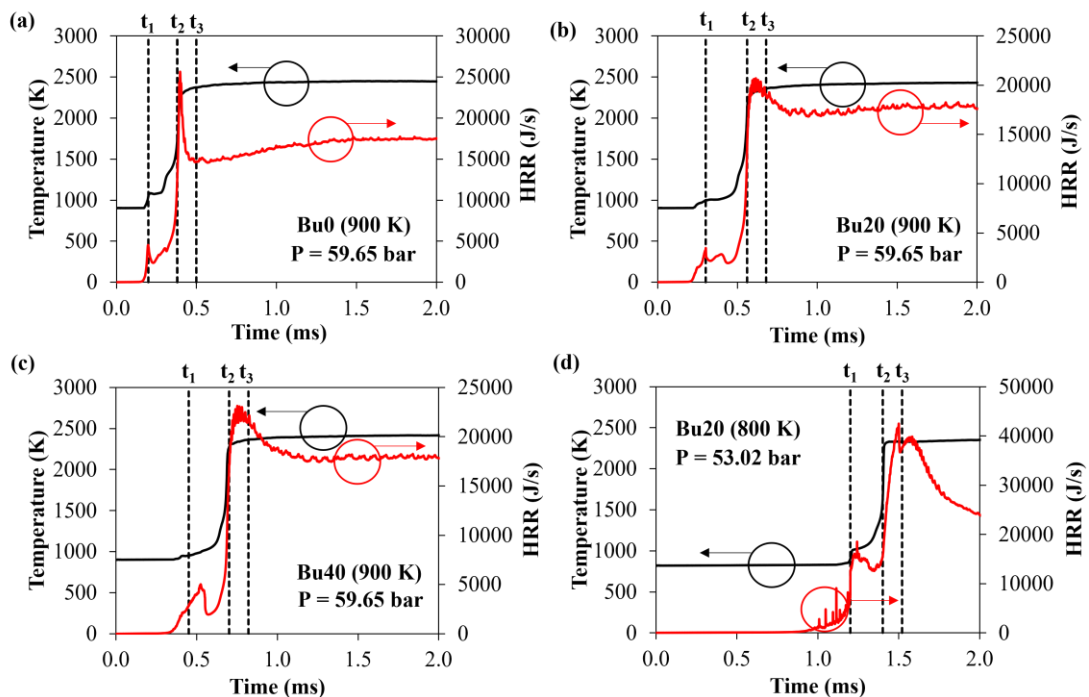


Figure 6-2: Temporal evolution of the flame temperature and HRR for (a) Bu0 (900 K), (b) Bu20 (900 K), (c) Bu40 (900 K) and (d) Bu20 (800 K).

Figure 6-3 to Figure 6-5 further present the contours of temperature, OH and CH<sub>2</sub>O at  $t_1$ ,  $t_2$  and  $t_3$ . The CH<sub>2</sub>O and OH species are selected as markers for low-temperature and high-temperature combustion, respectively [244–246]. In the contours, the black line is the stoichiometric line, where it is used to separate the fuel-lean and fuel-rich regions. Regions that are within and outside the stoichiometric line are considered as fuel-rich and fuel-lean, respectively. The mixture fraction of the spray is calculated based on the mass fractions of carbon and hydrogen atoms using the following equation [86]:

$$Z = \sum_{\alpha=1}^{N_s} (MW_c n_{c,\alpha} + MW_H n_{H,\alpha}) \frac{Y_\alpha}{MW_\alpha} \quad (6-1)$$

where  $MW_c$ ,  $MW_H$  and  $MW_\alpha$  are the molar mass for the carbon, hydrogen and species  $\alpha$ , respectively. Besides,  $n_{c,\alpha}$  and  $n_{H,\alpha}$  are the number of carbon and hydrogen atom of species  $\alpha$ , respectively, while  $Y_\alpha$  and  $N_s$  are the mass fraction of species  $\alpha$  and total number of species, respectively. It should be noted that in this calculation, the mass fractions of  $\text{CO}_2$  and  $\text{H}_2\text{O}$  are excluded [86].

According to the temperature contours in Figure 6-3, it could be seen that the first-stage ignition site for all cases except Bu20 (800 K) at  $t_1$  is at the spray periphery. This is because the liquid fuel that is further away from the liquid core undergoes vaporisation and mixes with the hot ambient air to form the combustible mixture. However, for Bu20 (800 K), the sufficiently long ID enhances the air-fuel mixing and the first-stage ignition is observed to occur at the spray head in addition to the spray periphery. A high amount of  $\text{CH}_2\text{O}$  is also found at the same location where the first-stage ignition occurs. The distribution of  $\text{CH}_2\text{O}$  and the first-stage ignition sites are also seen to be penetrating towards the fuel-lean region as n-butanol blending ratio increases and as the ambient temperature decreases. Since the latent heat of n-butanol is higher than n-dodecane [79], the vaporisation of n-dodecane-n-butanol liquid fuel within the spray core is difficult. Hence, only the liquid fuel that is at the outermost edge of the spray receives sufficient heat energy for vaporisation and undergoes air-fuel mixing with the surrounding ambient air. Likewise, at lower ambient temperatures, the heat of the surroundings decreases and air entrainment occurs only at the outermost of the spray jet because there is a lack of heat energy for fuel vaporisation within the inner spray core. Due to these reasons, the first-stage ignition is shifted towards to fuel-lean region at higher n-butanol blending ratio and at lower ambient temperature. Meanwhile, for all cases, the OH species is formed in the exact location where the first-stage ignition occurs.

As the combustion progresses to the second-stage ignition at  $t_2$ , Figure 6-4 shows that the high-temperature ignition sites occur at the spray periphery fuel-rich region for Bu0 (900 K) while it is at the fuel-rich region of the spray head for Bu20

(900 K), Bu40 (900 K) and Bu20 (850 K). For Bu20 (800 K), the high-temperature ignition sites cover both fuel-rich and fuel-lean regions in the vicinity of the spray head due to the enhance air-fuel mixing. From Figure 6-4, it could also be seen that  $\text{CH}_2\text{O}$  is built up at the upstream of the flame and it is mainly concentrated within the fuel-rich region but its distribution envelops both fuel-rich and fuel-lean regions for Bu20 (800 K). Moreover, for all test cases, the location of OH formation is also observed to coincide with the location where  $\text{CH}_2\text{O}$  is destructed, which is in line with the experimental findings that  $\text{CH}_2\text{O}$  is being replaced by OH as the combustion evolves from the first-stage ignition to the second-stage ignition [245].

During the occurrence of high-temperature combustion at  $t_3$ , Figure 6-5 shows that the flame for Bu0 (900 K) is more streamlined and the highest flame temperature occurs at the stoichiometric line. However, at higher n-butanol blending ratio and at lower ambient temperature, the flame expands radially and becomes thicker with the highest flame temperature occurring towards the fuel-lean region. This is evident in the OH contours in Figure 6-5, where OH is formed at the stoichiometric line for Bu0 (900 K) whereas it is formed in the fuel-lean region for the remaining cases. From Figure 6-5, the high-temperature flame for all cases except Bu20 (800 K) resembles an arrowed head, where the highest temperature ( $\sim 2300$  K) is at the leading edge of the flame and extends throughout the stoichiometric periphery. On the other hand, the flame temperature at the downstream fuel-rich region is slightly lower ( $\sim 1700$  K) since there is a deficiency in oxygen which slows the combustion reaction. However, due to an extended duration of air-fuel mixing, the flame of Bu20 (800 K) is in a circular shape and the flame temperature is much more uniform and evenly distributed. This indicates that the vapour fuel in the fuel-rich region managed to entrain sufficient oxygen and thus the combustion reaction is similar across the entire flame. As a result, there is a small portion of OH formed in the fuel-rich region of Bu20 (800 K) in addition to the fuel-lean region. At  $t_3$ , the  $\text{CH}_2\text{O}$  for all cases remain at the upstream of the spray during the high-temperature combustion since a large amount of OH is generated downstream, which inhibits the penetration of  $\text{CH}_2\text{O}$  into the high-temperature region.



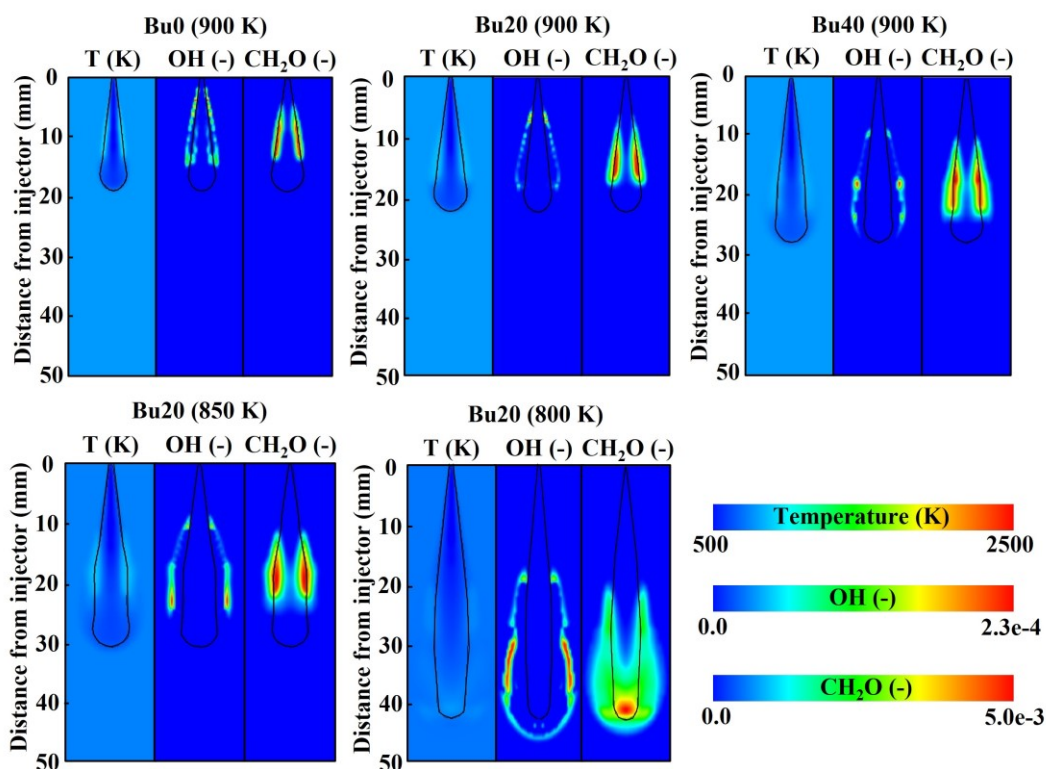


Figure 6-3: Predicted contours of temperature, OH and CH<sub>2</sub>O mass fractions for different test cases at  $t_1$ . Black line in the contour denotes the stoichiometric line.

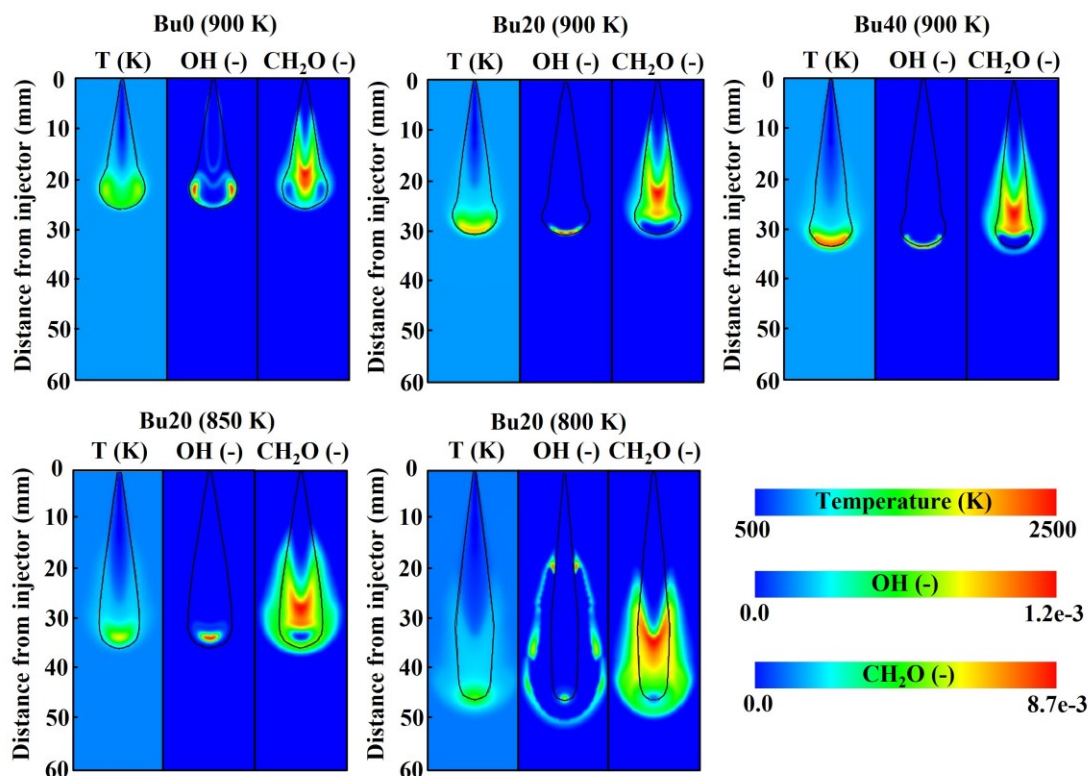


Figure 6-4: Predicted contours of temperature, OH and CH<sub>2</sub>O mass fractions for different test cases at  $t_2$ . Black line in the contour denotes the stoichiometric line.

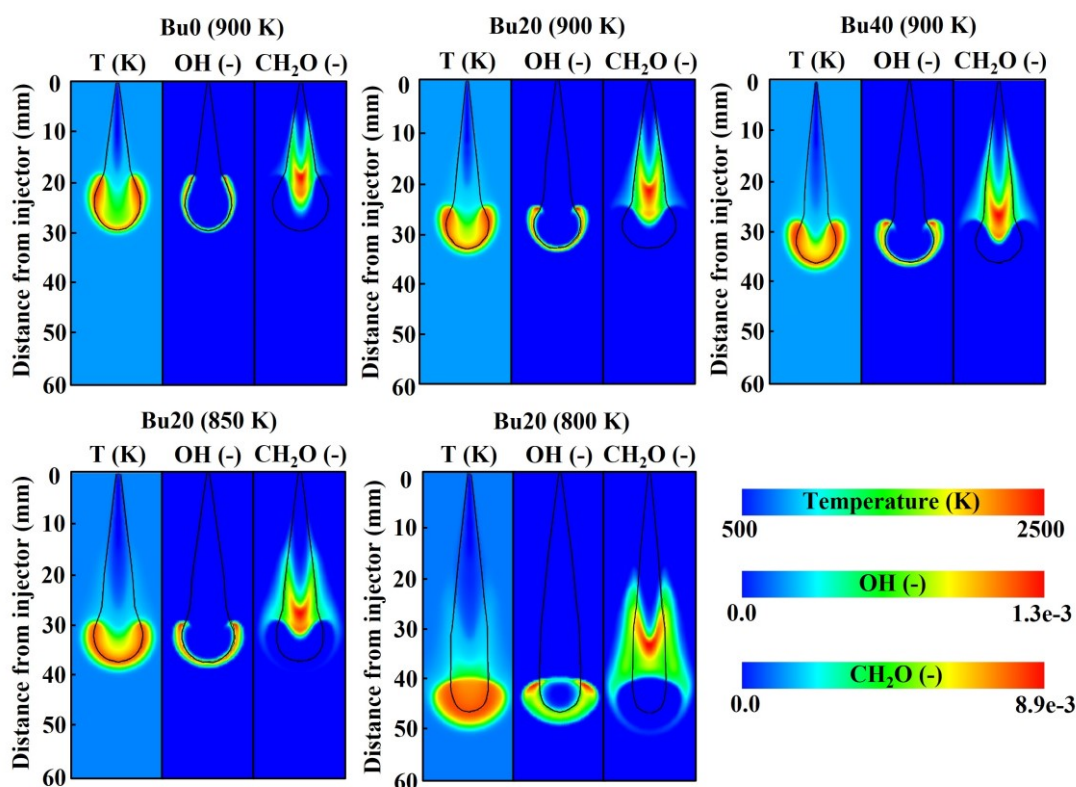


Figure 6-5: Predicted contours of temperature, OH and CH<sub>2</sub>O mass fractions for different test cases at  $t_3$ . Black line in the contour denotes the stoichiometric line.

With an aim to further investigate the oxidation of n-dodecane-n-butanol blend at various blending ratios and ambient temperatures, the mass fractions of key intermediate species such as OH, CH<sub>2</sub>O, HO<sub>2</sub> and H<sub>2</sub>O<sub>2</sub> are plotted across the main axis of the spray at  $t_1$ ,  $t_2$  and  $t_3$ , as shown in Figure 6-6 and Figure 6-7. The additional species of H<sub>2</sub>O<sub>2</sub> and HO<sub>2</sub> are studied here because the H<sub>2</sub>O<sub>2</sub> species plays a crucial role for the second-stage ignition and they are primarily formed through the combination of HO<sub>2</sub> species,  $\text{HO}_2 + \text{HO}_2 = \text{H}_2\text{O}_2 + \text{O}_2$  [245]. Subsequently, H<sub>2</sub>O<sub>2</sub> species is decomposed to form two OH species through the  $\text{H}_2\text{O}_2 = 2\text{OH}$  reaction and this resulted in a pool of OH species that accelerates the overall oxidation rate, which leads to a rapid rise in temperature during the second-stage ignition [245]. The HO<sub>2</sub> and H<sub>2</sub>O<sub>2</sub> species are thus considered as a precursor to ignition [247]. During the first-stage ignition at  $t_1$ , Figure 6-6 shows that the flame for all test cases is still weak and the OH mass fraction is lower than  $1\text{E}-03$ . Concurrently, CH<sub>2</sub>O is formed at the upstream of the spray close to the injector where cold liquid fuel is present. Among the test cases, the distribution and mass fraction of CH<sub>2</sub>O is the widest and the highest

for Bu20 (800 K) at  $t_1$ , which is due to the longer air-fuel mixing. The OH mass fraction is also the highest for Bu20 (800 K) at  $t_1$  because of the longer ID which causes a higher amount of cool flame to form as compared to the other cases. As the combustion progresses to  $t_2$  and subsequently to  $t_3$ , the  $\text{CH}_2\text{O}$  is being consumed by OH mainly through the reaction  $\text{CH}_2\text{O} + \text{OH} = \text{HCO} + \text{H}_2\text{O}$  as suggested by Zhu et al. [59] and the mass fraction of  $\text{CH}_2\text{O}$  starts to decrease at the location where OH is formed. It is noted that there are two OH peaks for Bu20 (800 K) at  $t_3$ . The first peak corresponds to the OH formation in fuel-rich region while the second peak is located at the leading edge of the flame. Besides, at the same initial temperature, a higher amount of OH is produced when the n-butanol blending ratio is higher. This could be attributed to the higher amount of oxygen content in the blend as n-butanol blending ratio increases, which promotes the OH formation during combustion. However, as the ambient temperature decreases, the flame temperature decreases and thus the OH formation also decreases. Furthermore, Figure 6-7 shows that the distributions of  $\text{HO}_2$  and  $\text{H}_2\text{O}_2$  are also located at the upstream of the spray similar to that of  $\text{CH}_2\text{O}$ . Generally, the location of the peak mass fractions for  $\text{HO}_2$  and  $\text{H}_2\text{O}_2$  species at  $t_1$  are in the similar order with the ID of the test cases prior to the first-stage ignition. As the duration of air-fuel mixing is extended, higher amount of fuel molecules undergo H atom abstraction to form  $\text{HO}_2$ , which then produces a higher amount of  $\text{H}_2\text{O}_2$ . Thereafter, the mass fractions of  $\text{HO}_2$  and  $\text{H}_2\text{O}_2$  further increase and remains at a steady value as the combustion progresses to  $t_2$  and  $t_3$ . Since  $\text{HO}_2$  and  $\text{H}_2\text{O}_2$  are precursors to ignition [247], they are not found at the downstream of the spray where the high-temperature flame will quickly consume those radical species for combustion [86].

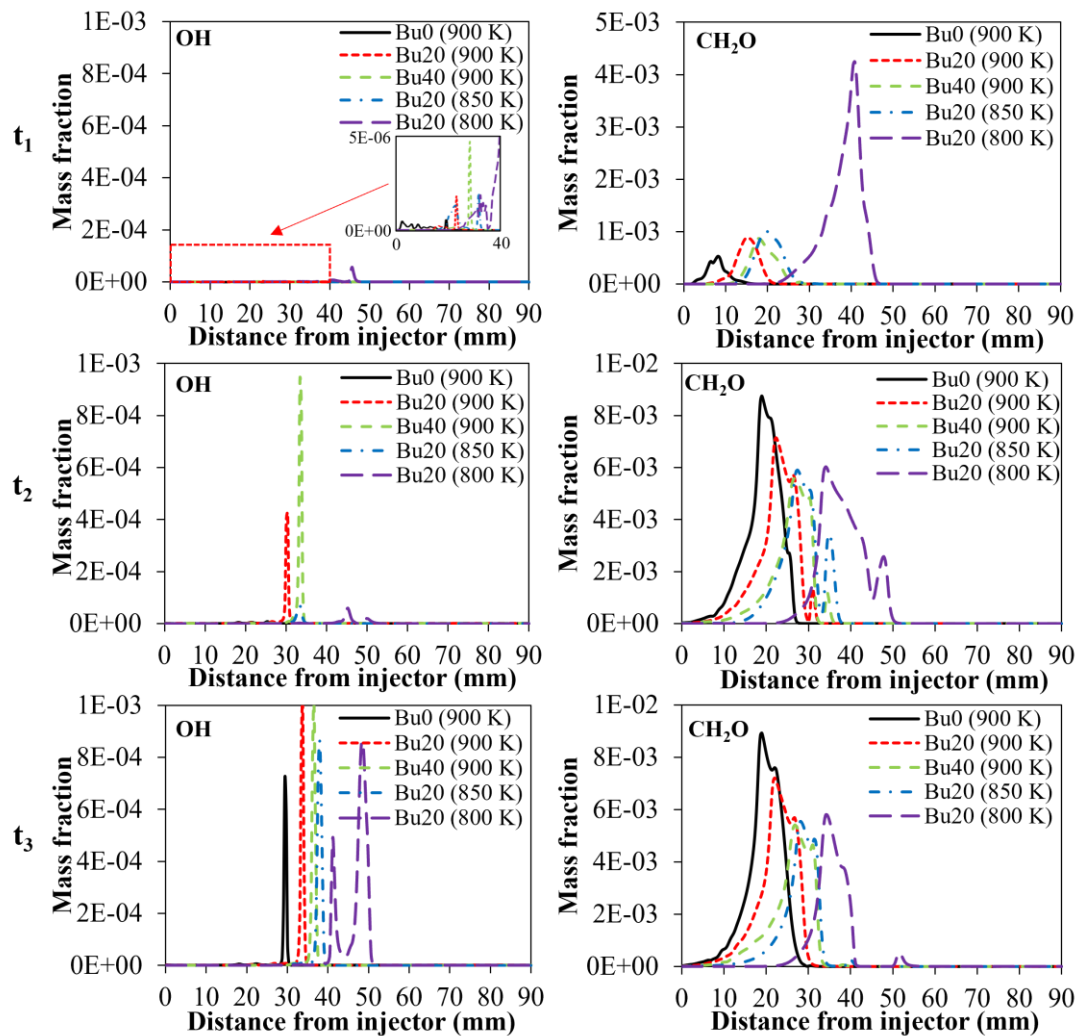


Figure 6-6: Predicted mass fraction profiles of OH and CH<sub>2</sub>O for different test cases along the centre spray axis at t<sub>1</sub> (first row), t<sub>2</sub> (second row) and t<sub>3</sub> (third row).

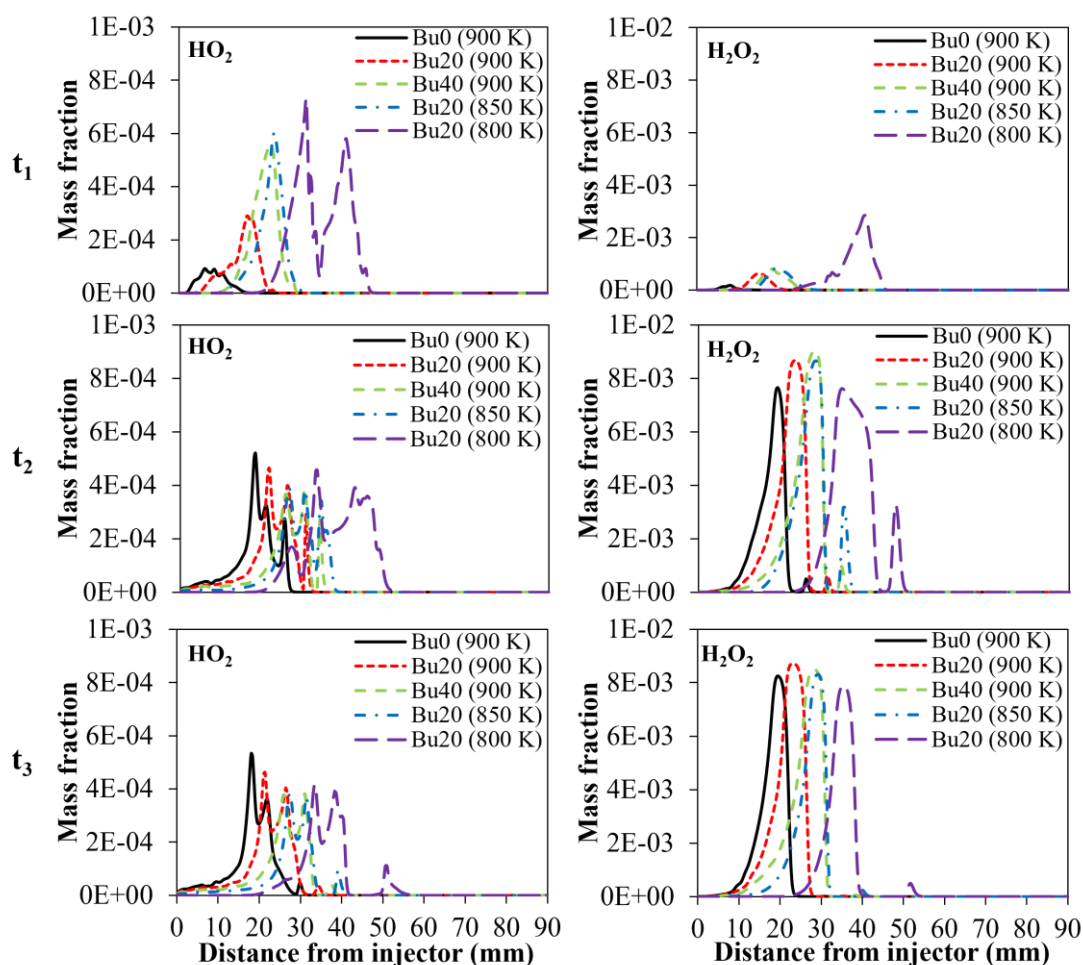


Figure 6-7: Predicted mass fraction profiles of  $\text{HO}_2$  and  $\text{H}_2\text{O}_2$  for different test cases along the centre spray axis at  $t_1$  (first row),  $t_2$  (second row) and  $t_3$  (third row).

#### 6.4 Transitioning to Quasi-Steady State

The flame evolution for n-dodecane-n-butanol blend at various n-butanol blending ratios and ambient temperatures from the auto-ignition stage up till quasi-steady state are presented in Figure 6-8, where the flame temperature is plotted against the mixture fraction space. The vertical black and red dash lines in Figure 6-8 are the stoichiometric and most reactive mixture fraction ( $Z_{\text{mr}}$ ) lines, respectively. The  $Z_{\text{mr}}$  is computed under 0D conditions in CHEMKIN-PRO and it is characterised as the mixture fraction that consists of the shortest ID [248,249]. According to Figure 6-8, it could be observed that the first-stage ignition at  $t_1$ , as denoted by the red scatter plots, occurs in the fuel-rich region for Bu0 (900 K) and moves towards fuel-lean region as the n-butanol blending ratio increases and as the ambient temperature decreases. While the combustion progresses to  $t_2$ , as denoted by the green scatter plots, it is observed

that the highest flame temperature for Bu0 (900 K), Bu20 (900 K) and Bu20 (850 K) are in the fuel-rich region. On the other hand, the highest flame temperature for Bu40 (900 K) and Bu20 (800 K) at  $t_2$  are located at the stoichiometric line. Nevertheless, once the flame reaches 3.0 ms, it stabilises and the highest flame temperature is located close to the stoichiometric line for all test cases. Besides, it could also be seen that the  $Z_{mr}$  occurs towards the fuel-lean region as n-butanol blending ratio increases and as ambient temperature decreases. This explains why the ignitions within the reacting spray tend to be shifted to the fuel-lean regions at higher n-butanol blending ratio and at lower ambient temperatures. From Figure 6-8, it is also noteworthy to mention that due to the differences in stoichiometric air-fuel ratio of the mixtures, the occurrence of overly fuel-rich mixture fraction ( $Z > 0.1$ ) within the flame is getting rarer at higher n-butanol blending ratio and lower ambient temperature.

During the flame evolution, Pei et al. [250] reported that there is a significant dilatation effect of the ambient air on the developing reacting spray. Therefore, in order to investigate the dilatational effect of the ambient air during combustion, Figure 6-9 shows the flame temperature contours for all cases that are overlapped with the velocity vectors, to illustrate the freestream velocity during the flame evolution. The first three timings in the flame temperature contours are the respective  $t_1$ ,  $t_2$  and  $t_3$  timings while the fourth and fifth timings are captured at 1.0 ms ASOI and 3.0 ms ASOI, respectively, for Bu0 (900 K), Bu20 (900 K) and Bu40 (900 K). Contrarily, the fourth and fifth timings of Bu20 (850 K) and Bu20 (800 K) are captured at 2.0 ms ASOI and 3.0 ms ASOI, respectively. At ambient temperature of 900 K, regardless of the n-butanol blending ratios, Figure 6-9 shows that the highest axial velocity is at the central axis of the spray jet. The ignition at  $t_1$  is initiated at the spray periphery and it can be noted that the velocity vectors start to diverge in that area due to the low-temperature combustion that causes the local pressure to increase. Subsequently, at  $t_2$ , the premixed combustion takes place and as a result, the intense burning from the premixed mixture causes the local pressure to further increase and the air in the vicinity of the spray head diverge even more. In the meantime, air entrainment is occurring at the upstream of the flame base and with the combination of the diverging flow at the downstream of the spray, an anti-clockwise vortex is created [250]. The magnitude of the vortex becomes higher at 1.0 ms ASOI as the high temperature flame

starts to expand in the axial and radial direction. At this time, the vortex is stronger and Pei et al. [250] suggested that these vortices are strong enough to carry the hot products and radicals from the downstream of the spray up to the flame base. This phenomena causes the cold upstream vapour fuel to ignite and shortens the FLOL. It is also interesting to observe that the vortex for Bu0 (900 K) is closer to the stoichiometric line where the highest temperature occurs whereas the vortex for Bu20 (900 K) and Bu40 (900 K) occur further outwards radially, towards to the leaner mixture side. As the intensity of the premixed combustion for Bu20 (900 K) and Bu40 (900 K) are higher, the sudden increase in local pressure causes the air nearby the spray to diverge outwards at a higher velocity and thus, the vortex is established at regions further away from the stoichiometric line. The high turbulence created by the vortex on the leaner mixture side then causes the flames of Bu20 (900 K) and Bu40 (900 K) to be marginally thicker than Bu0 (900 K) in the radial direction and also shifted the highest flame temperature to the fuel-lean region. Nevertheless, at 3.0 ms ASOI, the flame reaches quasi-steady state and the vortex moves downstream. This limits the vortex from carrying the hot products up to the flame base and therefore the flame stabilises at its FLOL. The stabilisation of FLOL can be further illustrated in Figure 6-10 where it first decreases and starts to maintain at a certain level as the spray duration approaches 3.0 ms ASOI.

Besides, Figure 6-9 also shows the dilatation effect on the flame evolution for Bu20 fuel at different ambient temperatures. The air flow pattern of Bu20 (850 K) and Bu20 (800 K) are very akin to those at Bu20 (900 K), where the premixed combustion causes the air close to the spray head to diverge. However, at  $t_3$ , comparing to Bu20 (900 K), the vortex at Bu20 (850 K) is more intense at the flame base. This leads to hot air entrainment by the cold vapours at the flame base and induces the high-temperature combustion. As a result, the high-temperature flame downstream is easier to propagate upwards towards the injector and join with the upstream cool flame. Similarly, the upstream vortex could be seen as early as  $t_2$  for Bu20 (800 K). The early vortex creation could be attributed to the longer ID and the turbulence created from the high velocity spray. It can also be observed that as the ambient temperature decreases, the vortex is located further outwards radially of the flame which causes the flame to be thicker.

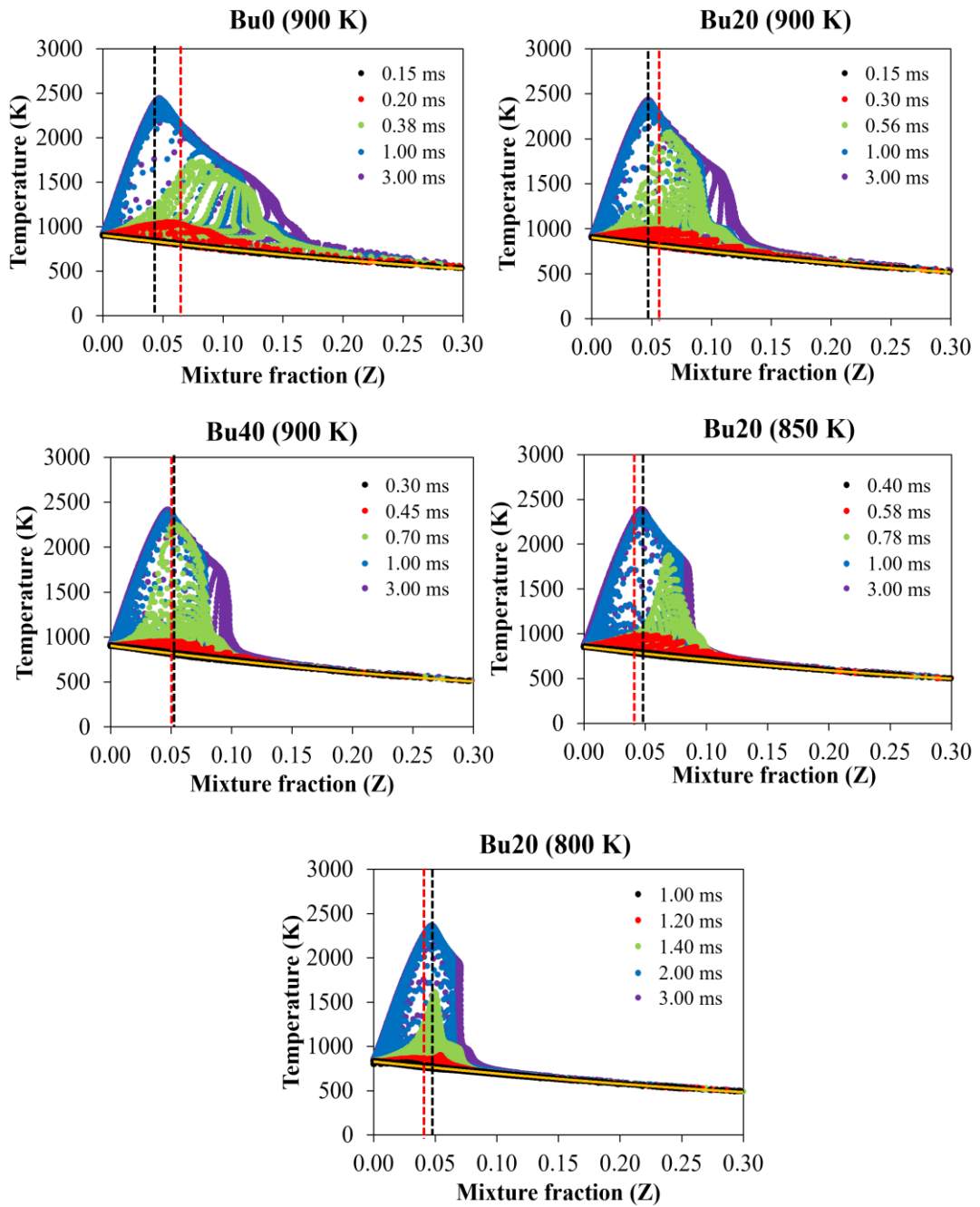


Figure 6-8: Temporal evolution of the temperature versus mixture fraction for different test cases. The vertical black and red dash line are the stoichiometric and  $Z_{mr}$  lines. The orange solid line is the adiabatic mixing line. The scatter plots legend are as follows: time prior to first-stage ignition (black),  $t_1$  (red),  $t_2$  (green), semi-developed flame (blue), quasi-steady flame (purple).



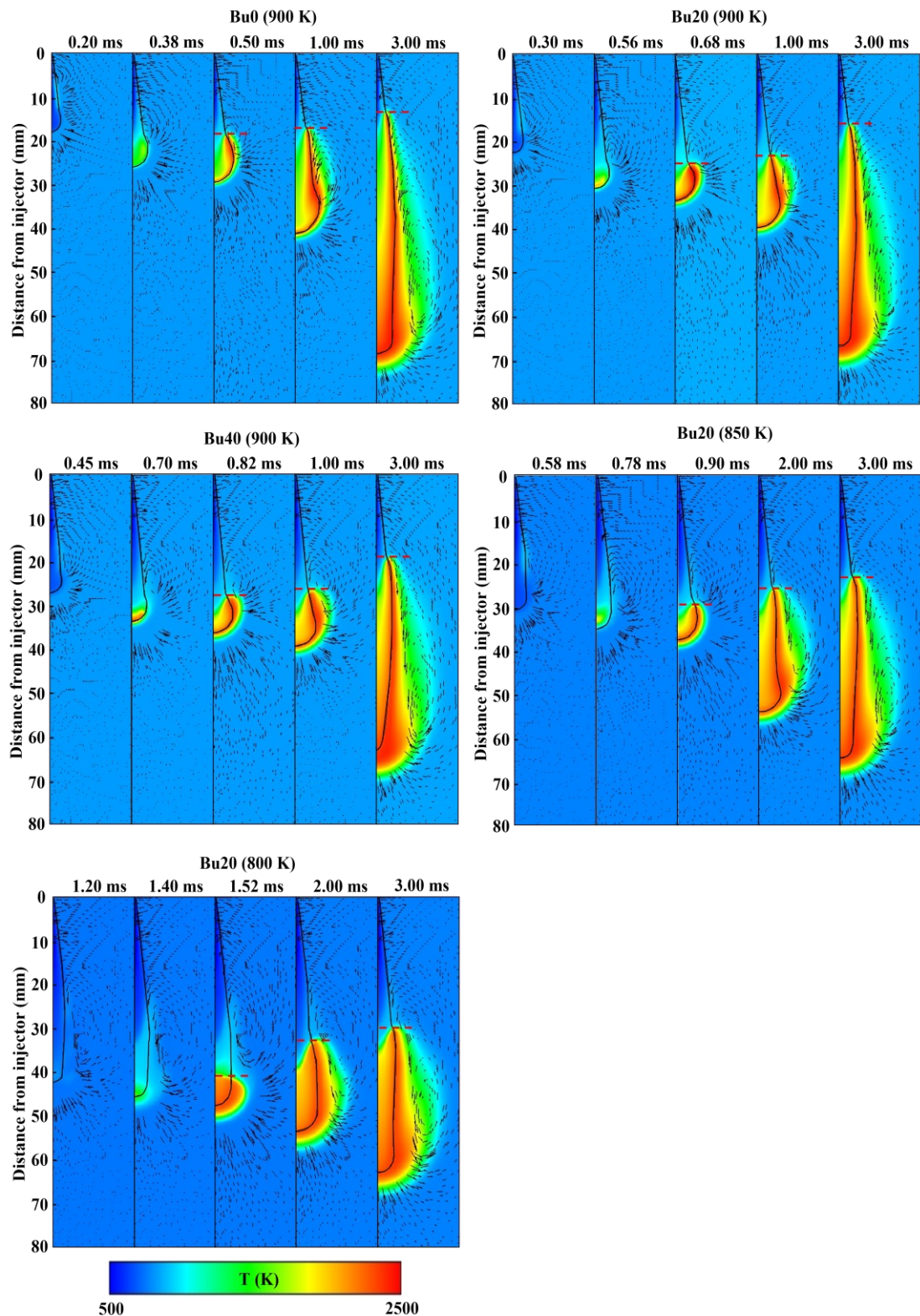


Figure 6-9: Temporal evolution of the flame overlapped with velocity vectors for different test cases. The black and red dash lines denote the stoichiometric line and FLOL, respectively.

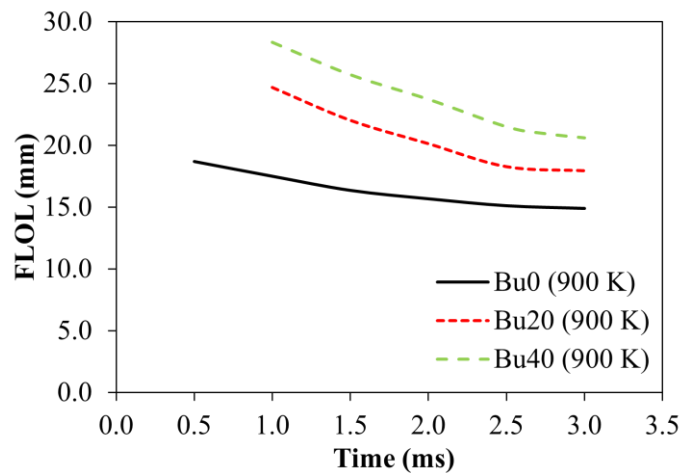


Figure 6-10: Temporal FLOL for the case of Bu0 (900 K), Bu20 (900 K) and Bu40 (900 K).

Furthermore, Figure 6-9 shows that the flame initially auto-ignites and then expands downstream but it is obvious that the rate of expansion is different among the test cases. The understanding of the rate of expansion or flame development rate is very helpful to problems related to flame impingement in diesel engine. As such, Figure 6-11 presents the computed axial flame development rate with respect to different n-butanol blending ratios and ambient temperatures. In order to calculate the flame development rate, the first axial location where the temperature exceeds 400 K relative to the initial temperature is determined as the flame front [250]. The flame development rate is then calculated by dividing the time period between two time-steps. From Figure 6-11, the flame development rate during the start of auto-ignition is high, reaching 330 m/s for Bu0 (900 K). As the cetane number of n-dodecane is higher than n-dodecane-n-butanol blends, auto-ignition occurs more rapidly for Bu0 (900 K) and the flame expands axially downstream at a faster rate. Nonetheless, the flame development rate is higher for Bu20 (850 K) and Bu20 (800 K) as compared to Bu20 (900 K) and this could be due to the longer duration of air-fuel mixing for Bu20 (850 K) and Bu20 (800 K), which consequently lead to a higher intensity of premixed combustion as the flame consumes the entire premixed charge rapidly. However, after 2.0 ms, the flame development rate for all test cases converge into a steady value as the flame is now at the diffusion combustion stage and is limited by the rate of air-fuel mixing. At this stage, the difference in flame development rate for all test cases is only marginal where it fluctuates within a certain range which then signifies that the

combustion behaviour of the n-dodecane-n-butanol diffusion flame is very similar regardless of the n-butanol blending ratio and ambient temperature.

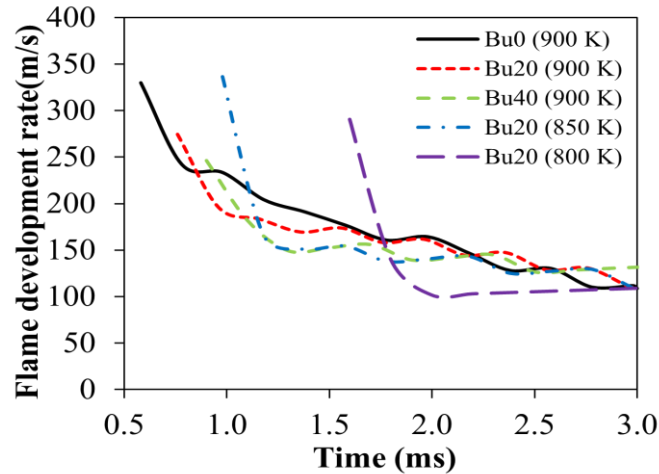


Figure 6-11: Predicted axial flame development rate for different test cases.

## 6.5 Quasi-Steady Flame

In this section, the effects of n-butanol blending ratio and ambient temperature on the quasi-steady flame structure of n-dodecane-n-butanol blend are investigated. The quasi-steady state here means that the changes in species and other properties such as temperature are very slow such that it can be considered to be constant. The contours of mixture fraction, flame temperature, mass fractions of OH, CH<sub>2</sub>O, HO<sub>2</sub>, H<sub>2</sub>O<sub>2</sub> and CO for various cases are depicted in Figure 6-12. The black line in Figure 6-12 represents the stoichiometric mixture fraction line. From Figure 6-12, the high-temperature combustion zone shrinks and the peak flame temperature is reduced at higher n-butanol blending ratio and at lower ambient temperature, which is due to the higher latent heat of n-butanol and the lower overall reactivity of the flame at lower ambient temperature. Besides, Figure 6-12 also shows that the OH species is mainly formed at the periphery of the flame close to the stoichiometric line where the flame temperature is the highest. In contrast, the distributions of CH<sub>2</sub>O, HO<sub>2</sub> and H<sub>2</sub>O<sub>2</sub> are mostly located in the upstream fuel-rich region of the spray for all test cases. CO is also located in the fuel-rich region of the spray but it could be seen that its distribution is getting smaller as n-butanol blending ratio increases and as ambient temperature decreases due to the increase in oxygen caused by the longer duration of air-fuel

mixing. Additionally, Figure 6-13 presents the scatter plots of the mass fractions of OH, CH<sub>2</sub>O, HO<sub>2</sub> and H<sub>2</sub>O<sub>2</sub> in the temperature – mixture fraction space. In Figure 6-13, only points in the computational domain that are higher than 40% of the respective peak mass fractions are plotted [248]. The vertical line represents the stoichiometric mixture fraction line. According to Figure 6-13, the OH species is found to be present only at temperatures above 2000 K and is close to the stoichiometric line. In spite of that, the distribution of OH species is shifted slightly to the leaner mixture side at higher n-butanol blending ratio and at lower ambient temperature. Meanwhile, the mass fractions of CH<sub>2</sub>O, HO<sub>2</sub> and H<sub>2</sub>O<sub>2</sub> are distributed over a wide range of fuel-rich mixture fractions and at ambient temperatures below 2000 K. During the high-temperature combustion, the CH<sub>2</sub>O and HO<sub>2</sub> species are consumed and thus they are not found at temperatures above 2000 K. Likewise, the H<sub>2</sub>O<sub>2</sub> species, which decomposes to form two OH radicals for the high-temperature combustion [245], is consumed and is not found at temperatures above 1750 K. With the increase in ID and the enhancement in air-fuel mixing at higher n-butanol blending ratio and at lower ambient temperature, the excess oxygen entrained by the vapour fuel shifts the formation of CH<sub>2</sub>O, HO<sub>2</sub> and H<sub>2</sub>O<sub>2</sub> to the fuel-lean region. Although the OH species distribution is also slightly shifted to the fuel-lean region at higher n-butanol blending ratio and lower ambient temperature, the effect is more pronounced for the distributions of CH<sub>2</sub>O, HO<sub>2</sub> and H<sub>2</sub>O<sub>2</sub> species. This indicates that the low-temperature combustion region of the quasi-steady n-dodecane-n-butanol flame is being influenced more significantly than the high-temperature combustion region at different n-butanol blending ratios and ambient temperatures.

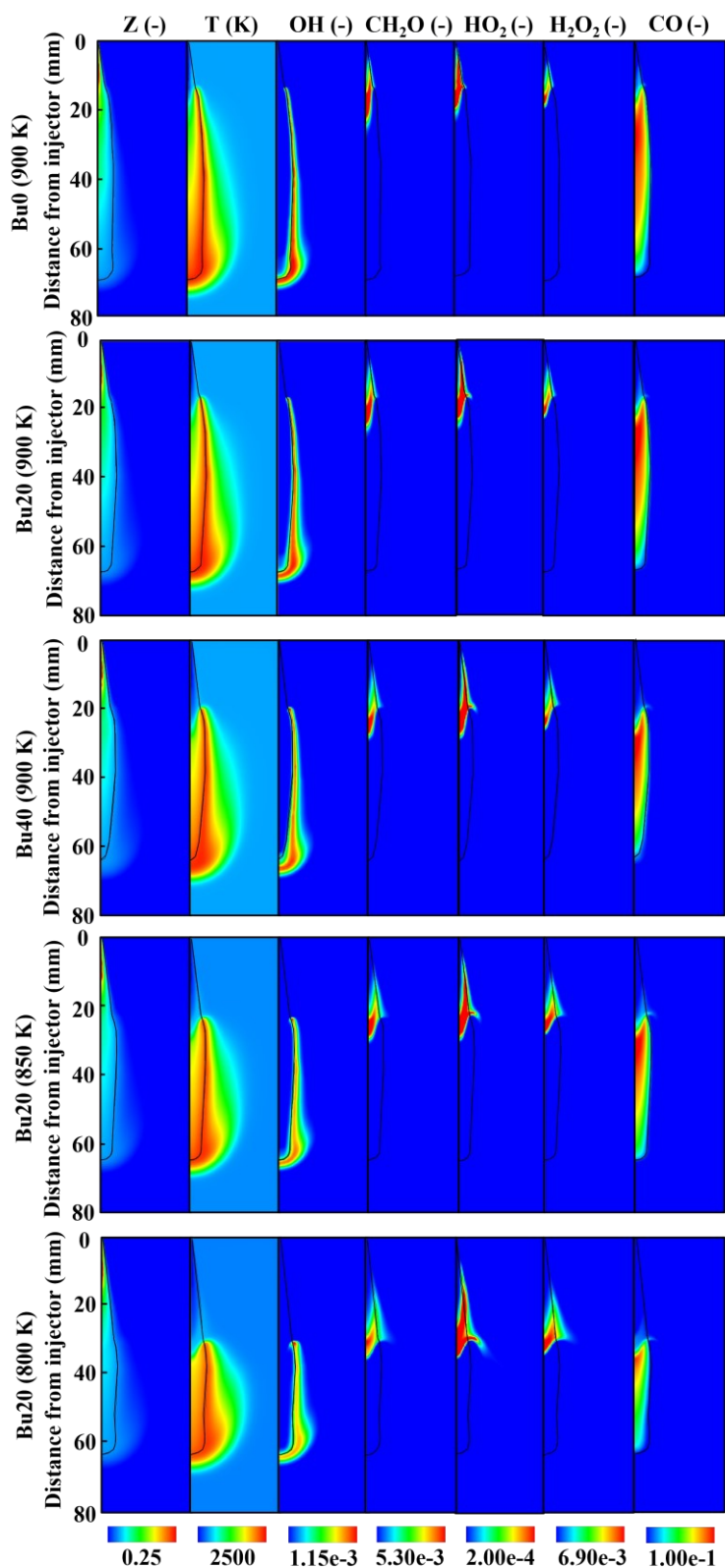


Figure 6-12: Predicted contours of mixture fraction, flame temperature, OH, CH<sub>2</sub>O, HO<sub>2</sub>, H<sub>2</sub>O<sub>2</sub> and CO at quasi-steady state for different test cases. The maximum value of the colour contour is listed in the corresponding colour bar while the minimum value is 500 K for temperature and zero for the mixture fraction and mass fractions.

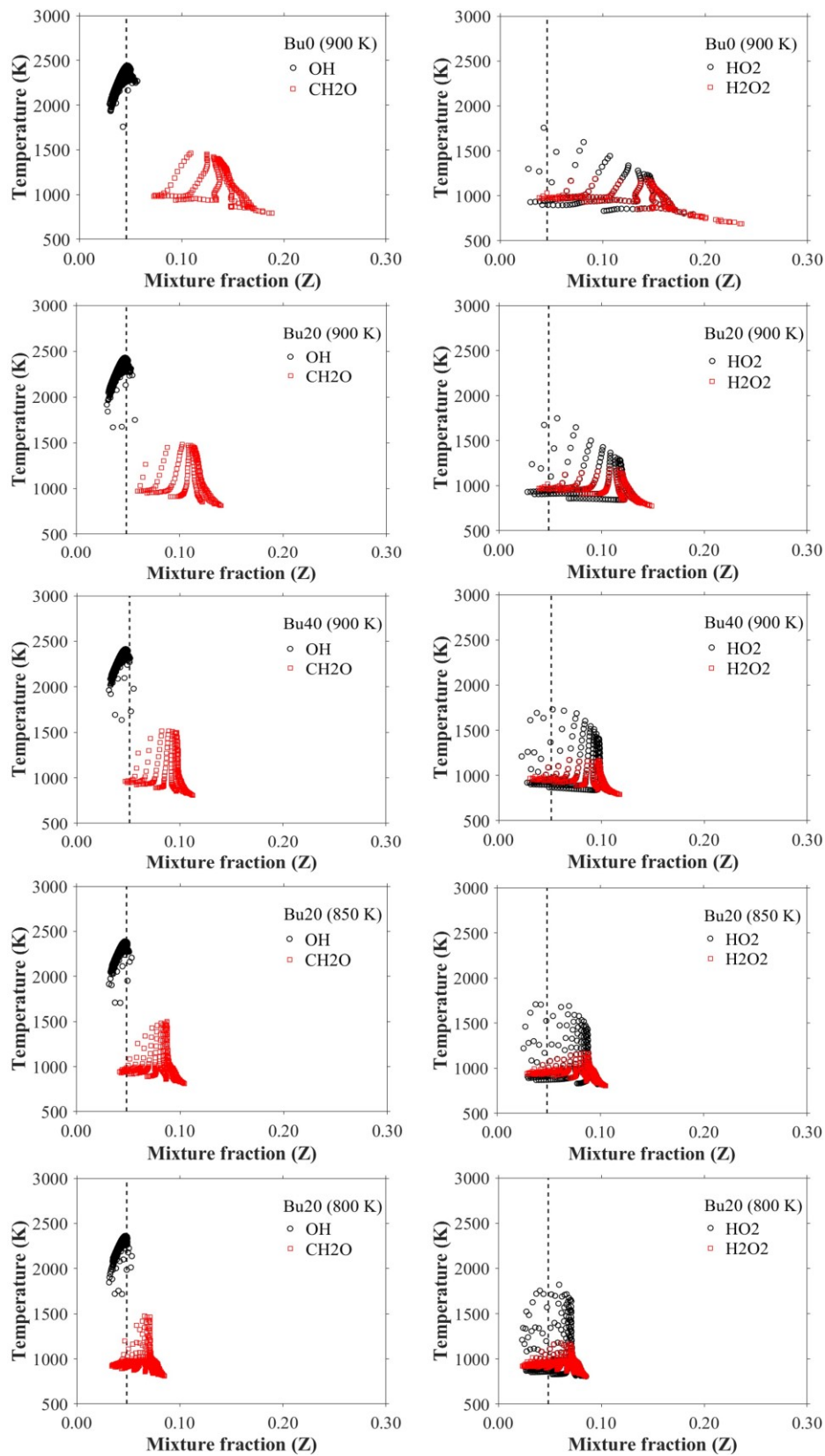


Figure 6-13: Maps of OH, CH<sub>2</sub>O, HO<sub>2</sub> and H<sub>2</sub>O<sub>2</sub> mass fractions onto the temperature versus mixture fraction space at quasi-steady state for different test cases. Vertical dash line is the stoichiometric mixture fraction line.

## 6.6 Combustion Mode Analysis

The ignition of n-dodecane and n-dodecane-n-butanol blend exhibited a two-stage ignition, as discussed previously. When the flame reaches quasi-steady state, the FLOL stabilises at a distance away from the injector and the flame comprises of spatially separated regions of low-temperature combustion/cool flames, premixed burning and non-premixed flame [245,246,251]. The identification of these combustion modes is beneficial to the understanding of pollutant formation and other intermediate species within the reacting flame [86]. Nevertheless, since experimental investigations are mostly limited by the spatial and temporal resolution, signal attenuation and the difficulties in recording weak emitting minor species, Krisman et al. [251] adopted the numerical approach to identify the different types of combustion modes with the aid of key species markers. Here,  $\text{CH}_2\text{O}$  and  $\text{OH}$  are selected as species markers to distinguish the different combustion modes in n-dodecane-n-butanol flame and the three main combustion modes are classified as follows [251]:

- M-LTC – region of the low-temperature combustion and is closely associated to the first-stage ignition and the appearance of cool flame. It is defined as:  $Y_{\text{CH}_2\text{O}} > Y_{\text{CH}_2\text{O}|\text{CRIT}}$ .
- M-HTC – region of the high-temperature combustion. It is defined as:  $Y_{\text{CH}_2\text{O}} < Y_{\text{CH}_2\text{O}|\text{CRIT}} \cap Y_{\text{OH}} < Y_{\text{OH}|\text{CRIT}}$ .
- M-HTC-diff – region of high-temperature combustion with the non-premixed flame concentration on the stoichiometric plane. This mode is defined as:  $Y_{\text{OH}} > Y_{\text{OH}|\text{CRIT}}$ .

where the  $Y_{\text{CH}_2\text{O}}$  and  $Y_{\text{OH}}$  are the mass fractions of  $\text{CH}_2\text{O}$  and  $\text{OH}$ , respectively, while the critical values adopted here are 5% of their respective maximum mass fraction value [251].

Figure 6-14 shows the temporal evolution of the fuel spray and the combustion modes for Bu0 (900 K), Bu40 (900 K) and Bu20 (800 K), with their corresponding HRR profile. The blue, green and red regions highlighted in the HRR profile are the stages for first-stage ignition, second-stage ignition and diffusion combustion, respectively. The left frame of the contours is the vapour fuel while the colour dots are the liquid particles. On the right frame, the blue, green and red coloured contours

denote the M-LTC, M-HTC and M-HTC-diff modes, respectively. The magenta and yellow dash lines for both frames are the stoichiometric and  $Z_{mr}$  lines, respectively. According to Figure 6-14, it could be seen that prior to the first-stage ignition, the M-LTC mode is weak for Bu0 (900 K) and Bu40 (900 K). However, due to the longer ID and air-fuel mixing process, a wide distribution of M-LTC mode is already present for Bu20 (800 K) at 1.0 ms, which also indicates that a large amount of cool flame is already present at that time. The M-LTC mode for Bu20 (800 K) is also concentrated at the fuel-lean region which corroborated the earlier findings that the first-stage ignition of Bu20 (800 K) is at the fuel-lean region. At the first-stage ignition, as seen from the first peak of the HRR, the amount of cool flame for Bu40 (900 K) and Bu20 (800 K) further increases and the M-LTC mode starts to penetrate into the fuel-rich region. However, the cool flame for Bu0 (900 K) is still weak and is concentrated at the spray periphery close to the stoichiometric line. Nevertheless, there are still no sign of M-HTC mode at the first-stage ignition for all cases. In the course of the second-stage ignition, the appearance of M-HTC mode is observed at the spray periphery for Bu0 (900 K) whereas it is located the spray head for Bu40 (900 K) and Bu20 (800 K). This phenomena is attributed to the higher latent heat of Bu40 (900 K) and Bu20 (800 K) which induces a higher evaporative cooling effect at regions near the LPL. As such, the lower temperatures at the spray periphery surrounding the LPL inhibits ignition from occurring. Contrarily, the vapour fuel that is at the uttermost downstream of the spray manages to undergo air-fuel mixing with the hot ambient air and thus ignition occurs at the spray head. Furthermore, in Figure 6-14, the presence of the M-HTC-diff mode is also seen close to the stoichiometric line where the flame temperature is the highest. Interestingly, a small amount of M-HTC mode is also observed at the flame base of Bu20 (800 K) and throughout the entire spray periphery. This is mainly due to the higher amount of cool flame accumulated prior to the second-stage ignition which then makes it easier for the well homogeneous air-fuel mixture that is closer to the ambient surroundings to ignite when the high-temperature combustion occurs at the downstream of the spray. Besides, the hot combustion products that are carried upstream by the vortex further increases the tendency of the high-temperature combustion of the upstream cool flame. Nevertheless, from Figure 6-14, once the high-temperature flame kernels are formed, the flame starts to enter the diffusion



combustion stage where the burning is controlled by air-fuel mixing instead of chemical kinetics. Accordingly, the regions that are previously dominated by the M-LTC mode prior to the second-stage ignition are slowly being replaced by the M-HTC mode. Consequently, the M-LTC mode moves upstream and remains there for the remaining combustion period. At the diffusion combustion stage, it can be seen that the distribution of the M-HTC mode is wider for Bu40 (900 K) and Bu20 (800 K) as compared to Bu0 (900 K), especially in the fuel-rich region. This could be due to the premixed combustion of the combustible mixture during the second-stage ignition because it is very unlikely for the cooler vapour fuel in the fuel-rich region to entrain fresh air for any subsequent combustion at the diffusion combustion stage. This explanation is also reasonable because the amount of premixed mixture formed by Bu40 (900 K) and Bu20 (800 K) is higher than Bu0 (900 K) due to longer ID. As a result, there is a possibility that the premixed combustion of Bu40 (900 K) and Bu20 (800 K) lasted until the diffusion combustion stage. On the other hand, the ID for Bu0 (900 K) is shorter and the amount of premixed mixture formed is lower. Therefore, the premixed combustion of Bu0 (900 K) could have ended by the time the flame enters the diffusion combustion stage. Nonetheless, after all the remaining unburned premixed mixture has been consumed, the M-HTC of Bu40 (900 K) and Bu20 (800 K) moves closer to the stoichiometric line and it remains at large in the fuel-lean region where the  $Z_{mr}$  is located.

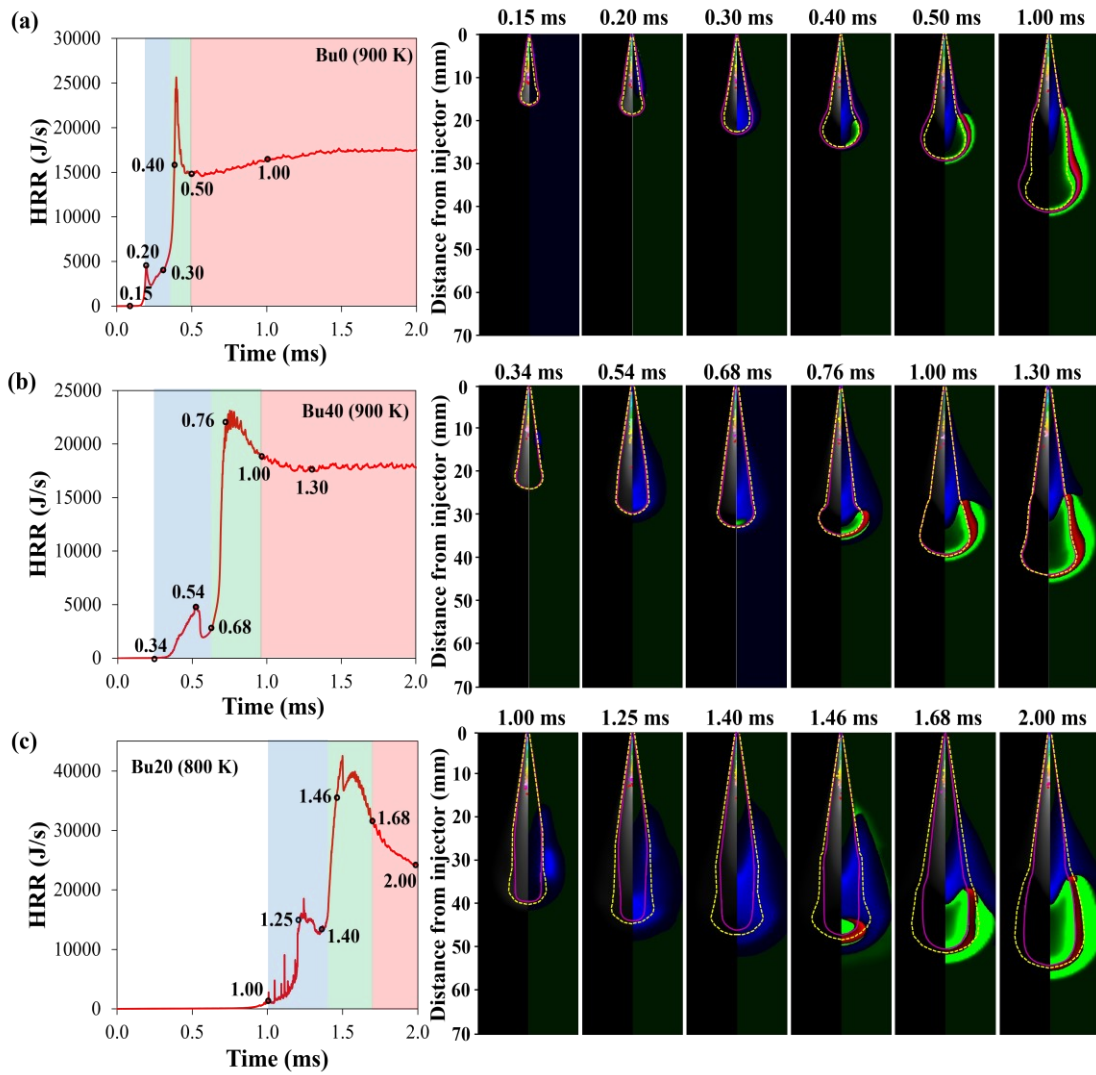


Figure 6-14: Evolution of combustion modes for (a) Bu0 (900 K), (b) Bu40 (900 K) and (c) Bu20 (800 K) with the corresponding HRR profile on the left.

## 6.7 Concluding Remarks

The ignition, combustion and flame characteristics of n-dodecane-n-butanol at various n-butanol blending ratios and ambient temperatures are studied in this chapter. Results show that n-dodecane-n-butanol blends undergo a two-stage ignition regardless of n-butanol blending ratio and ambient temperature. The first-stage ignition site is located at the spray periphery for all test cases except for Bu20 at 800 K. However, the second-stage ignition site moves to the spray head for all test cases but it remains at the spray periphery for Bu0. The mass fractions of  $\text{CH}_2\text{O}$ ,  $\text{OH}$ ,  $\text{HO}_2$  and  $\text{H}_2\text{O}_2$  species at quasi-steady state are also slightly shifted to the fuel-lean region at higher n-butanol blending ratio and lower ambient temperature. Furthermore, the longer ID at higher n-butanol blending ratio and lower ambient temperature leads to a wider distribution of the M-LTC mode. Meanwhile, the M-HTC and M-HTC-diff modes appear and are dominant from the second-stage ignition onwards. Overall, the work from this chapter extends the fundamental knowledge on the spray combustion of n-dodecane-n-butanol blend from the aspect of its ignition, combustion and flame characteristics.

# CHAPTER 7

## SOOT MODELLING OF N-DODECANE- N-BUTANOL SPRAY

### 7.1 Introductory Remarks

By using the same test cases in Chapter 6, the soot modelling study of n-dodecane-n-butanol blends at various n-butanol blending ratios and ambient temperatures are reported in this chapter. Section 7.2 first presents the transient SVF and soot particle size of the test cases. Subsequently, the temporal evolution of soot intermediate species are simulated and analysed in Section 7.3. Section 7.4 then shows the normalised results for the SVF, particle size and intermediate species among the test cases. The quasi-steady spatial distributions of soot and its intermediate species are presented in Section 7.5 while Section 7.6 shows the quasi-steady soot particle size and number density. The soot relevant rates of the test cases at quasi-steady state are further discussed in Section 7.7. Lastly, the results from this chapter are summarised in Section 7.8.

### 7.2 Transient SVF and Soot Particle Size

Figure 7-1 shows the temporal evolution of the SVF for the test cases at times of ID + 0.5 ms, ID + 1.0 ms and 3.0 ms to represent early soot formation, semi-developed soot and quasi-steady soot, respectively. The selection of timings here with respect to the ID of the case is similarly adopted by Wakale et al. [88] in their soot modelling study. This is because soot is only formed after combustion and there are certain cases where the ID is longer than 0.5 ms. Nevertheless, at 3.0 ms, all test cases have reached quasi-steady state since the changes in FLOL, species and other properties such as temperature are very slow that it is considered as constant.

From Figure 7-1(a), at time ID + 0.5 ms, the SVF for all test cases are generally lower than 0.2 ppm. Meanwhile, the soot onset location is in the ascending order of Bu0 (900 K), Bu20 (900 K), Bu40 (900 K), Bu20 (850 K) and Bu20 (800 K) and this trend is consistent with the ID times where they are at 0.35 ms, 0.50 ms, 0.70 ms, 0.86 ms and 1.38 ms, respectively [252]. However, as the combustion progresses, Figure

7-1 (b) shows the soot moves downstream due to the flame propagation. At this time, the SVF for all test cases increase while the soot cloud also enlarges in size, in which Pandurangi et al. [253] and Wakale et al. [88] also report similar findings. Nonetheless, it could be observed that the peak SVF and the soot cloud size increase at a slower rate for cases with higher n-butanol blending ratio and lower ambient temperature. Figure 7-1(c) further shows the quasi-steady SVF at 3.0 ms and it could be seen that the predicted peak SVF for Bu0 (900 K) is in good agreement with the experimental measurements [70,240]. Comparing among the test cases at 3.0 ms, the SVF and soot cloud size are the highest and largest for Bu0 (900 K) followed by Bu20 (900 K), Bu20 (850 K), Bu40 (900 K) and Bu20 (800 K). Additionally, the transient soot particle size for the test cases are shown in Figure 7-2 where the particles are assumed to be mono-dispersed and spherical in shape [130]. They are being computed using the equation from Vishwanathan and Reitz [239]. According to Figure 7-2(a), at time ID + 0.5 ms, the maximum soot particle size among the test cases is between 2.5 nm to 5 nm. However, as the combustion progresses, the soot particle size increases and moves downstream, as can be seen in Figure 7-2(b) and (c). At 3.0 ms, the predicted peak soot particle size is around 12 nm for Bu0 (900 K) and this is in the similar order as those recorded under the Spray A condition, where the mean diameter of the soot particle is between 8.8 nm and 11.2 nm [70]. On the contrary, the case of Bu20 (800 K) consists of the smallest peak soot particle size at only 4 nm. The location of the maximum soot particle size for the test cases at 3.0 ms is similar with the location where the maximum SVF occurs. Altogether, the trends of soot particle size predicted here are in qualitative agreement with the spray combustion simulation results of Vishwanathan and Reitz [239] and the conceptual model by Dec [2], where the size of the particle increases in the reacting jet, reaches a maximum and decreases in the flame front.

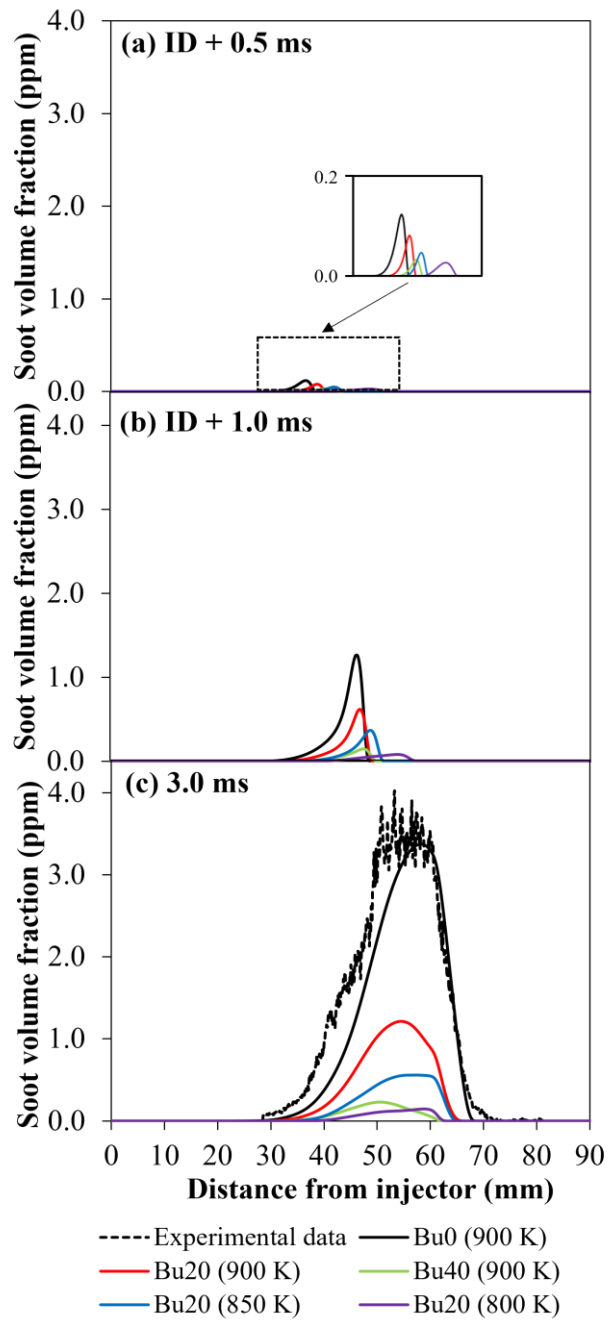


Figure 7-1: Predicted transient SVF for the test cases across the spray axis at (a) ID + 0.5 ms, (b) ID + 1.0 ms and (c) 3.0 ms. The experimental data is for Bu0 fuel at ambient temperature of 900 K.

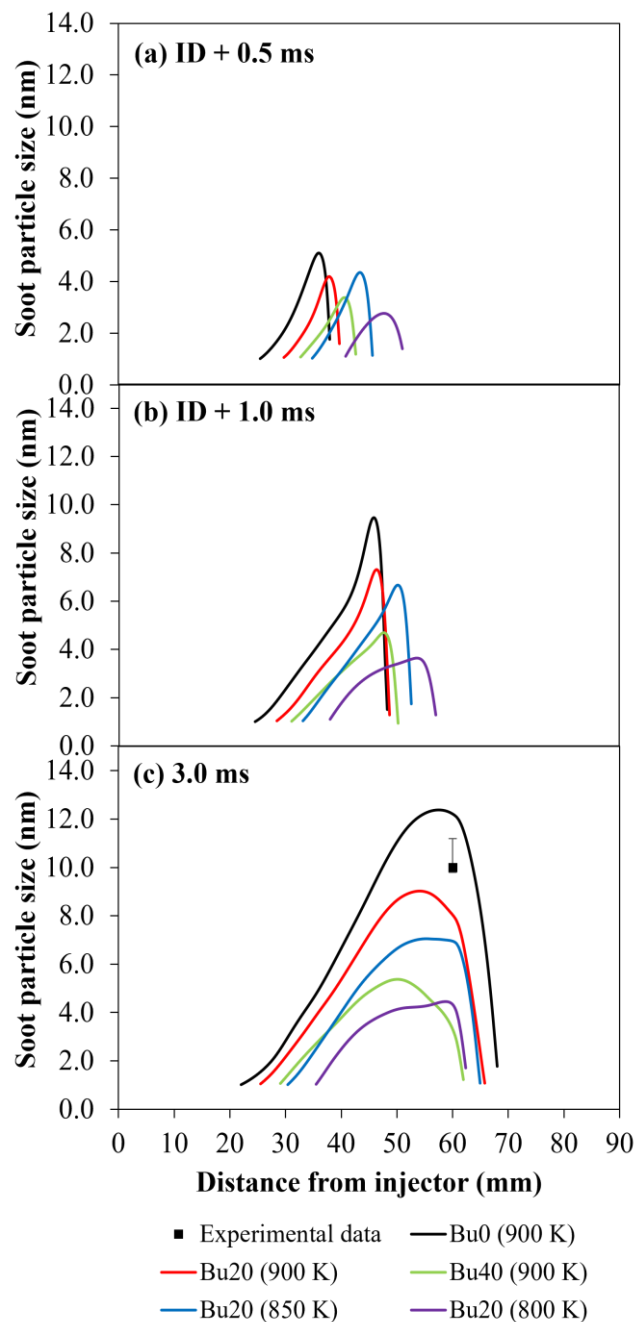


Figure 7-2: Predicted transient soot particle size for the test cases across the spray axis at (a) ID + 0.5 ms, (b) ID + 1.0 ms and (c) 3.0 ms. The experimental data is for Bu0 fuel at ambient temperature of 900 K.

### 7.3 Temporal Evolution of Soot Intermediate Species

In order to further investigate the effects of n-butanol blending ratio and ambient temperature on the evolution of soot intermediate species, the computed temporal mass fraction profiles for  $A_1$ ,  $A_4$ ,  $C_2H_2$  and OH are shown in Figure 7-3 to

Figure 7-6.  $A_1$  and  $A_4$  are considered as PAH species and they are mainly formed through the combination of smaller soot precursor species which is created during the fuel pyrolysis process [137]. Contrarily,  $C_2H_2$  supports the growth of PAH species through the HACA mechanism [140,141]. Therefore,  $A_1$ ,  $A_4$  and  $C_2H_2$  are considered as soot precursor species which are responsible for the soot formation. On the contrary, OH is a very reactive radical species that could promote soot oxidation and helps in reducing soot [87].

According to Figure 7-3(a), at time ID + 0.5 ms, the formation of  $A_1$  species is located at the furthestmost upstream for Bu0 (900 K) followed by Bu20 (900 K), Bu40 (900 K), Bu20 (850 K) and Bu20 (800 K). However, at times ID + 1.0 ms and 3.0 ms, as shown in Figure 7-3(b) and Figure 7-3(c), respectively, the distribution of  $A_1$  species for all test cases enlarges in size. Nevertheless, it can be seen that the distribution of  $A_1$  species enlarges at the fastest rate for Bu0 (900 K) and slowest for Bu20 (800 K) in which this results are consistent with the study of Zhou et al. [83]. Meanwhile, Figure 7-4 shows that  $A_4$  species is formed slightly more downstream as compared to  $A_1$  species where the studies by Bolla et al. [237] and Pang et al. [93] also similarly obtained this trend. The location of  $A_4$  species formation for the test cases exhibit similar trends with the  $A_1$  species at time ID + 0.5 ms, as shown in Figure 7-4(a). Subsequently, Figure 7-4(b) and Figure 7-4(c) show that at times ID + 1.0 ms and 3.0 ms, the distribution of  $A_4$  species also enlarges as the flame propagates downstream. It should be noted that the  $A_4$  mass fraction for Bu20 (800 K) at time ID + 0.5 ms is lower than  $1E-9$  and thus no trace of  $A_4$  mass fraction can be seen in Figure 7-4(a). However, even at time 3.0 ms, the mass fraction of  $A_4$  for Bu20 (800 K) is still low and is around two orders magnitude lower than Bu20 (850 K). Furthermore, Figure 7-5 shows that the mass fraction of  $C_2H_2$  is the highest for Bu0 (900 K) while the lowest for Bu20 (800 K). The distribution of  $C_2H_2$  for all test cases also closely follow those of the  $A_4$  species and this is because the  $C_2H_2$  species plays a crucial role for the formation of larger PAH species and is considered as a precursor for  $A_4$  species [140,141]. Nonetheless, from Figure 7-3 to Figure 7-5, it could be observed that the formation of soot precursor species are lower for cases with higher n-butanol blending ratio and at lower ambient temperature. Since n-butanol is an oxygenated fuel, the oxygen atom in n-butanol is able to bond with the carbon atom in n-dodecane to form



C–O bond [254]. However, these C–O bonds are not further broken down and as a result there is one less carbon atom in n-dodecane fuel to produce soot precursor [254]. In other words, the carbon atom in n-dodecane fuel, that is capable of producing soot precursor species, is being removed through the combination with the oxygen atom in n-butanol to form C – O bond. Consequently, the mass fractions of the soot precursor species such as  $A_1$ ,  $A_4$  and  $C_2H_2$  decrease at higher n-butanol blending ratio. Moreover, as the ambient temperature decreases, the energy surrounding the fuel spray also decreases, which leads to poor evaporation of the fuel from liquid to vapour phase. This results in a longer air-fuel mixing duration and the combustible mixture is diluted with more air that was entrained by the vapour fuel. Therefore, the combustion reaction is slowed down and the flame temperature decreases. This reduces the formation of soot precursor species because the lower flame temperature generates a lower amount of energy that is insufficient to break the fuel molecule apart for the production of soot precursor species [83].

Figure 7-6 shows the predicted OH mass fraction for all test cases. It should be noted that since the OH mass fraction here is computed across the spray axis, the peak OH mass fraction corresponds to the flame front, where the highest flame temperature is located. Based on Figure 7-6(a), at time ID + 0.5 ms, it could be seen that the peak OH is located at the most upstream for Bu0 (900 K) and followed by Bu20 (900 K), Bu40 (900 K), Bu20 (850 K) and Bu20 (800 K). This trend is in the similar order as the ID for the respective test cases. However, Figure 7-6(c) shows that at 3.0 ms, the location of the peak OH is in a completely opposite order as compared to at the time of ID + 0.5 ms. In a study by Pei et al. [250], they have suggested that the spontaneous ignition of the propagating flame front is according to the gradients of ID. As such, the above situation could be due to the higher cetane number of pure n-dodecane as compared to n-dodecane-n-butanol blends which leads to lower ID times and thus the sequential auto-ignition downstream is more intensive and this resulted in faster flame propagation. Meanwhile, with the collective contribution of the lower cetane number at higher n-butanol blending ratio and the lower combustion reaction at lower ambient temperature, the flame propagation of Bu20 (800 K) is the slowest among the test cases and thus the peak OH appears to be furthest upstream at 3.0 ms. Besides, it can also be seen in Figure 7-6(a) that initially at time ID + 0.5 ms, the OH mass fraction

of n-dodecane-n-butanol blends are higher than pure n-dodecane due to the promotion of OH species by the oxygen atom in n-butanol [8]. However, owing to the lower latent heat of vaporisation of pure n-dodecane, the temperature of the fully developed flame is the highest for Bu0 (900 K) and this leads to a higher OH mass fraction at 3.0 ms.

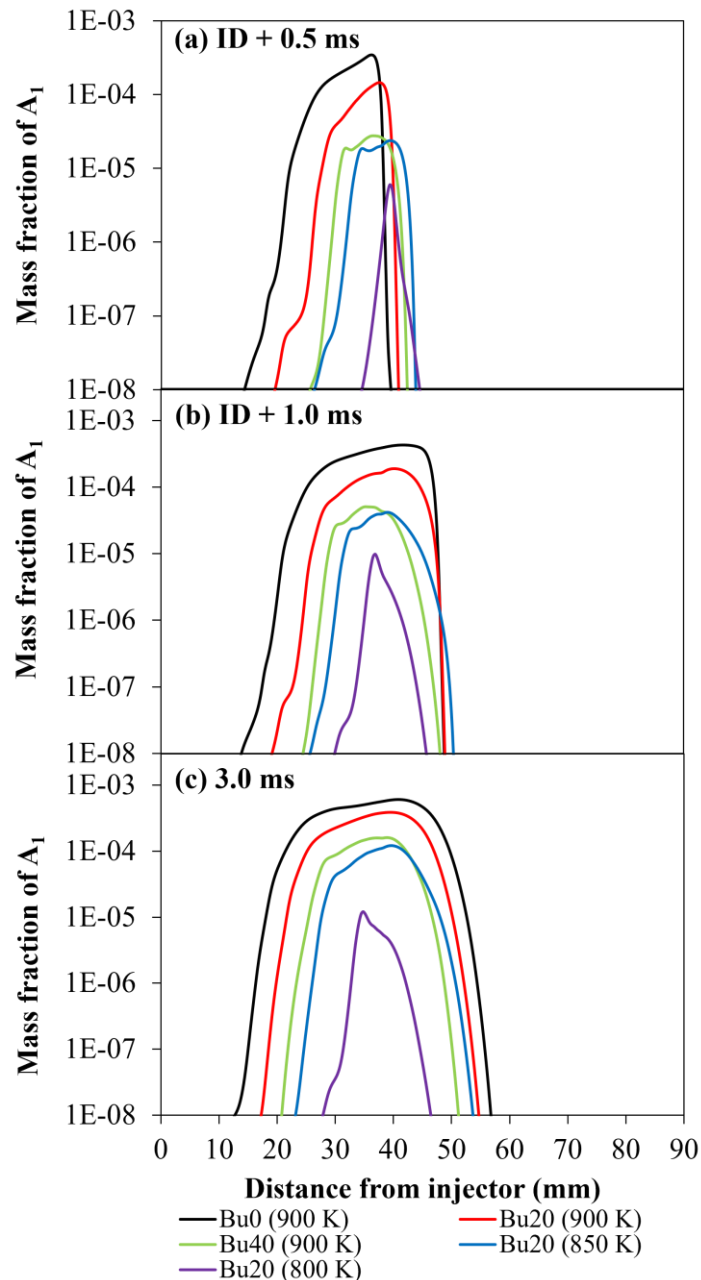


Figure 7-3: Predicted temporal evolution for the mass fractions of  $A_1$  at time (a) ID + 0.5 ms, (b) ID + 1.0 ms and (c) 3.0 ms for the test cases.

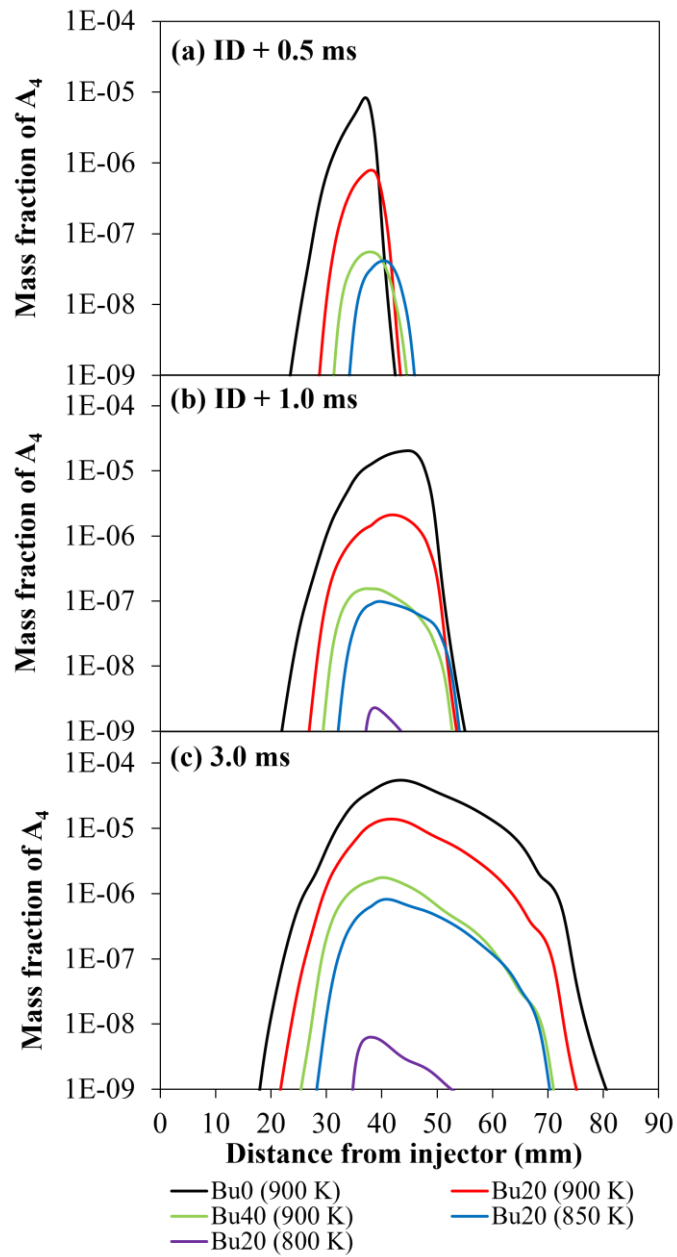


Figure 7-4: Predicted temporal evolution for the mass fractions of  $A_4$  at time (a) ID + 0.5 ms, (b) ID + 1.0 ms and (c) 3.0 ms for the test cases.

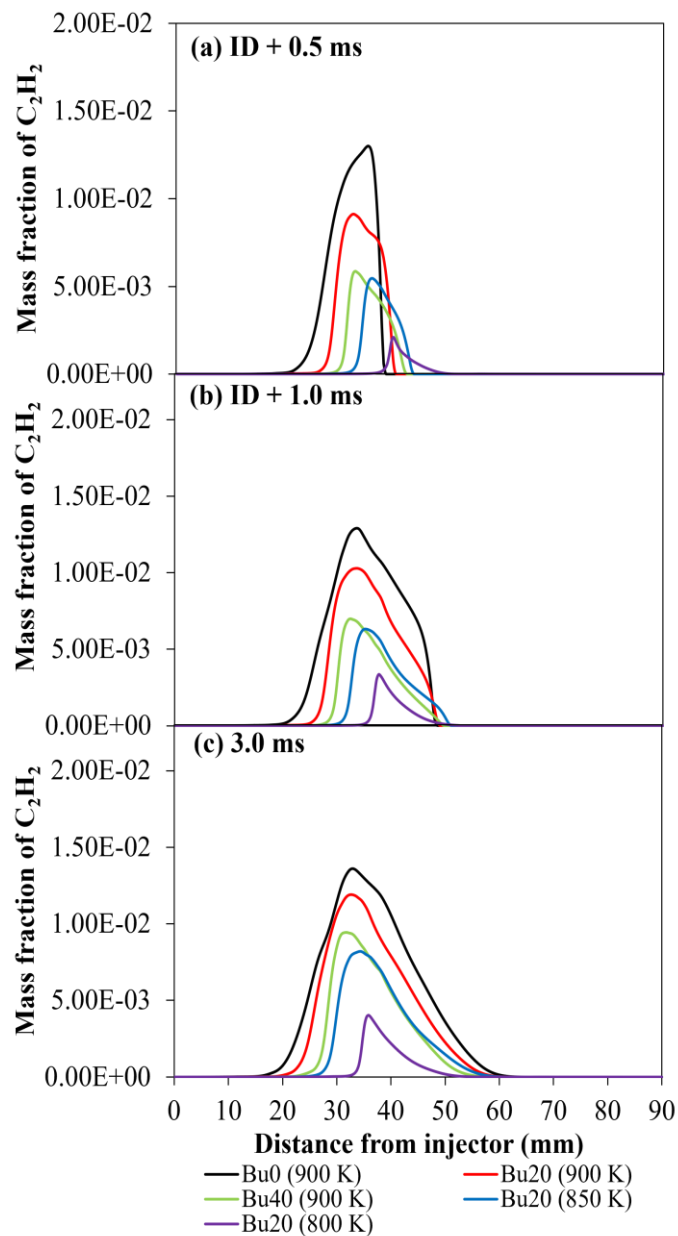


Figure 7-5: Predicted temporal evolution for the mass fractions of  $C_2H_2$  at time (a) ID + 0.5 ms, (b) ID + 1.0 ms and (c) 3.0 ms for the test cases.

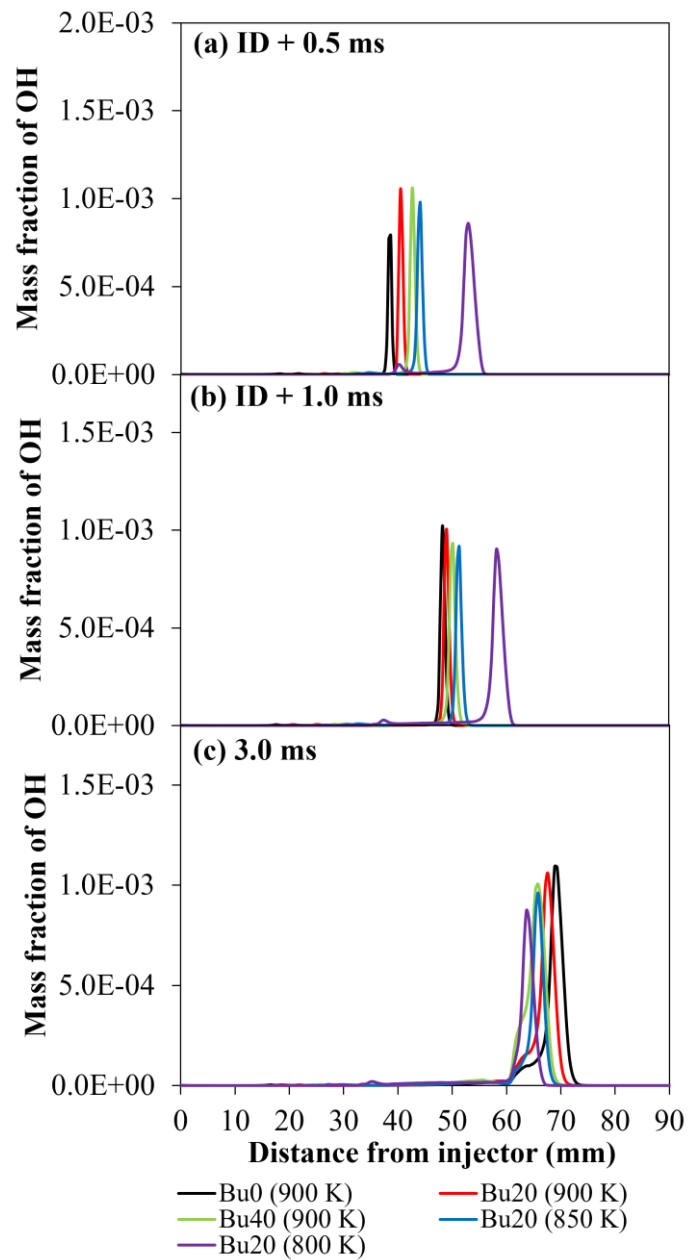


Figure 7-6: Predicted temporal evolution for the mass fractions of OH at time (a) ID + 0.5 ms, (b) ID + 1.0 ms and (c) 3.0 ms for the test cases.

#### 7.4 Normalised SVF, Particle Size and Intermediate Species

Figure 7-7 shows the normalised peak SVF and soot particle size for the test cases at 3.0 ms, where all the peak SVF and soot particle size are normalised against the case of Bu0 (900 K). From Figure 7-7, it could be seen that peak SVF and soot particle size of Bu40 (900 K) decrease by 93.11% and 56.58%, respectively, as compared to the case of Bu0 (900 K). However, for the case of Bu20 (800 K), the peak SVF and soot particle are only lowered by 88% and 50.62%, respectively, when comparing to the case of Bu20 (900 K). These results indicate that the SVF and soot particle size are affected more significantly at different n-butanol blending ratios than at different ambient temperatures. Besides, this also suggest that the addition of n-butanol with n-dodecane is probably more effective in reducing soot emission than the lowering of ambient temperature.

Figure 7-8 further presents the normalised peak mass fractions of  $A_1$ ,  $A_4$ ,  $C_2H_2$  and OH for the test cases at 3.0 ms. From Figure 7-8(a) and (b), it appears that the decrease in  $A_4$  species is more significant than  $A_1$  species as n-butanol blending ratio increases and as ambient temperature decreases. For instance, as compared to Bu0 (900 K), the mass fractions of  $A_1$  and  $A_4$  for Bu20 (900 K) decrease by 36.06% and 74.54%, respectively. Considering  $C_2H_2$  species is a precursor to the formation of  $A_4$  species, the higher magnitude of decrement for  $A_4$  species is attributed to the decrease in  $C_2H_2$  species at higher n-butanol blending ratio and at lower ambient temperature, as shown in Figure 7-8(c). Furthermore, Figure 7-8(d) shows that the decrease in OH is less significant as compared to  $A_1$ ,  $A_4$  and  $C_2H_2$  when n-butanol blending ratio increases and when the ambient temperature decreases. Among the test cases, Bu20 (800 K) produces the lowest OH mass fraction but this is just approximately 20% lower than those of Bu0 (900 K) in which the OH mass fraction is the highest.

Interestingly, it is found in Figure 7-7 that the peak SVF and soot particle size of Bu20 (850 K) are higher and larger than Bu40 (900 K) despite the formation of  $A_1$ ,  $A_4$ , and  $C_2H_2$  species are lower for Bu20 (850 K). This phenomena could possibly be explained as follows. Although the mass fractions of  $A_1$ ,  $A_4$  and  $C_2H_2$  species are lower for Bu20 (850 K), the lower ambient temperature of Bu20 (850 K) causes the overall combustion reaction to be lower and this resulted in a lower formation of OH

radical. On the other hand, despite Bu40 (900 K) produces a higher amount of  $A_1$ ,  $A_4$  and  $C_2H_2$  species, the higher oxygen content of the blend and higher ambient temperature produces a larger pool of OH species. As such, the soot oxidation is higher and this causes the SVF and soot particle size of Bu40 (900 K) to be lower and smaller than Bu20 (850 K). These discussions are in accordance with the predicted OH mass fraction for the test cases, as shown in Figure 7-8(d), where it could be seen that the OH mass fraction of Bu40 (900 K) is indeed slightly higher than Bu20 (850 K). Despite that, as ambient temperature decreases to 800 K, Figure 7-8(d) shows that the OH mass fraction of Bu20 (800 K) further decreases but the soot precursor species also decrease drastically. Hence, the SVF and soot particle size of Bu20 (800 K) are the lowest and smallest among the test cases because soot precursor species are already at extremely low levels.

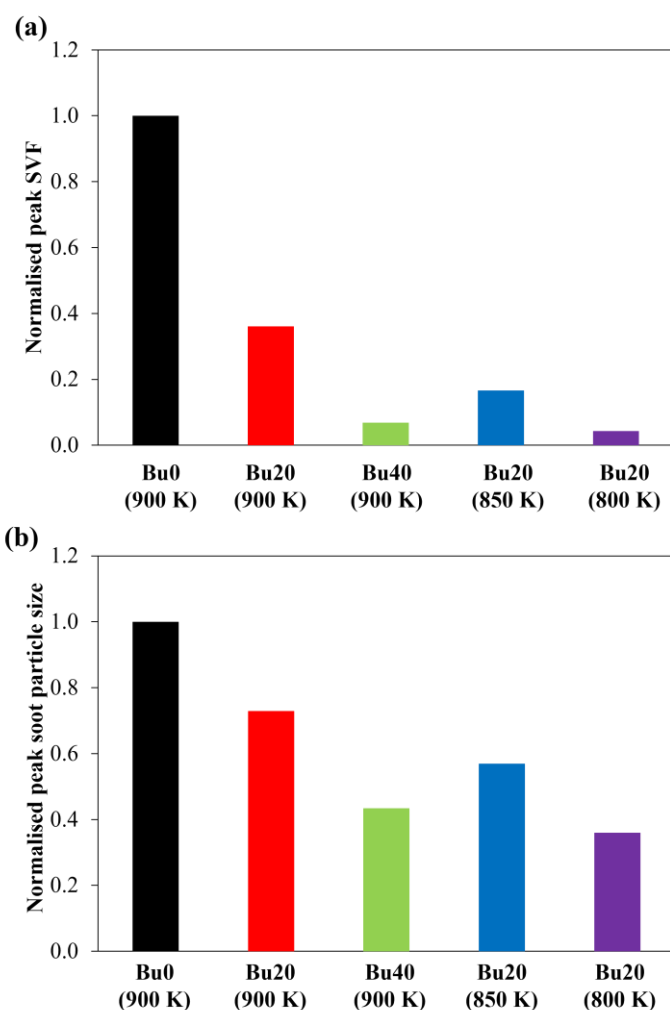


Figure 7-7: Normalised peak (a) SVF and (b) soot particle size for the test cases.

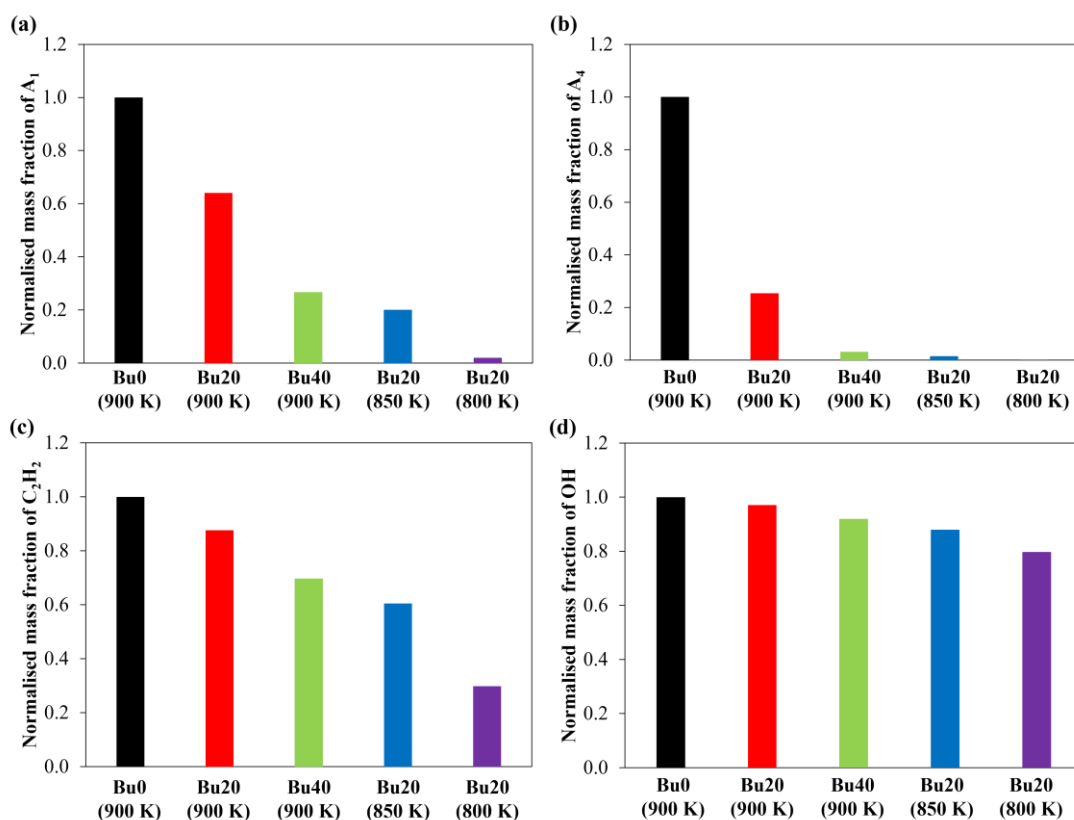


Figure 7-8: Normalised peak mass fractions of (a)  $A_1$ , (b)  $A_4$ , (c)  $C_2H_2$  and (d) OH for the test cases.

## 7.5 Quasi-Steady Spatial Distributions of Soot and its Intermediate Species

Figure 7-9 presents the spatial distributions of the flame temperature, equivalence ratio, SVF,  $C_2H_2$ ,  $A_1$ ,  $A_4$  and OH at different n-butanol blending ratios and ambient temperatures. These contours are selected at 3.0 ms after start of injection (ASOI) which corresponds to the flame at quasi-steady state. In those contours, the black line denotes the stoichiometric line and the regions that are within and outside of the stoichiometric line are considered as fuel-rich and fuel-lean, respectively. From Figure 7-9, the maximum difference in the peak flame temperature at different n-butanol blending ratios and ambient temperatures is only 100 K despite the latent heat of vaporisation for n-dodecane-n-butanol blend is higher than pure n-dodecane. However, the equivalence ratio within the spray jet is more uniform at higher n-butanol blending ratio and at lower ambient temperature. This is mainly due to the lower cetane number of higher n-butanol blends, which resulted in a longer ID and duration for air-fuel mixing. Likewise, as the ambient temperature decreases, more energy is needed to vaporise the fuel and this also causes the ID and air-fuel mixing



duration to increase. As a result, the combustible mixture is diluted and the local equivalence ratio decreases. Consequently, as seen in Figure 7-9, the peak SVF and the size of the soot cloud in the fuel-rich region decrease as the n-butanol blending ratio increases and as the ambient temperature decreases. In addition, results also show that the distributions of  $A_1$ ,  $A_4$  and  $C_2H_2$  shrink and its peak mass fractions decrease at higher n-butanol blending ratio and at lower ambient temperature due to the decrease in local equivalence ratio within the spray jet. These results are generally similar to those obtained by Hou et al. [87] where the spatial distributions of soot and its intermediate species decrease when the n-butanol blending ratio is increased. Meanwhile, the OH radical is formed at the periphery of the flame close to the stoichiometric line where the flame temperature is the highest. Within these regions, soot ceased to exist as the high flame temperature promotes high OH radicals which then oxidises soot.

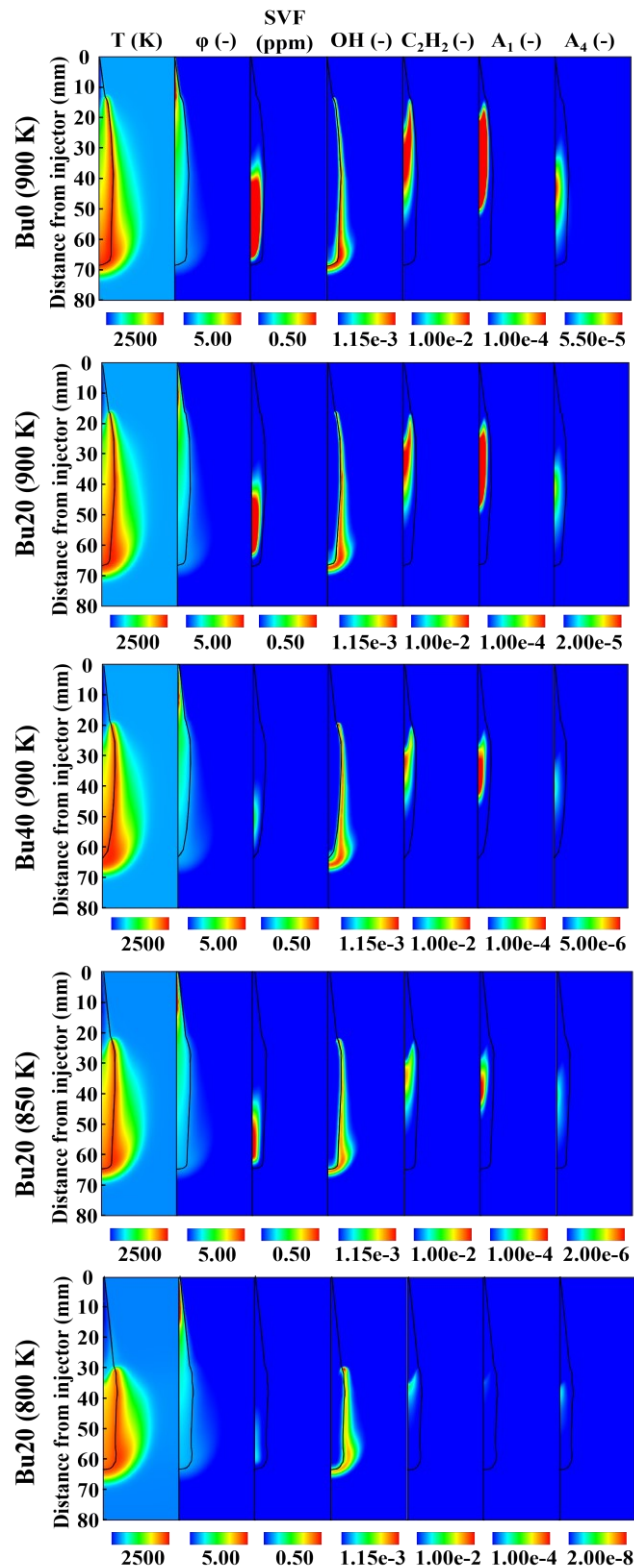


Figure 7-9: Spatial distributions of temperature, equivalence ratio, SVF,  $C_2H_2$ ,  $A_1$ ,  $A_4$  and OH for the test cases at quasi-steady state. The black line is the stoichiometric line. The maximum value of the colour contour is listed in the corresponding colour bar while the minimum value is 500 K for temperature and zero for the remaining contours.

Furthermore, Figure 7-10 shows the SVF and mass fractions of  $C_2H_2$ ,  $A_1$ ,  $A_4$  and OH plotted in the temperature – equivalence ratio space at different n-butanol blending ratios and ambient temperatures. In Figure 7-10, only points in the computational domain that are higher than 40% of the respective peak mass fractions are plotted [248]. The vertical dash line in Figure 7-10 is the stoichiometric line. The fuel-lean region is at the left side of the stoichiometric line while the fuel-rich region is at the right side. As expected, it can be observed in Figure 7-10 that soot and its precursors are mainly concentrated in the fuel-rich region. Within the spray jet, the location of soot coincides with the location of  $A_4$  species, which shows that soot inception is through  $A_4$  species. On the other hand, the distributions of  $A_1$  and  $C_2H_2$  species cover a wider range of temperatures and equivalence ratios, which envelops the formation of  $A_4$  species. Moreover, in Figure 7-10, it is found that the soot formation for the test cases occurs at temperatures and equivalence ratios of 1800 – 2300 K and 1.1 – 2.2, respectively. However, the maximum soot is mainly formed at around 2000 K and at equivalence ratio of 1.3. Beyond 2300 K, very low amount of soot is formed due to the large amount of OH present in that region, which could oxidise the soot. On the other hand, at temperatures below 1800 K, soot is also hardly seen because there is a low amount of  $A_4$  species that could form soot. Nonetheless, since there is only a marginal difference in the peak flame temperature between the test cases as mentioned previously, it can be seen that the addition of n-butanol and the decrease in ambient temperature causes the local equivalence ratio to decrease through the extension of ID and allows a larger degree of air-fuel mixing, which then leads to the shrinking of conditions that are favourable for the formation of soot and its precursor species. This could be observed in Figure 7-10, where the distributions of SVF,  $A_1$ ,  $A_4$  and  $C_2H_2$  are narrower and limited to lower equivalence ratios as there is an absence of high equivalence ratio regions within the spray for cases with higher n-butanol blending ratio and lower ambient temperature.

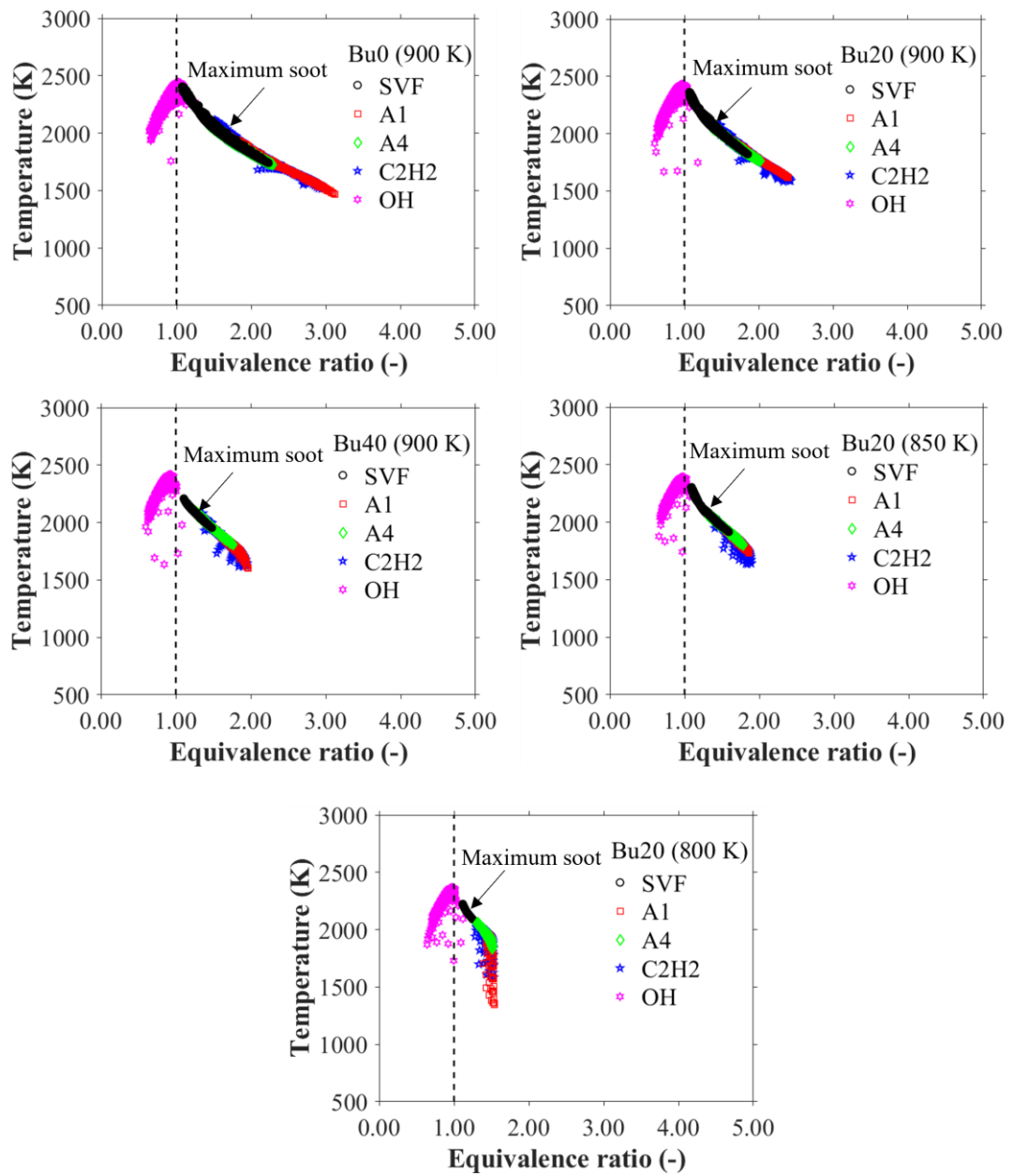


Figure 7-10: Maps of SVF, A<sub>1</sub>, A<sub>4</sub>, C<sub>2</sub>H<sub>2</sub> and OH onto the temperature-equivalence ratio space for the test cases at quasi-steady state. The black dash line denotes the stoichiometric line.

## 7.6 Quasi-Steady Distributions of Soot Particle Size and Number Density

The quasi-steady distributions of soot particle size for the test cases are shown in Figure 7-11. In Figure 7-11, the smallest soot particles are located at the upstream region of the spray whereas the largest soot particles are found in the fuel-rich region of the spray head. Meanwhile, the intermediate soot particles are observed to be at the periphery of the soot cloud. However, due to the longer duration of air-fuel mixing and the high oxygen content in the blend, the soot particle size of Bu40 (900 K) and Bu20 (800 K) are much more uniform across the entire soot cloud. The distributions of soot particle size predicted here are mainly in qualitative agreement with the reacting spray simulation results by Pang et al. [203] in a diesel engine. Furthermore, Figure 7-12 shows the soot number density for the test cases, where it decreases as the n-butanol blending ratio increases and as the ambient temperature decreases. Besides, it can be observed that the highest soot number density occurs at the spray head for all test cases and the observation here is in line with the conceptual model as discussed by Dec [2]. In Figure 7-12, it should also be noted that the highest soot number density location does not correspond to the location of the largest soot particle size. In fact, referring to Figure 7-11 and Figure 7-12, the largest soot particle size appears to be slightly further upstream than where the highest soot number density occurs. This is because the larger size soot particles are formed through the coagulation of several other smaller soot particles [203]. As a result, the soot number density decreases as the soot particle size increases.

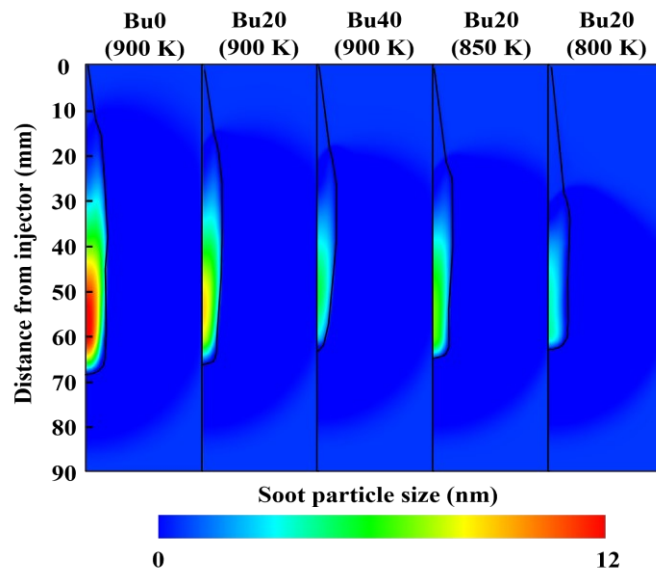


Figure 7-11: Spatial distributions of soot particle size for the test cases at quasi-steady state. Black line represents the stoichiometric line.

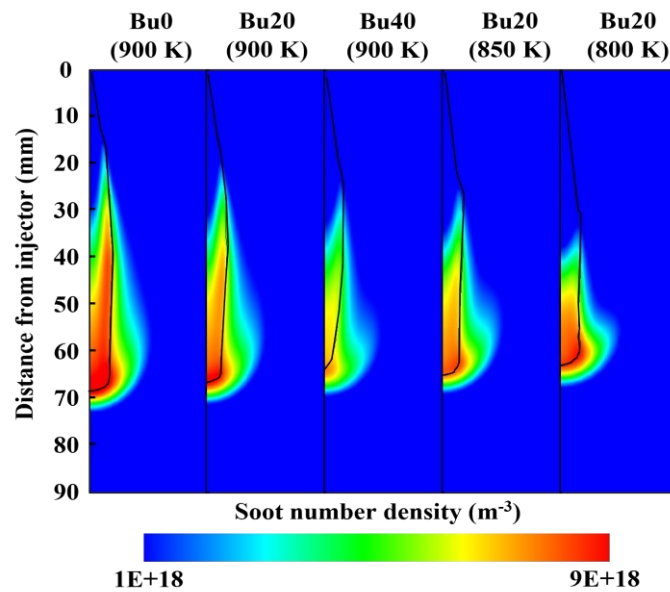


Figure 7-12: Spatial distributions of soot number density for the test cases at quasi-steady state. Black line denotes the stoichiometric line.

## 7.7 Soot Relevant Rates at Quasi-Steady State

In this section, the rates for soot mass nucleation, soot surface growth, soot coagulation and soot oxidation for the test cases are presented. In addition, the rate of soot is also shown to identify the soot creation and destruction regions. The soot relevant rates are captured at 3.0 ms ASOI to study the soot formation and oxidation mechanisms at quasi-steady state. In the Moss-Brookes soot model, the soot nucleation and surface growth processes are responsible for the creation of soot and are categorised as the soot formation mechanism. On the other hand, the soot oxidation mechanism is responsible for the destruction of soot. Meanwhile, the rate of coagulation does not affect the soot mass but rather only on the soot particle size. In the rate of soot contour, a positive value indicates soot creation whereas a negative value indicates soot destruction.

According to the rate of soot contours as shown in Figure 7-13, it is found that soot creation occurs in the central fuel-rich region of the spray jet whereas soot destruction is located at the fuel-rich region of the spray periphery close to the stoichiometric line. In particular for the case of Bu20 (800 K), the soot destruction is found to be concentrated only at the spray head. Nevertheless, the soot creation region becomes smaller with the increase in n-butanol blending ratio and with the decrease in ambient temperature. This phenomena could be attributed to the following reasons. First of all, as shown in Figure 7-13, the rate of soot mass nucleation decreases and its distribution becomes narrower as the n-butanol blending ratio increases and as the ambient temperature decreases. This is mainly due to the lower formation of soot precursor species such as  $A_1$  and  $A_4$  at higher n-butanol blending ratio and at lower ambient temperature. As a result, there are fewer sites for soot to further undergo surface growth. Accordingly, the rate of soot surface growth decreases and its distribution shrinks, which then leads to a smaller soot creation region. From Figure 7-13, it is noticeable that soot mass nucleation occurs in the fuel-rich region of the spray jet and extends upstream until approximately the FLOL. However, soot surface growth mainly occurs at the downstream of the spray jet and this coincides with the soot creation region. These observations are in conformity with the theory that the soot surface growth process is predominantly responsible for the soot mass [93]. On the

other hand, the rate of coagulation is well correlated to the soot particle size [203]. As shown in Figure 7-13, the coagulation rate for the test cases is the lowest at the upstream of the spray and increases to its maximum at the spray head. There, the smaller soot particles coagulate with each other to form larger soot particles and thus the size of the soot particles is larger in the vicinity of the spray head. While the processes of soot mass nucleation, surface growth and coagulation occur in the fuel-rich region, soot oxidation takes place close to the stoichiometric line that surrounds the soot creation region. Based on Figure 7-13, the soot oxidation rate is found to be the highest for Bu0 (900 K) while it decreases as the n-butanol blending ratio increases and as the ambient temperature decreases. This is attributed to the lower flame temperature at higher n-butanol blending ratio and at lower ambient temperature since the flame temperature plays a major role for the formation of OH radicals [87].

Moreover, in Figure 7-13, one interesting observation to note here is that while the highest soot oxidation rate is at the periphery of the spray for most of the test cases, it is entirely different for the case of Bu40 (900 K). The soot oxidation for Bu40 (900 K) is found to be more evenly distributed within the entire soot creation region even towards fuel-rich region, as can be seen in Figure 7-13(c). This indicates that the high amount of n-butanol in Bu40 (900 K) helps provide sufficient oxygen to penetrate into the fuel-rich region and this resulted in the promotion of soot oxidation. Therefore, the soot oxidation mechanism of Bu40 (900 K) is somehow enhanced, which is partly the reason that the SVF and soot particle size of Bu40 (900 K) are lower than Bu20 (850 K), as discussed previously. The smaller soot particle size of Bu40 (900 K) is also attributed to the lower coagulation rate as compared to Bu20 (850 K). Another contributing factor to the lower soot SVF for Bu40 (900 K) as compared to Bu20 (850 K) is the lower rates of soot mass nucleation and surface growth. This is interesting because Figure 7-8 shows that Bu40 (900 K) produces a higher amount of soot precursor species than Bu20 (850 K). Nevertheless, this situation could be attributed to the lower residence time of the PAH species in the reaction zone for Bu40 (900 K) as compared to Bu20 (850 K). Since soot nuclei is formed through the time-dependent growth process of PAH species from the gas-phase to solid-phase [136,138], the high oxygen concentration in Bu40 (900 K) could possibly oxidise the PAH species before



it could be converted to soot. In other words, the PAH species are being destroyed even before they have a chance to grow and form soot particles.

As discussed previously, the soot precursors and OH radical decrease at higher n-butanol blending ratio and at lower ambient temperature. However, it is noted in Figure 7-8 that the soot precursor species decrease more significantly than the OH radical. Therefore, as the soot precursor species determine the soot mass nucleation and surface growth processes, it can be concluded that the soot formation mechanism plays a dominant role for the resultant soot and the lower soot emission at higher n-butanol blending ratio and at lower ambient temperature is mainly due to the suppression of the soot formation mechanism, which is in line with the findings by Hou et al. [87]. At the same time, the soot oxidation mechanism also deteriorates due to the lower OH radical formed in lower flame temperatures. Nonetheless, the case of Bu40 (900 K) shows that the high oxygen concentration could help compensate the deterioration of the soot oxidation mechanism. As such, it can be deduced that a blend with high n-butanol blending ratio could suppress the soot formation mechanism while maintaining the performance of the soot oxidation mechanism simultaneously. Such deduction could explain the results in Figure 7-7, where the SVF and soot particle size decrease more significantly at different n-butanol blending ratios than at different ambient temperatures.

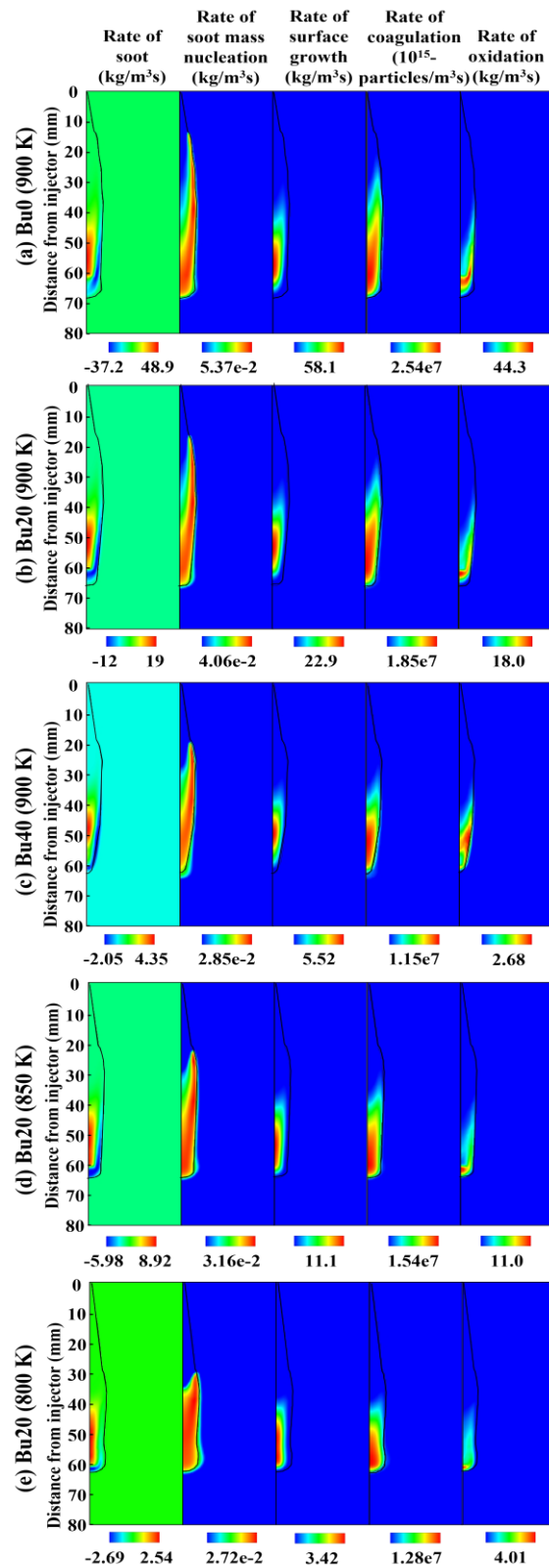


Figure 7-13: Predicted soot relevant rates for the test cases at quasi-steady state. Black line denotes stoichiometric line. The value in the corresponding colour bar for the rates of soot mass nucleation, surface growth, coagulation and oxidation are the maximum value.

## 7.8 Concluding Remarks

The effects of n-butanol blending ratio and ambient temperature towards the soot emission in n-dodecane-n-butanol spray flames are investigated in this chapter. Results show that the SVF and soot particle size decrease as the n-butanol blending ratio increases and as the ambient temperature decreases. Comparing to the case of Bu0 (900 K), both peak SVF and soot particle size of Bu40 (900 K) decreases by 93.11% and 56.58%, respectively. Similarly, Bu20 (800 K) shows a decrease of 88% and 50.62% in the peak SVF and soot particle size when comparing to Bu20 (900 K). The mass fractions of A1, A4, C2H2 and OH also decrease as the n-butanol blending ratio increases and as the ambient temperature decreases. Both soot formation and oxidation mechanisms are suppressed at higher n-butanol blending ratio and at lower ambient temperature but the soot formation mechanism plays a more dominant role in the resulting SVF and soot particle size. Nevertheless, the high oxygen concentration in high n-butanol blending ratio could help maintain the performance of the soot oxidation mechanism while suppressing the soot formation mechanism simultaneously. Therefore, the SVF and soot particle size decrease more significantly with the increase in n-butanol blending ratio than the decrease in ambient temperature.

# CHAPTER 8

## CONCLUSIONS AND FUTURE WORK

### 8.1 Conclusions

In this study, a new n-dodecane-n-butanol-PAH reduced mechanism is developed and validated under a wide range of engine operating conditions. Subsequently, the reduced mechanism is used for the applications under diesel spray combustion where the fundamental ignition, combustion and soot characteristics of n-dodecane-n-butanol spray flames are studied. In Section 8.1.1, the conclusion summarises the development and validation of the DB105 mechanism that is used to simulate the chemical kinetics of n-dodecane-n-butanol. Following that, Section 8.1.2 summarises the numerical setup for the 2D spray combustion simulations in a constant volume combustion chamber. The DB105 mechanism is integrated into CFD where the fidelity of the mechanism is further evaluated. Subsequently, the main findings from the study of the fundamental ignition, combustion and flame characteristics of n-dodecane-n-butanol spray under diesel engine conditions are highlighted in Section 8.1.3. The key soot processes of n-dodecane-n-butanol spray are further highlighted in Section 8.1.4. Lastly, suggestions on future works are presented in Section 8.2.

#### 8.1.1 Development and Validation of n-Dodecane-n-Butanol-PAH Mechanism

- A n-dodecane-n-butanol reduced mechanism that consists of 105 species and 584 reactions (DB105) is developed where n-dodecane is being used as the diesel surrogate fuel. A PAH mechanism that is able to describe the aromatic rings up to A<sub>4</sub> is also included in the mechanism for accurate soot prediction.
- For the n-dodecane ID times, the DB105 mechanism shows good agreement to the predictions by the SK54 mechanism and the experimental measurements at various initial pressures, initial temperatures and equivalence ratios conditions. Similarly, the n-butanol ID times are also well predicted by the DB105 mechanism where the predictions are able to replicate the detailed mechanism and the experimental measurements over the entire range of temperatures.

- The mole fractions of reactants ( $C_{12}H_{26}$ ,  $nC_4H_9OH$ ,  $O_2$ ), intermediate species ( $C_2H_2$ ,  $C_2H_4$ ,  $C_2H_6$ ,  $CH_4$ ) and products ( $CO$ ,  $CO_2$ ,  $H_2O$ ) for the combustion of n-dodecane and n-butanol under JSR conditions are also well predicted by the DB105 mechanism at temperatures of 550 – 1150 K and at equivalence ratios of 0.5 – 2.0.
- The DB105 mechanism also well-predicts the experimental n-dodecane laminar flame speed and the predictions from the SK54 mechanism at various unburned temperatures. However, the predictions by the DB105 mechanism starts to deviate to a maximum of 8 cm/s as the ambient pressure increases to 3.03 bar. Meanwhile, the experimental n-butanol laminar flame speeds at various unburned temperatures and equivalence ratios are generally over-predicted by the DB105 mechanism with a maximum deviation of 9 cm/s.
- Furthermore, under  $C_2H_4$  premixed flame, the mole fractions of  $C_2H_2$ ,  $C_2H_4$ ,  $C_4H_2$ ,  $C_4H_4$ ,  $A_1$  and  $A_2$  are well predicted by the DB105 mechanism but  $A_3$  and  $A_4$  are slightly under-predicted. Nevertheless, the maximum deviation of all the predictions are within the experimental uncertainties of an order magnitude. Moreover, the mole fractions of  $C_4H_9OH$ ,  $O_2$ ,  $CO$ ,  $CO_2$ ,  $H_2O$  and  $H_2$  under n-butanol premixed laminar flame conditions are well predicted by the DB105 mechanism with a maximum error of 20%.

### 8.1.2 Formulation and Validation of a CFD-Chemical Kinetic Modelling Approach in a Constant Volume Combustion Chamber

- The 2D spray combustion simulations are performed using ANSYS FLUENT 19.1. The experimental measurements are conducted under similar conditions to those of Spray A by ECN and the test fuels are Bu0, Bu20 and Bu40 at ambient temperatures of 800 K, 850 K and 900 K.
- To obtain high fidelity simulation results, the mesh independence test and various parametric test for the time-step, turbulence model and spray breakup model are conducted.
- For all test cases, the non-reacting LPL and VPL are well predicted with a maximum deviation of 4%. On the contrary, under reacting conditions, the

ID and FLOL predicted by the DB105 mechanism and CFD sub-models are in good agreement with the experimental measurements with a maximum deviation of 20% and 12%, respectively.

- Soot validations show that the DB105 mechanism is able to predict the experimental SVF of Bu0 fuel at 850 K and 900 K with maximum deviation of 1.0 ppm (100%) and 0.3 ppm (10%), respectively. The shape and experimental soot clouds are also well emulated by the simulations. More importantly, the predicted SVF contour agree well with the diesel combustion conceptual model, where soot is formed in the fuel-rich zone of the reacting spray jet.

### 8.1.3 Investigation on the Ignition and Combustion Characteristics of n-Dodecane-n-Butanol Spray

- N-dodecane-n-butanol blends undergo a two-stage ignition regardless of n-butanol blending ratios and ambient temperatures.
- The first-stage ignition site is located at the spray periphery for all test cases except Bu20 (800 K). Due to the enhance air-fuel mixing, the first-stage ignition of Bu20 (800 K) is extended to the spray head in addition to the spray periphery. Moreover, the second-stage ignition site is at the spray periphery for Bu0 (900 K) while it is at the spray head for Bu20 (900 K), Bu40 (900 K) and Bu20 (850 K). Meanwhile, the second-stage ignition site for Bu20 (800 K) covers both fuel-rich and fuel-lean regions in the vicinity of the spray head due to enhance air-fuel mixing.
- The flame velocity of Bu0 (900 K) is the highest among the test cases at the start of ignition due to having the highest cetane number but the difference in velocity between the test cases becomes only marginal when the flame enters the diffusion combustion stage.
- Analyses at quasi-steady state reveal that key species such as OH, CH<sub>2</sub>O, HO<sub>2</sub> and H<sub>2</sub>O<sub>2</sub> are shifted to fuel-lean region as n-butanol blending ratio increases and ambient temperature decreases.
- The M-LTC mode in n-dodecane-n-butanol flame is dominant at the first-stage ignition and is more widely distributed for Bu20 (800 K) due to the

longer ID. However, at the second-stage ignition, the occurrence of M-HTC is seen at the spray periphery for Bu0 (900 K) while it is at the spray head for Bu40 (900 K) and Bu20 (800 K). The M-HTC-diff mode is located at the stoichiometric line where the flame temperature is the highest. It is also noted that the M-HTC mode for Bu40 (900 K) and Bu20 (800 K) is present in the fuel-rich region during the diffusion combustion stage and this is possibly due to the left-over premixed combustion that was carried over into the diffusion combustion stage.

#### 8.1.4 Soot Modelling of n-Dodecane-n-Butanol Spray

- For all test cases, the transient SVF, soot particle size increase as the combustion progresses. Simultaneously, the mass fractions and distributions of  $A_1$ ,  $A_4$ ,  $C_2H_2$  and OH also increase. The SVF and soot particle size decrease more significantly at different n-butanol blending ratio than at different ambient temperature.
- At higher n-butanol blending ratio and at lower ambient temperature, the quasi-steady peak SVF, soot cloud size, distributions and peak mass fractions of  $A_1$ ,  $A_4$  and  $C_2H_2$  species decrease due to the lower local equivalence ratio.
- Soot particle size and soot number density decrease at higher n-butanol blending ratio and at lower ambient temperature. However, due to the longer duration of air-fuel mixing and the higher oxygen concentration in n-dodecane-n-butanol blends, the soot particle size of Bu40 (900 K) and Bu20 (800 K) are much more uniform across the entire soot cloud.
- The soot creation region becomes smaller with the increase in n-butanol blending ratio and with the decrease in ambient temperature. This is mainly due to the smaller distributions of the rates for soot mass nucleation and surface growth.
- The soot formation mechanism has a dominant role in determining the soot and the lower SVF and soot particle size at higher n-butanol blending ratio and lower ambient temperature are due to the suppression of soot formation

mechanism. The soot oxidation mechanism is also suppressed due to the lower OH formation caused by lower flame temperature. Nevertheless, the deteriorated soot oxidation mechanism could be compensated by the high oxygen concentration in high n-butanol blending ratio which means that the soot formation mechanism is suppressed but the soot oxidation mechanism is largely unaffected. This explains why the SVF and soot particle size decrease more significantly with the increase in n-butanol blending ratio than the decrease in ambient temperature.

## 8.2 Future work

For the mechanism development, multi-component diesel surrogate fuel that includes cycloalkanes and alkylbenzenes could be included to better represent the physiochemical properties of diesel fuel. However, care should be taken as these multi-component fuels will increase the mechanism size and cause high computational time. Validations of the mechanism under 0D and 1D conditions can also be extended to different blending ratios (e.g., 10% n-butanol-90% n-dodecane) but it is subjected to the availability of experimental data. Likewise, the validation for the 2D spray combustion simulations can be conducted under different types of oxygen concentrations and ambient density to improve the robustness of the mechanism.

Furthermore, if there are sufficient resources for high performance computation, the investigation on the fundamental combustion characteristics of n-dodecane-n-butanol spray could be conducted using large eddy simulations to acquire better understanding on the turbulence-chemistry interaction of the flame. The effects of oxygen concentration and ambient density are also the additional parameters that can be studied on the n-dodecane-n-butanol spray flames. In the present study, the two equation semi-empirical Moss-Brookes soot model is used to simulate soot. However, in future, more advanced soot models such as the multi-step phenomenological soot model is recommended where the sequential soot particle dynamics of n-dodecane-n-butanol could be further studied. Ultimately, the ignition, combustion and soot characteristics of n-dodecane-n-butanol blends could potentially be extended to 3D diesel engine conditions where the spatial and temporal evolutions of the in-cylinder events could be elucidated. Several parameters such as the engine speed, engine load



and n-butanol blending ratio are proposed to be tested out to observe the combustion and emission behaviour of n-dodecane-n-butanol in a diesel engine.

## REFERENCES

- [1] Dec JE. Advanced compression-ignition engines — understanding the in-cylinder processes. *Proc Combust Inst* 2009;32:2727–42. doi:10.1016/j.proci.2008.08.008.
- [2] Dec JE. A Conceptual Model of DI Diesel Combustion Based on Laser-Sheet Imaging \*. *SAE Tech Pap* 1997;970873. doi:doi.org/10.4271/970873.
- [3] Agarwal AK, Singh AP, Maurya RK. Evolution, challenges and path forward for low temperature combustion engines. *Prog Energy Combust Sci* 2017;61:1–56. doi:10.1016/j.pecs.2017.02.001.
- [4] Yao M, Zheng Z, Liu H. Progress and recent trends in homogeneous charge compression ignition (HCCI) engines. *Prog Energy Combust Sci* 2009;35:398–437. doi:10.1016/j.pecs.2009.05.001.
- [5] Hasan MM, Rahman MM. Homogeneous charge compression ignition combustion: Advantages over compression ignition combustion, challenges and solutions. *Renew Sustain Energy Rev* 2016;57:282–91. doi:10.1016/j.rser.2015.12.157.
- [6] Bendu H, Murugan S. Homogeneous charge compression ignition (HCCI) combustion: Mixture preparation and control strategies in diesel engines. *Renew Sustain Energy Rev* 2014;38:732–46. doi:10.1016/j.rser.2014.07.019.
- [7] Reitz RD. Directions in internal combustion engine research. *Combust Flame* 2013;160:1–8. doi:10.1016/j.combustflame.2012.11.002.
- [8] Xu Z, Duan X, Liu Y, Deng B, Liu J. Spray combustion and soot formation characteristics of the acetone-butanol-ethanol/diesel blends under diesel engine-relevant conditions. *Fuel* 2020;280:118483. doi:10.1016/j.fuel.2020.118483.
- [9] Qi DH, Geng LM, Chen H, Bian YZ, Liu J, Ren XC. Combustion and performance evaluation of a diesel engine fueled with biodiesel produced from soybean crude oil. *Renew Energy* 2009;34:2706–13. doi:10.1016/j.renene.2009.05.004.
- [10] Raman LA, Deepanraj B, Rajakumar S, Sivasubramanian V. Experimental investigation on performance, combustion and emission analysis of a direct injection diesel engine fuelled with rapeseed oil biodiesel. *Fuel* 2019;246:69–74. doi:10.1016/j.fuel.2019.02.106.
- [11] Abed KA, Gad MS, El Morsi AK, Sayed MM, Elyazeed SA. Effect of biodiesel fuels on diesel engine emissions. *Egypt J Pet* 2019;28:183–8. doi:10.1016/j.ejpe.2019.03.001.
- [12] Manigandan S, Gunasekar P, Devipriya J, Nithya S. Emission and injection characteristics of corn biodiesel blends in diesel engine. *Fuel* 2019;235:723–35. doi:10.1016/j.fuel.2018.08.071.

- [13] Hewu W, Longbao Z. Performance of a direct injection diesel engine fuelled with a dimethyl ether/diesel blend. *Proc Inst Mech Eng Part D J Automob Eng* 2003;217:819–24. doi:10.1177/095440700321700907.
- [14] Zhang JJ, Huang Z, Wu JH, Qiao XQ, Fang JH. Combustion and performance of heavy-duty diesel engines fuelled with dimethyl ether. *Proc Inst Mech Eng Part D J Automob Eng* 2008;222:1691–703. doi:10.1243/09544070JAUTO783.
- [15] Li W, Wang W, Wu WP. Experimental Investigation on Compound Combustion of Partial Premixed Charge Compression Ignition – Direct Injection Engine Fueled with Dimethyl Ether. *Adv Mater Res* 2012;516–517:165–9. doi:10.4028/www.scientific.net/amr.516-517.165.
- [16] Polat S. An experimental study on combustion , engine performance and exhaust emissions in a HCCI engine fuelled with diethyl ether – ethanol fuel blends. *Fuel Process Technol* 2016;143:140–50. doi:10.1016/j.fuproc.2015.11.021.
- [17] Calam A, Aydoğan B, Halis S. The comparison of combustion, engine performance and emission characteristics of ethanol, methanol, fusel oil, butanol, isopropanol and naphtha with n-heptane blends on HCCI engine. *Fuel* 2020;266:117071. doi:10.1016/j.fuel.2020.117071.
- [18] Qian Y, Ouyang L, Wang X, Zhu L, Lu X. Experimental studies on combustion and emissions of RCCI fueled with n-heptane/alcohols fuels. *Fuel* 2015;162:239–50. doi:10.1016/j.fuel.2015.09.022.
- [19] Zhang C, Zhang C, Xue L, Li Y. Combustion characteristics and operation range of a RCCI combustion engine fueled with direct injection n-heptane and pipe injection n-butanol. *Energy* 2017;125:439–48. doi:10.1016/j.energy.2017.02.148.
- [20] Second generation biofuel markets: State of play, trade and developing perspectives. 2016.
- [21] Wise TA, Cole E. Mandating Food Insecurity: The Global Impacts of Rising Biofuel Mandates and Targets. *Glob Dev Environ Inst Work Pap* 2015;15–01.
- [22] Mandating Hunger : The Impacts of Global Biofuels Mandates and Targets. n.d.
- [23] Mohr A, Raman S. Lessons from first generation biofuels and implications for the sustainability appraisal of second generation biofuels. *Energy Policy* 2013;63:114–22. doi:10.1016/j.enpol.2013.08.033.
- [24] Disadvantages of Biofuels. BiofuelOrgUK 2010. <http://biofuel.org.uk/disadvantages-of-biofuels.html> (accessed November 16, 2018).
- [25] Hansen AC, Zhang Q, Lyne PWL. Ethanol-diesel fuel blends - A review. *Bioresour Technol* 2005;96:277–85. doi:10.1016/j.biortech.2004.04.007.

- [26] Hansen AC, Kyritsis DC, Lee C, von F. Characteristics of biofuels and renewable fuel standards. *Biomass to Biofuels Strateg Glob Ind* 2010;1–26. doi:10.3109/08039489309103325.
- [27] Energy UD of. Ethanol Production and Distribution. *Altern Fuels Data Cent* n.d. [https://afdc.energy.gov/fuels/ethanol\\_production.html](https://afdc.energy.gov/fuels/ethanol_production.html).
- [28] Zabaniotou A, Ioannidou O, Skoulou V. Rapeseed residues utilization for energy and 2nd generation biofuels. *Fuel* 2008;87:1492–502. doi:10.1016/j.fuel.2007.09.003.
- [29] Gomez LD, Steele-king CG, McQueen-mason SJ. Sustainable liquid biofuels from biomass: the writing's on the walls. *New Phytol* 2008;178:473–85. doi:10.3390/s17112492.
- [30] No SY. Application of biobutanol in advanced CI engines – A review. *Fuel* 2016;183:641–58. doi:10.1016/j.fuel.2016.06.121.
- [31] Jin C, Yao M, Liu H, Lee CFF, Ji J. Progress in the production and application of n-butanol as a biofuel. *Renew Sustain Energy Rev* 2011;15:4080–106. doi:10.1016/j.rser.2011.06.001.
- [32] Ranjan A, Vijayanand SM. Biobutanol: science, engineering and economics. *Int J Energy Res* 2012;36:277–323. doi:10.1002/er.1948.
- [33] Bankar SB, Survase SA, Ojamo H, Granström T. Biobutanol: The outlook of an academic and industrialist. *RSC Adv* 2013;3:24734–57. doi:10.1039/c3ra43011a.
- [34] Roberto da Silva Trindade W, Gonçalves dos Santos R. Review on the characteristics of butanol, its production and use as fuel in internal combustion engines. *Renew Sustain Energy Rev* 2017;69:642–51. doi:10.1016/j.rser.2016.11.213.
- [35] Han X, Yang Z, Wang M, Tjong J, Zheng M. Clean combustion of n-butanol as a next generation biofuel for diesel engines. *Appl Energy* 2017;198:347–59. doi:10.1016/j.apenergy.2016.12.059.
- [36] Alasfour FN. Butanol - A single-cylinder engine study: Availability analysis. *Appl Therm Eng* 1997;17:537–49.
- [37] Dernote J, Mounaim-Rousselle C, Halter F, Seers P. Evaluation of Butanol-Gasoline Blends in a Port Fuel-injection, Spark-Ignition Engine. *Oil Gas Sci Technol* 2010;65:345–51. doi:10.2516/ogst/2009034.
- [38] Wallner T, Frazee R. Study of regulated and non-regulated emissions from combustion of gasoline, alcohol fuels and their blends in a DI-SI engine. *SAE Tech Pap Ser* 2010;1. doi:10.4271/2010-01-1571.
- [39] Gu X, Huang Z, Cai J, Gong J, Wu X, Lee C. Emission characteristics of a spark-ignition engine fuelled with gasoline-n-butanol blends in combination with EGR. *Fuel* 2012;93:611–7. doi:10.1016/j.fuel.2011.11.040.
- [40] Broustail G, Halter F, Seers P, Moréac G, Mounaim-Rousselle C. Comparison

- of regulated and non-regulated pollutants with iso-octane/butanol and iso-octane/ethanol blends in a port-fuel injection spark-ignition engine. *Fuel* 2012;94:251–61. doi:10.1016/j.fuel.2011.10.068.
- [41] Elfasakhany A. Experimental study on emissions and performance of an internal combustion engine fueled with gasoline and gasoline/n-butanol blends. *Energy Convers Manag* 2014;88:277–83. doi:10.1016/j.enconman.2014.08.031.
- [42] Yu L, Jinke G, Wenhua Y, Jun F, Bin Z, Yuqiang L. Experimental investigation on combustion, performance, and emissions characteristics of butanol as an oxygenate in a spark ignition engine. *Adv Mech Eng* 2017;9:1–13. doi:10.1080/17597269.2017.1358948.
- [43] Yu X, Guo Z, He L, Dong W, Sun P, Shi W, et al. Effect of gasoline/n-butanol blends on gaseous and particle emissions from an SI direct injection engine. *Fuel* 2018;229:1–10. doi:10.1016/j.fuel.2018.05.003.
- [44] Li L, Wang T, Duan J, Sun K. Impact of butanol isomers and EGR on the combustion characteristics and emissions of a SIDI engine at various injection timings. *Appl Therm Eng* 2019;151:417–30. doi:10.1016/j.applthermaleng.2019.01.082.
- [45] Rakopoulos DC, Rakopoulos CD, Giakoumis EG, Dimaratos AM, Kyritsis DC. Effects of butanol-diesel fuel blends on the performance and emissions of a high-speed DI diesel engine. *Energy Convers Manag* 2010;51:1989–97. doi:10.1016/j.enconman.2010.02.032.
- [46] Kumar V, Gupta D, Naseer Siddiquee MW, Nagpal A, Kumar N. Performance and Emission Characteristics of n-Butanol and Iso-Butanol Diesel Blend Comparison. *SAE Tech Pap* 2015-01-2819 2015. doi:10.4271/2015-01-2819.
- [47] Cheng X, LI S, Yang J, Dong S, Bao Z. Effect of n-butanol-diesel blends on partially premixed combustion and emission characteristics in a light-duty engine. *SAE Tech Pap* 2014-01-2675 2014. doi:10.4271/2014-01-2675.
- [48] Cheng X, Li S, Yang J, Liu B. Investigation into partially premixed combustion fueled with n-butanol-diesel blends. *Renew Energy* 2016;86:723–32. doi:10.1016/j.renene.2015.08.067.
- [49] Yun H, Choi K, Lee CS. Effects of biobutanol and biobutanol-diesel blends on combustion and emission characteristics in a passenger car diesel engine with pilot injection strategies. *Energy Convers Manag* 2016;111:79–88. doi:10.1016/j.enconman.2015.12.017.
- [50] Atmanli A, Yilmaz N. A comparative analysis of n-butanol/diesel and 1-pentanol/diesel blends in a compression ignition engine. *Fuel* 2018;234:161–9. doi:10.1016/j.fuel.2018.07.015.
- [51] Zheng Z, Li C, Liu H, Zhang Y, Zhong X, Yao M. Experimental study on diesel conventional and low temperature combustion by fueling four isomers of butanol. *Fuel* 2015;141:109–19. doi:10.1016/j.fuel.2014.10.053.

- [52] Yusri IM, Mamat R, Akasyah MK, Jamlos MF, Yusop AF. Evaluation of engine combustion and exhaust emissions characteristics using diesel/butanol blended fuel. *Appl Therm Eng* 2019;156:209–19. doi:10.1016/j.applthermaleng.2019.02.028.
- [53] Ning L, Duan Q, Chen Z, Kou H, Liu B, Yang B, et al. A comparative study on the combustion and emissions of a non-road common rail diesel engine fueled with primary alcohol fuels (methanol, ethanol, and n-butanol)/diesel dual fuel. *Fuel* 2020;266:117034. doi:10.1016/j.fuel.2020.117034.
- [54] He B-Q, Liu M-B, Yuan J, Zhao H. Combustion and emission characteristics of a HCCI engine fuelled with n-butanol–gasoline blends. *Fuel* 2013;108:668–74. doi:10.1016/j.fuel.2013.02.026.
- [55] Liu M, He B. Combustion and emission characteristics of a HCCI engine fuelled with different n-butanol-gasoline blends. *SAE Tech Pap* 2014. doi:10.4271/2014-01-2668. Copyright.
- [56] He B, Liu M, Zhao H. Comparison of combustion characteristics of n-butanol / ethanol – gasoline blends in a HCCI engine. *Energy Convers Manag* 2015;95:101–9. doi:10.1016/j.enconman.2015.02.019.
- [57] Uyumaz A. An experimental investigation into combustion and performance characteristics of an HCCI gasoline engine fueled with n-heptane, isopropanol and n-butanol fuel blends at different inlet air temperatures. *Energy Convers Manag* 2015;98:199–207. doi:10.1016/j.enconman.2015.03.043.
- [58] Li G, Zhang C, Zhou J. Study on the knock tendency and cyclical variations of a HCCI engine fueled with n-butanol/n-heptane blends. *Energy Convers Manag* 2017;133:548–57. doi:10.1016/j.enconman.2016.10.074.
- [59] Zhu J, Huang H, Zhu Z, Lv D, Pan Y, Wei H, et al. Effect of intake oxygen concentration on diesel–n-butanol blending combustion: An experimental and numerical study at low engine load. *Energy Convers Manag* 2018;165:53–65. doi:10.1016/j.enconman.2018.03.045.
- [60] Valentino G, Iannuzzi S, Corcione FE. Experimental investigation on the combustion and emissions of a light duty diesel engine fuelled with butanol-diesel blend. *SAE Tech Pap* 2013-01-0915 2013. doi:10.4271/2013-01-0915.
- [61] Wigg B, Coverdill R, Lee CF, Kyritsis D. Emissions characteristics of neat butanol fuel using a port fuel-injected, spark-ignition engine. *SAE 2011 World Congr Exhib* 2011. doi:10.4271/2011-01-0902.
- [62] Yanai T, Han X, Wang M, Reader GT, Zheng M, Tjong J. Clean combustion in a diesel engine using direct injection of neat n-butanol. *SAE Tech Pap* 2014-01-1298 2014. doi:10.4271/2014-01-1298.
- [63] Liu M, He B, Zhao H. Effect of air dilution and effective compression ratio on the combustion characteristics of a HCCI ( homogeneous charge compression ignition ) engine fuelled with n-butanol. *Energy* 2015;85:296–303.
- [64] Yanai T, Bryden G, Dev S, Reader GT, Zheng M. Investigation of ignition

- characteristics and performance of a neat n-butanol direct injection compression ignition engine at low load. *Fuel* 2017;208:137–48. doi:10.1016/j.fuel.2017.06.096.
- [65] Fagundez JLS, Golke D, Martins MES, Salau NPG. An investigation on performance and combustion characteristics of pure n-butanol and a blend of n-butanol/ethanol as fuels in a spark ignition engine. *Energy* 2019;176:521–30. doi:10.1016/j.energy.2019.04.010.
- [66] Szwaja S, Naber JD. Combustion of n-butanol in a spark-ignition IC engine. *Fuel* 2010;89:1573–82. doi:10.1016/j.fuel.2009.08.043.
- [67] Luo Z, Som S, Sarathy SM, Plomer M, Pitz WJ, Longman DE, et al. Development and validation of an n-dodecane skeletal mechanism for spray combustion applications. *Combust Theory Model* 2014;18:187–203. doi:10.1080/13647830.2013.872807.
- [68] Gimeno J, Bracho G, Martí-Aldaraví P, Peraza JE. Experimental study of the injection conditions influence over n-dodecane and diesel sprays with two ECN single-hole nozzles. Part I: Inert atmosphere. *Energy Convers Manag* 2016;126:1146–56. doi:10.1016/j.enconman.2016.07.077.
- [69] Payri R, Salvador FJ, Gimeno J, Peraza JE. Experimental study of the injection conditions influence over n-dodecane and diesel sprays with two ECN single-hole nozzles. Part II: Reactive atmosphere. *Energy Convers Manag* 2016;126:1157–67. doi:10.1016/j.enconman.2016.07.079.
- [70] Engine combustion network. Sandia Natl Lab n.d. <https://ecn.sandia.gov/>.
- [71] Algayyim SJM, Wandel AP, Yusaf T. The impact of injector hole diameter on spray behaviour for butanol-diesel blends. *Energies* 2018;11. doi:10.3390/en11051298.
- [72] Zhang X, Li T, He RT, Chen R. Study on the Physicochemical Properties and Spray and Combustion Characteristics of 1-Butanol/Diesel Fuel Blends in a Constant-Volume Combustion Chamber. *Energy and Fuels* 2019;33:10218–27. doi:10.1021/acs.energyfuels.9b01955.
- [73] Haozhong H, Chengzhong Z, WQingsheng L, Qingxin W, Xueqiang W. An experimental study on the combustion and emission characteristics of a diesel engine under low temperature combustion of diesel/gasoline/n-butanol blends. *Appl Energy* 2016;170:219–31. doi:10.1016/j.enconman.2016.09.090.
- [74] Zhang T, Jacobson L, Björkholtz C, Munch K, Denbratt I. Effect of using butanol and octanol isomers on engine performance of steady state and cold start ability in different types of Diesel engines. *Fuel* 2016;184:708–17. doi:10.1016/j.fuel.2016.07.046.
- [75] Wakale AB, Samah Y, Mohamed NN and MJM ali, Banerjee Raja HI and SMS. An Experimental and Numerical Study of N-Dodecane/Butanol Blends for Compression Ignition Engines. *SAE Tech Pap* 2018. doi:10.4271/2018-01-0240.

- [76] Zhang T, Andersson M, Munch K, Denbratt I. Optical diagnostics of spray characteristics and soot volume fractions of n-butanol, n-octanol, diesel, and hydrotreated vegetable oil blends in a constant volume combustion chamber. SAE Tech Pap 2019-01-0019 2019. doi:10.4271/2019-01-0019.
- [77] Kuszewski H. Effect of Injection Pressure and Air-Fuel Ratio on the Self-Ignition Properties of 1-Butanol-Diesel Fuel Blends: Study Using a Constant-Volume Combustion Chamber. *Energy and Fuels* 2019;33:2335–47. doi:10.1021/acs.energyfuels.8b04523.
- [78] Chen Z, Wu Z, Liu J, Lee C. Combustion and emissions characteristics of high n-butanol / diesel ratio blend in a heavy-duty diesel engine and EGR impact. *Energy Convers Manag* 2014;78:787–95. doi:10.1016/j.enconman.2013.11.037.
- [79] Nilaphai O, Hespel C, Chanchaona S, C. Mounaim-Rousselle. Spray and combustion characterizations of ABE/Dodecane blend in comparison to alcohol/Dodecane blends at high-pressure and high-temperature conditions. *Fuel* 2018;225:542–53. doi:10.1016/j.fuel.2018.03.184.
- [80] Nilaphai O, Hespel C, Moreau B, Contino F, Bourgeois N, Chanchaona S, et al. New High-Pressure and High-Temperature Chamber for Diesel Spray Characterization. ILASS – Eur. 2016, 27th Annu. Conf. Liq. At. Spray Syst., 2016.
- [81] Nilaphai O, Hespel C, Chanchaona S, Mounaim-Rousselle C. Spray and Combustion Characterization of the Alcohol Blends in the High-Pressure High-Temperature Conditions. ILASS–Asia 2017, 2017.
- [82] Wang H, Deneys R, Yao M, Yang B, Jiao Q, Qiu L. Development of an n-heptane-n-butanol-PAH mechanism and its application for combustion and soot prediction. *Combust Flame* 2013;160:504–19. doi:10.1016/j.combustflame.2012.11.017.
- [83] Zhou X, Song M, Huang H, Yang R, Wang M, Sheng J. Numerical study of the formation of soot precursors during low-temperature combustion of a n-butanol-diesel blend. *Energy and Fuels* 2014;28:7149–58. doi:10.1021/ef501370u.
- [84] Huang H, Zhu J, Zhu Z, Wei H, Lv D, Zhang P, et al. Development and validation of a new reduced diesel-n-butanol blends mechanism for engine applications. *Energy Convers Manag* 2017;149:553–63. doi:10.1016/j.enconman.2017.07.056.
- [85] Li Y, Chen Y, Wu G. A new skeletal mechanism for diesel-n-butanol blends combustion in engine. *Fuel* 2020;264:116856. doi:10.1016/j.fuel.2019.116856.
- [86] Wei H, Zhao W, Lu Z, Zhou L. Effects of oxygen concentrations on the ignition and quasi-steady processes of n-heptane spray flames using large eddy simulation. *Fuel* 2019;241:786–801. doi:10.1016/j.fuel.2018.12.097.
- [87] Hou J, Yan F, Lee TH, Chang W, Lee CF. Computational Investigation on



- Soot Mechanism of Diesel and Diesel/n-Butanol Blend in Constant Volume Chamber with Various Ambient Temperatures. *Energy & Fuels* 2017;31:916–31. doi:10.1021/acs.energyfuels.6b02650.
- [88] Wakale AB, Banerjee S, Banerjee R. Estimation of NO<sub>x</sub> and soot emission from a constant volume n-butanol/n-dodecane blended spray using unsteady flamelet model based on n-dodecane/n-butanol/NO<sub>x</sub>/PAH chemistry. *J Energy Inst* 2020;93:1868–82. doi:10.1016/j.joei.2020.04.002.
- [89] Pitz WJ, Mueller CJ. Recent progress in the development of diesel surrogate fuels. *Prog Energy Combust Sci* 2011;37:330–50. doi:10.1016/j.pecs.2010.06.004.
- [90] Herbinet O, Pitz WJ, Westbrook CK. Detailed chemical kinetic oxidation mechanism for a biodiesel surrogate. *Combust Flame* 2008;154:507–28. doi:10.1016/j.combustflame.2008.03.003.
- [91] Farrell JT, Cernansky NP, Dryer FL, Law CK, Friend DG, Hergart CA, et al. Development of an Experimental Database and Kinetic Models for Surrogate Diesel Fuels. *SAE Tech Pap Ser* 2007;2007-01–02.
- [92] Pei Y, Hawkes ER, Kook S. Transported probability density function modelling of the vapour phase of an n-heptane jet at diesel engine conditions. *Proc Combust Inst* 2013;34:3039–47. doi:10.1016/j.proci.2012.07.033.
- [93] Pang KM, Jangi M, Bai XS, Schramm J. Evaluation and optimisation of phenomenological multi-step soot model for spray combustion under diesel engine-like operating conditions. *Combust Theory Model* 2015. doi:10.1080/13647830.2015.1019929.
- [94] Yao T, Pei Y, Zhong BJ, Som S, Lu T, Luo KH. A compact skeletal mechanism for n-dodecane with optimized semi-global low-temperature chemistry for diesel engine simulations. *Fuel* 2017;191:339–49. doi:10.1016/j.fuel.2016.11.083.
- [95] Sahetchian KA, Blin N, Rigny R, Seydi A, Murat M. The oxidation of n-butane and n-heptane in a CFR engine. Isomerization reactions and delay of autoignition. *Combust Flame* 1990;79:242–9. doi:10.1016/0010-2180(90)90136-F.
- [96] Shankar V, Shankar B, Al-qurashi K, Ahmed A, Atef N, Chung SH, et al. Oxidation of Alkane Rich Gasoline Fuels and their Surrogates in a Motored Engine. *Proc Eur Combust Meet* 2015:1–6.
- [97] Yao T, Pei Y, Zhong B-J, Som S, Lu T. A Hybrid Mechanism for n-Dodecane Combustion with Optimized Low-Temperature Chemistry. *9th U S Natl Combust Meet* 2015:1–10.
- [98] Narayanaswamy K, Pitsch H, Pepiot P. A chemical mechanism for low to high temperature oxidation of n-dodecane as a component of transportation fuel surrogates. *Combust Flame* 2014;161:866–84. doi:10.1016/j.combustflame.2013.10.012.

- [99] Zeppieri SP, Klotz SD, Dryer FL. Modeling concepts for larger carbon number alkanes: A partially reduced skeletal mechanism for n-Decane oxidation and pyrolysis. *Proc Combust Inst* 2000;28:1587–95.
- [100] Bikas G, Peters N. Kinetic Modelling of n-Decane Combustion and Autoignition. *Combust Flame* 2001:1456–75.
- [101] Buda F, Bounaceur R, Warth V, Glaude PA, Fournet R, Battin-Leclerc F. Progress toward a unified detailed kinetic model for the autoignition of alkanes from C4 to C10 between 600 and 1200 K. *Combust Flame* 2005:170–86. doi:10.1016/j.combustflame.2005.03.005.
- [102] Moréac G, Blurock ES, Mauss F. Automatic generation of a detailed mechanism for the oxidation of n-decane. *Combust Sci Technol* 2006;178:2025–38. doi:10.1080/00102200600793262.
- [103] Westbrook CK, Pitz WJ, Herbinet O, Curran HJ, Silke EJ. A comprehensive detailed chemical kinetic reaction mechanism for combustion of n-alkane hydrocarbons from n-octane to n-hexadecane. *Combust Flame* 2009;156:181–99. doi:10.1016/j.combustflame.2008.07.014.
- [104] Niemeyer KE, Sung CJ, Raju MP. Skeletal mechanism generation for surrogate fuels using directed relation graph with error propagation and sensitivity analysis. *Combust Flame* 2010;157:1760–70. doi:10.1016/j.combustflame.2009.12.022.
- [105] Titova NS, Torokhov SA, Starik AM. On kinetic mechanisms of n-decane oxidation. *Combust Explos Shock Waves* 2011;47:129–46. doi:10.1134/S0010508211020018.
- [106] Chang Y, Jia M, Liu Y, Li Y, Xie M. Development of a new skeletal mechanism for n-decane oxidation under engine-relevant conditions based on a decoupling methodology. *Combust Flame* 2013;160:1315–32. doi:10.1016/j.combustflame.2013.02.017.
- [107] Chang Y, Jia M, Liu Y, Li Y, Xie M, Yin H. Application of a Decoupling Methodology for Development of Skeletal Oxidation Mechanisms for Heavy n - Alkanes from n - Octane to n - Hexadecane. *Energy & Fuels* 2013:3467–79. doi:10.1021/ef400460d.
- [108] Zeng M, Yuan W, Wang Y, Zhou W, Zhang L, Qi F, et al. Experimental and kinetic modeling study of pyrolysis and oxidation of n-decane. *Combust Flame* 2014;161:1701–15. doi:10.1016/j.combustflame.2014.01.002.
- [109] Jia Z, Huang H, Zhou W, Qi F, Zeng M. Experimental and modeling investigation of n-decane pyrolysis at supercritical pressures. *Energy and Fuels* 2014;28:6019–28. doi:10.1021/ef5009314.
- [110] Xi S, Xue J, Wang F, Li X. Reduction of large-size combustion mechanisms of n-decane and n-dodecane with an improved sensitivity analysis method. *Combust Flame* 2020;222:326–35. doi:10.1016/j.combustflame.2020.08.052.
- [111] You X, Egolfopoulos FN, Wang H. Detailed and simplified kinetic models of

- n-dodecane oxidation: The role of fuel cracking in aliphatic hydrocarbon combustion. *Proc Combust Inst* 2009;32:403–10. doi:10.1016/j.proci.2008.06.041.
- [112] Som S, Longman DE, Luo Z, Plomer M, Lu T. Three dimensional simulations of diesel sprays using n-dodecane as a Surrogate. *Fall Tech Meet East States Sect Combust Inst* 2011 2011:241–54.
- [113] Mzé-Ahmed A, Hadj-Ali K, Dagaut P, Dayma G. Experimental and modeling study of the oxidation kinetics of n-undecane and n-dodecane in a jet-stirred reactor. *Energy and Fuels* 2012;26:4253–8. doi:10.1021/ef300588j.
- [114] Wang H, Ra Y, Jia M, Reitz RD. Development of a reduced n-dodecane-PAH mechanism and its application for n-dodecane soot predictions. *Fuel* 2014;136:25–36. doi:10.1016/j.fuel.2014.07.028.
- [115] Frassoldati A, D’Errico G, Lucchini T, Stagni A, Cuoci A, Faravelli T, et al. Reduced kinetic mechanisms of diesel fuel surrogate for engine CFD simulations. *Combust Flame* 2015;162:3991–4007. doi:10.1016/j.combustflame.2015.07.039.
- [116] Zeng M, Yuan W, Li W, Zhang Y, Wang Y. Investigation of n-dodecane pyrolysis at various pressures and the development of a comprehensive combustion model. *Energy* 2018;155:152–61. doi:10.1016/j.energy.2018.04.177.
- [117] Mao Y, Raza M, Wu Z, Zhu J, Yu L, Wang S, et al. An experimental study of n-dodecane and the development of an improved kinetic model. *Combust Flame* 2020;212:388–402. doi:10.1016/j.combustflame.2019.11.014.
- [118] Mze-Ahmed A, Dagaut P, Dayma G, Diévert P, Hadj-Ali K. Experimental Study of the Oxidation of N-Tetradecane in a Jet-Stirred Reactor ( JSR ) and Detailed Chemical Kinetic Modeling. *Combust Sci Technol* 2014:594–606. doi:10.1080/00102202.2014.883256.
- [119] Sun X, Liang X, Shu G, Wang Y, Wang Y, Yu H. Development of a Reduced n - Tetradecane – Polycyclic Aromatic Hydrocarbon Mechanism for Application to Two-Stroke Marine Diesel Engines. *Energy & Fuels* 2017:941–52. doi:10.1021/acs.energyfuels.6b02708.
- [120] Zeng M, Yuan W, Li W, Zhang Y, Cao C, Li T, et al. Comprehensive Experimental and Kinetic Modeling Study of n-Tetradecane Combustion. *Energy & Fuels* 2017;31:12712–20. doi:10.1021/acs.energyfuels.7b01114.
- [121] Sun X, Liang X, Shu G, lin J, Wei H, Zhou P. Development of a surrogate fuel mechanism for application in two-stroke marine diesel engine. *Energy* 2018;153:56–64. doi:10.1016/j.energy.2018.03.042.
- [122] Ristori A, Dagaut P, Cathonnet M. The Oxidation of n-Hexadecane: Experimental and Detailed Kinetic Modeling. *Combust Flame* 2001:1128–37.
- [123] Chaos M, Kazakov A, Dryer FL, Zhao Z, Zeppieri SP. High temperature compact mechanism development for large alkanes: n-hexadecane. *6th Int*

Conf Chem Kinet 2005:2005.

- [124] Poon HM, Ng HK, Gan S, Pang KM, Schramm J. Evaluation and development of chemical kinetic mechanism reduction scheme for biodiesel and diesel fuel surrogates. *SAE Int J Fuels Lubr* 2013;6:2013-01-2630. doi:10.4271/2013-01-2630.
- [125] Poon HM, Ng HK, Gan S, Pang KM, Schramm J. Development and validation of chemical kinetic mechanism reduction scheme for large-scale mechanisms. *SAE Int J Fuels Lubr* 2014;7. doi:10.4271/2014-01-2576.
- [126] Kourdis PD, Bellan J. High-pressure reduced-kinetics mechanism for n-hexadecane autoignition and oxidation at constant pressure. *Combust Flame* 2015;162:571-9. doi:10.1016/j.combustflame.2014.09.008.
- [127] Tan JY, Bonatesta F, Ng HK, Gan S. Developments in computational fluid dynamics modelling of gasoline direct injection engine combustion and soot emission with chemical kinetic modelling. *Appl Therm Eng* 2016;107:936-59. doi:10.1016/j.applthermaleng.2016.07.024.
- [128] Chishty MA, Bolla M, Hawkes E, Pei Y, Kook S. Assessing the Importance of Radiative Heat Transfer for ECN Spray A Using the Transported PDF Method. *SAE Int J Fuels Lubr* 2016;9:100-7. doi:10.4271/2016-01-0857.
- [129] Bolla M, Chishty MA, Hawkes ER, Chan QN, Kook S. Influence of turbulent fluctuations on radiation heat transfer, NO and soot formation under ECN Spray A conditions. *Proc Combust Inst* 2017;36:3551-8. doi:10.1016/j.proci.2016.06.173.
- [130] Ong JC, Pang KM, Walther JH, Ho J-H, Ng HK. Evaluation of a Lagrangian Soot Tracking Method for the prediction of primary soot particle size under engine-like conditions. *J Aerosol Sci* 2018;115:70-95. doi:10.1016/j.jaerosci.2017.10.013.
- [131] Chishty MA, Bolla M, Hawkes ER, Pei Y, Kook S. Soot formation modelling for n-dodecane sprays using the transported PDF model. *Combust Flame* 2018:101-19. doi:10.1016/j.combustflame.2018.01.028.
- [132] Poon HM, Pang KM, Ng HK, Gan S, Schramm J. Development of multi-component diesel surrogate fuel models - Part II: Validation of the integrated mechanisms in 0-D kinetic and 2-D CFD spray combustion simulations. *Fuel* 2016;181:120-30. doi:10.1016/j.fuel.2016.04.114.
- [133] Zhao Z, Xu Z, Liu J, Wang M, Lee C, Chang W, et al. Experimental and Numerical Investigation of Soot Mechanism of Acetone-Butanol-Ethanol ( ABE ) with Various Oxygen Concentrations. *SAE Tech Pap* 2015;2015-01-03. doi:10.4271/2015-01-0389. Copyright.
- [134] Schuetz CA, Frenklach Mi. Nucleation of soot: Molecular dynamics simulations of pyrene dimerization. *Proc Combu* 2002;29:2307-14.
- [135] Wen Z, Yun S, Thomson MJ, Lightstone MF. Modeling soot formation in turbulent kerosene/air jet diffusion flames. *Combust Flame* 2003;135:323-40.

- [136] Richter H, Howard JB. Formation of polycyclic aromatic hydrocarbons and their growth to soot - a review of chemical reaction pathways. *Prog Energy Combust Sci* 2000;26:565–608.
- [137] Tree DR, Svensson KI. Soot processes in compression ignition engines. *Prog Energy Combust Sci* 2007;33:272–309. doi:10.1016/j.pecs.2006.03.002.
- [138] Appel J, Bockhorn H, Frenklach M. Kinetic modeling of soot formation with detailed chemistry and physics: Laminar premixed flames of C<sub>2</sub> hydrocarbons. *Combust Flame* 2000;121:122–36. doi:10.1016/S0010-2180(99)00135-2.
- [139] Dworkin SB, Zhang Q, Thomson MJ, Slavinskaya NA, Riedel U. Application of an enhanced PAH growth model to soot formation in a laminar coflow ethylene/air diffusion flame. *Combust Flame* 2011;158:1682–95. doi:10.1016/j.combustflame.2011.01.013.
- [140] Frenklach M, Wang H. Detailed modeling of soot particle nucleation and growth. *Symp Combust* 1990:1559–66.
- [141] Frenklach M, Wang H. Detailed mechanism and modeling of soot particle formation. *Springer Ser Chem Phys* 1994:165–92. doi:10.1007/978-3-642-85167-4\_10.
- [142] Frenklach M. Reaction mechanism of soot formation in flames. *Phys Chem Chem Phys* 2002;4:2028–37. doi:10.1039/b110045a.
- [143] Wang H, Frenklach M. A detailed kinetic modeling study of aromatics formation in laminar premixed acetylene and ethylene flames. *Combust Flame* 1997;110:173–221. doi:10.1016/S0010-2180(97)00068-0.
- [144] Marinov NM, Pitz WJ, Westbrook CK, Castaldi MJ, Senkan SM. Modeling of aromatic and polycyclic aromatic hydrocarbon formation in premixed methane and ethane flames. vol. 116–117. 1996. doi:10.1080/00102209608935550.
- [145] Marinov NM, Pitz WJ, Westbrook CK, Lutz AE, Vincitore AM, Senkan SM. Chemical kinetic modeling of a methane opposed-flow diffusion flame and comparison to experiments. *Symp Combust* 1998;27:605–13. doi:10.1016/S0082-0784(98)80452-9.
- [146] D’Anna A, Kent JH. Modeling of particulate carbon and species formation in coflowing diffusion flames of ethylene. *Combust Flame* 2006;144:249–60. doi:10.1016/j.combustflame.2005.07.011.
- [147] D’Anna A, Kent JH, Santoro RJ. Investigation of species concentration and soot formation in a co-flowing diffusion flame of ethylene. *Combust Sci Technol* 2007;179:355–69. doi:10.1080/00102200600812419.
- [148] Slavinskaya NA, Frank P. A modelling study of aromatic soot precursors formation in laminar methane and ethene flames. *Combust Flame* 2009;156:1705–22. doi:10.1016/j.combustflame.2009.04.013.

- [149] Slavinskaya NA, Riedel U, Dworkin SB, Thomson MJ. Detailed numerical modeling of PAH formation and growth in non-premixed ethylene and ethane flames. *Combust Flame* 2012;159:979–95. doi:10.1016/j.combustflame.2011.10.005.
- [150] Zeng W, Chen XX. A reduced reaction mechanism of polycyclic aromatic hydrocarbon formation in diesel partially premixed combustion. *Eng Appl Comput Fluid Mech* 2011;5:530–40. doi:10.1080/19942060.2011.11015392.
- [151] Wang H, Yao M, Yue Z, Jia M, Reitz RD. A reduced toluene reference fuel chemical kinetic mechanism for combustion and polycyclic-aromatic hydrocarbon predictions. *Combust Flame* 2015;162:2390–404. doi:10.1016/j.combustflame.2015.02.005.
- [152] Huang H, Zhu J, Lv D, Wei Y, Zhu Z, Yu B, et al. Development of a reduced n-heptane-n-butylbenzene-polycyclic aromatic hydrocarbon (PAH) mechanism for engine combustion simulation and soot prediction. *Energy* 2018;165:90–105. doi:10.1016/j.energy.2018.09.162.
- [153] Li G, Yang W, Tay KL, Yu W, Chen L. A reduced and robust reaction mechanism for toluene and decalin oxidation with polycyclic aromatic hydrocarbon predictions. *Fuel* 2020;259:116233. doi:10.1016/j.fuel.2019.116233.
- [154] Dong X, Chang Y, Niu B, Jia M. Development of a practical reaction model of polycyclic aromatic hydrocarbon (PAH) formation and oxidation for diesel surrogate fuel. *Fuel* 2020;267:117159. doi:10.1016/j.fuel.2020.117159.
- [155] Yoshihara Y, Kazakov A, Wang H, Frenklach M. Reduced mechanism of soot formation - Application to natural gas-fueled diesel combustion. *Symp Combust* 1994:941–8.
- [156] Moss JT, Berkowitz AM, Oehlschlaeger MA, Biet J, Warth V, Glaude P-A, et al. An experimental and kinetic modeling study of the oxidation of the four isomers of butanol. *J Phys Chem A* 2008;112:10843–55. doi:10.1021/jp806464p.
- [157] Grana R, Frassoldati A, Faravelli T, Niemann U, Ranzi E, Seiser R, et al. An experimental and kinetic modeling study of combustion of isomers of butanol. *Combust Flame* 2010;157:2137–54. doi:10.1016/j.combustflame.2010.05.009.
- [158] Geem KM Van, Pyl SP, Marin GB, Harper MR, Green WH. Accurate high-temperature reaction networks for alternative fuels: butanol isomers. *Ind Eng Chem Res* 2010;49:10399–420.
- [159] Yasunaga K, Mikajiri T, Sarathy SM, Koike T, Gillespie F, Nagy T, et al. A shock tube and chemical kinetic modeling study of the pyrolysis and oxidation of butanols. *Combust Flame* 2012;159:2009–27. doi:10.1016/j.combustflame.2012.02.008.
- [160] Sarathy SM, Vranckx S, Yasunaga K, Mehl M, Oßwald P, Metcalfe WK, et al. A comprehensive chemical kinetic combustion model for the four butanol isomers. *Combust Flame* 2012;159:2028–55.

doi:10.1016/j.combustflame.2011.12.017.

- [161] Frassoldati A, Grana R, Faravelli T, Ranzi E, Oßwald P, Kohse-Höinghaus K. Detailed kinetic modeling of the combustion of the four butanol isomers in premixed low-pressure flames. *Combust Flame* 2012;159:2295–311. doi:10.1016/j.combustflame.2012.03.002.
- [162] Black G, Curran HJ, Pichon S, Simmie JM, Zhukov V. Bio-butanol: Combustion properties and detailed chemical kinetic model. *Combust Flame* 2010;157:363–73. doi:10.1016/j.combustflame.2009.07.007.
- [163] Dagaut P, Sarathy SM, Thomson MJ. A chemical kinetic study of n-butanol oxidation at elevated pressure in a jet stirred reactor. *Proc Combust Inst* 2009;32:229–37. doi:10.1016/j.proci.2008.05.005.
- [164] Sarathy SM, Thomson MJ, Togbé C, Dagaut P, Halter F, Mounaim-Rousselle C. An experimental and kinetic modeling study of n-butanol combustion. *Combust Flame* 2009;156:852–64. doi:10.1016/j.combustflame.2008.11.019.
- [165] Harper MR, Van Geem KM, Pyl SP, Marin GB, Green WH. Comprehensive reaction mechanism for n-butanol pyrolysis and combustion. *Combust Flame* 2011;158:16–41. doi:10.1016/j.combustflame.2010.06.002.
- [166] Cai J, Zhang L, Zhang F, Wang Z, Cheng Z, Yuan W, et al. Experimental and kinetic modeling study of n-butanol pyrolysis and combustion. *Energy & Fuels* 2012;26:5550–68. doi:10.1021/ef3011965.
- [167] Zhang J, Wei L, Man X, Jiang X, Zhang Y, Hu E, et al. Experimental and modeling study of n-butanol oxidation at high temperature. *Energy & Fuels* 2012;26:3368–80. doi:10.1021/ef3005042.
- [168] Chang Y, Jia M, Xiao J, Li Y, Fan W, Xie M. Construction of a skeletal mechanism for butanol isomers based on the decoupling methodology. *Energy Convers Manag* 2016;128:250–60. doi:10.1016/j.enconman.2016.09.078.
- [169] Hui X, Niemeyer KE, Brady KB, Sung CJ. Reduced chemistry for butanol isomers at engine-relevant conditions. *Energy and Fuels* 2017;31:867–81. doi:10.1021/acs.energyfuels.6b01857.
- [170] Merchant SS, Zanoelo EF, Speth RL, Harper MR, Van Geem KM, Green WH. Combustion and pyrolysis of iso-butanol: Experimental and chemical kinetic modeling study. *Combust Flame* 2013;160:1907–29. doi:10.1016/j.combustflame.2013.04.023.
- [171] Feng H, Zhang J, Liu D, An M, Zhang W, Zhang X. Development of a reduced n-butanol mechanism with combined reduction methods. *Fuel* 2017;187:403–16. doi:10.1016/j.fuel.2016.09.073.
- [172] Díaz-González M, Treviño C, Prince JC. A reduced kinetic mechanism for the combustion of n-butanol. *Energy and Fuels* 2018;32:867–74. doi:10.1021/acs.energyfuels.7b03011.
- [173] Liu W, Kelley AP, Law CK. Non-premixed ignition, laminar flame

- propagation, and mechanism reduction of n-butanol, iso-butanol, and methyl butanoate. *Proc Combust Inst* 2011;33:995–1002.  
doi:10.1016/j.proci.2010.05.084.
- [174] Brady KB, Hui X, Sung CJ. Comparative study of the counterflow forced ignition of the butanol isomers at atmospheric and elevated pressures. *Combust Flame* 2016;165:34–49. doi:10.1016/j.combustflame.2015.09.026.
- [175] Liu F, Hua Y, Wu H, Lee C-F, Wang Z. Experimental and kinetic investigation on soot formation of n-butanol-gasoline blends in laminar coflow diffusion flames. *Fuel* 2018;213:195–205.  
doi:10.1016/j.fuel.2017.10.106.
- [176] Golovitchev VI, Calik AT, Montorsi L. Analysis of combustion regimes in compression ignited engines using parametric  $\phi$ -T dynamic maps. *SAE Tech Pap* 2007:781–93. doi:10.4271/2007-01-1838.
- [177] Sarathy SM, Oßwald P, Hansen N, Kohse-Höinghaus K. Alcohol combustion chemistry. *Prog Energy Combust Sci* 2014;44:40–102.  
doi:10.1016/j.pecs.2014.04.003.
- [178] Li Y, Lou B, Tang W, Abubakar S, Liu G. A more realistic skeletal mechanism with compact size for n-butanol combustion in diesel engines. *Proc Inst Mech Eng Part D J Automob Eng* 2021;235:3082–100.  
doi:10.1177/09544070211007105.
- [179] Li Y, Zhao J, Tang W, Abubakar S, Wu G, Huang J. Development and application of a practical diesel-n-butanol-PAH mechanism in engine combustion and emissions prediction. *Energy Sources, Part A Recover Util Environ Eff* 2021;00:1–15. doi:10.1080/15567036.2021.1929576.
- [180] Lu T, Law CK. A directed relation graph method for mechanism reduction. *Proc Combust Inst* 2005;30:1333–41. doi:10.1016/j.proci.2004.08.145.
- [181] Nagy T, Turányi T. Reduction of very large reaction mechanisms using methods based on simulation error minimization. *Combust Flame* 2009;156:417–28. doi:10.1016/j.combustflame.2008.11.001.
- [182] Lu T, Law CK. Linear time reduction of large kinetic mechanisms with directed relation graph: N-Heptane and iso-octane. *Combust Flame* 2006;144:24–36. doi:10.1016/j.combustflame.2005.02.015.
- [183] Pepiot P, Pitsch H. Systematic reduction of large chemical mechanisms. 4th Jt Meet US Sect Combust Inst 2005:1–6.
- [184] Pepiot-Desjardins P, Pitsch H. An efficient error-propagation-based reduction method for large chemical kinetic mechanisms. *Combust Flame* 2008;154:67–81. doi:10.1016/j.combustflame.2007.10.020.
- [185] Niemeyer KE, Sung CJ. On the importance of graph search algorithms for DRGEP-based mechanism reduction methods. *Combust Flame* 2011;158:1439–43. doi:10.1016/j.combustflame.2010.12.010.



- [186] Niemeyer K, Sung C-J. DRGEP-based mechanism reduction strategies: graph search algorithms and skeletal primary reference fuel mechanisms. 49th AIAA Aerosp. Sci. Meet. Incl. New Horizons Forum Aerosp. Expo., 2011, p. 1–13. doi:10.2514/6.2011-508.
- [187] Cormen TH, Leiserson CE, Rivest RL, Stein C. Introduction to Algorithms, Second Edition. McGraw-Hill Book Company; 2001. doi:10.1016/0964-1955(93)90018-A.
- [188] Zheng XL, Lu TF, Law CK. Experimental counterflow ignition temperatures and reaction mechanisms of 1,3-butadiene. Proc Combust Inst 2007;31 I:367–75. doi:10.1016/j.proci.2006.07.182.
- [189] Huang H, Fairweather M, Griffiths JF, Tomlin AS, Brad RB. A systematic lumping approach for the reduction of comprehensive kinetic models. Proc Combust Inst 2005;30:1309–16. doi:10.1016/j.proci.2004.08.001.
- [190] Ahmed SS, Mauß F, Moréac G, Zeuch T. A comprehensive and compact n-heptane oxidation model derived using chemical lumping. Phys Chem Chem Phys 2007;9:1107–26. doi:10.1039/b614712g.
- [191] Lu T, Law CK. Strategies for mechanism reduction for large hydrocarbons: n-heptane. Combust Flame 2008;154:153–63. doi:10.1016/j.combustflame.2007.11.013.
- [192] Stagni A, Cuoci A, Frassoldati A, Faravelli T, Ranzi E. Lumping and reduction of detailed kinetic schemes: An effective coupling. Ind Eng Chem Res 2014;53:9004–16. doi:10.1021/ie403272f.
- [193] Huang H, Zhu Z, Zhu J, Lv D, Pan Y, Wei H, et al. Experimental and numerical study of pre-injection effects on diesel-n-butanol blends combustion. Appl Energy 2019;249:377–91. doi:10.1016/j.apenergy.2019.04.163.
- [194] Kattela SP, Vysyaraju RKR, Surapaneni SR, Ganji PR. Effect of n-butanol/diesel blends and piston bowl geometry on combustion and emission characteristics of CI engine. Environ Sci Pollut Res 2019;26:1661–74. doi:10.1007/s11356-018-3704-5.
- [195] Zhang Z, Tian J, Li J, Lv J, Wang S, Zhong Y. Investigation on combustion, performance and emission characteristics of a diesel engine fueled with diesel/alcohol/n-butanol blended fuels. Fuel 2022;320:123975. doi:10.1016/j.fuel.2022.123975.
- [196] Kuti OA, Sarathy SM, Nishida K. Spray combustion simulation study of waste cooking oil biodiesel and diesel under direct injection diesel engine conditions. Fuel 2020;267. doi:10.1016/j.fuel.2020.117240.
- [197] Reitz RD, Beale JC. Modeling Spray Atomization With the Kelvin-Helmholtz/Rayleigh-Taylor Hybrid Model. At Sprays 1999;9:623–50. doi:10.1615/atomizspr.v9.i6.40.
- [198] Reitz RD. Modeling Atomization Processes in High-Pressure Vaporizing

- Sprays. *At Spray Technol* 1987;3:309–37.
- [199] Levich VG. *Physicochemical hydrodynamics*. Englewood Cliffs, N.J., Prentice-Hall; 1962.
- [200] Pei Y, Hawkes ER, Kook S, Goldin GM, Lu T. Modelling n-dodecane spray and combustion with the transported probability density function method. *Combust Flame* 2015;162:2006–19. doi:10.1016/j.combustflame.2014.12.019.
- [201] ANSYS FLUENT theory guide. ANSYS, Inc., Canonsburg, PA, USA; 2018.
- [202] Brookes SJ, Moss JB. Predictions of soot and thermal radiation properties in confined turbulent jet diffusion flames. *Combust Flame* 1999;116:486–503. doi:https://doi.org/10.1016/S0010-2180(98)00056-X.
- [203] Pang KM, Ng h, Gan S. In-cylinder diesel spray combustion simulations using parallel computation: A performance benchmarking study. *Appl Energy* 2012;93:466–78. doi:10.1016/j.apenergy.2011.12.023.
- [204] Tan JY, Ng HK, Gan S, Bonatesta F. Numerical Simulations of Constant-Volume Spray Combustion of n-Heptane with Chemical Kinetics. *Indian J Sci Technol* 2017;10:1–5. doi:10.17485/ijst/2017/v10i7/111458.
- [205] Fenimore CP, Jones GW. Oxidation of Soot by Hydroxyl Radicals. *J Phys Chem* 1967;71:593–7.
- [206] Pepiot-Desjardins P, Pitsch H. An automatic chemical lumping method for the reduction of large chemical kinetic mechanisms. *Combust Theory Model* 2008;12:1089–108. doi:10.1080/13647830802245177.
- [207] Vié A, Franzelli B, Gao Y, Lu T, Wang H, Ihme M. Analysis of segregation and bifurcation in turbulent spray flames: A 3D counterflow configuration. *Proc Combust Inst* 2015;35:1675–83. doi:10.1016/j.proci.2014.06.083.
- [208] Niemeyer KE, Sung CJ. Mechanism reduction for multicomponent surrogates: A case study using toluene reference fuels. *Combust Flame* 2014;161:2752–64. doi:10.1016/j.combustflame.2014.05.001.
- [209] ANSYS.Inc. CHEMKIN-PRO RELEASE 17.2 2016.
- [210] Wang X, Liu H, Zheng Z, Yao M. Development of a reduced n-butanol/biodiesel mechanism for a dual fuel engine. *Fuel* 2015;157:87–96. doi:10.1016/j.fuel.2015.04.053.
- [211] Cheng X, Ng HK, Gan S, Ho JH, Pang KM. Development and validation of a generic reduced chemical kinetic mechanism for CFD spray combustion modelling of biodiesel fuels. *Combust Flame* 2015;162:2354–70. doi:10.1016/j.combustflame.2015.02.003.
- [212] Shen HPS, Steinberg J, Vanderover J, Oehlschlaeger MA. A Shock tube study of the ignition of n-heptane, n-decane, n-dodecane, and n-tetradecane at elevated pressures. *Energy and Fuels* 2009;23:2482–9. doi:10.1021/ef8011036.

- [213] Vasu SS, Davidson DF, Hong Z, Vasudevan V, Hanson RK. n-dodecane oxidation at high-pressures: Measurements of ignition delay times and OH concentration time-histories. *Proc Combust Inst* 2009;32 I:173–80. doi:10.1016/j.proci.2008.05.006.
- [214] Shao J, Choudhary R, Peng Y, Davidson DF, Hanson RK. A shock tube study of n-heptane, iso-octane, n-dodecane and iso-octane/n-dodecane blends oxidation at elevated pressures and intermediate temperatures. *Fuel* 2019;243:541–53. doi:10.1016/j.fuel.2019.01.152.
- [215] Heufer KA, Fernandes RX, Olivier H, Beeckmann J, Röhl O, Peters N. Shock tube investigations of ignition delays of n-butanol at elevated pressures between 770 and 1250 K. *Proc Combust Inst* 2011;33:359–66. doi:10.1016/j.proci.2010.06.052.
- [216] Vranckx S, Heufer KA, Lee C, Olivier H, Schill L, Kopp WA, et al. Role of peroxy chemistry in the high-pressure ignition of n-butanol - experiments and detailed kinetic modelling. *Combust Flame* 2011;158:1444–55. doi:10.1016/j.combustflame.2010.12.028.
- [217] Ji C, Dames E, Wang YL, Wang H, Egolfopoulos FN. Propagation and extinction of premixed C5-C12 n-alkane flames. *Combust Flame* 2010;157:277–87. doi:10.1016/j.combustflame.2009.06.011.
- [218] Kumar K, Sung C-J. Laminar flame speeds and extinction limits of preheated n-decane/O<sub>2</sub>/N<sub>2</sub> and n-dodecane/O<sub>2</sub>/N<sub>2</sub> mixtures. *Combust Flame* 2007;151:209–24. doi:10.1016/j.combustflame.2007.05.002.
- [219] Hui X, Sung CJ. Laminar flame speeds of transportation-relevant hydrocarbons and jet fuels at elevated temperatures and pressures. *Fuel* 2013;109:191–200. doi:10.1016/j.fuel.2012.12.084.
- [220] Veloo PS, Wang YL, Egolfopoulos FN, Westbrook CK. A comparative experimental and computational study of methanol, ethanol, and n-butanol flames. *Combust Flame* 2010;157:1989–2004. doi:10.1016/j.combustflame.2010.04.001.
- [221] Gu X, Huang Z, Wu S, Li Q. Laminar burning velocities and flame instabilities of butanol isomers-air mixtures. *Combust Flame* 2010;157:2318–25. doi:10.1016/j.combustflame.2010.07.003.
- [222] Castaldi MJ, Marinov NM, Melius CF, Huang J, Senkan SM, Pitz WJ, et al. Experimental and Modeling Investigation of Aromatic and Polycyclic Aromatic Hydrocarbon Formation in a Premixed Ethylene Flame. *Symp Combust* 1996;26:693–702.
- [223] Hansen N, Harper MR, Green WH. High-temperature oxidation chemistry of n-butanol - experiments in low-pressure premixed flames and detailed kinetic modeling. *Phys Chem Chem Phys* 2011;13:20262–74. doi:10.1039/c1cp21663e.
- [224] Choo EJC, Cheng X, Ng HK, Gan S, Scribano G. Development and validation of a new n-dodecane-n-butanol-PAH reduced mechanism under diesel engine-

- relevant conditions. *Fuel* 2022;319:123829. doi:10.1016/j.fuel.2022.123829.
- [225] Som S, Aggarwal SK. Effects of primary breakup modeling on spray and combustion characteristics of compression ignition engines. *Combust Flame* 2010;157:1179–93. doi:10.1016/j.combustflame.2010.02.018.
- [226] Han Z, Uludogan A, Hampson GJ, Reitz RD. Mechanism of soot and NOx emission reduction using multiple-injection in a diesel engine. *SAE Tech Pap* 1996. doi:10.4271/960633.
- [227] Bhattacharjee S, Haworth DC. Simulations of transient n-heptane and n-dodecane spray flames under engine-relevant conditions using a transported PDF method. *Combust Flame* 2013;160:2083–102. doi:10.1016/j.combustflame.2013.05.003.
- [228] Liu F, Shi Z, Zhang Z, Li Y, Sun C. Numerical study on critical ambient temperature for auto-ignition of the diesel spray under cold-start conditions. *Fuel* 2019;258:116191. doi:10.1016/j.fuel.2019.116191.
- [229] Senecal APK, Pomraning E, Richards KJ, Briggs TE, Choi CY, Patterson MA. Multi-Dimensional Modeling of Direct-Injection Diesel Liquid Length and Flame Lift-off Length using CFD Parallel Detailed Chemistry. *SAE Trans* 2003;112:1331–51.
- [230] Higgins B, Siebers D. Measurement of the flame lift-off location on di diesel sprays using OH chemiluminescence. *SAE Tech Pap* 2001;110:739–53. doi:10.4271/2001-01-0918.
- [231] Zhang S, Wu W, Xu Z, Lee C-FF. Numerical Study on Spray and Flame Lift-Off Length of Acetone-Butanol-Ethanol and Diesel Blends in a Constant Volume Chamber. *Proc ASME 2016 Intern Combust Engine Fall Tech Conf* 2016:1–10.
- [232] Poon HM. Development of integrated chemical kinetic mechanism reduction scheme for diesel and biodiesel fuel surrogates for multi-dimensional CFD applications. PhD Thesis. University of Nottingham Malaysia, 2016.
- [233] Mohamed Ismail H, Ng HK, Gan S. Evaluation of non-premixed combustion and fuel spray models for in-cylinder diesel engine simulation. *Appl Energy* 2012;90:271–9. doi:10.1016/j.apenergy.2010.12.075.
- [234] Siebers D, Higgins B. Flame lift-off on direct-injection diesel sprays under quiescent conditions. *SAE Tech Pap* 2001. doi:10.4271/2001-01-0530.
- [235] Siebers D, Higgins B, Pickett L. Flame lift-off on direct-injection diesel fuel jets: Oxygen concentration effects. *SAE Tech Pap* 2002. doi:10.4271/2002-01-0890.
- [236] Leung KM, Lindstedt RP, Jones WP. A simplified reaction mechanism for soot formation in nonpremixed flames. *Combust Flame* 1991;87:289–305. doi:10.1016/0010-2180(91)90114-Q.
- [237] Bolla M, Wright YM, Boulouchos K, Borghesi G, Mastorakos E. Soot

- formation modeling of n-heptane sprays under diesel engine conditions using the conditional moment closure approach. *Combust Sci Technol* 2013;185:766–93. doi:10.1080/00102202.2012.752362.
- [238] Pang KM, Jangi M, Bai X-S, Schramm J. Investigation of Chemical Kinetics on Soot Formation Event of n-Heptane Spray Combustion. *SAE Tech Pap* 2014-01-1254 2014. doi:10.4271/2014-01-1254.
- [239] Vishwanathan G, Reitz RD. Development of a Practical Soot Modeling Approach and Its Application to Low-Temperature Diesel Combustion. *Combust Sci Technol* 2010;182:10550–1082. doi:10.1080/00102200903548124.
- [240] Cenker E, Bruneaux G, Pickett L, Schulz C. Study of soot formation and oxidation in the engine combustion network (ECN), Spray A: Effects of ambient temperature and oxygen concentration. *SAE Int J Engines* 2013;6:352–65. doi:10.4271/2013-01-0901.
- [241] Cheng X, Gan S, Ng HK. A numerical study on the quasi-steady spray and soot characteristics for soybean methyl ester and its blends with ethanol using CFD-reduced chemical kinetics approach. *Energy* 2020;200:117540. doi:10.1016/j.energy.2020.117540.
- [242] Liu H, Lee C-F, Liu Y, Huo M, Yao M. Spray and combustion characteristics of n-butanol in a constant volume combustion chamber at different oxygen concentrations. *SAE Tech Pap* 2011-01-1190 2011. doi:10.4271/2011-01-1190.
- [243] Salehi F, Cleary MJ, Masri AR, Ge Y, Klimenko AY. Sparse-Lagrangian MMC simulations of an n-dodecane jet at engine-relevant conditions. *Proc Combust Inst* 2017;36:3577–85. doi:10.1016/j.proci.2016.07.074.
- [244] Skeen SA, Manin J, Pickett LM. Simultaneous formaldehyde PLIF and high-speed schlieren imaging for ignition visualization in high-pressure spray flames. *Proc Combust Inst* 2015;35:3167–74. doi:10.1016/j.proci.2014.06.040.
- [245] Musculus MPB, Miles PC, Pickett LM. Conceptual models for partially premixed low-temperature diesel combustion. *Prog Energy Combust Sci* 2013;39:246–83. doi:10.1016/j.pecs.2012.09.001.
- [246] Idicheria CA, Pickett LM. Formaldehyde Visualization Near Lift-off Location in a Diesel Jet. *SAE Tech Pap* 2006-01-3434 2006:1–13.
- [247] Irannejad A, Banaeizadeh A, Jaber F. Large eddy simulation of turbulent spray combustion. *Combust Flame* 2015;162:431–50. doi:10.1016/j.combustflame.2014.07.029.
- [248] Pang KM, Jangi M, Bai XS, Schramm J, Walther JH, Glarborg P. Effects of ambient pressure on ignition and flame characteristics in diesel spray combustion. *Fuel* 2019;237:676–85. doi:10.1016/j.fuel.2018.10.020.
- [249] Ong JC, Pang KM, Walther JH. Prediction method for ignition delay time of

- liquid spray combustion in constant volume chamber. *Fuel* 2021;287:119539. doi:10.1016/j.fuel.2020.119539.
- [250] Pei Y, Hawkes ER, Bolla M, Kook S, Goldin GM, Yang Y, et al. An analysis of the structure of an n-dodecane spray flame using TPDF modelling. *Combust Flame* 2016;168:420–35. doi:10.1016/j.combustflame.2015.11.034.
- [251] Krisman A, Hawkes ER, Talei M, Bhagatwala A, Chen JH. Characterisation of two-stage ignition in diesel engine-relevant thermochemical conditions using direct numerical simulation. *Combust Flame* 2016;172:326–41. doi:10.1016/j.combustflame.2016.06.010.
- [252] Choo EJC, Cheng X, Scribano G, Ng HK, Gan S. Numerical investigation on the ignition and flame characteristics of n-dodecane-n-butanol spray under diesel engine conditions. *Fuel* 2022;325:124881. doi:10.1016/j.fuel.2022.124881.
- [253] Pandurangi SS, Bolla M, Wright YM, Boulouchos K, Skeen SA, Manin J, et al. Onset and progression of soot in high-pressure n-dodecane sprays under diesel engine conditions. *Int J Engine Res* 2016:1–17. doi:10.1177/1468087416661041.
- [254] Westbrook CK, Pitz WJ, Curran HJ. Chemical kinetic modeling study of the effects of oxygenated hydrocarbons on soot emissions from diesel engines. *J Phys Chem A* 2006;110:6912–22.

# APPENDIX

## Appendix A: Chemical Reactions for the DB105 Mechanism

H+O2<=>OH+O	9.756e+13	0.000	14842.26
O+H2<=>H+OH	4.589E+04	2.700	6260.00
OH+H2<=>H2O+H	1.024e+08	1.600	3298.28
OH+OH<=>O+H2O	3.973E+04	2.400	-2110.00
H+O2(+M)<=>HO2(+M)	5.116E+12	0.440	0.00
LOW / 6.328E+19	-1.400	0.00 /	
TROE/ 0.5	1E-30	1E+30	/
O2/0.85/ H2O/11.89/ CO/1.09/ CO2/2.18/ AR/0.40/			
HO2+H<=>OH+OH	7.485E+13	0.000	295.00
H2+O2<=>HO2+H	5.916E+05	2.433	53502.00
HO2+OH<=>H2O+O2	2.891e+13	0.000	-501.91
HO2+H<=>O+H2O	3.970E+12	0.000	671.00
HO2+O<=>OH+O2	4.000E+13	0.000	0.00
HO2+HO2<=>O2+H2O2	1.300E+11	0.000	-1630.00
DUPLICATE			
HO2+HO2<=>O2+H2O2	3.658E+14	0.000	12000.00
DUPLICATE			
H2O2+H<=>OH+H2O	2.410E+13	0.000	3970.00
H2O2+H<=>HO2+H2	6.050E+06	2.000	5200.00
H2O2+O<=>OH+HO2	9.630E+06	2.000	3970.00
H2O2+OH<=>HO2+H2O	2.000E+12	0.000	427.00
DUPLICATE			
H2O2+OH<=>HO2+H2O	2.670E+41	-7.000	37600.00
DUPLICATE			
OH+OH(+M)<=>H2O2(+M)	1.110E+14	-0.370	0.00
LOW / 2.010E+17	-0.584	-2293.00 /	
TROE / 0.7346	94.	1756.00	5182.0 /
H2/2.0/ H2O/6.00/ CO/1.75/ CO2/3.6/ AR/0.7/			

H+H+M<=>H2+M	1.780E+18	-1.000	0.00
H2/0.0/ H2O/0.0/ CO2/0.0/ AR/0.63/			
H+OH+M<=>H2O+M	4.400E+22	-2.000	0.00
H2/2.0/ H2O/6.30/ CO/1.75/ CO2/3.6/ AR/0.38/			
O+O+M<=>O2+M	1.200E+17	-1.000	0.00
H2/2.4/ H2O/15.4/ CO/1.75/ CO2/3.6/ AR/0.83/			
H+H+H2<=>H2+H2	9.000E+16	-0.600	0.00
H+H+H2O<=>H2+H2O	5.624E+19	-1.250	0.00
H+H+CO2<=>H2+CO2	5.500E+20	-2.000	0.00
O+H+M<=>OH+M	9.428E+18	-1.000	0.00
H2/2.0/ H2O/12.0/ CO/1.75/ CO2/3.6/ AR/0.7/			
CO+OH<=>CO2+H	7.046E+04	2.053	-355.67
DUPLICATE			
CO+OH<=>CO2+H	5.757E+12	-0.664	331.83
DUPLICATE			
CO+HO2<=>CO2+OH	1.570E+05	2.180	17942.61
CO+O(+M)=CO2(+M)	1.362E+10	0.000	2384.00
LOW / 1.173E+24 -2.79 4191. /			
H2/2.0/ H2O/12/ CO/1.75/ CO2/3.6/ AR/0.7/			
CO+O2<=>CO2+O	1.119E+12	0.000	47700.00
HCO+M<=>CO+H+M	1.870E+17	-1.000	17000.00
H2/2.0/ H2O/0.0/ CO/1.75/ CO2/3.6/			
HCO+H<=>CO+H2	1.200E+14	0.000	0.00
HCO+O<=>CO+OH	3.000E+13	0.000	0.00
HCO+O<=>CO2+H	3.000E+13	0.000	0.00
HCO+OH<=>CO+H2O	3.020E+13	0.000	0.00
HCO+O2<=>CO+HO2	1.204E+10	0.807	-727.00
HCO+H2O<=>CO+H+H2O	2.244E+18	-1.000	17000.00
CO+H2(+M)<=>CH2O(+M)	4.300E+07	1.500	79600.00
LOW / 5.070E+27 -3.420 84350.00 /			
TROE/ 0.9320 197.00 1540.00 10300. /			
H2/2.0/ H2O/6.0/ CH4/2.0/ CO/1.5/ CO2/2.0/ C2H6/3.0/ AR/0.7/			
HCO+H(+M)<=>CH2O(+M)	1.090E+12	0.480	-260.00



LOW / 1.350E+24 -2.570 1425.00 /  
 TROE/ 0.7824 271.0 2755.00 6570.0 /  
 H2/2.0/ H2O/6.0/ CH4/2.0/ CO/1.5/ CO2/2.0/ C2H6/3.0/ AR/0.7 /  
 CH2+H(+M)<=>CH3(+M) 2.500E+16 -0.800 0.00  
 LOW / 3.200E+27 -3.140 1230.00 /  
 TROE/ 0.6800 78.00 1995.0 5590.0 /  
 H2/2.0/ H2O/6.0/ CH4/2.0/ CO/1.5/ CO2/2.0/ C2H6/3.0/ AR/0.7/  
 CH2+O<=>HCO+H 8.000E+13 0.000 0.00  
 CH2+OH<=>CH2O+H 2.000E+13 0.000 0.00  
 CH2+H2<=>H+CH3 5.000E+05 2.000 7230.00  
 CH2+O2<=>HCO+OH 1.060E+13 0.000 1500.00  
 CH2+O2<=>CO2+H+H 2.640E+12 0.000 1500.00  
 CH2+HO2<=>CH2O+OH 2.000E+13 0.000 0.00  
 CH2+CH2<=>C2H2+H2 3.200E+13 0.000 0.00  
 CH2\*+N2<=>CH2+N2 1.500E+13 0.000 600.00  
 CH2\*+AR<=>CH2+AR 9.000E+12 0.000 600.00  
 CH2\*+O<=>CO+H2 1.500E+13 0.000 0.00  
 CH2\*+O<=>HCO+H 1.500E+13 0.000 0.00  
 CH2\*+OH<=>CH2O+H 3.000E+13 0.000 0.00  
 CH2\*+H2<=>CH3+H 7.000E+13 0.000 0.00  
 CH2\*+O2<=>H+OH+CO 2.800E+13 0.000 0.00  
 CH2\*+O2<=>CO+H2O 1.200E+13 0.000 0.00  
 CH2\*+H2O<=>CH2+H2O 3.000E+13 0.000 0.00  
 CH2\*+CO<=>CH2+CO 9.000E+12 0.000 0.00  
 CH2\*+CO2<=>CH2+CO2 7.000E+12 0.000 0.00  
 CH2\*+CO2<=>CH2O+CO 1.400E+13 0.000 0.00  
 CH2O+H(+M)<=>CH3O(+M) 5.400E+11 0.454 2600.00  
 LOW / 2.200E+30 -4.800 5560.00 /  
 TROE/ 0.7580 94.00 1555.0 4200.00 /  
 H2/2.0/ H2O/6.0/ CH4/2.0/ CO/1.5/ CO2/2.0/ C2H6/3.0/  
 CH2O+H<=>HCO+H2 2.300E+10 1.050 3275.00  
 CH2O+O<=>HCO+OH 3.900E+13 0.000 3540.00  
 CH2O+OH<=>HCO+H2O 3.430E+09 1.180 -447.00

CH2O+O2<=>HCO+HO2	1.000E+14	0.000	40000.00
CH2O+HO2<=>HCO+H2O2	1.000E+12	0.000	8000.00
CH3+H(+M)<=>CH4(+M)	1.270E+16	-0.630	383.00
LOW /	2.477E+33	-4.760	2440.00 /
TROE/	0.7830	74.00	2941.00 6964.0 /
H2/2.0/ H2O/6.0/ CH4/2.0/ CO/1.5/ CO2/2.0/ C2H6/3.0/ AR/0.7/			
CH3+O<=>CH2O+H	8.430E+13	0.000	0.00
CH3+OH<=>CH2+H2O	5.600E+07	1.600	5420.00
CH3+OH<=>CH2*+H2O	2.501E+13	0.000	0.00
CH3+O2<=>O+CH3O	3.083E+13	0.000	28800.00
CH3+O2<=>OH+CH2O	3.600E+10	0.000	8940.00
CH3+HO2<=>CH4+O2	1.000E+12	0.000	0.00
CH3+HO2<=>CH3O+OH	1.340E+13	0.000	0.00
CH3+H2O2<=>CH4+HO2	2.450E+04	2.470	5180.00
CH3+HCO<=>CH4+CO	8.480E+12	0.000	0.00
CH3+CH2O<=>CH4+HCO	3.320E+03	2.810	5860.00
CH3+CH2<=>C2H4+H	4.000E+13	0.000	0.00
CH3+CH2*<=>C2H4+H	1.200E+13	0.000	-570.00
CH3+CH3(+M)<=>C2H6(+M)	2.120E+16	-0.970	620.00
LOW /	1.770E+50	-9.670	6220.00 /
TROE/	0.5325	151.0	1038.00 4970.0 /
H2/2.0/ H2O/6.0/ CH4/2.0/ CO/1.5/ CO2/2.0/ C2H6/3.0/ AR/0.7/			
CH3+CH3<=>H+C2H5	4.990E+12	0.100	10600.00
CH3O+H<=>CH2O+H2	2.000E+13	0.000	0.00
CH3O+H<=>CH3+OH	3.200E+13	0.000	0.00
CH3O+H<=>CH2*+H2O	1.600E+13	0.000	0.00
CH3O+O<=>CH2O+OH	1.000E+13	0.000	0.00
CH3O+OH<=>CH2O+H2O	5.000E+12	0.000	0.00
CH3O+O2<=>CH2O+HO2	4.280E-13	7.600	-3530.00
CH4+H<=>CH3+H2	6.600E+08	1.620	10840.00
CH4+O<=>CH3+OH	1.020E+09	1.500	8600.00
CH4+OH<=>CH3+H2O	1.000E+08	1.600	3120.00
CH4+CH2<=>CH3+CH3	2.460E+06	2.000	8270.00

CH4+CH2* $\rightleftharpoons$ CH3+CH3	1.600E+13	0.000	-570.00
C2H3 (+M) $\rightleftharpoons$ C2H2+H (+M)	3.860E+07	1.620	37048.2
LOW / 2.565E+27 -3.400 35798.72 /			
TROE/ 1.9816 5383.7 4.2932 -0.0795 /			
H2/2.0/ H2O/6.0/ CH4/2.0/ CO/1.5/ CO2/2.0/ C2H6/3.0/ AR/0.7/ C2H2/3.00/ C2H4/3.00/			
C2H2+O $\rightleftharpoons$ CH2+CO	4.080E+06	2.000	1900.00
C2H2+OH $\rightleftharpoons$ CH3+CO	4.830E-04	4.000	-2000.00
C2H2+HCO $\rightleftharpoons$ C2H3+CO	1.000E+07	2.000	6000.00
C2H2+CH3 $\rightleftharpoons$ aC3H5	2.68E+53	-12.82	35730.0
C2H3+H(+M) $\rightleftharpoons$ C2H4(+M)	6.080E+12	0.270	280.00
LOW / 1.400E+30 -3.860 3320.00 /			
TROE/ 0.7820 207.50 2663.00 6095.00/			
H2/2.0/ H2O/6.0/ CH4/2.0/ CO/1.5/ CO2/2.0/ C2H6/3.0/ AR/0.7/ C2H2/3.00/ C2H4/3.00/			
C2H3+H $\rightleftharpoons$ C2H2+H2	9.000E+13	0.000	0.00
C2H3+O $\rightleftharpoons$ CH3+CO	4.800E+13	0.000	0.00
C2H3+OH $\rightleftharpoons$ C2H2+H2O	3.011E+13	0.000	0.00
C2H3+O2 $\rightleftharpoons$ C2H2+HO2	1.340E+06	1.610	-383.40
C2H3+O2 $\rightleftharpoons$ CH2CHO+O	3.000E+11	0.290	11.00
C2H3+O2 $\rightleftharpoons$ HCO+CH2O	4.600E+16	-1.390	1010.00
C2H3+HO2 $\rightleftharpoons$ CH2CHO+OH	1.000E+13	0.000	0.00
C2H3+H2O2 $\rightleftharpoons$ C2H4+HO2	1.210E+10	0.000	-596.00
C2H3+HCO $\rightleftharpoons$ C2H4+CO	9.033E+13	0.000	0.00
C2H3+HCO $\rightleftharpoons$ C2H3CHO	1.800E+13	0.00	0.0
C2H3+CH3 $\rightleftharpoons$ C2H2+CH4	3.920E+11	0.000	0.00
C2H3+CH3 (+M) $\rightleftharpoons$ C3H6(+M)	2.500E+13	0.000	0.00
LOW / 4.270E+58 -11.940 9769.80 /			
TROE / 0.175 1340.6 60000.0 10139.8 /			
H2/2/ H2O/6/ CH4/2/ CO/1.5/ CO2/2/ C2H6/3/ AR/0.7/C2H2/3.00/ C2H4/3.00/			
C2H3+CH3 $\rightleftharpoons$ aC3H5+H	1.500E+24	-2.830	18618.0
C2H3+C2H3 $\rightleftharpoons$ C2H2+C2H4	9.600E+11	0.00	0.
CH2CHO $\rightleftharpoons$ CH3+CO	7.800E+41	-9.147	46900.00
CH2CHO+H $\rightleftharpoons$ CH3+HCO	9.000E+13	0.000	0.00
CH2CHO+O2 $\rightleftharpoons$ CH2O+CO+OH	1.800E+10	0.000	0.00

$C_2H_4+H(+M) \rightleftharpoons C_2H_5(+M)$                       3.975e+09   1.280   1290.63  
 LOW / 4.715e+18   0.000   755.26  
 /  
 TROE/ 0.76   40.00   1025.00   /  
 H2/2.0/ H2O/6.0/ CH4/2.0/ CO/1.5/ CO2/2.0/ C2H6/3.0/ AR/0.7/  
 $C_2H_4+H \rightleftharpoons C_2H_3+H_2$                       5.070E+07   1.900   12950.00  
 $C_2H_4+O \rightleftharpoons C_2H_3+OH$                       1.510E+07   1.900   3740.00  
 $C_2H_4+O \rightleftharpoons CH_3+HCO$                       1.920E+07   1.830   220.00  
 $C_2H_4+O \rightleftharpoons CH_2+CH_2O$                       3.840E+05   1.830   220.00  
 $C_2H_4+OH \rightleftharpoons C_2H_3+H_2O$                       3.600E+06   2.000   2500.00  
 $C_2H_4+HCO \rightleftharpoons C_2H_5+CO$                       1.000E+07   2.000   8000.00  
 $C_2H_4+CH_2 \rightleftharpoons aC_3H_5+H$                       2.000E+13   0.000   6000.00  
 $C_2H_4+CH_2^* \rightleftharpoons aC_3H_5+H$                       5.000E+13   0.000   0.00  
 $C_2H_4+CH_3 \rightleftharpoons C_2H_3+CH_4$                       2.270E+05   2.000   9200.00  
 $NC_3H_7 \rightleftharpoons CH_3+C_2H_4$                       9.600e+13   0.000   31022.94  
 $C_2H_4+O_2 \rightleftharpoons C_2H_3+HO_2$                       4.220E+13   0.000   60800.00  
 $C_2H_4+C_2H_3 \rightleftharpoons C_4H_7$                       7.93E+38   -8.47   14220.0  
 $C_2H_5+H(+M) \rightleftharpoons C_2H_6(+M)$                       5.210E+17   -0.990   1580.00  
 LOW / 1.990E+41   -7.080   6685.00   /  
 TROE / 0.8422   125.0   2219.00   6882.0 /  
 H2/2.0/ H2O/6.0/ CH4/2.0/ CO/1.5/ CO2/2.0/ C2H6/3.0/ AR/0.7/  
 $C_2H_5+H \rightleftharpoons C_2H_4+H_2$                       2.000E+12   0.000   0.00  
 $C_2H_5+O \rightleftharpoons CH_3+CH_2O$                       1.604E+13   0.000   0.00  
 $C_2H_5+O_2 \rightleftharpoons C_2H_4+HO_2$                       2.000E+10   0.000   0.00  
 $C_2H_5+HO_2 \rightleftharpoons C_2H_6+O_2$                       3.000E+11   0.000   0.00  
 $C_2H_5+HO_2 \rightleftharpoons C_2H_4+H_2O_2$                       3.000E+11   0.000   0.00  
 $C_2H_5+HO_2 \rightleftharpoons CH_3+CH_2O+OH$                       2.400E+13   0.000   0.00  
 $C_2H_5+H_2O_2 \rightleftharpoons C_2H_6+HO_2$                       8.700E+09   0.000   974.00  
 $C_2H_5+C_2H_3(+M) \rightleftharpoons C_4H_8(+M)$                       1.50E+13   0.00   0.0  
 LOW / 1.55E+56   -11.79   8984.5   /  
 TROE / 0.198   2277.9   60000.0   5723.2   /  
 H2/2/ H2O/6/ CH4/2/ CO/1.5/ CO2/2/ C2H6/3/ AR/0.7/  
 $C_2H_5+C_2H_3 \rightleftharpoons aC_3H_5+CH_3$                       3.90E+32   -5.22   19747.0

$C_2H_6+H \rightleftharpoons C_2H_5+H_2$	1.15E+08	1.900	7530.00
$C_2H_6+O \rightleftharpoons C_2H_5+OH$	8.98E+07	1.920	5690.00
$C_2H_6+OH \rightleftharpoons C_2H_5+H_2O$	3.54E+06	2.120	870.00
$C_2H_6+CH_2^* \rightleftharpoons C_2H_5+CH_3$	4.00E+13	0.000	-550.00
$C_2H_6+CH_3 \rightleftharpoons C_2H_5+CH_4$	6.14E+06	1.740	10450.00
$aC_3H_5+H(+M) \rightleftharpoons C_3H_6(+M)$	2.00E+14	0.00	0.0
LOW / 1.33E+60 -12.00 5967.8 /			
TROE / 0.020 1096.6 1096.6 6859.5 /			
H2/2/ H2O/6/ CH4/2/ CO/1.5/ CO2/2/ C2H6/3/ AR/0.7/			
$aC_3H_5+O \rightleftharpoons C_2H_3CHO+H$	6.00E+13	0.00	0.0
$aC_3H_5+OH \rightleftharpoons C_2H_3CHO+H+H$	4.20E+32	-5.16	30126.0
$aC_3H_5+O_2 \rightleftharpoons C_2H_3CHO+OH$	1.82E+13	-0.41	22859.0
$aC_3H_5+HO_2 \rightleftharpoons C_3H_6+O_2$	2.66E+12	0.00	0.0
$aC_3H_5+HO_2 \rightleftharpoons OH+C_2H_3+CH_2O$	6.60E+12	0.00	0.0
$aC_3H_5+HCO \rightleftharpoons C_3H_6+CO$	6.00E+13	0.00	0.0
$aC_3H_5+CH_3(+M) \rightleftharpoons C_4H_8(+M)$	1.00E+14	-0.32	-262.3
LOW / 3.91E+60 -12.81 6250.0 /			
TROE / 0.104 1606.0 60000.0 6118.4 /			
H2/2/ H2O/6/ CH4/2/ CO/1.5/ CO2/2/ C2H6/3/ AR/0.7/			
$C_3H_6+H(+M) \rightleftharpoons NC_3H_7(+M)$	1.33E+13	0.00	3260.7
LOW / 6.26E+38 -6.66 7000.0 /			
TROE / 1.000 1000.0 1310.0 48097.0 /			
H2/2/ H2O/6/ CH4/2/ CO/1.5/ CO2/2/ C2H6/3/ AR/0.7/			
$C_3H_6+H \rightleftharpoons C_2H_4+CH_3$	8.00E+21	-2.39	11180.0
$C_3H_6+H \rightleftharpoons aC_3H_5+H_2$	1.73E+05	2.50	2490.0
$C_3H_6+O \rightleftharpoons C_2H_3CHO+H+H$	0.40E+08	1.65	327.0
$C_3H_6+O \rightleftharpoons C_2H_5+HCO$	3.50E+07	1.65	-972.0
$C_3H_6+O \rightleftharpoons aC_3H_5+OH$	1.80E+11	0.70	5880.0
$C_3H_6+OH \rightleftharpoons aC_3H_5+H_2O$	3.10E+06	2.00	-298.0
$C_3H_6+HO_2 \rightleftharpoons aC_3H_5+H_2O_2$	9.60E+03	2.60	13910.0
$C_3H_6+CH_3 \rightleftharpoons aC_3H_5+CH_4$	2.20E+00	3.50	5675.0
$C_2H_3CHO+H \rightleftharpoons C_2H_4+HCO$	1.08E+11	0.454	5820.00
$C_2H_3CHO+O \rightleftharpoons C_2H_3+OH+CO$	3.00E+13	0.00	3540.00

$C_2H_3CHO+OH \rightleftharpoons C_2H_3+H_2O+CO$	3.43E+09	1.18	-447.00
$NC_3H_7+H \rightleftharpoons C_2H_5+CH_3$	3.70E+24	-2.92	12505.0
$NC_3H_7+H \rightleftharpoons C_3H_6+H_2$	1.80E+12	0.00	0.0
$NC_3H_7+O \rightleftharpoons C_2H_5+CH_2O$	9.60E+13	0.00	0.0
$NC_3H_7+OH \rightleftharpoons C_3H_6+H_2O$	2.40E+13	0.00	0.0
$NC_3H_7+O_2 \rightleftharpoons C_3H_6+HO_2$	9.00E+10	0.00	0.0
$NC_3H_7+HO_2 \rightleftharpoons C_2H_5+OH+CH_2O$	2.40E+13	0.00	0.0
$NC_3H_7+CH_3 \rightleftharpoons CH_4+C_3H_6$	1.10E+13	0.00	0.0
$C_4H_7+H(+M) \rightleftharpoons C_4H_8(+M)$	3.60E+13	0.00	0.0
LOW / 3.01E+48 -9.32 5833.6 /			
TROE / 0.498 1314.0 1314.0 50000.0 /			
H2/2/ H2O/6/ CH4/2/ CO/1.5/ CO2/2/ C2H6/3/ AR/0.7/			
$C_4H_7+H \rightleftharpoons CH_3+aC_3H_5$	2.00E+21	-2.00	11000.0
$C_4H_7+HO_2 \rightleftharpoons CH_2O+OH+aC_3H_5$	2.40E+13	0.00	0.0
$C_4H_7+HCO \rightleftharpoons C_4H_8+CO$	6.00E+13	0.00	0.0
$C_4H_8+H(+M) \rightleftharpoons pC_4H_9(+M)$	1.33E+13	0.00	3260.7
LOW / 6.26E+38 -6.66 7000.0 /			
TROE / 1.000 1000.0 1310.0 48097.0 /			
H2/2/ H2O/6/ CH4/2/ CO/1.5/ CO2/2/ C2H6/3/ AR/0.7/			
$C_4H_8+H \rightleftharpoons C_2H_4+C_2H_5$	1.60E+22	-2.39	11180.0
$C_4H_8+H \rightleftharpoons C_3H_6+CH_3$	3.20E+22	-2.39	11180.0
$C_4H_8+H \rightleftharpoons C_4H_7+H_2$	6.50E+05	2.54	6756.0
$C_4H_8+O \rightleftharpoons NC_3H_7+HCO$	3.30E+08	1.45	-402.0
$C_4H_8+O \rightleftharpoons C_4H_7+OH$	1.50E+13	0.00	5760.0
dupliCate			
$C_4H_8+O \rightleftharpoons C_4H_7+OH$	2.60E+13	0.00	4470.0
dupliCate			
$C_4H_8+OH \rightleftharpoons C_4H_7+H_2O$	7.00E+02	2.66	527.0
$C_4H_8+O_2 \rightleftharpoons C_4H_7+HO_2$	2.00E+13	0.00	50930.0
$C_4H_8+HO_2 \rightleftharpoons C_4H_7+H_2O_2$	1.00E+12	0.00	14340.0
$C_4H_8+CH_3 \rightleftharpoons C_4H_7+CH_4$	4.50E-01	3.65	7153.0
$!pC_4H_9 \rightleftharpoons C_2H_5+C_2H_4$	2.500e+11	0.000	28824.09
$pC_4H_9+H \rightleftharpoons C_2H_5+C_2H_5$	3.70E+24	-2.92	12505.0

pC4H9+H<=>C4H8+H2	1.80E+12	0.00	0.0
pC4H9+O<=>NC3H7+CH2O	9.60E+13	0.00	0.0
pC4H9+OH<=>C4H8+H2O	2.40E+13	0.00	0.0
pC4H9+O2<=>C4H8+HO2	2.70E+11	0.00	0.0
pC4H9+HO2<=>NC3H7+OH+CH2O	2.40E+13	0.00	0.0
pC4H9+CH3<=>C4H8+CH4	1.10E+13	0.00	0.0
C5H9=>aC3H5+C2H4	2.500e+13	0.000	30019.12
C5H9=>C2H3+C3H6	2.500e+13	0.000	30019.12
C5H10+H(+M)<=>PXC5H11(+M)	1.33E+13	0.00	3260.7
LOW / 6.26E+38 -6.66 7000.0 /			
TROE / 1.000 1000.0 1310.0 48097.0 /			
H2/2/ H2O/6/ CH4/2/ CO/1.5/ CO2/2/ C2H6/3/ AR/0.7/			
C5H10+H<=>C2H4+NC3H7	8.00E+21	-2.39	11180.0
C5H10+H<=>C3H6+C2H5	1.60E+22	-2.39	11180.0
C2H4+NC3H7<=>PXC5H11	3.00E+11	0.00	7300.0
C6H12+H(+M)<=>PXC6H13(+M)	1.33E+13	0.00	3260.7
LOW / 6.26E+38 -6.66 7000.0 /			
TROE / 1.000 1000.0 1310.0 48097.0 /			
H2/2/ H2O/6/ CH4/2/ CO/1.5/ CO2/2/ C2H6/3/ AR/0.7/			
C6H12+H<=>C2H4+pC4H9	8.00E+21	-2.39	11180.0
C6H12+H<=>C3H6+NC3H7	1.60E+22	-2.39	11180.0
C2H4+pC4H9<=>PXC6H13	3.00E+11	0.00	7300.0
C7H14+H(+M)<=>PXC7H15(+M)	1.33E+13	0.00	3260.7
LOW / 6.26E+38 -6.66 7000.0 /			
TROE / 1.000 1000.0 1310.0 48097.0 /			
H2/2/ H2O/6/ CH4/2/ CO/1.5/ CO2/2/ C2H6/3/ AR/0.7/			
C7H14+H<=>C2H4+PXC5H11	8.00E+21	-2.39	11180.0
C7H14+H<=>C3H6+pC4H9	1.60E+22	-2.39	11180.0
C2H4+PXC5H11<=>PXC7H15	3.00E+11	0.00	7300.0
C8H16+H(+M)<=>PXC8H17(+M)	1.33E+13	0.00	3260.7
LOW / 6.26E+38 -6.66 7000.0 /			
TROE / 1.000 1000.0 1310.0 48097.0 /			
H2/2/ H2O/6/ CH4/2/ CO/1.5/ CO2/2/ C2H6/3/ AR/0.7/			



C8H16+H<=>C2H4+PXC6H13	8.00E+21	-2.39	11180.0
C8H16+H<=>C3H6+PXC5H11	1.60E+22	-2.39	11180.0
C2H4+PXC6H13<=>PXC8H17	3.00E+11	0.00	7300.0
C9H18+H(+M)<=>PXC9H19(+M)	1.33E+13	0.00	3260.7
LOW / 6.26E+38 -6.66 7000.0 /			
TROE / 1.000 1000.0 1310.0 48097.0 /			
H2/2/ H2O/6/ CH4/2/ CO/1.5/ CO2/2/ C2H6/3/ AR/0.7/			
C9H18+H<=>C2H4+PXC7H15	8.00E+21	-2.39	11180.0
C9H18+H<=>C3H6+PXC6H13	1.60E+22	-2.39	11180.0
C2H4+PXC7H15<=>PXC9H19	3.00E+11	0.00	7300.0
C10H20+H(+M)<=>PXC10H21(+M)	1.33E+13	0.00	3260.7
LOW / 6.26E+38 -6.66 7000.0 /			
TROE / 1.000 1000.0 1310.0 48097.0 /			
H2/2/ H2O/6/ CH4/2/ CO/1.5/ CO2/2/ C2H6/3/ AR/0.7/			
C10H20+H<=>C2H4+PXC8H17	8.00E+21	-2.39	11180.0
C10H20+H<=>C3H6+PXC7H15	1.60E+22	-2.39	11180.0
C2H4+PXC8H17<=>PXC10H21	3.00E+11	0.00	7300.0
C12H24<=>PXC7H15+C5H9	3.500e+16	0.000	70936.90
C2H4+PXC10H21<=>PXC12H25	3.00E+11	0.00	7300.0
PXC12H25<=>S3XC12H25	3.67E+12	-0.60	14400.0
C3H6+PXC9H19<=>SXC12H25	3.00E+11	0.00	7300.0
C4H8+PXC8H17<=>SXC12H25	3.00E+11	0.00	7300.0
C5H10+PXC7H15<=>S3XC12H25	3.00E+11	0.00	7300.0
C10H20+C2H5<=>S3XC12H25	3.00E+11	0.00	7300.0
C6H12+PXC6H13<=>S3XC12H25	3.00E+11	0.00	7300.0
C9H18+NC3H7<=>S3XC12H25	3.00E+11	0.00	7300.0
C7H14+PXC5H11<=>S3XC12H25	3.00E+11	0.00	7300.0
C8H16+pC4H9<=>S3XC12H25	3.00E+11	0.00	7300.0
PXC10H21+C2H5<=>NC12H26	1.88E+14	-0.50	0.0
PXC9H19+NC3H7<=>NC12H26	1.88E+14	-0.50	0.0
PXC8H17+pC4H9<=>NC12H26	1.88E+14	-0.50	0.0
PXC7H15+PXC5H11<=>NC12H26	1.88E+14	-0.50	0.0
PXC6H13+PXC6H13<=>NC12H26	1.88E+14	-0.50	0.0





NC12H26+H<=>PXC12H25+H2	1.30E+06	2.54	6756.0
NC12H26+H<=>SXC12H25+H2	2.60E+06	2.40	4471.0
NC12H26+H<=>S3XC12H25+H2	3.90E+06	2.40	4471.0
NC12H26+O<=>PXC12H25+OH	1.90E+05	2.68	3716.0
NC12H26+O<=>SXC12H25+OH	9.52E+04	2.71	2106.0
NC12H26+O<=>S3XC12H25+OH	14.28E+04	2.71	2106.0
NC12H26+OH<=>PXC12H25+H2O	3.40E+03	2.66	527.0
NC12H26+OH<=>SXC12H25+H2O	7.40E+04	2.39	393.0
NC12H26+OH<=>S3XC12H25+H2O	10.10E+04	2.39	393.0
NC12H26+O2<=>PXC12H25+HO2	4.00E+13	0.00	50930.0
NC12H26+O2<=>SXC12H25+HO2	8.00E+13	0.00	47590.0
NC12H26+O2<=>S3XC12H25+HO2	12.00E+13	0.00	47590.0
NC12H26+HO2<=>PXC12H25+H2O2	6.76E+04	2.55	16490.0
NC12H26+HO2<=>SXC12H25+H2O2	8.90E+04	2.60	13910.0
NC12H26+HO2<=>S3XC12H25+H2O2	8.850E+04	2.60	13910.0
NC12H26+CH3<=>PXC12H25+CH4	1.81E+00	3.65	7153.0
NC12H26+CH3<=>SXC12H25+CH4	6.00E+00	3.46	5480.0
NC12H26+CH3<=>S3XC12H25+CH4	9.00E+00	3.46	5480.0
PXC12H25+O2=>C12H25O2	5.000e+13	0.000	0.00
C12H25O2=>PXC12H25+O2	2.750e+13	0.000	27400.0
SXC12H25+O2=>C12H25O2	5.000e+13	0.000	0.00
C12H25O2=>SXC12H25+O2	2.750e+13	0.000	27400.0
S3XC12H25+O2=>C12H25O2	5.000e+13	0.000	0.00
C12H25O2=>S3XC12H25+O2	2.750e+13	0.000	27400.0
C12H25O2=>C12OOH	1.510E+12	0.00	19000.0
C12OOH=>C12H25O2	1.000e+11	0.000	11500.00
PXC12H25+O2=>C12H24+HO2	3.500e+11	0.000	6000.00
C12H24+HO2=>PXC12H25+O2	3.160E+11	0.00	19500.0
SXC12H25+O2=>C12H24+HO2	3.500e+11	0.000	6000.00
C12H24+HO2=>SXC12H25+O2	3.160E+11	0.00	19500.0
S3XC12H25+O2=>C12H24+HO2	3.500e+11	0.000	6000.00
C12H24+HO2=>S3XC12H25+O2	3.160E+11	0.00	19500.0
C12OOH+O2=>O2C12H24OOH	4.6e+10	0.00	0000.00

$O_2C_{12}H_{24}OOH \Rightarrow C_{12}OOH + O_2$  2.510E+13 0.00 27400.0  
 $O_2C_{12}H_{24}OOH \rightleftharpoons OC_{12}H_{23}OOH + OH$  8.900e+10 0.000 17000  
 $OC_{12}H_{23}OOH \Rightarrow 3C_2H_4 + C_2H_5 + 2CH_2CHO + OH$  1.80e+15 0.000 42065  
 $HCO + HO_2 \Rightarrow CO_2 + H + OH$  3.0E13 0.0 0.0E0  
 $2HCO \Rightarrow H_2 + 2CO$  3.0E12 0.0 0.0E0  
 $OCHO + OH = HO_2CHO$  2.0E13 0.0 0.0E0  
 $H + CO_2 = OCHO$  7.5E13 0.0 2.9E4  
 $2HCO = CH_2O + CO$  1.8E13 0.0 0.0E0  
 $H + O + M = OH^* + M$  1.5E13 0.0 5.975E3  
 H2/1.0/  
 H2O/6.5/  
 O2/0.4/  
 N2/0.4/  
 $OH^* + H_2O = OH + H_2O$  5.93E12 0.5 -8.6E2  
 $OH^* + H_2 = OH + H_2$  2.95E12 0.5 -4.44E2  
 $OH^* + N_2 = OH + N_2$  1.08E11 0.5 -1.242E3  
 $OH^* + OH = 2OH$  6.01E12 0.5 -7.64E2  
 $OH^* + H = OH + H$  1.31E12 0.5 -1.67E2  
 $OH^* + O_2 = OH + O_2$  2.1E12 0.5 -4.78E2  
 $OH^* + CO_2 = OH + CO_2$  2.75E12 0.5 -9.68E2  
 $OH^* + CO = OH + CO$  3.23E12 0.5 -7.87E2  
 $OH^* + CH_4 = OH + CH_4$  3.36E12 0.5 -6.35E2  
 $CH + O_2 = CO + OH^*$  4.04E13 0.0 0.0E0  
 $HOCHO = CO + H_2O$  2.45E12 0.0 6.047E4  
 $HOCHO = CO_2 + H_2$  2.95E9 0.0 4.852E4  
 $OCHO + HO_2 = HOCHO + O_2$  3.5E10 0.0 -3.275E3  
 $HOCHO + OH \Rightarrow H_2O + CO_2 + H$  2.62E6 2.06 9.16E2  
 $HOCHO + OH \Rightarrow H_2O + CO + OH$  1.85E7 1.51 -9.62E2  
 $HOCHO + H \Rightarrow H_2 + CO_2 + H$  4.24E6 2.1 4.868E3  
 $HOCHO + H \Rightarrow H_2 + CO + OH$  6.03E13 -0.35 2.988E3  
 $HOCHO + CH_3 \Rightarrow CH_4 + CO + OH$  3.9E-7 5.8 2.2E3  
 $OCHO + H_2O_2 = HOCHO + HO_2$  2.4E12 0.0 1.0E4  
 $HOCHO + HO_2 \Rightarrow H_2O_2 + CO + OH$  1.0E12 0.0 1.192E4

$\text{HOCHO} + \text{O} \Rightarrow \text{CO} + 2\text{OH}$  1.77E18 -1.9 2.975E3  
 $\text{CH}_2\text{O} + \text{OCHO} = \text{HOCHO} + \text{HCO}$  5.6E12 0.0 1.36E4  
 $\text{CH}_3\text{O} + \text{CH}_3 = \text{CH}_2\text{O} + \text{CH}_4$  1.2E13 0.0 0.0E0  
 $\text{CH}_3\text{O} + \text{HO}_2 = \text{CH}_2\text{O} + \text{H}_2\text{O}_2$  3.01E11 0.0 0.0E0  
 $\text{CH}_2\text{O} + \text{H}(+\text{M}) = \text{CH}_2\text{OH}(+\text{M})$  5.4E11 0.454 3.6E3  
 H2/2.0/  
 H2O/6.0/  
 CO/1.5/  
 CO2/2.0/  
 CH4/2.0/  
 C2H6/3.0/  
 LOW/1.27E32 -4.82E0 6.53E3/  
 TROE/7.187E-1 1.03E2 1.291E3 4.16E3/  
 $\text{CH}_2\text{OH} + \text{O}_2 = \text{CH}_2\text{O} + \text{HO}_2$  1.51E15 -1.0 0.0E0  
 DUP  
 $\text{CH}_2\text{OH} + \text{O}_2 = \text{CH}_2\text{O} + \text{HO}_2$  2.41E14 0.0 5.017E3  
 DUP  
 $\text{CH}_2\text{OH} + \text{H} = \text{CH}_2\text{O} + \text{H}_2$  6.0E12 0.0 0.0E0  
 $\text{CH}_2\text{OH} + \text{HO}_2 = \text{CH}_2\text{O} + \text{H}_2\text{O}_2$  1.2E13 0.0 0.0E0  
 $\text{CH}_2\text{OH} + \text{HCO} = 2\text{CH}_2\text{O}$  1.8E14 0.0 0.0E0  
 $\text{OH} + \text{CH}_2\text{OH} = \text{H}_2\text{O} + \text{CH}_2\text{O}$  2.4E13 0.0 0.0E0  
 $\text{O} + \text{CH}_2\text{OH} = \text{OH} + \text{CH}_2\text{O}$  4.2E13 0.0 0.0E0  
 $\text{CH}_3 + \text{OH}(+\text{M}) = \text{CH}_2^* + \text{H}_2\text{O}(+\text{M})$  1.128E15 -0.63327 -4.9315597E2  
 HIGH/2.394E-3 4.096E0 -1.241875E3/  
 TROE/2.122E0 8.37667E2 2.32605E3 4.432E3/  
 $\text{CH}_3 + \text{OH}(+\text{M}) = \text{CH}_2\text{O} + \text{H}_2(+\text{M})$  2.82320078E5 1.46878 -3.27056495E3  
 HIGH/5.88E-14 6.721E0 -3.022227E3/  
 TROE/1.671E0 4.34782E2 2.93421E3 3.919E3/  
 $\text{CH}_3 + \text{OH}(+\text{M}) = \text{CH}_2\text{OH} + \text{H}(+\text{M})$  6.58E9 0.996 3.191122E3  
 HIGH/5.86E-6 5.009E0 1.8864578E3/  
 TROE/1.349E0 6.1215E2 2.29627E3 4.411E3/  
 $\text{CH}_3 + \text{OH}(+\text{M}) = \text{H} + \text{CH}_3\text{O}(+\text{M})$  1.2E9 1.014 1.1947831E4  
 HIGH/1.78E-46 1.859E1 -2.741384E1/

TROE/2.897E0 1.873279E3 3.32316E3 3.675E3/  
 CH3+OH(+M)=HCOH+H2(+M) 6.39E8 0.82548 -3.0979636E3  
 HIGH/3.0E-11 6.225E0 -3.125551E3/  
 TROE/2.386E0 8.06021E2 2.2017E3 4.44E3/  
 HCOH+OH=HCO+H2O 2.0E13 0.0 0.0E0  
 HCOH+H=CH2O+H 2.0E14 0.0 0.0E0  
 HCOH+O=CO2+2H 5.0E13 0.0 0.0E0  
 HCOH+O=CO+OH+H 3.0E13 0.0 0.0E0  
 HCOH+O2=CO2+H+OH 5.0E12 0.0 0.0E0  
 HCOH+O2=CO2+H2O 3.0E13 0.0 0.0E0  
 CH3+O2(+M)=CH3O2(+M) 7.812E9 0.9 0.0E0  
 LOW/6.85E24 -3.0E0 0.0E0/  
 TROE/6.0E-1 1.0E3 7.0E1 1.7E3/  
 CH3O2+CH3=2CH3O 2.54E12 0.0 -1.411E3  
 2CH3O2=>O2+2CH3O 1.4E16 -1.61 1.86E3  
 CH3O2+H=CH3O+OH 9.6E13 0.0 0.0E0  
 CH3O2+O=CH3O+O2 3.6E13 0.0 0.0E0  
 CH2\*+H=CH+H2 3.0E13 0.0 0.0E0  
 CH2\*+O2=CH2+O2 1.5E13 0.0 6.0E2  
 CH2+O2=CH2O+O 1.26E6 2.4202 1.604E3  
 CH2+O2=CO2+H2 2.05E9 0.9929 -2.694E2  
 CH2+O=>CO+2H 5.0E13 0.0 0.0E0  
 CH2+H=CH+H2 1.0E18 -1.56 0.0E0  
 DUP  
 CH2+OH=CH+H2O 1.13E7 2.0 3.0E3  
 CH+O2=HCO+O 3.3E13 0.0 0.0E0  
 CH+O=CO+H 5.7E13 0.0 0.0E0  
 CH+OH=HCO+H 3.0E13 0.0 0.0E0  
 CH2+H=CH+H2 2.7E11 0.67 2.57E4  
 DUP  
 CH+H2O=H+CH2O 1.713E13 0.0 -7.55E2  
 CH+CO2=HCO+CO 1.7E12 0.0 6.85E2  
 C2H6+CH=C2H5+CH2 1.1E14 0.0 -2.6E2

2C2H4=C2H5+C2H3 4.82E14 0.0 7.153E4  
CH3+C2H5=CH4+C2H4 1.18E4 2.45 -2.921E3  
2CH3(+M)=C2H5+H(+M) 4.989E12 0.099 1.06E4  
HIGH/3.802E-7 4.838E0 7.71E3/  
SRI/1.641E0 4.334E3 2.725E3 1.0E0 0.0E0/  
C2H5+O=CH3CHO+H 1.1E14 0.0 0.0E0  
C2H5+O2=CH3CHO+OH 4.908E-6 4.76 2.543E2  
PLOG/4.0E-2 4.908E-6 4.76E0 2.543E2/  
PLOG/1.0E0 6.803E-2 3.57E0 2.643E3/  
PLOG/1.0E1 8.265E2 2.41E0 5.285E3/  
CH3CHO(+M)=CH3+HCO(+M) 2.45E22 -1.74 8.635502E4  
LOW/1.02976E59 -1.13E1 9.591249E4/  
TROE/2.49E-3 7.1811861E2 6.08949E0 3.78001844E3/  
CH3CHO(+M)=CH4+CO(+M) 2.72E21 -1.74 8.635502E4  
LOW/1.14418E58 -1.13E1 9.591249E4/  
TROE/2.49E-3 7.1811861E2 6.08949E0 3.78001844E3/  
CH3CHO+H=CH2CHO+H2 2.72E3 3.1 5.21E3  
CH3CHO+OH=CH3+HOCHO 3.0E15 -1.076 0.0E0  
CH3CHO+OH=CH2CHO+H2O 1.72E5 2.4 8.15E2  
CH3CO3H=CH3CO2+OH 5.01E14 0.0 4.015E4  
CH3CO2+M=CH3+CO2+M 4.4E15 0.0 1.05E4  
CH2CHO(+M)=CH2CO+H(+M) 1.43E15 -0.15 4.56E4  
LOW/6.0E29 -3.8E0 4.3423898E4/  
TROE/9.85E-1 3.93E2 9.8E9 5.0E9/  
CH2CHO(+M)=CH3+CO(+M) 2.93E12 0.29 4.03E4  
LOW/9.52E33 -5.07E0 4.13E4/  
TROE/7.13E-17 1.15E3 4.99E9 1.79E9/  
CH2CHO+O2=CH2CO+HO2 1.88E5 2.37 2.373E4  
PLOG/1.0E-2 1.88E5 2.37E0 2.373E4/  
PLOG/1.0E-1 1.88E5 2.37E0 2.737E4/  
PLOG/1.0E0 2.51E5 2.33E0 2.38E4/  
PLOG/1.0E1 7.05E7 1.63E0 2.529E4/  
CH2+CO(+M)=CH2CO(+M) 8.1E11 0.0 0.0E0

H2/2.0/  
H2O/6.0/  
CO/1.5/  
CO2/2.0/  
CH4/2.0/  
C2H6/3.0/  
LOW/2.69E33 -5.11E0 7.095E3/  
TROE/5.907E-1 2.75E2 1.226E3 5.185E3/  
CH2CO+H=HCCO+H2 1.40068E15 -0.17131 8.78315059E3  
CH2CO+H=CH3+CO 7.70374E13 -0.17131 4.18315059E3  
CH2CO+O=CH2+CO2 1.75E12 0.0 1.35E3  
CH2CO+O=HCCO+OH 1.0E13 0.0 8.0E3  
CH2CO+OH=HCCO+H2O 1.0E13 0.0 2.0E3  
CH2CO+OH=CH2OH+CO 2.0E12 0.0 -1.01E3  
CH2CO+CH3=C2H5+CO 4.769E4 2.31199 9.468E3  
CH2\*+CH2CO=C2H4+CO 1.6E14 0.0 0.0E0  
HCCO+OH=>H2+2CO 1.0E14 0.0 0.0E0  
HCCO+O=>H+2CO 8.0E13 0.0 0.0E0  
HCCO+H=CH2\*+CO 1.0E14 0.0 0.0E0  
HCCO+O2=>OH+2CO 1.91E11 -0.02 1.02E3  
HCCO+O2=>CO2+CO+H 4.78E12 -0.142 1.15E3  
CH+CO+M=HCCO+M 7.57E22 -1.9 0.0E0  
CH+CH2O=H+CH2CO 9.46E13 0.0 -5.15E2  
CH+HCCO=CO+C2H2 5.0E13 0.0 0.0E0  
C2H4+O=CH2CHO+H 6.775E6 1.88 1.83E2  
C2H4+OH=CH3+CH2O 5.35E0 2.92 -1.732664E3  
PLOG/1.0E-2 5.35E0 2.92E0 -1.732664E3/  
PLOG/2.5E-2 3.19E1 2.71E0 -1.17233E3/  
PLOG/1.0E-1 5.55E2 2.36E0 -1.80817E2/  
PLOG/1.0E0 1.78E5 1.68E0 2.060519E3/  
PLOG/1.0E1 2.37E9 5.6E-1 6.006701E3/  
PLOG/1.0E2 2.76E13 -5.0E-1 1.1455055E4/  
C2H4+OH=CH3CHO+H 2.37E-7 5.3 -2.050584E3

PLOG/1.0E-2 2.37E-7 5.3E0 -2.050584E3/  
 PLOG/2.5E-2 8.73E-5 4.57E0 -6.17957E2/  
 PLOG/1.0E-1 4.03E-1 3.54E0 1.881689E3/  
 PLOG/1.0E0 2.38E-2 3.91E0 1.722729E3/  
 PLOG/1.0E1 8.25E8 1.01E0 1.0507256E4/  
 PLOG/1.0E2 6.8E9 8.1E-1 1.3867273E4/  
 C2H4+OH=C2H3OH+H 1.04E4 2.6 4.121038E3  
 PLOG/1.0E-2 1.04E4 2.6E0 4.121038E3/  
 PLOG/2.5E-2 1.07E4 2.6E0 4.128986E3/  
 PLOG/1.0E-1 1.52E4 2.56E0 4.238271E3/  
 PLOG/1.0E0 3.19E5 2.19E0 5.255615E3/  
 PLOG/1.0E1 1.94E8 1.43E0 7.82878E3/  
 PLOG/1.0E2 8.55E10 7.5E-1 1.1490821E4/  
 C2H4+OH=pC2H4OH 1.74E43 -10.46086 7.69872927E3  
 PLOG/1.0E-2 1.74E43 -1.046086E1 7.69872927E3/  
 PLOG/2.5E-2 3.25E37 -8.62888E0 5.21465591E3/  
 PLOG/1.0E-1 1.84E35 -7.75006E0 4.90885935E3/  
 PLOG/1.0E0 2.56E36 -7.75206E0 6.94610961E3/  
 PLOG/1.0E1 3.7E33 -6.57294E0 7.60589462E3/  
 PLOG/1.0E2 1.12E26 -4.10119E0 5.75695429E3/  
 C2H3OH+O2=CH2CHO+HO2 5.31E11 0.21 3.983E4  
 C2H3OH+O=CH2CHO+OH 1.875E6 1.9 -8.6E2  
 C2H3OH+OH=CH2CHO+H2O 3.33E9 1.1 5.405E2  
 C2H3OH+CH3=CH2CHO+CH4 2.03E-8 5.9 1.052E3  
 C2H3OH+H=CH2CHO+H2 1.48E3 3.077 7.22E3  
 C2H3OH+H=pC2H4OH 3.01E8 1.577 3.67E3  
 C2H3OH+HO2=CH3CHO+HO2 1.49E5 1.67 6.81E3  
 C2H3OH=CH3CHO 7.42E46 -10.56 6.742E4  
 PLOG/1.0E-1 7.42E46 -1.056E1 6.72E4/  
 PLOG/1.0E0 4.42E42 -9.09E0 6.7069198E4/  
 PLOG/1.0E2 2.9E27 -4.35E0 6.1612896E4/  
 C2H3OH=C2H3+OH 6.899E21 -1.564 1.107E5  
 REV/2.41E13 0.0E0 0.0E0/

$C_2H_3OH=CH_2CHO+H$  3.643E15 -0.397 9.539E4  
 REV/2.4E13 0.0E0 1.251E4/  
 $CH+CH_4=C_2H_4+H$  6.0E13 0.0 0.0E0  
 $C_2H_3+O_2=>H+CO+CH_2O$  5.19E15 -1.26 3.31262E3  
 $C_2H_2+O=HCCO+H$  2.958E9 1.28 2.472E3  
 $C_2H_2+OH=CH_2CO+H$  1.578E3 2.56 -8.445E2  
 PLOG/1.0E-2 1.578E3 2.56E0 -8.445E2/  
 PLOG/2.5E-2 1.518E4 2.28E0 -2.921E2/  
 PLOG/1.0E-1 3.017E5 1.92E0 5.981E2/  
 PLOG/1.0E0 7.528E6 1.55E0 2.106E3/  
 PLOG/1.0E1 5.101E6 1.65E0 3.4E3/  
 PLOG/1.0E2 1.457E4 2.45E0 4.477E3/  
 $CH_3OCO=CH_2OCHO$  1.629E12 -0.18 4.067E4  
 $CH_3+CO_2=CH_3OCO$  4.76E7 1.54 3.47E4  
 $CH_3O+CO=CH_3OCO$  1.55E6 2.02 5.73E3  
 $CH_2O+HCO=CH_2OCHO$  1.5E11 0.0 1.19E4  
 $H+C_3H_6=NC_3H_7$  2.5E11 0.51 2.62E3  
 $C_3H_6+O=>CH_2CO+CH_3+H$  2.5E7 1.76 7.6E1  
 $C_3H_6+O=>CH_3CHCO+2H$  2.5E7 1.76 7.6E1  
 $C_3H_6+C_2H_5=aC_3H_5+C_2H_6$  1.0E11 0.0 9.8E3  
 $C_3H_6+OH=C_3H_6OH$  9.93E11 0.0 -9.6E2  
 $C_3H_6OH+O_2=HOC_3H_6O_2$  1.2E11 0.0 -1.1E3  
 $HOC_3H_6O_2=>CH_3CHO+CH_2O+OH$  1.25E10 0.0 1.89E4  
 $C_3H_4-a+H=aC_3H_5$  9.6E61 -14.67 2.6E4  
 PLOG/1.0E-1 9.6E61 -1.467E1 2.6E4/  
 PLOG/1.0E0 1.52E59 -1.354E1 2.6949E4/  
 PLOG/2.0E0 3.78E57 -1.298E1 2.6785E4/  
 PLOG/5.0E0 7.34E54 -1.209E1 2.6187E4/  
 PLOG/1.0E1 2.4E52 -1.13E1 2.54E4/  
 PLOG/1.0E2 6.9E41 -8.06E0 2.13E4/  
 $aC_3H_5+H=C_3H_4-a+H_2$  1.232E3 3.035 2.582E3  
 $aC_3H_5+OH=C_3H_4-a+H_2O$  6.0E12 0.0 0.0E0  
 $aC_3H_5+CH_3=C_3H_4-a+CH_4$  3.0E12 -0.32 -1.31E2



aC3H5+C2H5=C2H6+C3H4-a 4.0E11 0.0 0.0E0  
aC3H5+C2H5=C2H4+C3H6 4.0E11 0.0 0.0E0  
aC3H5+C2H3=C2H4+C3H4-a 1.0E12 0.0 0.0E0  
2aC3H5=C3H4-a+C3H6 8.43E10 0.0 -2.62E2  
aC3H5+O2=C3H4-a+HO2 4.99E15 -1.4 2.2428E4  
PLOG/1.0E0 4.99E15 -1.4E0 2.2428E4/  
PLOG/1.0E1 2.18E21 -2.85E0 3.0755E4/  
C3H4-a+HO2=>CH2CO+CH2+OH 4.0E12 0.0 1.9E4  
C3H4-a+OH=CH2CO+CH3 3.12E12 0.0 -3.97E2  
C3H4-a+O=C2H4+CO 2.0E7 1.8 1.0E3  
C3H4-a+O=C2H2+CH2O 3.0E-3 4.61 -4.243E3  
C3H4-a+HO2=>C2H4+CO+OH 1.0E12 0.0 1.4E4  
C2H2+CH3=C3H4-a+H 2.4E9 0.91 2.07E4  
PLOG/1.0E-1 2.4E9 9.1E-1 2.07E4/  
PLOG/1.0E0 5.14E9 8.6E-1 2.2153E4/  
PLOG/2.0E0 1.33E10 7.5E-1 2.2811E4/  
PLOG/5.0E0 9.2E10 5.4E-1 2.395E4/  
PLOG/1.0E1 5.1E11 3.5E-1 2.5E4/  
PLOG/1.0E2 7.3E12 1.1E-1 2.85E4/  
CH3CHCO+OH=C2H5+CO2 1.73E12 0.0 -1.01E3  
CH3CHCO+H=C2H5+CO 4.4E12 0.0 1.459E3  
CH3CHCO+O=CH3CHO+CO 3.2E12 0.0 -4.37E2  
NC3H7+O2=NC3H7O2 4.52E12 0.0 0.0E0  
NC3H7O2=C3H6+HO2 4.308E36 -7.5 3.951E4  
C2H3+C2H5=C4H8 9.0E12 0.0 0.0E0  
NC3H7CHO+O2=NC3H7CO+HO2 1.2E5 2.5 3.756E4  
NC3H7CHO+OH=NC3H7CO+H2O 2.0E6 1.8 -1.3E3  
NC3H7CHO+H=NC3H7CO+H2 4.14E9 1.12 2.32E3  
NC3H7CHO+O=NC3H7CO+OH 5.94E12 0.0 1.868E3  
NC3H7CHO+HO2=NC3H7CO+H2O2 4.09E4 2.5 1.02E4  
NC3H7CHO+CH3=NC3H7CO+CH4 2.89E-3 4.62 3.21E3  
NC3H7CO=NC3H7+CO 1.0E11 0.0 9.6E3  
NC4H9OH(+M)=CH3+C3H6OH(+M) 3.79E24 -2.23 8.807E4

LOW/1.782E60 -1.228E1 8.398E4/  
TROE/2.352E-1 7.24E2 5.0E9 5.0E9/  
NC4H9OH(+M)=C2H5+pC2H4OH(+M) 5.53E24 -2.23 8.901E4  
LOW/6.632E59 -1.213E1 8.472E4/  
TROE/2.438E-1 7.4406E2 5.0E9 5.0E9/  
NC4H9OH(+M)=NC3H7+CH2OH(+M) 3.02E23 -1.88 8.571E4  
LOW/1.416E59 -1.193E1 8.398E4/  
TROE/7.646E-1 8.344E9 7.248E2 8.214E9/  
NC4H9OH(+M)=C4H81+H2O(+M) 3.52E13 0.0 6.723E4  
LOW/1.69E75 -1.704E1 6.475E4/  
TROE/8.0E-2 1.0E0 9.924E9 9.924E9/  
H+C4H8OH-1=NC4H9OH 4.0E13 0.0 0.0E0  
NC4H9OH+H=C4H8OH-1+H2 8.789E4 2.68 2.915E3  
NC4H9OH+OH=C4H8OH-1+H2O 3.61E3 2.89 -2.291E3  
NC4H9OH+O=C4H8OH-1+OH 1.45E5 2.47 8.76E2  
NC4H9OH+O2=HO2+C4H8OH-1 2.0E13 0.0 4.68E4  
NC4H9OH+HO2=C4H8OH-1+H2O2 3.5E-5 5.26 8.268E3  
NC4H9OH+CH3=C4H8OH-1+CH4 1.993E1 3.37 7.634E3  
NC4H9OH+HCO=C4H8OH-1+CH2O 1.0E7 1.9 1.7E4  
NC4H9OH+C2H5=C4H8OH-1+C2H6 2.01E11 0.0 7.9E3  
C2H3OH+C2H5=C4H8OH-1 8.8E3 2.48 6.13E3  
NC3H7CHO+H=C4H8OH-1 8.0E12 0.0 9.5E3  
C4H7OH1-1+H=C4H8OH-1 2.5E11 0.51 2.62E3  
C4H7OH1-1+HO2=NC3H7CHO+HO2 1.49E5 1.67 6.81E3  
C2H3OH+HOCHO=CH3CHO+HOCHO 2.81E-2 3.286 -4.509E3  
REV/7.04E4 1.209E0 5.56E2/  
C4H7OH1-1+HOCHO=NC3H7CHO+HOCHO 2.81E-2 3.286 -4.509E3  
REV/7.04E4 1.209E0 5.56E2/  
C4H7OH1-1=NC3H7CHO 8.59E11 0.318 5.59E4  
C4H7OH1-1+H=C4H81+OH 6.26E13 0.0 4.5E3  
C4H7OH1-1+H=C2H3OH+C2H5 6.26E13 0.0 4.5E3  
C4H7OH1-1=C2H5+CH2CHO 2.214E22 -1.576 9.752E4  
C4H8OH-1+O2=NC3H7CHO+HO2 3.78E20 -2.429 3.09E3

PLOG/1.0E-3 5.26E17 -1.637E0 8.38E2/  
 PLOG/1.0E-2 5.26E17 -1.637E0 8.38E2/  
 PLOG/1.0E-1 5.26E17 -1.637E0 8.38E2/  
 PLOG/1.0E0 5.28E17 -1.638E0 8.39E2/  
 PLOG/1.0E1 1.54E18 -1.771E0 1.12E3/  
 PLOG/1.0E2 3.78E20 -2.429E0 3.09E3/  
 C4H8OH-1+O2=C4H8OH-1O2 6E12 0.0 0.0E0  
 C4H8OH-1O2=C4H7OH-1OOH-3 2.5E10 0.0 2.045E4  
 C4H8OH-1O2=C4H7OH1-1+HO2 4.308E36 -7.5 3.951E4  
 C4H7OH-1OOH-3=>OH+HOCHO+C3H6 1.0E13 0.0 3.0E4  
 C4H7OH-1OOH-3+O2=C4H7OH-1OOH-3O2 7.54E12 0.0 0.0E0  
 C4H7OH-1OOH-3O2=C4OHket1-3+OH 1.25E10 0.0 1.545E4  
 C4OHket1-3=>OH+CH2OCHO+CH3CHO 1E16 0.0 3.9E4  
 H2+C2H<=>C2H2+H 0.1080E+14 0.0000 0.2165E+04  
 C2H2+C2H<=>C4H2+H 0.9030E+14 0.0000 0.0000E+00  
 C2H2+OH<=>C2H+H2O 0.6000E+14 0.0000 0.1292E+05  
 C2H2+M<=>C2H+H+M 0.1140E+18 0.0000 0.1068E+06  
 O2/ 0.400/ H2O/ 6.500/ CO/ 0.750/  
 C4H2+O<=>C3H2+CO 0.7890E+13 0.0000 0.1348E+04  
 C4H2+OH<=>C3H2+HCO 0.6680E+13 0.0000 -.4087E+03  
 2CH2<=>C2H2+2H 0.1080E+15 0.0000 0.7959E+03  
 C2H+C2H3<=>2C2H2 0.1900E+14 0.0000 0.0000E+00  
 C2H+OH<=>CH2+CO 0.1810E+14 0.0000 0.0000E+00  
 C3H3+O<=>C2H2+CO+H 0.1390E+15 0.0000 0.0000E+00  
 C3H3+OH<=>C3H2+H2O 0.2000E+14 0.0000 0.0000E+00  
 C4H3+M<=>C4H2+H+M 0.1120E+17 0.0000 0.4651E+05  
 O2/ 0.400/ H2O/ 6.500/ CO/ 0.750/  
 C2H2+CH2<=>C3H3+H 0.1200E+14 0.0000 0.6577E+04  
 2C2H2<=>C4H2+H2 0.1510E+14 0.0000 0.4242E+05  
 2C2H3<=>C4H5+H 0.4000E+14 0.0000 0.0000E+00  
 C2H3+CH2O<=>C2H4+HCO 0.5420E+04 2.8100 0.5824E+04  
 C2H4+C2H<=>C4H4+H 0.1200E+14 0.0000 0.0000E+00  
 C3H2+O<=>C2H+H+CO 0.6800E+14 0.0000 0.0000E+00

$C_3H_2+OH \rightleftharpoons C_2H_2+CO+H$  0.5000E+14 0.0000 0.0000E+00  
 $C_3H_3+O \rightleftharpoons CH_2O+C_2H$  0.1400E+15 0.0000 0.0000E+00  
 $C_3H_3+H \rightleftharpoons C_3H_2+H_2$  0.5000E+13 0.0000 0.0000E+00  
 $C_3H_3+OH \rightleftharpoons HCO+C_2H_3$  0.4000E+14 0.0000 0.0000E+00  
 $C_4H_2+H \rightleftharpoons C_4H_3$  0.1100E+31 -4.9200 0.1073E+05  
 $C_4H_2+H_2 \rightleftharpoons C_4H_4$  0.4000E+15 0.0000 0.5325E+05  
 $C_2H_2+C_2H \rightleftharpoons C_4H_3$  0.4170E+37 -7.3000 0.8723E+04  
 $C_3H_2+CH_2 \rightleftharpoons C_4H_3+H$  0.3000E+14 0.0000 0.0000E+00  
 $C_4H_3+H \rightleftharpoons C_4H_2+H_2$  0.5000E+14 0.0000 0.0000E+00  
 $C_4H_3+O \rightleftharpoons CH_2CO+C_2H$  0.2000E+14 0.0000 0.0000E+00  
 $C_4H_3+OH \rightleftharpoons C_4H_2+H_2O$  0.3000E+14 0.0000 0.0000E+00  
 $C_4H_3+H_2 \rightleftharpoons C_2H_2+C_2H_3$  0.5010E+11 0.0000 0.1987E+05  
 $C_4H_3+C_2H_3 \rightleftharpoons 2C_3H_3$  0.4000E+13 0.0000 0.0000E+00  
 $C_4H_4 \rightleftharpoons 2C_2H_2$  0.3400E+14 0.0000 0.7664E+05  
 $C_4H_4+M \rightleftharpoons C_4H_3+H+M$  0.1100E+21 0.0000 0.9863E+05  
 $C_4H_4+O \rightleftharpoons HCO+C_3H_3$  0.3200E+09 1.4400 0.5494E+03  
 $C_3H_3+CH_2 \rightleftharpoons H+C_4H_4$  0.4000E+14 0.0000 0.0000E+00  
 $C_4H_4+C_2H \rightleftharpoons C_4H_2+C_2H_3$  0.1000E+14 0.0000 0.0000E+00  
 $C_4H_4+C_2H \rightleftharpoons C_4H_3+C_2H_2$  0.4000E+14 0.0000 0.0000E+00  
 $C_4H_5 \rightleftharpoons C_2H_3+C_2H_2$  0.1000E+15 0.0000 0.4361E+05  
 $C_4H_5(+M) \rightleftharpoons C_4H_4+H(+M)$  0.1000E+15 0.0000 0.4968E+05  
LOW/0.2000E+16 0.0000E+00 0.4173E+05/  
 $C_4H_5+O_2 \rightleftharpoons C_4H_4+HO_2$  0.1000E+13 0.0000 0.2980E+04  
 $C_4H_5+H \rightleftharpoons C_4H_4+H_2$  0.1000E+15 0.0000 0.0000E+00  
 $C_4H_5+OH \rightleftharpoons C_4H_4+H_2O$  0.2000E+08 2.0000 0.9991E+03  
 $C_4H_5+C_2H \rightleftharpoons 2C_3H_3$  0.4000E+13 0.0000 0.0000E+00  
 $C_3H_3+C_2H_3 \rightleftharpoons C_5H_5+H$  0.9600E+41 -7.8000 0.2863E+05  
 $C_3H_3+C_2H_2 \rightleftharpoons C_5H_5$  0.2400E+12 0.0000 0.9995E+04  
 $C_5H_5+O \rightleftharpoons C_4H_5+CO$  0.1000E+14 0.0000 0.0000E+00  
 $C_5H_5+OH \rightleftharpoons CH_2O+2C_2H_2$  0.2000E+13 0.0000 0.0000E+00  
 $C_6H_5O \rightleftharpoons C_5H_5+CO$  0.7400E+12 0.0000 0.4391E+05  
 $2C_3H_3 \rightleftharpoons A_1$  0.1000E+37 -7.1800 0.8413E+04  
 $2C_3H_3 \rightleftharpoons A_1+H$  0.3000E+36 -7.1800 0.8413E+04

C4H3+C2H3<=>A1 0.3000E+14 0.0000 0.0000E+00  
 C4H3+C2H3<=>A1-+H 0.6000E+13 0.0000 0.0000E+00  
 C2H3+C4H4<=>A1+H 0.1900E+13 0.0000 0.2484E+04  
 C4H3+C2H2<=>A1- 0.5000E+14 0.0000 0.1480E+05  
 C4H4+C2H2<=>A1-+H 0.1000E+10 0.0000 0.2980E+05  
 C4H5+C2H2<=>A1+H 0.1600E+16 -1.3300 0.5365E+04  
 C4H5+C2H3<=>A1+H2 0.1800E-12 7.0700 -.3577E+04  
 C4H5+C2H<=>A1 0.1000E+14 0.0000 0.0000E+00  
 C4H5+C2H<=>A1-+H 0.6000E+13 0.0000 0.0000E+00  
 A1<=>A1-+H 0.9000E+15 0.0000 0.1074E+06  
 A1<=>C4H4+C2H2 0.9000E+15 0.0000 0.1074E+06  
 A1+O2<=>A1-+HO2 0.6000E+14 0.0000 0.6259E+05  
 A1+O<=>A1-+OH 0.2000E+14 0.0000 0.1470E+05  
 A1+O<=>C6H5O+H 0.2200E+14 0.0000 0.4530E+04  
 A1+H<=>A1-+H2 0.2510E+15 0.0000 0.1602E+05  
 A1+OH<=>A1-+H2O 0.1450E+14 0.0000 0.4491E+04  
 A1+C2H<=>A1-+C2H2 0.2000E+14 0.0000 0.0000E+00  
 A1-+O<=>C5H5+CO 0.1000E+15 0.0000 0.0000E+00  
 A1-+OH<=>C6H5O+H 0.5000E+14 0.0000 0.0000E+00  
 C4H5+C4H2<=>A1C2H+H 0.3160E+12 0.0000 0.1788E+04  
 A1C2H-+H(+M)<=>A1C2H(+M) 0.1000E+15 0.0000 0.0000E+00  
 LOW/0.6600E+76 -.1630E+02 0.1391E+05/  
 TROE/0.1000E+01 0.1000E+00 0.5849E+03 0.6113E+04/  
 H2/ 2.000/ H2O/ 6.000/ CO/ 1.500/  
 C4H3+C4H2<=>A1C2H- 0.9600E+71 -17.7700 0.3112E+05  
 A1-+C4H2<=>A1C2H+C2H 0.2000E+14 0.0000 0.2186E+05  
 A1-+C2H3<=>A1C2H+H2 0.7900E+13 0.0000 0.6358E+04  
 A1-+C4H4<=>A1C2H+C2H3 0.3200E+12 0.0000 0.1352E+04  
 A1+C2H<=>A1C2H+H 0.1000E+13 0.0000 0.0000E+00  
 A1-+C2H<=>A1C2H 0.5240E+15 -0.5000 0.5961E+03  
 A1C2H+O<=>A1C2H-+OH 0.1100E+14 0.0000 0.8147E+04  
 A1C2H+O<=>C6H5O+C2H 0.2200E+14 0.0000 0.4491E+04  
 A1C2H+H<=>A1C2H-+H2 0.2700E+14 0.0000 0.9701E+04

A1C2H+H<=>A1-+C2H2 0.2000E+15 0.0000 0.9701E+04  
 A1C2H+OH<=>A1C2H-+H2O 0.2100E+14 0.0000 0.4570E+04  
 A1C2H+OH<=>A1-+CH2CO 0.2180E-03 4.5000 -.9935E+03  
 A1C2H+C2H<=>A1C2H-+C2H2 0.2000E+14 0.0000 0.0000E+00  
 2C4H4<=>A1C2H3 0.1800E+21 -1.9000 0.4020E+05  
 C4H5+C4H4<=>A1C2H3+H 0.3160E+12 0.0000 0.5961E+03  
 A1+C2H3<=>A1C2H3+H 0.7900E+12 0.0000 0.6358E+04  
 A1-+C2H3<=>A1C2H3 0.1060E+27 -4.0000 0.5266E+04  
 A1-+C2H4<=>A1C2H3+H 0.2510E+13 0.0000 0.6150E+04  
 A1C2H3+O<=>A1-+CH2CHO 0.3000E+09 1.4500 0.8942E+03  
 A1C2H3+O<=>A1-+CH3+CO 0.1920E+08 1.8300 0.2186E+03  
 C4H5+A1=>A2+H2+H 0.5000E+12 0.0000 0.2987E+04  
 2C5H5<=>A2+2H 0.4300E+14 0.0000 0.9713E+04  
 2C5H5<=>A2+H2 0.4300E+37 -6.3000 0.4537E+05  
 A1-+C4H3<=>A2 0.3180E+24 -3.2000 0.4232E+04  
 A1-+C4H3<=>A2-+H 0.2000E-09 7.1000 0.1562E+04  
 A1-+C4H4<=>A2+H 0.3300E+34 -5.7000 0.2533E+05  
 A1C2H-+C2H2<=>A2- 0.4000E+14 0.0000 0.1013E+05  
 A2+O<=>CH2CO+A1C2H 0.2200E+14 0.0000 0.4501E+04  
 A2+O<=>A2-+OH 0.2000E+14 0.0000 0.1470E+05  
 A2+H<=>A2-+H2 0.2500E+15 0.0000 0.1590E+05  
 A2+OH<=>A2-+H2O 0.2100E+14 0.0000 0.4570E+04  
 A2+OH=>A1C2H+CH2CO+H 0.1300E+14 0.0000 0.1053E+05  
 A2-+H<=>A2 0.7800E+14 0.0000 0.0000E+00  
 A1C2H-+C4H4<=>A2r5+H 0.1600E+17 -1.3300 0.6557E+04  
 A2-+C2H2<=>A2r5+H 0.1900E+32 -5.2600 0.2086E+05  
 A2r5<=>A1C2H+C4H2 0.2000E+17 0.0000 0.1152E+06  
 A2r5+OH<=>A2-+CH2CO 0.1000E+14 0.0000 0.9935E+04  
 C4H2+A2r5=>A4 0.2413E+03 2.2313 -.1131E+04  
 A1C2H+A1C2H-<=>A4+H 0.1100E+25 -2.9200 0.1592E+05  
 A2+A1-<=>A4+H+H2 0.1000E+12 0.0000 0.4968E+04  
 A2-+A1<=>A4+H+H2 0.1000E+13 0.0000 0.4968E+04  
 A2-+A1=>A4+H2 0.4300E+38 -6.3000 0.4477E+05

A1C2H+A1<=>A3+H 0.1100E+24 -2.9200 0.1592E+05  
A1C2H+A1<=>A3+H 0.1100E+24 -2.9200 0.1592E+05  
A2+C4H4<=>A3+H 0.3300E+34 -5.7000 0.2533E+05  
A2+C4H2<=>A3- 0.3300E+34 -5.7000 0.2533E+05  
A2r5+C2H2=>A3 0.2765E+05 2.4500 0.2908E+05  
A2+C4H2=>A3 0.2765E+05 2.4500 0.2908E+05  
A3+O<=>A3+OH 0.2000E+14 0.0000 0.1470E+05  
A3+H<=>A3+H2 0.2500E+15 0.0000 0.1590E+05  
A3+OH<=>A3+H2O 0.1700E+13 1.4200 0.1496E+04  
A3+O2=>CO+HCO+A2r5 0.2000E+13 0.0000 0.7352E+04  
A3+H<=>A3 0.1000E+15 0.0000 0.0000E+00  
A3+C2H2<=>A4+H 0.6600E+25 -3.3600 0.1768E+05  
A4+OH<=>A3+CH2CO 0.2000E+14 0.0000 0.4173E+05